Proceeding of

The 22nd International Symposium on Advanced Technology (ISAT-22)

Advanced Technologies for Carbon Neutrality and SDGs Achievement

October 19-20, 2023
Southern Taiwan University of Science and Technology
Tainan, Taiwan

Directed by

Ministry of Education, Republic of China (Taiwan)

Organized by

Southern Taiwan University of Science and Technology, Taiwan

Co-organized by

Kogakuin University, Japan
Danang University of Science and Technology, Vietnam
University of the Philippines Los Baños, Philippines

Edited by
The 22nd International Symposium on Advanced Technology (ISAT-22)

Contents

Director

Ministry of Education, Republic of China (Taiwan)
https://english.moe.gov.tw/mp-1.html

Organizer

Southern Taiwan University of Science and Technology
https://www.stust.edu.tw/en/

Co-organizer

Kogakuin University, Japan
https://www.kogakuin.ac.jp/english/

Danang University of Science and Technology, Vietnam
https://dut.udn.vn/EN

University of the Philippines Los Baños, Philippines
https://uplb.edu.ph/

Welcome Message from President of STUST

President

October 19th, 2023 **Dr. Cheng-Wen Wu**

Welcome to "The 22nd International Symposium on Advanced Technology (2023 ISAT)". On behalf of Southern Taiwan University of Science and Technology (STUST), it is our great honor and pleasure to welcome all of you to Tainan, and appreciate your participation and contribution.

This conference is organized and held alternately every year by Kogakuin University, Japan, Danang University of Science and Technology, Vietnam, University of the Philippines Los Baño, the Philippines, and Southern Taiwan University of Science and Technology, Taiwan. The main theme of the ISAT-22 focuses on "Advanced Technologies for Carbon Neutrality and SDGs Achievement". This purpose of this symposium is to provide an international scientific forum to experts and scholars for discussion and exchange of ideas on the up-to-date research, development and application of advanced technologies. With strong support and contribution from ISAT-22 participants, there are more than 100 attendees from 2 countries. More than 70 papers have been received in this conference, including 1 keynote lecture, 31 oral presentations and 41 poster presentations covering the topics of ISAT-22.

We would like to express our sincere appreciation of valued contribution to Prof. Hanwool Woo from Kogakuin University, Japan as keynote to give remarkable lecture. We would like to express our sincere thanks to all of the invited VIPs and participants of ISAT-22. We sincerely appreciate the generous financial support from Ministry of Education.

Finally, we would like to deeply appreciate all the participants for your support and contribution to this conference. We would also like to express our sincere wishes for the success of the conference. We hope you all enjoy the conference and have a wonderful stay in Tainan and in Taiwan.

Cheng-Wen Wu

我謹代表南臺科技大學的全體師生，誠摯地歡迎各位蒞臨南臺科技大學，參加「第 22 屆先端科技國際研討會」，同時也感謝各位的參與及貢獻。

ISAT 國際研討會，是由日本工學院大學、越南峴港科技大學、菲律賓大學洛斯巴尼奧斯分校，以及南臺科技大學等四校每年輪流主辦。ISAT-22 的主題為「碳中和和實現永續發展目標的先端技術」，本屆會議的目的是為專家學者就先進技術的最新研究、開發和應用提供一個國際性的科學論壇，進行廣泛的討論和交流。在與會者的全力支持與貢獻下，共有來自 2 個國家的 100 多位國內外學者專家參與此次的國際研討會。本屆研討會總計有 70 餘篇投稿論文，其中有特邀主題演講 1 篇、口頭發表 31 篇以及海報發表 41 篇；內容涵蓋本屆大會各項議題。

我們誠摯的感謝日本工學院大學 Hanwool Woo 教授擔任特邀主題講座，發表卓越演說，對大會的重大貢獻，也謹向來自各國的貴賓以及與會者表達感謝之意。我們衷心感謝教育部對本屆大會經費的慷慨支持。

最後，我們感謝所有與會者對本屆研討會的支持與貢獻，並祝福大會圓滿成功。我們希望大家能享受這次的研討會，並在臺南市和臺灣度過愉快的時光。

Organization Committee

Chairperson

- **Prof. Cheng-Wen Wu**

  President of Southern Taiwan University of Science and Technology

Co-Chairperson

- **Prof. Huu Hieu Nguyen**

  President of Danang University of Science and Technology
- **Prof. Shinichiro ITO**

  President of Kogakuin University
- **Prof. Jose V. Camacho, Jr.**

  Chancellor of University of the Philippines Los Baños

Vice-Chairperson

- **Prof. Ruey-Hsing Chang**

  Vice President of Southern Taiwan University of Science and Technology
- **Prof. Le Tien Dung**

  Vice President of Danang University of Science and Technology
- **Prof. Miyuki KAMACHI**

  Vice President of Kogakuin University
- **Prof. Jean O. Loyola**

  Vice Chancellor of University of the Philippines Los Baños
- **Prof. Yasushi NOZAWA**

  Vice President of Kogakuin University

Executive Chairperson

- **Prof. Cheng-Chien Wang**

  Southern Taiwan University of Science and Technology

Vice Executive Chairperson

- **Prof. Ming-Tsung Tsai**

  Southern Taiwan University of Science and Technology

Executive Committee Members

- Prof. Sheng-Chang Wang

  Southern Taiwan University of Science and Technology

- **Prof. Yeou-Jiunn Chen**

  Southern Taiwan University of Science and Technology
- **Prof. Gwo-Jiun Horng**

  Southern Taiwan University of Science and Technology
- **Prof. Lih-Yang Wang**

  Southern Taiwan University of Science and Technology
- **Prof. Chang-Ning Huang**

  Southern Taiwan University of Science and Technology
- **Prof. Ruey-Ching Twu**

  Southern Taiwan University of Science and Technology
- **Prof. Da-Wei Huang**

  Southern Taiwan University of Science and Technology

Program Chairperson

- **Prof. Cheng-Chien Wang**

  Southern Taiwan University of Science and Technology

Program Committee Members

- **Prof. Sheng-Chang Wang**

  Southern Taiwan University of Science and Technology
- **Prof. Keh-Moh Lin**

  Southern Taiwan University of Science and Technology
- **Prof. Yu-Sheng Lin**

  Southern Taiwan University of Science and Technology
- **Prof. Nai-Shang Liou**

  Southern Taiwan University of Science and Technology

Secretariat

- **Prof. Nai-Shang Liou**

  Southern Taiwan University of Science and Technology

2023 International Symposium on Advanced Technology (ISAT-22) Program

Southern Taiwan University of Science and Technology, Tainan, Taiwan

October 19 - 20, 2023

<table>
<tr><th colspan="4">October 19th, 2023 [Thursday]</th></tr>
<tr><td>11:00-12:00</td><td colspan="3">Registration</td></tr>
<tr><td>12:00-13:30</td><td colspan="3">Lunch</td></tr>
<tr><td>13:30-14:00</td><td colspan="3">Opening Ceremony (Building L / L008)
Opening Remark: Prof. Te-Kuang Chou
The Vice President of Southern Taiwan University of Science and Technology, Taiwan</td></tr>
<tr><td>14:00-14:10</td><td colspan="3">Group Photo</td></tr>
<tr><td>14:10-14:50</td><td colspan="3">Keynote Lecture (Building L / L008)
Prof. Hanwool Woo
Faculty of Engineering, Kogakuin University, Tokyo, Japan
Title: Towards Human-Robot Coexistence: Development of Autonomous Navigation Technologies
Chair: Prof. Shuichi Torii</td></tr>
<tr><td>15:00-16:10</td><td>Oral Session - A
Topics 1 & 7
(Building L / L008)
JP-12
TW-21
TW-24
JP-27
JP-52
JP-60

Chair: Prof. Yung-Peng Wang</td><td>Oral Session - B
Topics 3 & 4
(Building L / L001)
JP-25
TW-17
TW-25
JP-17
JP-29
JP-51

Chair: Prof. Ching-Hua Wei</td><td rowspan="2">Poster Session

Chair: Prof. Kai-Chieh Chuang</td></tr>
<tr><td>16:10-16:30</td><td colspan="2">Coffee Break</td></tr>
<tr><td>16:30-17:40</td><td>Oral Session - C
Topics 3 & 5
(Building L / L008)
TW-19
TW-26
JP-13
JP-18
JP-28
JP-34

Chair: Prof. Chin-Juei Tung</td><td>Oral Session - D
Topic 8
(Building L / L001)
JP-24
JP-54
TW-13
TW-14
TW-27

Chair: Prof. Masaki Tamura</td><td></td></tr>
<tr><td>18:30-21:00</td><td colspan="3">Banquet
(Queena Plaza Hotel)</td></tr>
<tr><th colspan="4">October 20th, 2023 [Friday]</th></tr>
<tr><td>10:20-11:10</td><td>Oral Session - E
Topic 5
(Building L / L008)
JP-35
JP-43
JP-44
JP-65

Chair: Prof. Wei-Chin Chang</td><td>Oral Session - F
Topic 6
(Building L / L001)
JP-40
JP-47
JP-64
TW-20

Chair: Prof. Chin-Tu Lu</td><td></td></tr>
<tr><td>11:20-12:00</td><td colspan="3">Closing Ceremony (Building L / L008)
Closing Remark: Prof. Te-Kuang Chou
The Vice President of Southern Taiwan University of Science and Technology, Taiwan</td></tr>
<tr><td>12:00-13:30</td><td colspan="3">Lunch</td></tr>
<tr><td>14:00-17:00</td><td colspan="3">City Tour
Anping Tree House, Anping Fort</td></tr>
</table>

2023 International Symposium on Advanced Technology (ISAT-22)

Oral Session

Session A 10/19 15:00-16:10 (L008) *Chair: Prof. Yung-Peng Wang*	
Paper No.	**Title / Author / Affiliation**
JP-12	**SSVEP-BCI Text Spelling System Mimicking Keyboard Layout** Na Qianwen, Tanaka Hisaya *Graduate School of Kogakuin University*
TW-21	**The effect of the drying methods on the texture properties of banana** Quoc Thien Pham[1], Pawan Rajput[2], Sheng-En Lu[2], Yu-Hsuan Huang[2], Cheng-Hsuan Chiang[2], Nai-Shang Liou[2] *[1]HUTECH University; [2]Southern Taiwan University of Science and Technology*
TW-24	**Image-based Classification and Analysis of Hospital Dishes for Nutritional Monitoring and Personalized Care** Yao-Lin Zhang[1], Wen Yao She[2] and Yu-Sheng Lin[1] *[1]Southern Taiwan University of Science and Technology; [2]National Kaohsiung University of Science and Technology*
JP-27	**Survey and Estimation of the Actual Amount of Scrap in Residential Ceramic Siding Processing Factories and On-Site Treatment** Hiwatashi Natsu, Tamura Masaki *Kougakuin University*
JP-52	**LCCO₂ Evaluation and Proposal of the Measures for Environmental Impact Reduction focusing on the Material Manufacturing, Fabrication, and Construction on site Phases of Steel-framed Buildings in Japan** Takuto Kobayashi, Masaki Tamura, Kenji Yamaoka, and Kazuaki Miyagawa *Kogakuin University*
JP-60	**Development and basic property evaluation of mortar for 3D printer using sea shells waste with blue carbon fixation properties** Natsuka HOSODA, Kikuno IGUCHI, Masaki TAMURA, Tetsuya SASAKI, Takashi SAITO, Ryota OZEKI, Taichi YAMAMOTO, Ayano KOSEKI *Kogakuin University*

Session B 10/19 15:00-16:10 (L001) *Chair: Prof. Ching-Hua Wei*	
Paper No.	**Title / Author / Affiliation**
JP-25	**A Study on Link Load Balancing Method in Elastic Optical Networks Using Superposition Coding** Shota Okochi and Ken-ichi Baba *Kogakuin University*
TW-17	**Microstrip Grid Array with Two Elements for WLAN 5.8GHz Band** Bing-Hong Cai and Wen-Shan Chen *Southern Taiwan University of Science and Technology*
TW-25	**Using Discrete Cosine Transform for Automated Pattern Recognition**

	Kai-Hsien Chen, Zheng-Quan Wang, Ming-Hua Chen, and Gwo-Jiun Horng *Southern Taiwan University of Science and Technology*
JP-17	**Implementation and Evaluation of Key Sharing Method in Information-Centric Networking based Wireless Sensor Networks** Takafumi Taya, Osamu Mizuno *Kogakuin University*
JP-29	**Investigation of the thermosensitive mechanism in the interface of TiO_2/Cu_2O thin-film temperature sensors** Reika Miyajima, Ichiro Takano *Kogakuin University*
JP-51	**Three-dimensional Residual Stress Estimation of a Resistance Spot-welded Plate using the Eigenstrain Theory and X-ray Diffraction** Kensei Miyoshi, Toshinori Tanaka, and Masaru Ogawa *Graduate School of Kogakuin University*

Session C 10/19 16:30-17:40 (L008) *Chair: Prof. Chin-Juei Tung*	
Paper No.	**Title / Author / Affiliation**
TW-19	**Antennas on Smart Watch for GPS/BT/Wi-Fi 6E Applications** Yong-Zhi Su and Wen-Shan Chen *Southern Taiwan University of Science and Technology*
TW-26	**Application of Face Image Recognition in Sleep-deprived Driving Warning System** Yen-Yu Chen, Huai-Wen Hsu, and Gwo-Jiun Horng *Southern Taiwan University of Science and Technology*
JP-13	**Non-destructive evaluation of 3-D creep strain in the whole turbine blade using surface displacement** Satoshi Fujii, and Masaru Ogawa *Graduate School of Kogakuin University*
JP-18	**Jet Vectoring using Coanda Surface with Distributed Suction Slots** K. Suzuki[1], K. Nishibe[2], K. Sato[1] *[1]Kogakuin University; [2]Tokyo City University*
JP-28	**Behavior of Jet Flow with Coanda Curvature on One Side of Slot Outlet** Hiroki Tezuka, Kaito Yabu, Koichi Nishibe, and Kotaro Sato *Kogakuin University*
JP-34	**Development of Accelerated Calendar-life Evaluation Method for Lithium-Sulfur Batteries** Kento Okanishi[a], Uran Tsunoda[a], Masayoshi Watanabe[b] and Shiro Seki[a] *[a]Kogakuin University; [b]Yokohama National University*

Session D 10/19 16:30-17:40 (L001) *Chair: Prof. Masaki Tamura*	
Paper No.	**Title / Author / Affiliation**
JP-24	**Terrain Roughness Estimation Using 3D LiDAR for Mobile Robots** Tsubasa Abe and Hanwool Woo

	Kogakuin University
JP-54	**Automatic Exploration Method for Identification of Multiple Radiation Sources** Yurika TAKAHASHI and Hanwool WOO *Kogakuin University*
TW-13	**The Development and Achievement of Contactless Transport Stage with Acoustic Levitation Technology** Yu-Ting Chen, and Sheng-He Wang *Southern Taiwan University of Science and Technology*
TW-14	**Developement and Achievement of An Intelligent Safety System for Robot Arm Operation Based on Vision Learning Technology** Wei Fu, Kuo, Sheng He, Wang *Southern Taiwan University of Science and Technology*
TW-27	**Development of a Bluetooth-Based Rehabilitation Ball and Its Corresponding Interactive Games** Jeng-Han Li, Yu-Chin Lin, Wei-Ting Hou, Tien-Yu Hsu, Yu-Xiang Hong, and You-Cheng Kang *Southern Taiwan University of Science and Technology*

Session E 10/20 10:20-11:10 (L008) *Chair: Prof. Wei-Chin Chang*	
Paper No.	**Title / Author / Affiliation**
JP-35	**Behavior of Synthetic Jet Produced by Double Slots** M. Takano[1], M. Katano[1], K. Nishibe[2], and K. Sato[1] *[1]Kogakuin University; [2]Tokyo City University*
JP-43	**Entrainment Characteristics of Plane Jets Passing Over Tow-Dimensional Flat Plates** Kota Ishiwata[1], Koichi Nishibe[2] and Kotaro Sato[1] *[1]Kogakuin University; [2]Tokyo City University*
JP-44	**Elucidation of the behavior of synthetic jets impinging on the flat plate** Michiya Yasumiba[1], Koichi Nishibe[2], and Kotaro Sato[1] *[1]Kogakuin University; [2]Tokyo City University*
JP-65	**Dynamic Behavior of Two Cavitation Bubbles Induced near a Rigid Boundary** Y. KUBOTA[1], D. KANG[2], A. KIYAMA[2] and K. SATO[1] *[1]Kogakuin University; [2]Saitama University*

Session F 10/20 10:20-11:10 (L001) *Chair: Prof. Chin-Tu Lu*	
Paper No.	**Title / Author / Affiliation**
JP-40	**Semiconductor Properties of Ti-doped ZnO Transparent Conductive Thin Films** Naoya Utsu, Ichiro Takano *Kogakuin University*
JP-47	**Influence of TiO_2 film thickness variation on photocatalytic properties of TiO_2/Ti-Cu-O photocatalysts**

	Ritsuki Kakizawa, Ichiro Takano *Kogakuin University*
JP-64	**Phase Control of Copper Oxides by Changing Temperatures and Gas Types in Growth of Mist CVD** N. Sugita, S. Yoshida, H. Nagai, T. Onuma, T. Honda, and T. Yamaguchi *Kogakuin University*
TW-20	**532nm Green Laser Annealing for Improving the Physical Properties of ITO/Ag/ITO and AZO/Ag/AZO Transparent Conducting Electrodes** Manikandan Rajendran[1], Keh-Moh Lin[1], Wen-Tse Hsiao[2] *[1]Southern Taiwan University of Science and Technology; [2]National Applied Research Laboratories*

2023 International Symposium on Advanced Technology (ISAT-22)

Poster Session

10/19 15:00-16:10

Chair: Prof. Kai-Chieh Chuang

Paper No.	Title / Author / Affiliation
JP-11	**A Study on a Vision Transformer Model with Squeeze-and-Excitation Blocks for a Generative Adversarial Network Model** Tatsuhiko Ikeda and Hidetoshi Saito *Kogakuin University*
JP-14	**Measuring Facial Sway Using the Front Camera of a Smartphone** Shunki SUZUKI and Hisaya TANAKA *Kogakuin University*
JP-15	**Nonhazardous Extraction of Gold from Electronic Waste** Miku Yoshizawa and Tomohide Takami *Kogakuin University*
JP-16	**Enhancing Trust in Human-Machine Collaboration: An Analysis of Contributing Factors to Transportation Accidents** Kazuma Shirakawa and Daigo Misaki *Kogakuin University*
JP-19	**Demand Forecasting of Bus Ridership in Sightseeing Areas with Considering both Passenger Convenience and Business Profitability** Ibuki Enomoto, Yoshio Miki *Kogakuin University of Technology & Engineering*
JP-20	**Diversity Experience using the Human Augmentation and impact on Design** Samu Hong and Daigo Misaki *Kogakuin University of Mechanical Engineering*
JP-21	**Adapting Design Thinking to engineering education in the Asian context** Daigo Misaki *Kogakuin University*
JP-22	**Relation between composition ratio and electrical properties in MgNiZnO films prepared by RF magnetron sputtering** A. Ishikawa[1], M. Murayama[1], T. Akiba[1], T. Yamaguchi[1], T. Honda[1], K. Sasaki[2], A. Kuramata[2] and T. Onuma[1] *[1]Kogakuin University; [2]Novel Crystal Technology, Inc.*
JP-23	**Optical transitions in rocksalt-structured MgZnO based metal-semiconductor-metal-type VUV sensor** H. Kusaka[1], K. Ogawa[1], T. Mitomi[1], K. Kaneko[2], T. Yamaguchi[1], T. Honda[1], S. Fujita[3] and T. Onuma[1] *[1]Kogakuin University; [2]Ritsumeikan University; [3]Kyoto University*
JP-26	**Positive Preparation and Electrochemical Characterization Containing Highly-Concentrated Electrolyte for High Performance Clay-Type All-Solid-State Batteries** Keigo Suzuki, Takaaki Ichikawa, Rintaro Mogi and Shiro Seki *Kogakuin University*
JP-30	**An Objective Method to Compare CT Data of Normal and Malformed Cochlea**

	Yuta Miura[1], Taku Ito[2], Takeshi Tsutsumi[2] and Yutaka Fukuoka[1] *[1]Kogakuin University; [2]Tokyo Medical and Dental University*
JP-31	**Evaluation Methods for Learning Attitude Using Head Sway Assessment System** Hiroki Horiuchi[1,2] and Hisaya Tanaka[1] *[1]Graduate School of Kogakuin University; [2]Kanagawa Prefectural Yokohama Shuyukan High School*
JP-32	**A proposal of a method to get recommendations for unknown different fields from known preference information** Ami Ehara and Yoshio Miki *Kogakuin University of Technology and Engineering*
JP-36	**Forming and Mechanical Properties of Thin Porous Metals** Haruto Tada and Masanori Shiomi *Kogakuin University*
JP-37	**Improvement of photoelectric conversion efficiency of Cu_xO/TiO_2 thin film solar cells** Shunta Endo and Ichiro Takano *Kogakuin university*
JP-38	**HCl-assisted Mist CVD Growth and Electrical Properties of α-In_2O_3 Films Using Various In-based Materials** T. Yamamoto, A. Taguchi, R. Yamada, H. Nagai, T. Onuma, T. Honda, and T. Yamaguchi *Kogakuin University*
JP-39	**Sn-doped α-Ga_2O_3 Films Grown Using Sn Source Solutions with Different Aging Times and Their Electrical Properties** Ko. Yamada, T. Yamamoto, R. Yamada, Ka. Yamada, H. Nagai, S. Aikawa1, T. Onuma, T. Honda and T. Yamaguchi *Kogakuin University*
JP-41	**Research on UIUX Evaluation using Heart Rate Variability of Wearable Devices** Kota Yamamoto and Daigo Misaki *Kogakuin University*
JP-42	**Study on high-speed growth of β-Ga_2O_3 by Mist CVD method** M. Sugitani[1], T. Yamaguchi[1], K. Sasaki[2], A. Kuramata[2], T. Honda[1], and T. Onuma[1] *[1]Kogakuin University; [2]Novel Crystal Technology, Inc.*
JP-45	**Realization of Cathodoluminescence in 190 nm Wavelength Range in Rocksalt-Structured MgZnO Films Grown by Mist Chemical Vapor Deposition** Kotaro Ogawa[1], Wataru Kosaka[1], Hiroya Kusaka[1], Yuichi Ota[2], Tomohiro Yamaguchi[1], Tohru Honda[1], Kentaro Kaneko[3], Shizuo Fujita[4] and Takeyoshi Onuma[1] *[1]Kogakuin University; [2]Tokyo Metropolitan Industrial Technology Research Institute; [3]Ritsumeikan University; [4]Kyoto University*
JP-46	**Proposal for Teaching Methods of Programmatic Thinking in the Field of Programming Education** Masato Tasaki and Yoshio Miki *Kogakuin University of Technology and Engineering*
JP-48	**Evaluation of ZnO thin film on Ar plasma treated CNF** Kai Ishikawa and Ichiro Takano *Kogakuin University*

JP-49	**Comparison of α-particle Detection Property of α-Ga_2O_3 and α-GIO Alloys Grown by Mist CVD** Kai Yamada[1], Kotono Yamada[1], Rie Yamada[1], Takumi Yamamoto[1], Tatsuhiro Sakurai[2], Ryohei Kudo[2], Takeyoshi Onuma[1], Tomohiro Yamaguchi[1], Toru Aoki[2], Takayuki Nakano[2] and Tohru Honda[1] *[1]Kogakuin University; [2]Shizuoka University*
JP-50	**Assessing Spatial Elements for Enhanced Creativity: A Comparative Study Within Kogakuin University's Campus** Keigo Hayakawa and Daigo Misaki *Kogakuin University*
JP-53	**Analysis of Echocardiographic Probe Attitude for Improve Technical Proficiency** Daiki Sekine[1], Junji Yamato[1], Dan Mikami[1], Yasuyoshi Takei[2] *[1]Kogakuin University; [2]Tokyo Medical University*
JP-55	**Early Detection of Cognitive Decline Using Anteroposterior Asymmetry of Brain Activity During Visual Attention Task** Hiroyuki ABE[1], Hisaya TANAKA[1], Akito TSUGAWA[2], Naoto TAKENOSHITA[2], Tomohiko SATO[2] and Soichiro SHIMIZU[2] *[1]Kogakuin University; [2]Tokyo Medical University*
JP-57	**Dependence of N^+ or N_2^+ ion implantation on photocatalytic properties of anodic niobium oxides** Masayuki Ikeya, Hidetaka Asoh and Ichiro Takano *Kogakuin university*
JP-58	**Improved Simulation for Statistical Integrated Analysis Method of MicroRNA and Gene Expression** Keita Kodama and Yutaka Fukuoka *Kogakuin University*
JP-59	**Formation of ITO electrodes on InGaN-based p-n junction ordered nanocolumn arrays with different column periods** R. Shindo[1], H. Akagawa[1], T. Yamaguchi[1], R. Togashi[2], I. Nomura[2], T. Onuma[1], T. Honda[1], and K. Kishino[2] *[1]Kogakuin University; [2]Sophia University*
JP-61	**Inter-Disaster Communities and Memorial and Media in Disaster and Non-disaster Areas: Inter-disaster communities and memorials to share Knowledge from the Great East Japan Earthquake and the Great Kanto Earthquake** Haruka Sakuma *Kogakuin University Graduate School*
JP-62	**Functionally Graded Porous Metals with Multiple Materials** Hidekazu Miyazaki and Masanori Shiomi *Kogakuin University*
JP-63	**Fabrication of top-down and bottom-up MOSFET using α-In_2O_3 films grown by Mist CVD** Y. Hayashi, A. Taguchi, S. Yamadera, T. Yamamoto, S. Aikawa, T. Onuma, H. Honda, T. Yamaguchi *Kogakuin University*
TW-11	**Integrating Generative AI into Electronic Engineering Curricula: A Case Study on Digital System Design** Jung-Lin Yang and Yi-Wen Chan *Southern Taiwan University of Science and Technology*
TW-12	**Controllable Hortensia-like MnO_2 as an Efficient Electrocatalyst for**

	Supercapacitor Yu-Ming Chang[1], Chao-Ming Huang[2] and Yu-Chu M. Li[1] *[1]Southern Taiwan University of Science and Technology; [2]Kun Shan University*
TW-15	**Fabrication of Birefringent PEN Transducer for Flow Speed Variation Measurements** Chang-Hui Chen, Wen-Chi Hsu and Ruey-Ching Twu *Southern Taiwan University of Science and Technology*
TW-16	**Effect of Film Thickness on the Ethanol Sensing Sensitivity of Titanium Dioxide Gas Sensor** Hsyi-En Cheng[1], Bo-Jia Lin[2] and Zu-Po Yang[2] *[1]Southern Taiwan University of Science and Technology; [2]National Yang Ming Chiao Tung University*
TW-18	**Using FreeCAD as BIM Modeling tool** Po-Ming Lee *Southern Taiwan University of Science and Technology*
TW-22	**The Effect of Moisture on the Texture Properties of Dry Fruit (Banana)** Quoc Thien Pham[1], Md Niyaz Ahmad[2], Sheng-En Lu[2], Ya-Chi Kuo[2], Cheng-Wei Shih[2], De-Xian Lai[2] and Nai-Shang Liou[2] *[1]HUTECH University; [2]Southern Taiwan University of Science and Technology*
TW-23	**Based on Photography 3D Reconstruction Algorithm Combined with Autonomous Drone** Jia-Shing Shih, Cheng-Dian Zhan, FAN WEI-CHIEH, Ming-Sian Chen and Chong-Xiang Jian *Southern Taiwan University of Science and Technology*
TW-28	**A Deep Learning Framework for Steady-State Visual Evoked Potential Rapid Recognition - TransRANet** Yeou-Jiunn Chen and Pin-Wei You *Southern Taiwan University of Science and Technology*
TW-29	**Optical-Sensing Devices with Resonant-Cavity-Enhanced Structures of Porous-Silicon for Applications in Si-based Optoelectronic Integrated Circuits (OEIC's)** Kuen-Hsien Wu and Hung-Yi Li *Southern Taiwan University of Science and Technology*

Keynote Lecture

Prof. Hanwool Woo

Faculty of Engineering, Kogakuin University, Tokyo, Japan

E-mail: woo@cc.kogakuin.ac.jp

Education

PhD, Precision Engineering, 2018 The University of Tokyo, Tokyo, Japan

Professional Experience

- 2010-2014, Researcher, CTO HA Research Center, LG Electronics, South Korea
- 2018-2019, Postdoctoral Fellowship JSPS, Department of Precision Engineering, the University of Tokyo, Japan
- 2019-2020, Assistant Professor, Department of Intelligent Mechatronics, Akita Prefectural University, Japan
- 2020-2022, Project Lecturer, Institute of Engineering Innovation, the University of Tokyo, Japan
- 2022-Currently, Associate Professor, Department of Mechanical Systems Engineering, Faculty of Engineering, Kogakuin University, Japan
- Member of JSAE, RSJ, and IEEE

Research Interests

- Autonomous Driving, Robotics, and Teleoperation

Towards Human-Robot Coexistence: Development of Autonomous Navigation Technologies

Hanwool Woo

Faculty of Engineering, Kogakuin University, Tokyo, Japan
E-mail: woo@cc.kogakuin.ac.jp

Abstract

Conventional commercialized robots have been performing tasks in a controlled environment where has few external factors, therefore, stable operation can be achieved. On the other hand, future robots will be required to operate stably even in a crowded environment. Our research group have been working on autonomous navigation systems that guarantee the safe and robust operations in crowded environments. This paper introduces our approaches to realize autonomous navigation for mobile robots and self-driving cars.

1. Introduction

In an environment without human interruption, robots can perform their tasks and achieve stable operations. Most of conventional commercialized robots assume the controlled environments where has few unexpectable factors and interruptions. On the other hand, future robots will be required to operate stably even in a crowded environment. Our research group have been working on autonomous navigation systems that guarantee the safe and robust operations in crowded environments.

This paper describes our previous works related to autonomous navigation techniques. Autonomous navigation systems for mobile robots, self-driving cars, and advanced driving assistance systems are introduced.

2. Our works

Mobility systems that operate in crowded environments should be designed to be acceptable to humans. In order for mobility to be socially acceptable, it is necessary to respect the social manners, give importance to safety, and achieve moving efficiency. Conventional systems often operate under rules such as giving priority to humans first for safety. However, this may lead to decrease moving efficiency and fail their missions. Although safety would be improved, there are concerns that other traffic participants behind the host mobility are kept waiting large amounts of time or that it may reduce service satisfaction. To solve these problems, our approach is to predict future actions of surrounding traffic participants and make a decision based on the prediction results.

For autonomous mobile robots, we proposed a novel approach to foresee the future trajectories of surrounding pedestrians and accordingly plan safe paths to avoid any possible collision [1]. A prediction method based on an encoder-decoder framework using bidirectional recurrent neural network (BiRNN) was proposed. The proposed method handles the difficulty of incorporating social interactions between surrounding pedestrians through the special structure of BiRNN. Consequently, the proposed method is able to predict the future state of the pedestrians.

In addition, we proposed a method allowing the robot to keep an adapting distance from the pedestrians and performing safe navigation even in high density environments [2]. The proposed method considers the relationship between uncomfortable distance and pedestrian density, then, it is applied in reward shaping of deep reinforcement learning to get the resilient social distance. Hence, the proposed method achieves the social compliance to other pedestrians.

For self-driving cars, we proposed an advanced adaptive cruise control to evaluate the collision risk between adjacent vehicles and adjust the distance between them seeking to improve driving safety [3]. The proposed method allows estimating the operation characteristics of each driver and applying the estimated results to obtain the trajectory prediction. Then, the collision risk is evaluated based on such prediction. It was demonstrated that almost 35 % of the collision risk can be decreased by applying the proposed method compared to that of human drivers.

3. Conclusion

This paper introduced our previous works related to autonomous navigation in crowded environments. As future work, we plan to construct a navigation method to respect the social manners, especially autonomous driving. We are trying to construct a navigation method to consider both safety and efficiency.

References:

[1] J. Wu, H. Woo, Y. Tamura, A. Moro, S. Massaroli, A. Yamashita and H. Asama, Pedestrian trajectory prediction using BiRNN encoder–decoder framework, *Advanced Robotics*, **33** (18), 956–969 (2019).

[2] X. Lu, H. Woo, A. Faragasso, A. Yamashita and H. Asama, Socially aware robot navigation in crowds via deep reinforcement learning with resilient reward functions, *Advanced Robotics*, **36** (8), 388–403 (2022).

[3] H. Woo, H. Madokoro, K. Sato, Y. Tamura, A. Yamashita and H. Asama, Advanced adaptive cruise control based on operation characteristic estimation and trajectory prediction, *Applied Sciences*, **9** (22), (2019).

南臺科技大學
Southern Taiwan University of Science and Technology

校園導覽地圖

A棟	電機系(一) Dept. of Electrical Engineering (I)
B棟	電機系(二) Dept. of Electrical Engineering (II)
C棟	資工系 Dept. of Computer Science & Information Engineering
D棟	普通教室 General Classroom
E棟	修齊大樓 \ 圖書館 \ 計算機與網路中心 \ 商管學院 Shiu-Chi Building \ Library \ Computer & Information Network Center \ College of Business(EMBA \ GMBA)
F棟	學務處衛生保健組 \ 諮商輔導組 Office of Student Affairs(Health Care Division \ Counseling & Guidance Division)
G棟	學生社團大樓 \ 體育中心 Student Clubs \ Physical Education Center
I棟	工學院 \ 化工系 \ 食品系 College of Engineering \ Dept. of Chemical & Materials Engineering \ Dept. of Biotechnology & Food Technology
J棟	電子系 Dept. of Electronic Engineering
K棟	機械系 Dept. of Mechanical Engineering
L棟	行政大樓 Administration Building 學務處生活輔導組 \ 課外活動組 Office of Student Affairs(Living Supervision Division \ Extracurricular Activities Division) 教務處 Office of Academic Affairs 總務處 Office of General Affairs 祕書室 Office of the Secretariat 稽核室 Office of Internal Audit 人事室 Office of Personnel Services 會計室 Accounting Office 研發處 Office of Research and Development 國際處 Office of International Affairs 校務發展中心 Center for Institutional Development USR中心 Center for University Social Responsibility 環安室 Office of Environmental Safety and Health 軍訓室 Office of Military Training
M棟	人文藝術中心 \ 通識中心 Center for Arts and Humanities \ Center for General Education
N棟	文病館 \人文社會學院 \應英系 \應日系 \幼保系 \人文社會學院教育經營碩士班 \ 師培中心 Wen-Ping Building \ College of Humanities & Social Sciences \ Dept. of Applied English \ Dept. Applied Japanese \ Dept. of Child Care & Education \ Master of Educational Administration, College of Humanities and Social Sciences \ Center for Teacher Education
O棟	高福系 Dept. of Senior Welfare and Services
P棟	電子系及產設系專業教室 Classrooms of Electronic Engineering Dept.& Creative Product Design Dept.
Q棟	光電系 Dept. of Electro-Optical Engineering
R棟	機械系專業教室 Classrooms of Mechanical Engineering Dept.
S棟	管科大樓 \ 國企系 \ 財金系 \ 企管系 \ 會資系 Management Science Building \ Dept. of International Business \ Dept. of Finance \ Dept. of Business Administration\ Dept. of Accounting Information
T棟	教學研究大樓 \ 語言中心 \ 行銷與流通管理系 \ 休閒事業管理系 \餐旅管理系 \資訊管理系 \工業管理與資訊系 Teaching and Research Building \ Language Center\ Dept. of Marketing & Logistics Management \ Dept. of Leisure, Recreation & Tourism Management \ Dept. of Hospitality Management \ Dept. of Information Management \ Dept. of Industrial Management & Information
U棟	優活館 Yohas Center
V棟	能源館工程館 \ 機械系專業教室 Energy Engineering Building \ Classrooms of Mechanical Engineering Dept.
W棟	磅礴館\數位設計學院 \ 多樂系 \ 視傳系 \ 資傳系 \ 流音系 Pomposo Hall \ College of Digital Design \Dept. of Multimedia & Entertainment Science \Dept. of Visual Communication Design \Dept. of Information and Communication \Dept. of Popular Music Industry
X棟	創思設計坊 \ 產設系 Design Cube \ Dept. of Creative Product Design
Y棟	三連堂 San-Lian Memorial Gym.
Z棟	西進館 \ 學務處服務學習組 Shim-Hwai Memorial Hall \ Office of Student Affairs(Service Learning Division)
H1~H6	第一 ~ 第六宿舍 Dormitory (I ~ VI)

2023 International Symposium on Advanced Technology (ISAT-22)
Tainan City, Taiwan, October 19-20, 2023

SSVEP-BCI Text Spelling System Mimicking Keyboard Layout

Na Qianwen ,Tanaka Hisaya

Department of Informatics, Graduate School of Kogakuin University, Tokyo, Japan
E-mail: em23031@ns.kogakuin.ac.jp

Abstract

Spelling is an important application of brain-computer interfaces (BCIs). Previous BCI spelling systems have been designed with LED stimulation interfaces following the sequence of 26 English letters or the Japanese Hiragana characters. Consequently, during the spelling process, the interface often presents numerous stimuli with different frequencies, leading to potential spelling errors. In this paper, we introduce a novel stimulation interface that mimics the arrangement of a computer keyboard, using groups of three letters as stimuli. After two rounds of stimulus selection, the system outputs the intended word. Leveraging individuals' familiarity with the layout of computer keyboard letters, this approach enhances the efficiency of the spelling system. By reducing the number of stimuli and introducing a two-step selection process for character input, the accuracy of the system is improved.

Introduction:

A Brain-Computer Interface (BCI) is a technology that enables direct communication between the central nervous system and machines [1] . Patients with neuromuscular disorders or those who have lost their limbs can use BCI systems to recognize brain activity and communicate with their surroundings [2] , control robotic arms [3], spell words [4], operate wheelchairs [5], and more. Although the number of BCI application types is extensive, spelling receives more and more attention. BCI technology can be categorized into invasive and non-invasive approaches. Signals used for non-invasive BCI systems include slow cortical potentials, P300, sensorimotor rhythms, steady-state visually evoked potentials (SSVEP), and other potential oscillatory brain activities [6]. So far, most BCI spellers are based on the P300 component, which is elicited by an oddball paradigm [7]. In a P300 speller, characters are arranged in a matrix array where the amplification of rows or columns is random. Once the user directs their attention to the target character, a strong P300 component is elicited when that row or column is amplified.

BCI spellers can also be implemented using SSVEP, which is a periodic response elicited by visual stimuli oscillating at a constant frequency [8] . Due to the high signal-to-noise ratio (SNR) in electroencephalogram (EEG) recordings and the high information transfer rate (ITR) required for BCI performance, most existing SSVEP-based BCI systems are gaze-dependent. In gaze based SSVEP BCI systems, multiple target stimuli flicker at different frequencies [9] [10] . When the user directs their attention to one of these targets, the visual cortex generates SSVEP responses at the flicker frequency and its harmonics. The target can then be identified by detecting the dominant frequency of the SSVEP. Compared to P300-based BCIs, this type of BCI offers advantages such as simpler system configuration, less user training, and higher ITR. SSVEP is widely utilized in BCIs. Therefore, this study is also based on an SSVEP-based BCI speller.

However, many of the currently developed SSVEP-BCI systems predominantly utilize stimulation interfaces arranged in the order of 26 English letters or the Japanese fifty sounds (Hiragana and Katakana). Consequently, such interfaces present numerous stimuli at different frequencies, making it challenging for users to focus their attention on the intended target stimulus. Furthermore, the presence of multiple stimuli targets leads to closely spaced flashing character blocks, which can affect data measurements and reduce the accuracy of text input.

Low and mid-frequency SSVEPs exhibit larger

amplitudes compared to the high-frequency range, making SSVEP detection easier and resulting in higher accuracy and higher ITR. However, due to the need for participants to focus on the flickering stimulus interface in this experiment, using stimuli above 10 Hz reduces the risk of visual fatigue and photosensitive epilepsy, ensuring the safety of participants.

The aim of this study is to design a novel stimulus interface that leverages people's sensitivity to keyboard letter arrangement to enhance text input speed. By reducing the number of stimulus targets on the interface, discomfort experienced by participants when interacting with the stimulus interface is minimized. Additionally, the use of a two-stage selection process enhances the accuracy of text input.

Methods:

The SSVEP-BCI-Speller, also known as the Steady-State Visual Evoked Potential Brain-Computer Interface Speller, is a technology that allows individuals to communicate using their brain activity. It is a specialized type of brain-computer interface (BCI) that utilizes the steady-state visual evoked potential (SSVEP) phenomenon to enable users to spell out words or select symbols on a screen without using their muscles.

This research uses Unity to implement the stimulation of the stimulation interface, and the designed stimulation screen is shown in Figure 1. The frequency set for each text block is shown in Figure 2. Setting block ‘123’ to 11Hz, block ‘456’ to 12Hz, block ‘789’ to 13Hz, blocks ‘0 DEL’ to 14Hz, blocks ‘QWE’ to 15Hz, blocks ‘RTY’ to 16Hz, blocks 'UIOP’ to 17Hz, blocks ‘ASD’ to 18Hz, blocks ‘FGH’ to 19Hz, blocks ‘JKL’ to 20Hz, blocks ‘ZXC’ to 21Hz, blocks ‘VBN’ to 23Hz, and blocks ‘M , .’ to 27Hz. After the first selection, the chosen blocks are arranged sequentially within the central four blocks and flicker at frequencies of 11Hz, 12Hz, 13Hz, and 14Hz. After the second selection, the final chosen letter is displayed in the topmost block on the screen.

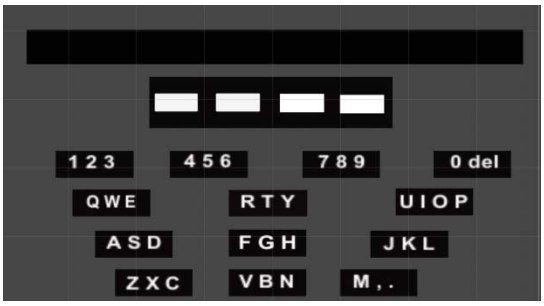

Figure 1. stimulation screen

Figure 2. The frequency set for each text block

The present study employed the sinusoidal stimulation method as designed in [11] for visual stimulus presentation, aimed at inducing SSVEP responses. On the LCD screen, the initial text selection displayed thirteen flickering targets. The modulation of the flickering frequency of the targets is as follows. The stimulus frequency for the i-th target is denoted as f_i and the stimulus intensity of the i-th target on the screen is given by equation (1).

$$\mathrm{Stim}(n, f_i) = \frac{1}{2}\left\{1 + \sin\left[2\pi f_i \left(\frac{n}{R}\right)\right]\right\} \qquad (1)$$

where sin() generates a sine wave, R can be interpreted as the screen refresh rate, or the sampling rate for sine wave modulation. n represents the frame index. The dynamic range spans from 0 to 1, where 0 represents black and 1 represents white. One of the advantages of this method is its ability to achieve stimuli at any frequency up to half of the refresh rate. As an example, Figure 3 illustrates the temporal sequence and Figure 4 spectrum of an 11 Hz stimulus.

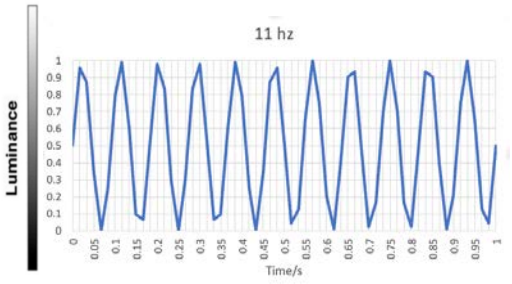

Figure 3. temporal sequence

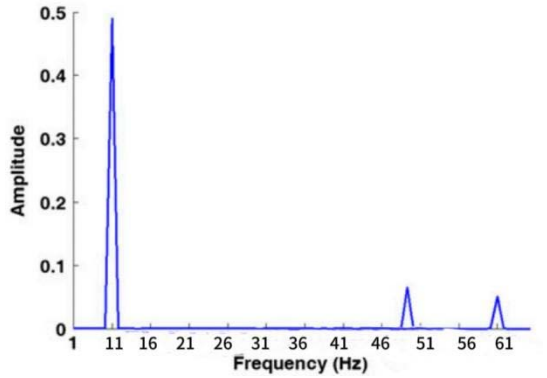

Figure 4 spectrum of an 11 Hz stimulus

FFT, which stands for Fast Fourier Transform, is a mathematical algorithm used to transform a signal from the time domain to the frequency domain. In the processing of brainwave data, FFT is widely utilized for analyzing electroencephalogram (EEG) signals to gain a better understanding of the frequency distribution and characteristics of brain activity. In the context of SSVEP-BCI (Brain-Computer Interface) systems, identifying the specific stimulus frequency that the subject is focusing on is crucial. By employing FFT, the strongest frequency components can be identified in a spectrum plot, allowing determination of the subject's selection. This is particularly essential for applications like SSVEP spellers. FFT not only provides information about frequency components but also offers insights into the amplitude and phase of each frequency. This is highly valuable for comprehending the strength and phase synchronization of SSVEP waves.

To evaluate the performance of the BCI system, we calculated ITR as well as the classification accuracy. The ITR defined by Wolpaw et al. [12] was calculated via [13] [14] .

$$ITR = \frac{60}{T} * [log_2^N + p * log_2^p + (1-p) * log_2^{(\frac{1-p}{N-1})}]$$

[2]

where N is the number of targets, p is the mean accuracy averaged over all targets and T (seconds/target) is the time for a selection.

Experiment:

In this experiment, we will utilize the EEG1000 brainwave recorder from Nihon Kohden, featuring a high sampling rate of 1 kHz. The positioning of the participants' eyes and the display was adjusted to maintain 50 centimeters between them. And keep a head-up LED screen. The electrode placement in this study follows the "International 10-20 System for Electrode Placement," and involves the use of electrodes C3, C4, P3, Pz, P4, PO3, POz, PO4, O1, and O2 for EEG data collection and analysis. As shown in Figure 5. The participant is a healthy 20-year-old male university student.

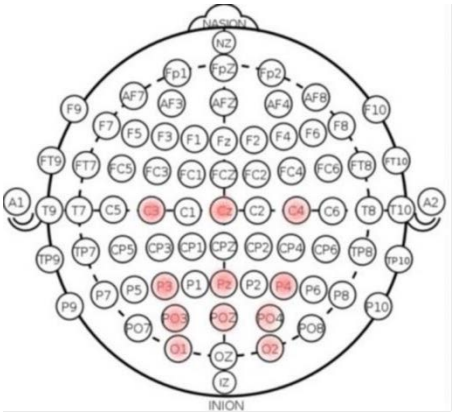

Figure 5. electrode placement

The participant sequentially fixated their gaze on thirteen flickering text blocks displayed on the LED screen. Each text block was fixated for 5 seconds. The acquired EEG data was subjected to FFT analysis.

The experimental subjects are allowed to randomly select the text they want to output. In the first step, they are instructed to gaze at the text box for 5 seconds. Subsequently, by analyzing the subject's brainwave data, the text box they are fixating on is determined. The letters within this text box are then sequentially displayed within four central squares, which start flashing. The experimental subjects continue to gaze at the text they wish to input. Once again, brainwave data is analyzed to confirm the

inputted text, which is then displayed in the input field at the top.

Results:

Figure 6 depicts the spectrum of the participant's EEG responses while receiving each flickering text block stimulus. Visual stimulation resulted in a clear peak on each of the stimulus frequencies as well as on the harmonics. These results indicate that the brain synchronized precisely with the visual stimulation [15] and further suggest that each stimulus frequency can be successfully generated by the sampled sinusoidal stimulation.

As shown in Figure 7, after the first five seconds of stimulation during the experiment, the content of the text block the participant intends to input is organized in sequential order within the four central squares, based on the analysis of brainwave data. As illustrated in Figure 8, after the central four squares flash for five seconds, further analysis of the participant's brainwave data reveals that the intended input is the letter "T." The experiment was repeated ten times to verify the consistency between the text the participant intended to input, and the text obtained through the analysis of brainwave data. Furthermore, across the ten experiments, we achieved an impressive accuracy rate of 80 percent.

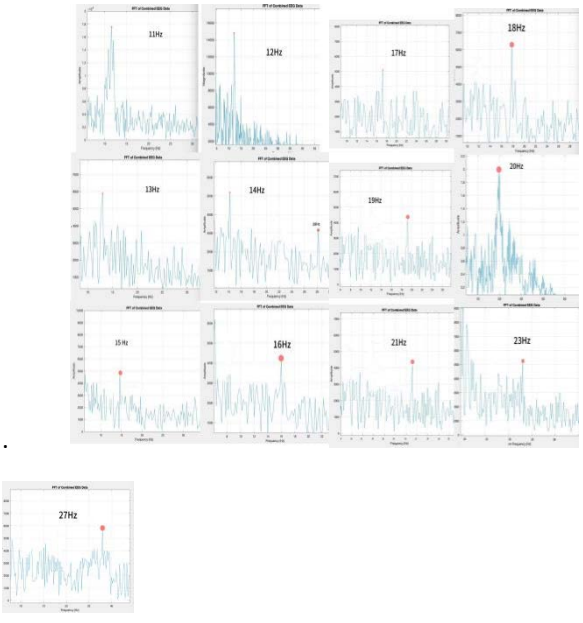

Figure 6. Frequency spectra of each single stimulus

Figure 7. The results obtained from the first gaze fixation.

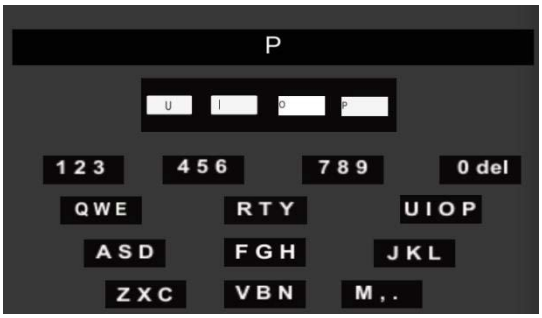

Figure 8. The results obtained from the second gaze fixation.

As mentioned above, a BCI speller can be also based on the P300 potential or motor imagery. However, such BCI systems generally require a training session. Additionally, to produce sufficiently strong signals, these systems require significant mental effort, which means that users may easily become fatigued. Additionally, they cannot achieve high ITR. By contrast, an SSVEP speller has the advantage of little training.

Conclusion and Future work:

Currently, this study utilizes visual stimuli to evoke SSVEP waves and analyze their dominant frequencies, which allows us to determine the targets the participants are fixating on.

Additionally, the research demonstrates that the newly designed stimulation interface yields a higher accuracy rate during text input. However, there remain several aspects that require improvement in both the system and the experimental setup. Since this study only used data from a single participant, future work will involve recruiting a more diverse pool of participants for experimentation. Furthermore, the time required for text input through two gaze fixations could be reduced. Considering that participants have

varying degrees of adaptation to the BCI system, those who are more adept will likely achieve faster input efficiency and higher Information Transfer Rates (ITR). In terms of data analysis, beyond FFT analysis, we intend to employ CCA and SRN analyses. This will enable us to establish a more accurate relationship between EEG data and flicker frequencies.

References:

[1] Wolpaw, J. R., Birbaumer, N., McFarland, D. J., Pfurtscheller, G., & Vaughan, T. M. (2002). Brain-computer interfaces for communication and control. Clinical Neurophysiology, 113(6), 767-791.

[2] Wolpaw, J. R., Birbaumer, N., & McFarland, D. J. (2011). Brain-computer interfaces for communication and control. ACM, 54(11), 60-66.

[3] Quiles, E., Davone, J., Chio, N., & Garcia, E. (2022). Cross-Platform Implementation of an SSVEP-Based BCI for the Control of a 6-DOF Robotic Arm. Sensors, 22(13).

[4] Brunner, P., Joshi, S., Briskin, S., Wolpaw, J. R., Bischof, H., & Schalk, G. (2010). Does the 'P300' speller depend on eye gaze? Journal of Neural Engineering, 7(5), 056013.

[5] Leeb, R., Friedman, D., Müller-Putz, G. R., Scherer, R., Slater, M., & Pfurtscheller, G. (2007). Self-paced (asynchronous) BCI control of a wheelchair in virtual environments: a case study with paraplegics. Computational Intelligence and Neuroscience, 79642.

[6] Lotte, F., Congedo, M., Lécuyer, A., Lamarche, F., & Arnaldi, B. (2007). A review of classification algorithms for EEG-based brain-computer interfaces. Journal of Neural Engineering, 4, R1-R13.

[7] Donchin, E., Spencer, K. M., & Wijesinghe, R. (2000). The mental prosthesis: assessing the speed of a P300-based brain-computer interface. IEEE Transactions on Rehabilitation Engineering, 8(2), 174-179.

[8] Hillyard, S., Hinrichs, H., Tempelmann, C., Morgan, S., Hansen, J., Scheich, H., & Heinze, H-J. (1997). Combining steady-state visual evoked potentials and fMRI to localize brain activity during selective attention. Human Brain Mapping, 5(4), 287-292.

[9] Cecotti, H. (2010). A self-paced and calibration-less SSVEP-based brain-computer interface speller. IEEE Transactions on Neural Systems and Rehabilitation Engineering, 18(2), 127-133.

[10] Chen, X., Chen, Z., Gao, S., & Gao, X. (2014). A high-ITRS SSVEP-based BCI speller. Brain-Computer Interfaces, 1(3-4), 181-191.

[11] Wolpaw, J. R., Ramoser, H., McFarland, D. J., &Pfurtscheller, G. (1998). EEG-Based communication: improved accuracy by response verification. IEEE Transactions on Rehabilitation Engineering, 6(3), 326-333.

[12] Billinger, M., Daly, I., Kaiser, V., Jin, J., Allison, B. Z., Müller-Putz, G. R., & Brunner, R. (2013). Is it significant? Guidelines for reporting BCI Performance. In Toward practical brain-computer interfaces: Biological and medical physics (pp. 333-354). Springer.

[13] Yuan, P., Gao, X., Allison, B., Wang, Y., Bin, G., & Gao, S. (2013). A study of the existing problems of estimating the information transfer rate in online brain–computer interfaces. Journal of Neural Engineering, 10(2), 026014.

[14] Yuan, P., Gao, X., Allison, B. Z., Wang, Y., Bin, G., & Gao, S. (2013). A study of the existing problems of estimating the information transfer rate in online brain-computer interfaces. Journal of Neural Engineering, 10, 026014.

[15] Regan, D. (1989). Human Brain. Electrophysiology: Evoked Potentials and Evoked Magnetic Fields in Science and Medicine. New York: Elsevier.

Non-destructive evaluation of 3-D creep strain in the whole turbine blade using surface displacement

Satoshi Fujii*, and Masaru Ogawa

Mechanical Engineering, Graduate School of Kogakuin University, 1-24-2, Nishishinjuku, Shinjuku-ku, Tokyo, Japan
*Corresponding author's email: am22054@g.kogakuin.jp

Abstract

Gas turbine blades for power generation are used in harsh, high-temperature environments, and ensuring safety has become one of the most important issues. Therefore, highly accurate remaining blade life diagnosis technology is required. One method is to estimate the distribution of creep strain throughout the entire component using an inverse problem analysis based on the surface displacement on the turbine blade caused by creep strains. The authors have proposed an iterative method for solving non-linear problems in which the relationship between creep strain and displacement is non-linear due to the relatively large creep strain values generated in turbine blades. In this study, the method is applied to a model that assumes an actual gas turbine, and the estimation accuracy is evaluated.

Introduction

Gas turbine blades for power generation are used in severe high-temperature environments, and ensuring safety has become one of the most important issues. Non-destructive and accurate diagnosis of remaining blade life would improve power generation efficiency while ensuring sufficient safety. In a previous study, a method for non-destructively evaluating three-dimensional creep strains based on the contour information of a blade before and after deformation was proposed[1][2]. This method assumes a linear relationship between creep strain and displacement. However, the creep strain generated in an actual gas turbine is relatively large, and the relationship between the creep strain and displacement becomes non-linear, resulting in lower estimation accuracy. Therefore, this study uses an inverse problem analysis method that can estimate the creep strain with relatively high accuracy even for such non-linear problems[3]. The effectiveness of the proposed method is verified by numerical analysis of an FEM model that is relatively close to a gas turbine rotor blade.

Numerical analysis method

To evaluate the estimation accuracy of the method, this study compares the correct creep strains with estimated values by performing an inverse problem analysis using the surface displacements obtained from the known exact creep strains. Specifically, first a micro-deformation analysis in which the correct creep strain was input to the pre-deformation model was performed, and show that the conventional inverse problem method can correctly estimate the creep strains from the surface displacements. Next, it has been clarified that the conventional method does not provide a correct solution for non-linear large deformation problems. In this study, an inverse analysis method was applied, which can also solve non-linear problems. In this method, displacements are obtained by carrying out a large deformation analysis where the estimated creep strain is input to the model, and the creep strain, which represents the difference between this value and the measured displacement, is obtained by inverse analysis and added to the estimated creep strain value. The solution is then converged by performing such iterative calculations.

FEM model and analysis condition

To validate the method, an FEM model of a gas turbine blade with a length of 700 mm, width of 200 mm, and thickness of 20 mm was used. Torsion was gradually applied from y = 0 mm to y = 350 mm in the radial direction, so that a 45° deviation occurs between y = 0 mm and y = 350 mm. The Young's modulus is 207 GPa, Poisson's ratio is 0.3, and the number of nodes and elements are 4769 and 896, respectively. The model was fixed at the root of the blade (y = 0 mm) so that there were no constraints around it and no rigid body movement or rotation occurred. The creep strain in the y-directional component with a magnitude of 0.01 was set for the entire gas turbine rotor blade. A y-directional component value with a magnitude of 0.02 was employed as the peak value for eight elements in the region of $5 \leqq x \leqq 10$ mm, $300 \leq y \leq 400$ mm, $0 \leqq z \leqq 200$ mm in the torsion-free model. The displacements used in the inverse analysis were three-directional components at $x = 20$ mm, $0 \leq y \leq 700$ mm, $z = 200$ mm in the pre-torsion model. In order to evaluate the estimation accuracy of this method, the correct creep strains were compared with the estimated values using the root mean square (RMS) of the following equation where ε^* is the creep strain and N is the total number of elements.

$$RMS(\varepsilon^*) = \sqrt{\frac{\sum_{i=1}^{N}\left(\varepsilon^*_{i,\text{exact}} - \varepsilon^*_{i,\text{estimated}}\right)^2}{N}} \quad (1)$$

Results

Figure 1 compares the peak creep strain estimated using surface exact displacements with the correct value. Iterative calculations was used this method with the correct value. The horizontal axis in this figure represents the number of iterations, and the vertical axis is the creep strain value. The figure shows that as the number of iterations increases, the values converge to the correct values successfully.

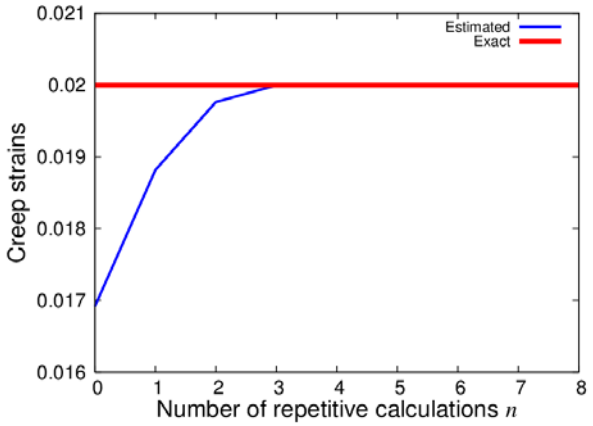

Fig. 1 Exact and estimated creep strains.

Next, the *RMS* for the entire structure is shown in Fig. 2. The horizontal axis in this figure represents the number of iterations, and the vertical axis represents the RMS. The figure shows that the values become smaller as the number of iterations increases. This means that the estimated creep strain converges to the correct solution for the entire structure.

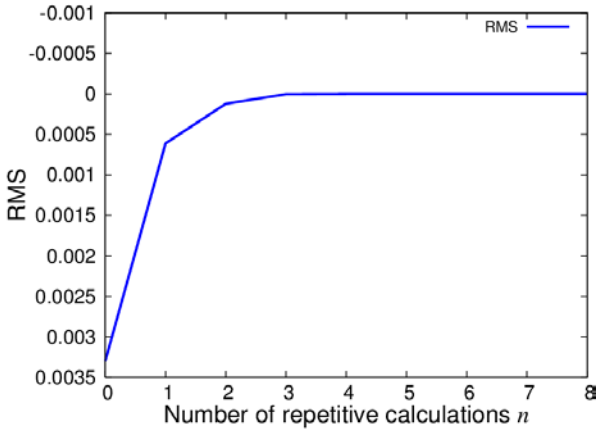

Fig. 2 RMS of creep strain

Conclusion

If three-dimensional creep strains can be non-destructively based on on-site measurements, remaining useful time can be evaluated. Aiming for practical application of the three-dimensional creep strain estimation method, this study applied this method to a twisted model similar to a real turbine rotor blade and evaluated its estimation accuracy using numerical analysis. The actual creep strains produced are relatively large, and the relationship between creep strain and displacement becomes non-linear. This study used the iterative calculation method to solve non-linear problems. Estimation using the value of the surface displacement without measurement error allowed convergence to the correct value. Future work will be directed toward conducting demonstration tests on actual gas turbine rotor blades.

References:

[1] M. Ogawa, T. Inohara, K. Hatano, and H. *Proceedings of the Annual Meeting of Kanto Branch, JSME*, (2018), OS0715.

[2] F. Fukushima, M. Ogawa, T. Inohara, K. Hatano, and H. Nakamura, *Proceedings of JSME M&M2019 Conference on Mechanics of Materials*, (2019), PS21.

[3] Fujii, S. Ogawa, M. and Hirabayashi, D., Mechanical Engineering Journal, Vol. 10, Issue 4 (2023), Paper No. 23-00191, pp. 1-12, DOI: 10.1299/mej.23-00191.

2023 International Symposium on Advanced Technology (ISAT-22)
Tainan City, Taiwan, October 19-20, 2023

Implementation and Evaluation of Key Sharing Method in Information-Centric Networking based Wireless Sensor Networks

Takafumi Taya, Osamu Mizuno

Graduate School of Electric and Electrics Engineering, Kogakuin University, Tokyo, Japan
E-mail: cm22032@ns.kogakuin.ac.jp

Abstract

We have proposed Information-Centric Networking based Wireless Sensor Networks (ICSN), which apply ICN to sensor networks to realize multiple IoT services. ICSN has problems when malicious nodes in the sensor network generate malicious sensor data. To solve these problems, we have proposed a mutual authentication method to authenticate new sensor nodes and have confirmed its usefulness. However, only the mutual authentication method does not address the Content ID leakage risk by eavesdropping packets flowing in ICSN. To address this problem, obfuscation of Content ID is a possible way to address this issue. However, since ICN communicates based on Content ID, it is difficult to encrypt an end-to-end message. Therefore, ICSN adopts a hop-by-hop encryption method. To achieve it, each node must possess the shared key. This paper proposes a cryptographic key-sharing method in which a shared key is shared among nodes for hop-by-hop encryption of Content ID. We also implement the method using Cefore, software ICN router, and we evaluate the proposed method from experimental results.

1. Introduction

Japanese government indicates policies called Society 5.0 and Industry 4.0 [1]. They realize so-called “Cyber-physical systems” that connect the sensor data generated by IoT devices in a virtual space and feed it back to the physical space. Examples of IoT services include environmental monitoring using temperature and humidity sensors and remote monitoring services using motion sensors and cameras. Such IoT services often need to build a sensor network for each service. In this case, the cost of creating a sensor network is incurred when introducing a new service. In addition, the management and operation cost of the sensor network is also incurred as sensor devices are added and removed. Figure 1 shows an overview of a sensor network with multiple IoT services. In Figure 1, the surveillance service requests data from cameras and motion sensors, and the agricultural service requests sensor data from rainfall and temperature sensors. Multiple IoT services request various types of sensor data, and when the requested sensor data overlap, the services share the sensor data with each other. If sensor data can be shared in a single sensor network for each service, then it is possible to reduce the sensor network's creation, management, and operation costs.

Based on this model, we have proposed ICSN, which applies ICN (Information-Centric Networking) to sensor networks to provide multiple IoT services in a single sensor network [2]. ICSN is expected to reduce data acquisition time and power consumption of sensor nodes by having sensor nodes retain cache functions. However, there is a problem when a malicious node sends invalid or abnormal data in ICSN. Therefore, we have proposed a mutual authentication method to authenticate new sensor nodes to be added to an ICSN to avoid connection

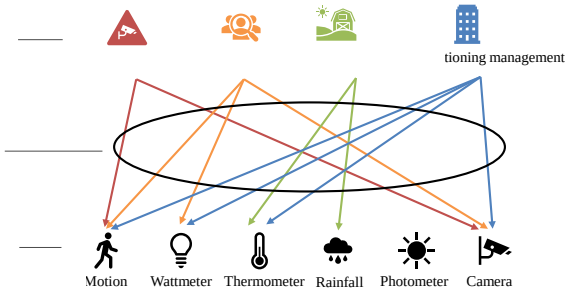

Fig. 1. An Overview of a Sensor Network with Multiple IoT Services

with malicious nodes and have shown its usefulness [3]. On the other hand, if an attacker eavesdrops on packets exchanged in an ICSN, the Content ID contained in the packet may be leaked [4]. It is difficult to address this issue only by new sensor nodes authentication. Although obfuscation of the Content ID is a possible solution to this problem, it is difficult to encrypt it end-to-end because ICN communicates data based on the Content ID. Therefore, ICSN adopts a hop-by-hop encryption method in which encrypted data is transmitted between each node. To perform encryption communication between each node, the nodes must share the encryption key. This paper proposes a method to share the encryption key among nodes. We also implement the proposed method using Cefore and evaluate it based on experimental results.

2. ICN-based Wireless Sensor Networks

2.1. Overview and operation

ICN is a content-oriented network that communicates using Content ID, a content identifier. Interest packets are used to request data, and Data packets are used to send data. The Interest packet contains the Content ID, which is a content identifier,

and the Data packet contains the Content ID and data. ICN does not depend on the device's location, such as IP address or MAC address, and can acquire data based on Content ID alone. In addition, the relay node caches the data. Suppose the cached data matches the Interest received by the relay node. In that case, a reply is sent from the cache, which is expected to reduce the number of communications and the data acquisition time.

ICSN is a content-oriented sensor network that applies ICN protocol to sensor networks. The sensor nodes in the sensor network are divided into several areas, and a cluster head is selected for each area. The cluster head maintains a cache function and caches only the data generated by the sensor nodes belonging to its area. Other sensor nodes do not have a cache. Figure 2 shows an example of the clustering method applied to ICSN. Figure 2 consists of two sink nodes and sensor nodes divided into two areas. Sink node α sends an Interest to the CH in Area A to request sensor data from the temperature sensor in Area B. The CH in Area A forwards the Interest to the CH in Area B because Area B is the target of the Interest request. The CH in area B forwards Interest to the temperature sensor in its area because it is the target area of the request. The temperature sensor receives the Interest, stores the sensor data in Data, and sends it back to the CH in Area B. The CH in Area B belongs to its area. The CH in Area B caches the data generated by the sensor node in its area and forwards it to the CH in Area A. The CH in Area A does not cache the data because it does not exist in its area and forwards the data to the sink node. Next, sink node β sends the same Interest as sink node α to the CH in area B. Since the CH in area B is the target area of the request, it checks its cache and returns Data from the cache when it holds the data. Thus, applying ICN to a sensor network can reduce the number of communications between sensor nodes. It can reduce the power consumption of sensors.

2.2. Problems in ICSN

Since Content ID is stored in both Interest and Data in ICSN, Content ID may be leaked if an attacker sniffs packets. The leakage of the Content ID can also allow the attacker to infer the popularity of the Data requested by the sink node. If the attacker knows the popularity of the requested Data, they can send invalid Interests, which require popular Data, to the CH. It causes degrade the cache function [5]. Figure 3 shows the problems in an ICSN. An attacker can leak the Content ID by eavesdropping on packets exchanged. After eavesdropping on the Content ID, the attacker guesses the popularity of the data the sink node requests and sends an invalid Interest to the CH. Since the CH cannot cache highly popular data, it sends an Interest to the sensor node whenever it receives an Interest. ICSN assumes a low-resource sensor node, so the sensor node's battery may run out of power due to the increase in the number of communications. This may cause human costs to replace the battery of the sensor node and may affect the operation of IoT services.

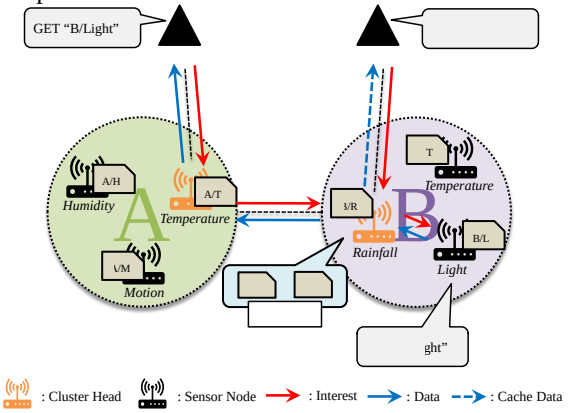

Fig. 2. An Operational Example of the ICSN

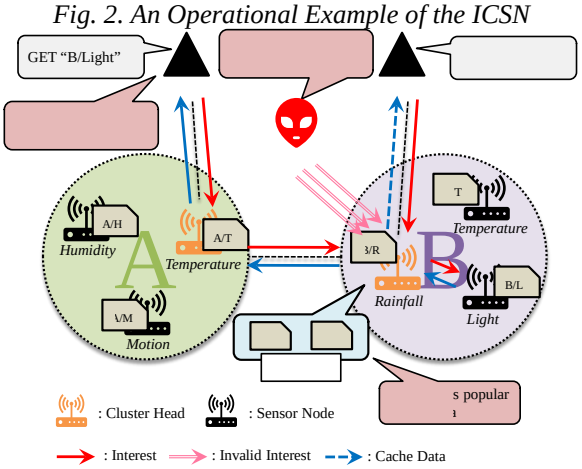

Fig. 3. Problems in ICSN

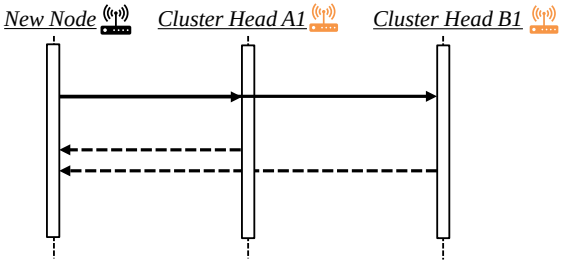

Fig. 4. Sequence of CH discovery phase

3. Proposal Method

3.1. Mutual authentication method

Key sharing between nodes is done after adding a new sensor node to ICSN. This section describes the mutual authentication method in ICSN. This method authenticates new sensor nodes to prevent them from being connected to malicious nodes. This method consists of the CH discovery phase and the authentication and registration phase.

1) Cluster head discovery phase

In this phase, a new sensor node selects an area to which it belongs. Figure 4 shows the sequence diagram—first, the new sensor node multicasts an Interest to the CH requesting its ID. When the CH receives the message, it stores its ID in Data and

sends it back. The new sensor node selects the CH that receives the Data earliest as the destination of the authentication request.

2) Authentication and Registration phase

In this phase, mutual authentication is performed between the new sensor node and the KM(Key Manager). If the authentication is successful, the routing information of the new sensor node is added to the FIB of the CH. The sequence diagram is shown in Figure 5. A new sensor node sends an Interest containing its ID to the CH selected in the CH discovery phase. The CH receives the Interest and forwards it to the sink node, and the sink node forwards it to the KM. KM generates a random number and calculates the predicted response using the 128-bit secret information shared with the new sensor node in advance. The predicted response and the random number are stored in the Data and sent to the sink node. The sink node holds the predicted response value and transfers only the random number to the CH. The CH transfers the Data to the new sensor node. The new sensor node receives the data and calculates the response value using the random number and the shared secret information. The new sensor node generates a new random number to authenticate the KM, and it calculates the predicted response value with the shared secret information. The new sensor node stores the response value and the random number in Interest and sends it to CH. The CH forwards them to the sink node, which verifies that the response value is the same as the predicted response value generated by the KM. If they are not the same, the sink node discards the Interest and terminates the authentication operation. If the values are the same, it forwards the Interest to the KM. The KM generates a response value from the random number stored in the Interest and the shared secret information and sends it to the sink node. The sink node adds information about the successful authentication and the new sensor node to the Data and forwards it to the CH. If the CH has successful authentication information, it adds the route information of the new sensor node to the FIB and forwards the Data to the latest sensor node. The new sensor node compares the response value of KM with its own predicted response value, and if the values are the same, it sends Data to the subsequent Interest.

3.2. Key sharing method in ICSN

Figure 6 shows the sequence diagram of the cryptographic key-sharing method. After the authentication operation, the new sensor node sends an Interest to KM, which contains the sensor ID of the CH obtained in the CH discovery phase and the sensor ID of the new sensor node. KM receives the Interest, stores the value of X that satisfies (1) in Data, and sends it back to the new sensor node. The relay

$$(PSK_{NN} \oplus RAND) \oplus X = (PSK_{CH} \oplus RAND) \oplus X \quad (1)$$

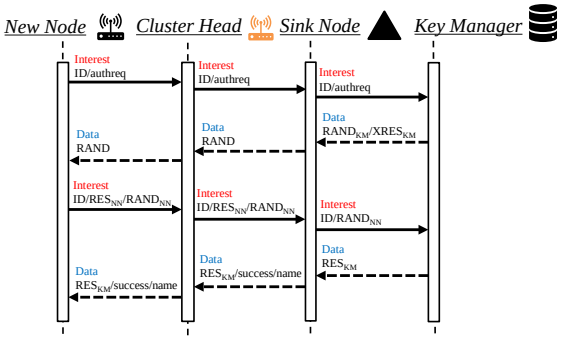

Fig. 5. Sequence of Authentication and Registration Phase

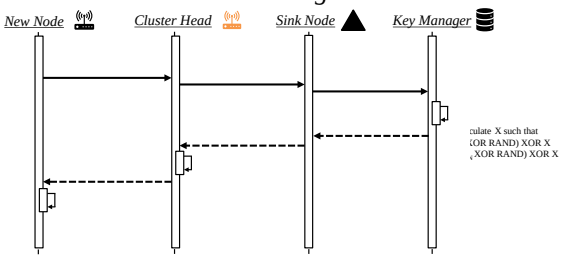

Fig. 6. Sequence of key sharing method

Table. 1. Equipment and Software

	Host	Virtual Machine
Product	LENOVO THINKSTATION P520C	VMware Workstation Player™
OS	Windows 10 Pro for Workstations	Ubuntu 20.04
Memory	32[GB]	4[GB]
Core	4	1
Processor	Intel(R) Xeon(R) W-2223 CPU 3.60Hz	Intel(R) Xeon(R) W-2223 CPU 3.60GHz
Software		**Version**
Cefore		0.8.3a

node CH reads X and RAND from Data and calculates the right side of (1). The new sensor node that receives Data calculates the left side of (1). In this way, our method can share cryptographic keys without distributing shared secret information or shared keys among sensor nodes on the sensor network by using a random number and the value of X. Moreover, since the exclusive OR (XOR) of the random number and the shared secret information is computed, a different shared key is generated each time a different random number is used.

4. Implementation and Experiment

To evaluate the key-sharing method, we implemented ICSN software on six virtual machines on a single host machine for implementation. Table 1 shows the equipment and software used for the implementation. For the implementation, we used Cefore [5], a software for ICN communication. Figure 7 shows the experimental topology. The environment consists of one Key Manager, two sink nodes, two cluster heads, and two areas (A and B). When one new sensor node was added to this environment, the key sharing was performed after the authentication operation. In this experiment, key sharing between the new sensor and

the CH was performed. The experimental results showed that key sharing and the CHs executed correctly, as shown in the sequence diagram, regardless of which CH the new sensor nodes selected. We also confirmed that the new sensor node generates a different key each time key sharing is performed.

5. Security Analysis

Several attacks are expected on the key-sharing method. This section proves that the proposed method is secure against replay and password-guessing attacks.

1) Replay attack

A replay attack is an attack in which an attacker attempts to gain unauthorized access by intercepting communications between nodes and retransmitting them. In the key sharing method, even if an attacker compromises the information stored in Interest and Data, there is no possibility that the shared secret information held by sensor nodes and Key Manager is compromised. Therefore, even if an attacker who intercepts the communication tries a replay attack, the shared key generated between sensor nodes is not compromised, and it is difficult for the attacker to gain unauthorized access.

2) Password guessing attack

Password guessing attacks occur when an attacker attempts unauthorized access by trying various passwords. The key-sharing method generates a shared key using a 128-bit random number and shared secret information. Since the random number cannot be predicted in advance, it is difficult to guess the shared key to be shared among nodes. Also, the shared key will have a different value each time the random number is changed.

6. Conclusion

We have proposed ICSN, which applies ICN to a sensor network to realize multiple IoT services in a single sensor network. In ICSN, if a malicious node exists in a sensor network, the service may be stopped or may behave abnormally by using the malicious sensor data generated by the malicious node. Therefore, we have proposed a mutual authentication method for ICSN and confirmed its usefulness. On the other hand, if there is an attacker who intercepts communications in an ICSN, there is a possibility that the Content ID may be leaked to the attacker. However, since ICNs communicate based on Content IDs, end-to-end encryption makes it difficult to transfer Interest and Data at relay nodes. Therefore, ICSN uses a hop-by-hop encryption method to perform encrypted communication between nodes. In order to perform encryption communication between nodes, it is necessary to share a shared key among nodes. Therefore, this paper proposes a cryptographic key-sharing method to share a shared key among nodes. We have also implemented and experimented with the proposed method using a virtual machine and Cefore and have shown through security analysis that the key sharing the method can cope with the expected attacks.

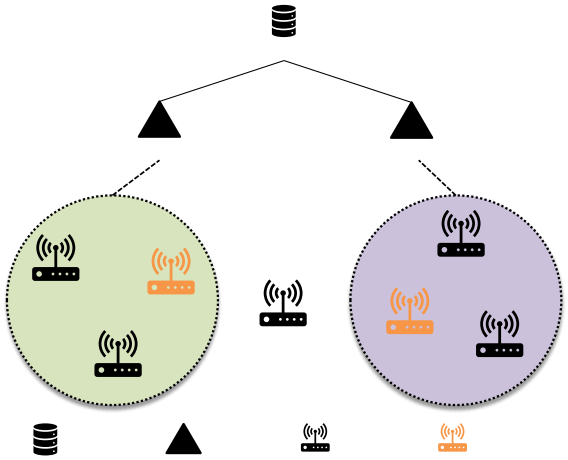

Fig. 7. Experimental topology

Acknowledgments

Part of this research was funded by the Japan Society for the Promotion of Science (JSPS) KAKENHI Grant Number JP22K12014.

References:

[1] Ministry of Internal Affairs and Communications. "Chapter 4: Beyond 5G." https://www.soumu.go.jp/johotsusintokei/whitepaper/ja/r02/pdf/n4100 000.pdf, (accessed July 24, 2023)

[2] K. Kimura and O. Mizuno, "Performance requirements evaluation of network functions in information-centric networking based wireless sensor network, " IEEJ Trans. Information and Systems (in Japanese), vol. 140, no. 6, pp. 583–584, June 2020.

[3] T. Taya, E. Nagaoka, O. Mizuno, "Implementation and Evaluation of Mutual Authentication Schemes in Information-Centric Networking based Wireless Sensor Networks," IEICE Technical Report, IN2022-113, Mar. 2023.

[4] A. Chaabane, E.D., Cristofaro, M.-A. Kaafar, and E. Uzun, " Privacy in content-oriented networking: threats and countermeasures, " ACM SIGCOMM Computer Communication Review, vol.43, no.3, pp.25– 33, 2013.

[5] Cefore, https://cefore.net, (accessed Sep. 11. 2023).

2023 International Symposium on Advanced Technology (ISAT-22)
Tainan City, Taiwan, October 19-20, 2023

Jet Vectoring using Coanda Surface with Distributed Suction Slots

[*1]K. Suzuki*, K. [*2]Nishibe, [*1]K. Sato

[*1]Mechanical Engineering Program in the Graduate School of Engineering, Kogakuin University
2665-1 Nakano-cho, Hachioji-shi, Tokyo 192-0015, Japan
E-mail: am23036@ns.kogakuin.ac.jp
Department of of Mechanical Engineering, Tokyo City University
1-28-1 Tamatsuzumi, Setagaya-ku, Tokyo 158-8557, Japan
E-mail: knishibe@tcu.ac.jp

Abstract

Research on fluidic thrust vectoring, which allows directional control of jet streams without the need for changes in geometric shape, has been conducted extensively. However, when it comes to discussions regarding the controllable range and controllable angles of jet streams, it is difficult to claim that they are sufficient. Therefore, this study discussed the differences in jet deflection based on the combinations of multiple secondary suction slots provided on a Coanda surface. Among the main results obtained, it was evident that the spacing (angle difference) between the slots had an impact on the deflection characteristics of the primary jet when multiple secondary slots were operated at various positions (angles).

Research on fluidic thrust vectoring is actively conducted. Thus far, studies have focused on the directional control of primary flow using secondary flow associated with the Coanda surface. In Kobayashi et al. research, it was reported that the maximum deflection angle is approximately 47 degrees [1]. Additionally, in recent years, there has been a focus on expanding the controllable range. Studies have been conducted involving the placement of five secondary suction slots at 30-degree intervals on the Coanda surface, revealing that the deflection angle varies depending on the combination of activated secondary slots [2]. However, these studies have continuously altered the combinations using the five available secondary slots, leaving many uncertainties regarding the differences in deflection angles caused by discontinuous combinations. In this study, we will discuss the impact of the combination of activated secondary slots, specifically those located at an angle difference $\Delta\theta$ with respect to the i-th slot, while keeping the i-th slot activated. It should be noted that the secondary slot numbers are designated as i, ii, iii, iv, v, in order from upstream.

In this study, we primarily conducted flow visualization experiments and time averaged velocity distribution measurements. For details on the experimental methods, please refer to [2]. It should be noted that the velocity of the primary jet, U_1, was set to $10\,\mathrm{m/s}$, and the velocity of the secondary jet, U_2, was set to $-5\,\mathrm{m/s}$.

Figure 1 shows (a) visualization photographs and (b) time averaged velocity distributions when the secondary slot located at $\Delta\theta = 60$ degrees and Figure 2 shows (a) visualization photographs and (b) time averaged velocity distributions when the secondary slot located at $\Delta\theta = 90$ degrees are activated along with slot i. When slots i and iii were activated, the influence of slot iii caused the primary jet to deflect by approximately 110 degrees. However, when slots i and iv were activated, the influence of slot iv was not present, resulting in deflection similar to when only slot i was activated, as shown in [2]. For $\Delta\theta = 60$ degrees, the reason for the deflection of the primary jet due to the influence of the rear slots can be attributed to the wide region where the pressure gradient became negative due to suction between the slots. On the other hand, for $\Delta\theta = 90$ degrees, it is believed that separation occurred at the same position as when only slot i was activated due to the widened region where the pressure gradient near the two slots that were not activated became positive.

Therefore, it is suggested that directional control of the primary jet is possible when the angle difference between the activated secondary slots is within $\Delta\theta = 60$ degrees or less.

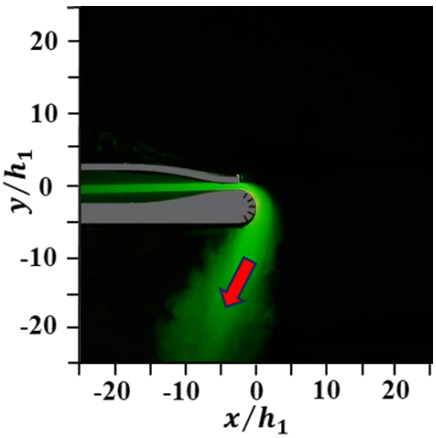

(a) Visualization

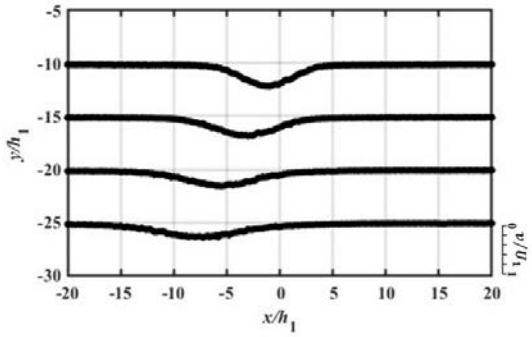

(b) Time-averaged velocity distributions

Figure 1. Behavior of jet controlled by suction slot i, iii ($U_1 = 10\ m/s, U_{2,i} = U_{2,iii} = -5\ m/s, Re = 6.7 \times 10^3$).

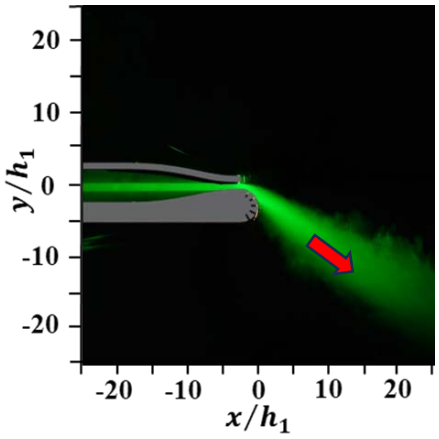

(a) Visualization

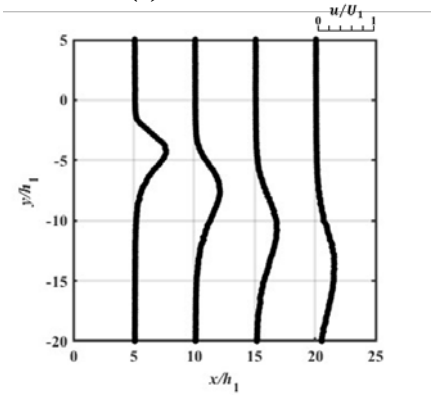

(b) Time-averaged velocity distributions

Figure 2. Behavior of jet controlled by suction slot i, iv ($U_1 = 10\ m/s, U_{2,i} = U_{2,iv} = -5\ m/s, Re = 6.7 \times 10^3$).

References:

[1] R. Kobayashi, Y. Watanabe, Y. Tamanoi, K. Nishibe, D. Kang and K. Sato, "Jet vectoring using Secondary Coanda Synthetic Jets", Bulletin of the JSME, Mechanical Engineering Journal, Vol. 7, No. 5 (2020), 20-00215.

[2] K. Suzuki, M. Nakagawa, K. Nishibe, D. Kang and K. Sato, "Direction Control of Jet Flow by Multiple Suction Slots on a Coanda Sirface", The 33th International Symposium on Transport Phenomena, (2023).

2023 International Symposium on Advanced Technology (ISAT-22)
Tainan City, Taiwan, October 19-20, 2023

Terrain Roughness Estimation Using 3D LiDAR for Mobile Robots

Tsubasa Abe* and Hanwool Woo

Department of Mechanical Engineering, Kogakuin University, Tokyo, Japan
E-mail: am23002@ns.kogakuin.ac.jp

Abstract

This paper proposes a terrain roughness estimation method using a 3D laser scanner for mobile robots. Since delivery robots need to carry fragile items, it is necessary for robots to consider road conditions and pass a flat surface as much as possible. The proposed system uses a 3D laser scanner to acquire the ground shapes, and the terrain roughness is estimated through plane approximation based on point clouds. It is demonstrated that the proposed method can classify flat and rough terrain.

1. Introduction

In recent years, the demand for mobile robots has been increasing, and they are widely used for delivery services or other eating establishments. Since these delivery robots need to carry fragile items, it is necessary for robots to consider road conditions and pass a flat surface as much as possible.

In previous research, Leanza et al. proposed a terrain roughness estimation method using a stereo camera to enhance the autonomous mobility of agricultural robots in a rural environment [1]. The locations where the ground surface was measured in this study included a smooth concrete surface, a plowed terrain along the edge of a vineyard, and a compact agricultural terrain in an olive grove to identify unevenness levels. It is necessary to measure the ground surface with respect to roads and areas containing drainage ditches in order to expand the travel range of this mobile robot. Wirges et al. proposed a method for estimating the ground surface from LiDAR (Light Detection And Ranging) measurements of automated vehicles [2]. The ground surface is modeled by a curve called a uniform B-spline, which is robust to changes in measurement density and has a single parameter that controls the smoothness pre-condition. The method is modeled as an optimization problem using the least-squares method and reformulated into a linear problem, which can be solved efficiently; the performance of the proposed method was evaluated using the Semantic KITTI dataset and also validated in a real-world scenario. It was demonstrated that the method outperforms other ground surface estimation methods. This research has five LiDARs mounted on self-driving cars, and the cost of mounting them on autonomous mobile robots or other types of platforms is also high. Therefore, it is necessary to build a system that can measure the ground surface with a reduced number of LiDARs to be mounted on other platforms.

Based on the above situations, this paper proposes a terrain roughness estimation method using a 3D LiDAR. The proposed system uses a 3D LiDAR to acquire ground shapes, and the terrain roughness is estimated through plane approximation based on point clouds.

2. Proposed Method

Using 3D point clouds acquired by a 3D LiDAR, the proposed method applies RANSAC (Random Sample Consensus) which is one of the algorithms for robust estimation [3]. RANSAC is a robust estimation algorithm that aims to reduce the influence of outliers in the given observations. The algorithm of RANSAC is to randomly select some points from the data, match the model to the sample, and estimate the parameters. The error between the extracted model and the overall model is calculated, and the data that are not outliers below a threshold are combined. The parameters are finalized by repeating this process. Plane approximation is performed using RANSAC. 3D point clouds that are estimated to be planar are depicted as red color in this paper.

The equation of the plane output from the plane approximation is the distance between a point and a plane in the xyz coordinate plane as follows.

$$ax + by + cz + d = 0 \tag{1}$$

The above equation represents the plane. The distance between the plane and the point (x_0, y_0, z_0) is derived as follows.

$$\frac{ax_0+by_0+cz_0+d}{\sqrt{a^2+b^2+c^2}} = 0 \tag{2}$$

Using this equation, the distance from the plane is obtained and the acquired 3D point cloud is checked to see if the roughness of the ground surface can be measured by finding the variance and standard deviation as follows.

$$\sigma^2 = \frac{1}{n}\sum_{i=1}^{n}(x_i - \mu)^2 \tag{3}$$

n is the number of data, x_i is the value of each data, and μ is the mean. This standard deviation can be used to determine the roughness of the ground surface. It is possible to evaluate the ground surface because the standard deviation is larger in areas with rougher topography and smaller in areas with flatter topography.

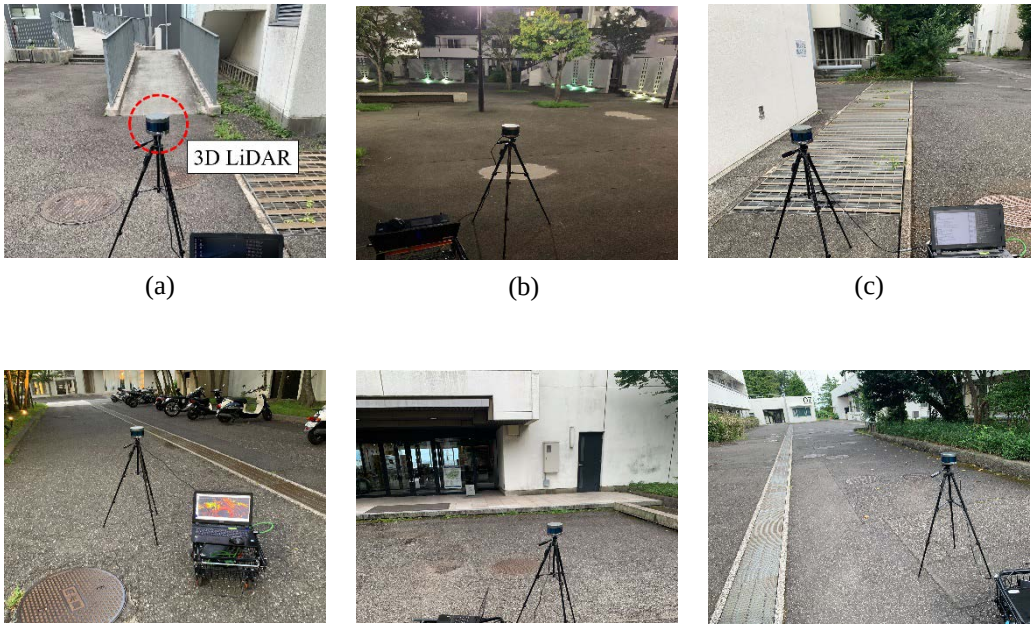

(a) (b) (c)

(d) (e) (f)

Fig. 1. Six locations where ground surface estimation was performed using LiDAR

3. Experiments

The ground shape is measured using rs-lidar-16, which stands for a LiDAR, a sensor that uses laser light to measure the distance and position of an object. As shown in Fig. 1, measurements were taken at six locations (a, b, c, d, e, and f) with a LiDAR parallel to the ground, changing the position of a LiDAR three times at each location.

As shown in Fig. 1, three measurements were taken at each of three locations, one on a flat surface (a, b, c) and one on a rough surface (d, e, f), with the LiDAR parallel to the ground.

For (a), only the slope in front of the LiDAR was measured to check if the flatness of the slope indicated less roughness when the plane was estimated. For (b), the area was flat and had little shaking when the robot was moved, so we measured it to see if the roughness was small as a result of the measurement. Regarding point (c), the ditch is a drainage ditch for roads and cultivation, so it has holes in the shape of a grid. The measurement was conducted to confirm whether this drainage ditch is also recognized as a flat surface. For point (d), we confirmed that the surface roughness is large even to the human eye, so we also checked whether the measurement results are also large. For (e), the drainage ditch is flat, so measurements were taken at the same time as the measurement of the rough ground surface to see if the measurement results were also rough. For (f), measurements were taken to see if the influence of manholes on the ground surface is significant.

4. Experimental Results

The results when the LiDAR was parallel to the ground are shown in Fig. 2. The mean standard deviations for each location were 0.567 cm for (a), 0.638 cm for (b), 0.876 cm for (c), 1.607 cm for (d), 1.489 cm for (e), and 1.644 cm for (f).

The standard deviation for (a) was the lowest compared to the others. This result indicates that the slope can be measured as a flat surface. (b) has a low standard deviation and is found to be flat as in (a). (c) was found to be flat because the standard deviation was low when the measurement was made only at the drainage ditch, indicating that the ground surface had little influence on the measurement.

In case (d), the standard deviation was the largest compared to the others, indicating that the ground surface is rough not only by human eyes but also from the 3D point cloud data obtained from LiDAR. In (e), the standard deviation was larger than in (c), whereas the drainage ditch was recognized as flat. This indicates that the rough ground surface has a greater influence on the measurement of roughness than the drainage ditch. In case (f), the mean of the three standard deviations was higher than in case (a). This indicates that objects attached to the road surface, such as manholes, have a significant effect on the ground surface measurement.

Next, the results of plane estimation by RANSAC are shown in Fig. 3 and 4. Fig. 3 shows (a)', the third result of (a), (b)', the third result of (b), and (c)', the first result of (c), where the standard deviation was small. Figure 4 shows (d)', the fifth result of (d), (e)', the second result of (e), and (f)', the third result of (f), where the standard deviation was large. Fig. 3 shows that almost all of the point clouds are displayed in red, indicating that the standard deviation is low and flat. However, the result in (c)' has a slightly different color. This is thought to be due to the fact that the laser enters the holes in the grid and makes measurements. Therefore, there are places where the point cloud is not red.

Figure 4 shows that the ground surface is rougher

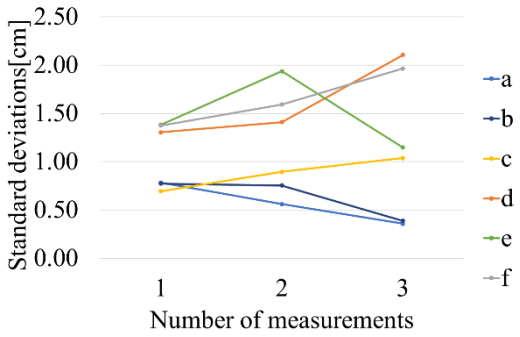

Fig. 2. Standard deviation results for estimated ground surface roughness

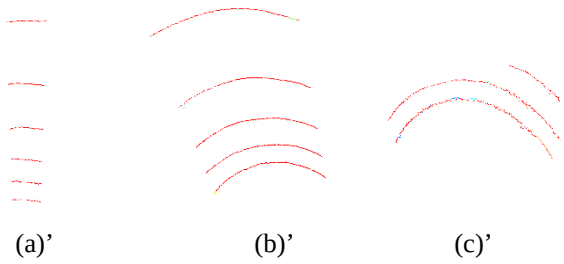

Fig. 3. RANSAC results when estimating flat areas

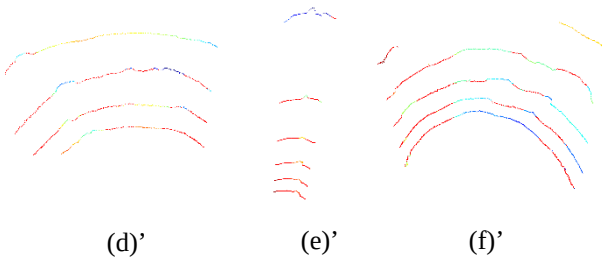

Fig. 4. RANSAC results for the estimated coarse ground shape

than Fig. 3, as indicated by the small number of points that are displayed in red. There are two points in particular where the color changed: when the points were measured at a distance from LiDAR, and when the points were raised up like mountains. The measurement accuracy of the far away points may have decreased as the distance increased. As for the mountain-like raised areas, it is considered that the area between the manhole or drainage ditch and the ground surface, or simply the area where the ground surface is rough, is not estimated as a flat surface. This indicates that the ground surface is rougher near objects attached to the ground surface such as drainage ditches and manholes.

From this result, flat areas have a smaller standard deviation and rough areas have a larger standard deviation, so identification based on the resulting standard deviation after using our proposed RANSAC can be successfully estimated.

5. Conclusion

In this study, LiDAR was used to measure the ground surface at various different locations. As a result, it was found that the influence of the ground surface itself was small, and the influence of manholes and drainage ditches installed for the safety of the road surface was large.

Future plans include improving the measurement accuracy of the roughness of the ground surface and confirming whether it can be measured when the robot is mounted on a mobile robot.

References:

[1] A. Leanza, R. Galati, G. Reina and A. Milella, "Increasing autonomy in agricultural robots: unevenness estimation of the terrain ahead," 2021 IEEE International Workshop on Metrology for Agriculture and Forestry (MetroAgriFor), Trento-Bolzano, Italy, 2021, pp. 442-447, doi:10.1109/MetroAgriFor52389.2021.9628698.

[2] S. Wirges, K. Rösch, F. Bieder and C. Stiller, "Fast and Robust Ground Surface Estimation from LiDAR Measurements using Uniform B-Splines," 2021 IEEE 24th International Conference on Information Fusion (FUSION), Sun City, South Africa, 2021, pp. 1-7, doi: 10.23919/FUSION49465.2021.9626921.

[3] R. Raguram, O. Chum, M. Pollefeys, J. Matas and J. -M. Frahm, "USAC: A Universal Framework for Random Sample Consensus," in IEEE Transactions on Pattern Analysis and Machine Intelligence, vol. 35, no. 8, pp. 2022-2038, Aug. 2013, doi: 10.1109/TPAMI.2012.257.

2023 International Symposium on Advanced Technology (ISAT-22)
Tainan City, Taiwan, October 19-20, 2023

A Study on Link Load Balancing Method in Elastic Optical Networks Using Superposition Coding

Shota Okochi and Ken-ichi Baba

Graduate School of Engineering, Kogakuin University, Tokyo, Japan
E-mail: cm23012@ns.kogakuin.ac.jp

Abstract

We evaluated an impact of the five elements expected to contribute the link load balancing in elastic optical networks using superposition coding. As the result of simulation evaluation, the control based on link congestion contributed the most to the load balancing, and reduced the call blocking probability the most.

1 Introduction

All photonic networks (APNs) have been studied to cope with ever-increasing communication traffics. APNs enable low latency and energy saving networks because they do not perform photoelectric conversion at relay nodes. Furthermore, elastic optical networks (EONs) have been attracted as a new technology in the field of optical backbone network [1]. EONs can use frequency resources more efficiently than currently used weave length division multiplexing (WDM) networks through the use of optical OFDM. However, a fragmentation of frequency slots occurs in EONs because subdivided frequency bands, called slots, are allocated as much as needed for each request.

In the field of wireless network, a superposition coding technique has been proposed, and it can transmit two signals on the same frequency by superimposing and separating signals [2]. Thus, superposition coding can save frequency resources. Figure 1 shows an example of using superposition coding for EONs. Frequency resources saved by superposition coding can be allocated to other path requests. Previous studies have proposed a path establishment method applying superposition coding to EONs [3][4]. In addition, other study has proposed the method considering reallocation of existing optical path in EONs using superposition coding, in order to further improve frequency efficiency [5]. These studies showed that reducing the call blocking probability and improving the frequency efficiency.

However, these studies establish optical paths by the shortest route based on *K*-shortest path algorithm, so a load was concentrated on some links and this was one of the reasons for rejection of the path requests.

In this paper, we focus on the five elements in order to distribute link load and reduce the call blocking probability, and evaluate their effects of load balancing in EONs using superposition coding.

2 Proposed Load Balancing Method

We can use superposition coding when the following conditions are satisfied between the two paths [3]: 1) the source node is the same, 2) the destination node is different, 3) one route completely encompasses the other, and 4) the hop count difference to the destination is *D* or more. Therefore, it is not possible to use superposition coding to accommodate path requests in all cases, and some of the requests are accommodated as a normal path without applying superposition coding. In this study, we describe a control method for load balancing when accommodating a new request as a normal path. We focus on the following five elements: 1) the sum of number of frequency slots in use for each link, 2) the maximum of number of frequency slots in use for each link, 3) the sum of number of frequency fragmentations for each link, 4) the frequency slots used for the entire route, and 5) the sum of the number of normal paths for each link. The element 1) and 2) are expected to control for link congestion. The element 3) is focused on the fragmentation, since the link with a high number of fragmentations are considered to have a high link utilization rate. The element 4) is expected to reduce the link load by reducing entire path resource use. The element 5) is selected a route with fewer normal paths, and it is expected to make a new request easier to apply superposition coding and accommodate it.

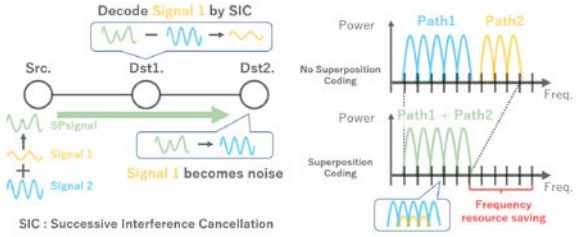

Fig. 1. Example using superposition coding for EONs

First, the candidate routs up to the *K*th are calculated based on *K*-shortest paths algorithm when a new path request arrives. One element is selected from the above five elements and the path cost of the selected element is calculated for each candidate routs. The calculated path costs are compared, and the new request is accommodated in the network by the route with the least cost. If the route with the least cost cannot be accommodated, the candidate route with the next least cost is adopted. If all candidate routes cannot be accommodated, the request is rejected.

Figure 2 shows an example of the cost calculation and accommodating a new request when the element 1), which focuses on the sum of the frequency slots in use, is chosen as the path cost. The path costs are determined by adding up the number of slots in use on

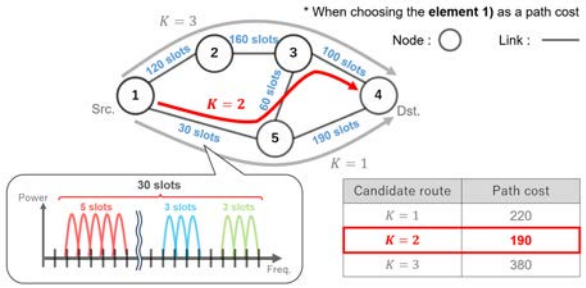

Fig. 2. Example of the proposed load balancing method

Table 1. The number of required frequency slots

Distance [km]	Modulation method	Required slots
~1200	8-QAM	3
1201~2400	4-QAM	5
2401~	BPSK	7

the link for each calculated candidate path. In this case, the new request is accommodated on the K=2 route with the least path cost.

3 Performance Evaluation

3.1 Simulation Environment

We evaluated the performance through a simulation using JPN12 topology with 12 nodes and 17 links [6]. The bandwidth per slot is 12.5 GHz, and the number of slots per link is 320. The traffic model is as follows. The arrival rate of requests follows a Poisson distribution with an average of λ, the duration of paths follows an exponential distribution has an average of 30 seconds, and the selection of source and destination nodes follows a uniform distribution. The modulation method and the number of required frequency slots follow Table 1. The parameters are the number of candidate routes K, required hop count difference D, and reallocation time t_{sw}; here $K = 3$, $D = 2$ and $t_{sw} = 1.0$ [s] unless overwise noted. We use the conventional method without calculating the path cost as a comparison method.

3.2 Performance of Proposed Method

Figure 3 shows the call blocking probability in the JPN12 topology. All elements reduced the call blocking probability compared to the conventional method, and the element 1), which focuses on the sum of frequency slots in use, reduced the most. For instance, at the arrival rate $\lambda = 6.6$, the probability for the element 1) was reduced by 93.2%. Furthermore, the arrival rate λ that satisfies 10^{-3} increased from 5.2 to 6.6 compared to the conventional method, that is 26.6% more traffic could be accommodated.

Figure 4 is the box-and-whisker plot showing the distribution of link utilization for each element. This is the result of evaluating load balancing by measuring the average number of slots in use for each link. This figure shows that a link load balancing was achieved for all elements. In particular, the element 1), which reduced the call blocking probability the most, improved the standard deviation from 48.9 to 37.1.

4 Conclusion

We proposed and evaluated a link load balancing method in order to distribute the load that was concentrated on some links in the conventional method. As a result of simulation evaluation, the proposed method could reduce the call blocking probability and distribute the link load. As a future work, we will consider a method that combines the five elements verified this time.

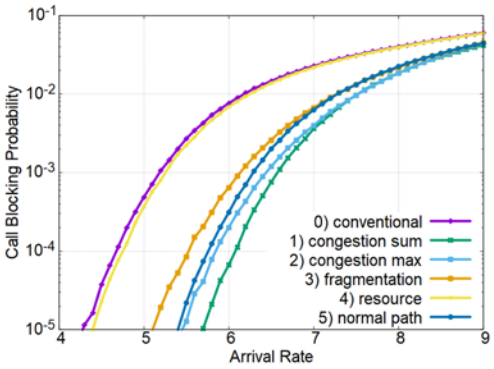

Fig. 3. Call blocking probability in JPN12 topology

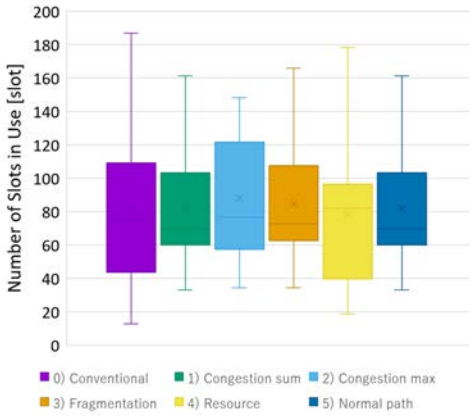

Fig. 4. Distribution of link utilization in JPN12 topology

References:

[1] M. Jinno, et al., “Spectrum-efficient and scalable elastic optical path network: architecture, benefits, and enabling technologies.” IEEE commun. Mag., vol. 47, no. 11, pp. 66-73, Nov. 2009.

[2] X. Su and S. Chan, “High-throughput routing with superposition coding and successive interference cancellation” in Proc. of ICC 2011, Jun. 2011, pp. 1-6

[3] Y. Hirota, et al., “A spectrum assignment design for 1:2 transmissions based on superposition coding in elastic optical networks,” in Proc. of OECC/PSC2019, Jul. 2019, pp. 1-3.

[4] H. Sato, K. Baba and Y. Hirota, “Path establishment method considering resource utilization status using superposition coding in elastic optical network,” IEICE Technical Report (PN2021-72), vol. 121, no. 386, pp. 104-109, Mar. 2022.

[5] S. Okochi and K. Baba, “A path establishment method with reallocation in elastic optical networks using superposition coding,” IEICE Technical Report (PN2022-67), vol 122, no. 398, pp. 136-141, Mar. 2023.

[6] T. Sakano, et al.,”A study on a photonic network model based on the regional characteristics of Japan” IEICE Technical Report (PN2013-1), vol. 113, no. 91, pp. 1-6, Jun. 2013.

Survey and Estimation of the Actual Amount of Scrap in Residential Ceramic Siding Processing Factories and On-Site Treatment

First. Hiwatashi Natsu. Author, Tamura Masaki. Professor.

Department of Architecture, Kougakuin University, Shinjuku, Japan
E-mail: db20285@g.kogakuin.jp

Abstract

In this study, scraps of ceramic siding for residential use were investigated on-site and at a precut factory. The characteristics of each scrap material, collection method of scraps, and emissions are estimated. In addition, we attempted to establish an equation for obtaining the amount of scrap material using a parameter.

1. Housing Characteristics in Asian Countries

A variety of exterior wall materials are used for housing around the world. In Taiwan, bricks and tiles are mostly used for exterior walls, and RC and stone structures are common. In South Korea, bricks and tiles are used for exterior walls, and RC is the most common construction method. In both countries, single-family houses are rare, and apartments are common. In Japan, on the other hand, about 80% of all houses are detached, and more than 80% are wooden. Ceramic siding is often used as the exterior wall material, accounting for about 80% of the total.

2. Housing in Japan

The current housing stock in Japan is approximately 60 million units for a population of 124.56 million. According to the Ministry of Land, Infrastructure, Transport, and Tourism (MLIT), new housing starts in 2022 show a 3:3:4 ratio of approximately 250,000 owner-occupied units, 260,000 for sale, and 350,000 for rent. On the other hand, less than 1 million units are built annually for residential use, and ceramic siding is used for the exterior of approximately 80% of all owner-occupied, rental, and condominium units. In recent years, ceramic siding has also been used for relatively large apartment buildings (apartments, etc.).

3. Classification of Scrap of Ceramic Siding and Purpose of the Study

Although a path has been established for converting scrap wood from product factories into raw materials for cement, a) processing scrap at pre-cut factories for new construction, b) cutting scrap at construction sites, etc., are still being discharged in large quantities. a) is considered to have been recycled into raw materials rationally and disposed of appropriately due to technological advances such as complete pre-cutting technology and the wide-area certification system for waste disposal (2004), However, the figures for a) are not clear. On the other hand, as for b), although a certain number of emissions are actually generated by individual houses, etc., the number of emissions due to b) for the entire country remains unaccounted for.
The purpose of this study is to reconstruct the mechanism of building exterior construction with an eye on resource recycling and SDGs by investigating and estimating emissions differentiated by building

Table1 Exterior wall material in each country

country	exterior wall materials	Standard
Taiwan	bricks and tiles	CNS 382 CNS 461
South Korea	bricks and tiles	KSL 4201 KSL 1001
Japan	ceramic siding	JIS A 5422

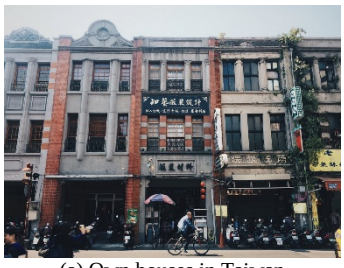

(a) Own houses in Taiwan

(b) Own houses in South Korea

(c) Own houses in Japan

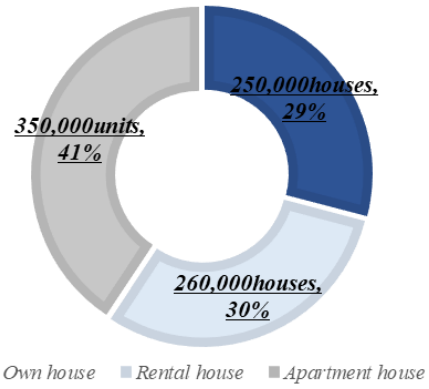

Figure1 Percentage of housing type in Japan

use and building scale by surveying the amount of ceramic siding scraps for new houses by focusing on the emissions of a) and b)

4. Research Outline

4.1 Interviews with ceramic siding contractors and survey analysis

4.1.1 Type of house ordered and role of installer

1) Owner-occupied house

In owner-occupied houses, also called custom-built houses, the builder (A), who places the order, is predetermined, and the designer (B), who is a house builder or construction company, charges the builder for the processing cost of ceramic siding offcuts, and the construction company (C2) (or pre-cut contractor (C3)) collects the offcuts.

2) Houses for sale

Houses for sale, also called "built-for-sale houses," do not have an owner (A) who actually lives in the house from the beginning, and the burden of disposal costs is passed on to the contractor (C2) (or pre-cut contractor (C3)).

3) Rental house

Rental houses include row houses and some built-for-sale houses.

As in the case of housing for sale, the processing cost is charged to the builder (C2).

4.1.2 Estimation of the ratio between the size of the house and the exterior wall area

The assumed exterior wall area S1 to the building area for a new housing site is as shown in Figure 3 based on interviews with the construction contractor,

The S1 of the assumed exterior wall area relative to the building area of a new housing site can be expressed approximately by the equation (1) as shown in Figure 3 based on interviews with the construction contractors. The accuracy of this S1 is verified, and values related to the area of each part of S2 to S7 shown in Table 1 and evaluation values of R4, R5, and R6 are derived to finally estimate the amount of ceramic siding edge material.

For a house with building area S[m²] and number of floors n, Assumed exterior wall area

$S1[m^2] = S \times (n+1)$ ... (1)

4.2 Residential Ceramic Siding Scrap Discharge Characteristics at New Construction Sites

4.2.1 Actual Wall Volume Measurements at New Construction Sites

A total of two surveys were conducted at new housing sites, Survey 1 and Survey 2. In Survey 1, the error between the assumed exterior wall area S1 and the actual exterior wall area S4 was 4.636 [%]. In Survey 2, the errors were 2.41[%] for Building C and 1.91[%] for Building D. The accuracy rate of the calculation formula R6 at the new housing site was 95.4[%], which indicates a high degree of construction accuracy.

4.2.2 Actual measurement and estimation of end material quantity at a new construction site

The following equation is used to measure the amount

Table2 Research Summary

No	Research Item	Survey/Research Contents
(1)	Interviews with specialty contractors at new housing sites	Survey of siding allocation methods, characteristics of edge materials, characteristics of openings, etc. at new housing sites to specialty contractors (Surveys 1 and 2) (11/18/2020-present, Machida City, Kanagawa Prefecture/Tama City, Tokyo)
(2)	Interviews with pre-cut processing factories for new construction	Survey (Survey 3) (2023/6/8-Present, Iruma City, Saitama Prefecture) of pre-cut processing factories for siding types, edge material quantity rate (%), opening area (m²), etc. for newly constructed houses.
(3)	(1) Calculation of the amount of scrap wood at (1) site/ (2) factory	Calculate multiple amounts of end material at each new housing site and pre-cut processing factory (Surveys 1, 2, and 3)
(4)	Accuracy rate of estimated exterior wall area calculation/ Yield ratio Calculation of scrap wood volume ratio	Calculate the accuracy rate/ yield rate/ fractional wood volume (%) of the assumed exterior wall area calculation formulas at each of the new housing sites and pre-cut fabrication plants (Studies 1, 2, and 3) Calculation Method S1=S0×(n+1) … (1) S1: Assumed exterior wall area [m²]. S0: Building area [m²]. N: Number of floors S2: Assumed area of siding applied from S1 S3: Actual floor area S6=S5-S4+S7… (2) S6: Amount of scrap of material [m²], S5: Area of ordered siding [m²] S4: Actual exterior wall area [m²] S7: opening area [m²]. R4=(S5-S6)/S5 ... (3) R4: Yield rate as a percentage of exterior wall use relative to S5 [%]. R5=S6/S5... (4) R6=S4/S1×100... (5) R5: Percentage of scrap of materials [%] R6: Accuracy rate of calculation formula [%].

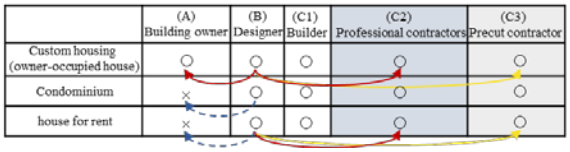

※C2 and C3 are only one of them. * The arrow indicates the flow of billing for scrap material collection costs.

Figure2 Flow of Waste Material Disposal Cost

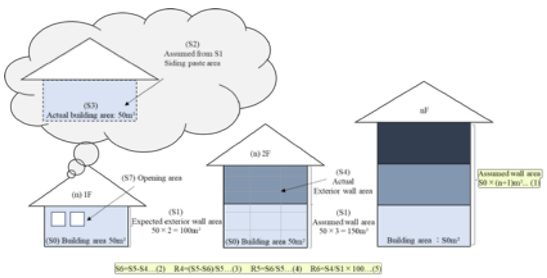

Figure3 Calculation formula for building area and exterior wall area

of end material. Assuming that the amount of edge material S6, the area of the forming plate ordered S5, the actual measured exterior wall area S4, and the opening area S7 (which is deducted in advance from S5),

S6=S5-S4... (2)

In addition, the yield ratio R4, which is the ratio of the area of the forming plate actually used for the exterior wall, and the edge material volume ratio R5, which is the edge material ratio, are

R4=(S5-S6)/S5... (3)

R5=S6/S5... (4)

Based on the results of Surveys 1 and 2, the average of R5 for the site was 15.472 [%].

4.2.3 Methods of Collecting and Disposing of Edgewood at New Construction Sites

At the new housing sites, there was a large amount of end material and powder end material due to cutting edges of overlap and eave sections from the ordered plate, 24-hour ventilation, electrical lines, and other cutting sections. However, because the cost is borne by the builder, many of them are sent to the final disposal site because it is less expensive and they are not collected by a specialized collection company for reuse. Although some ceramic siding manufacturers do collect siding, the system is not being used by individual homeowners.

In addition, the end-of-powder materials are not collected. In addition, the powder end materials have to be disposed of at the final disposal site, and the establishment of a recycling method is urgently needed.

4.3 Characteristics of End-Wood Discharge at a Pre-Cutting Plant

4.3.1 Measured wall volume in a pre-cut shop

In the pre-cut fabrication shop, we consider six data sets, mainly custom-built houses. As shown in Fig. 4 a) d), the accuracy rate of R6 shows a considerable difference compared to that of the field. This may be due to the fact that the calculation formula in (1) was created based on the thinking in the field. It is necessary to increase the number of data and establish a calculation formula for pre-cut processing plants in the future. As for actual values, the average of R6 was 85.763 [%], a difference of 11.252 [%] from the on-site average of 97.015 [%].

4.3.2 Measured and Estimated Amount of scrap in Pre-cut Processing Plants

In the data from the pre-cut processing plants, as shown in Figure 4 a) b) d) e), the yield rate was high, while the edge material volume rate tended to be low. The average values were 89.465[%] for the yield ratio and 10.535[%] for the edge material volume ratio. In addition, it was found that about 40[kg] of powder end material could be recovered per building, which is considered to be a reduction of powder end material emissions compared to on-site cutting.

4.3.3 Waste Collection and Disposal Methods in Pre-cut Processing Plants

Table3 Details of Survey2

Survey2: apartment house in Seiseki Sakuragaoka (Building C)		
Building type/n: Number of floors	Residential / 2F	
Subject site	Sekido, Tama City, Tokyo	
	Building C	Building D
S0: Building area	82.72[m²]	82.01[m²]
S1: Assumed wall area	248.16[m²]	246.03[m²]
S4: Actual Wall Area	254.289[m²]	250.821[m²]
S5: Area of ordered siding	286.751[m²]	303.303 [m²]
S7: Opening area	53.637 [m²]	53.637 [m²]
S6: Scrap material quantity	86.099 [m²]	106.119 [m²]
R4: Retention rate	69.974 [%]	65.012 [%]
R5: Scrap material quantity rate	30.026 [%]	34.988 [%]
R6: Calculation correct rate	97.59[%]	98.09[%]
		
a) Subject Residences	b) Scrap of board	
		
c) Scrap material at the corner	d) Powder scraps	

Table4 Details of Survey3

Survey 3: Interviews with pre-cut processing factories and housing examples	
Building type/n: Number of floors	Custom-built house/2nd floor
Subject site	Kamakura, Kanagawa
S0: Building area	49.29[m²]
S1: Assumed wall area	197.16[m²]
S4: Actual Wall Area	253. 59[m²]
S5: Area of ordered siding	77.75[%]
S7: Opening area	273.273［m²］
S6: Scrap material quantity	27.27［m²］
R4: Retention rate	47.253[m²]
R5: Scrap material quantity rate	82.709[%]
R6: Calculation correct rate	17.291[%]
S0: Building area	77.75[%]
	
a) Subject building elevation	b) Pre-cut work
	
d) Box for collecting scrap	d) Creating a corner from scraps

Although the pre-cut processing factory generates the same amount of end material as the new housing site, there is no waste because the factory cuts from CAD data. In particular, the factory creates the corners for orders, and the difference in R4 (R5) and R6 between the site and the factory was observed to be significant. The values averaged 11.252[%]/4.936[%] as shown in Figure 4 g). In addition, the environmental impact of cutting at the pre-cut factory is lower than that at the job site, because the pre-cut factory suctions the powder end material during cutting, creates the out-corners from the end material, and uses the recycling plants of the siding manufacturers.

5. Summary

The following findings were obtained from this study

1) In a survey and estimation of the amount of scrap wood in processing plants and on-site treatment of residential ceramic siding, parameters S0-S7 and R4-R6 were set, and the respective values were measured and estimated.
2) Comparison of data from three new housing sites and six pre-cut processing plants showed a large difference in the amount of end material and calculation accuracy rates. The difference was approximately 5[%] and 11[%], indicating that pre-cutting reduces the amount of end material.
3) The amount of end material during cutting was obtained from both the new housing construction site and the pre-cut processing plant.
4) The amount of end products from cutting is thought to be about 28,000[t] per year during the construction of new houses from both new house construction sites and pre-cut processing plants. Therefore, it is necessary to establish a method to recycle the powder end material.
5) There was a considerable difference in R6, which corresponds to the accuracy rate of the calculation formula, between the new housing construction site and the pre-cut processing factory. This is thought to be due to the fact that R6 is a formula used onsite. Therefore, it is necessary to examine the correction value in (5) in order to establish a new R6 for pre-cut fabrication shops.

Acknowledgments:

The authors would like to thank the NPO Exterior Ecology System and Tatenda Kenko for their great help in interviews and site surveys in conducting this study.

References:

[1] Ministry of Land, Infrastructure, Transport and Tourism website
[2] Kurihara, Tamura, Development of Recycled Finish Building Materials Using Ceramic Siding

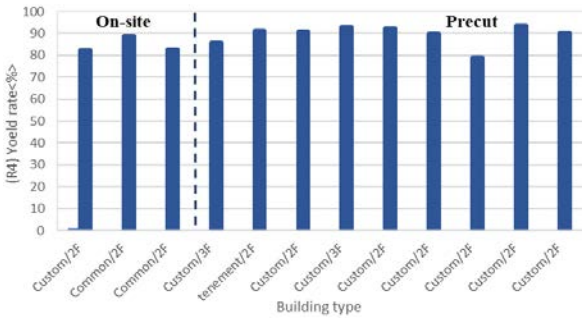

a) Yield ratio by building type (R4)

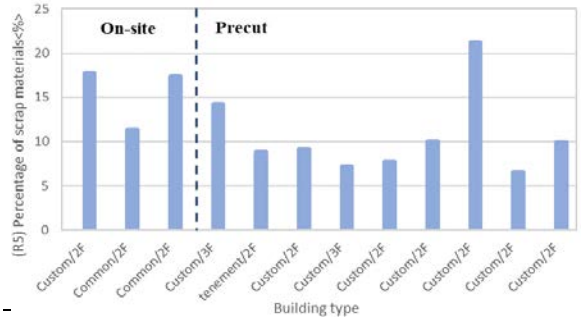

b) Percentage of scrap lumber by building type (R5)

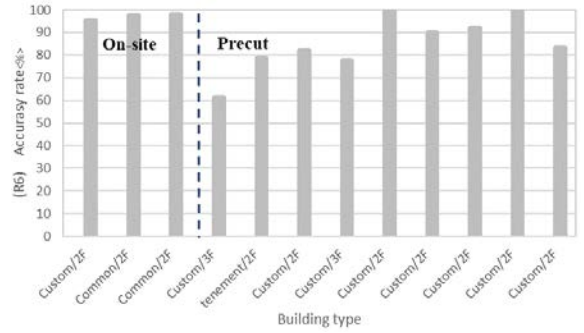

c) Accuracy rate by building type (R6)

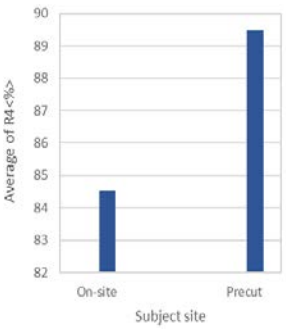

d) Average yield rate by type (R4)

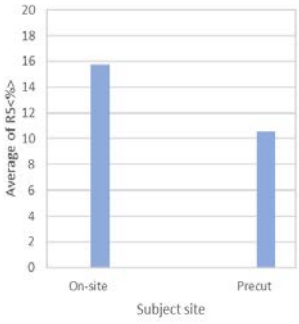

e) Average of the percentage of scraps by type (R5)

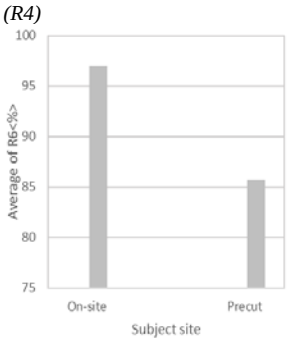

f) Accuracy rate by type (R6)

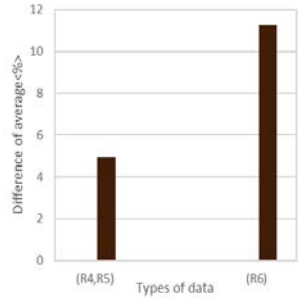

g) Difference of percentage

Figure4 Various ratios by building type (R4, R5, R6)

Behavior of Jet Flow with Coanda Curvature on One Side of Slot Outlet

Hiroki Tezuka*, Kaito Yabu, Koichi Nishibe, and Kotaro Sato

Mechanical Engineering Program in the Graduate School of Engineering, Kogakuin University, 2665-1 Nakano-cho, Hachioji, Tokyo 192-0046, Japan
E-mail: am22042@ns.kogakuin.ac.jp

Abstract

A basic study was conducted on the effect of the momentum ratio between the primary and secondary flow on the directional control of the jet when a Coanda surface was applied to one side of the slot outlet. A steady jet was used for the primary jet and a steady suction with a circular Coanda surface for the secondary flow. The effect of the secondary flow on the primary jet with a circular Coanda surface on one side of the slot was discussed. The results showed that as the momentum ratio of the primary jet to the secondary flow was increased, the maximum deflection angle was observed at a certain value, after which the deflection of the jet slowed down. The results indicate the possibility of controlling a wide range of jet flow directions when a Coanda surface is applied to one side of the slot outlet.

The method of controlling the direction of the primary jet by the secondary flow is called fluidic thrust vectoring. It has been demonstrated that this method can adjust the direction of the primary jet by adjusting the momentum of the secondary flow generated near a curved surface (Coanda surface) such as a cylinder [1]-[4]. Recently, Kobayashi et al. demonstrated the possibility of controlling the jet flow direction by the momentum ratio of the primary jet and secondary flow by placing circular Coanda surfaces on both sides of the slot and using a steady jet for the primary flow and steady jet, steady suction, and synthetic jet for the secondary flow, respectively [1]. On the other hand, studies on the directional control of the jet flow when a Coanda surface is applied to one side of the slot outlet are limited. In this study, we investigate the effect of momentum ratio on the flow characteristics of the jet flow controlled by the secondary flow near the Coanda surface. Typical flow patterns are presented and the jet deflection characteristics are discussed, mainly through flow visualization and velocity profile measurements.

In this experiment, a steady jet is applied as the primary jet and steady suction is applied as the secondary flow. For details of the experimental method and coordinate system, please refer to the references [1], [2].

Figure 1 shows the visualization results and velocity distribution in a typical flow field with second-order steady-state suction. The experimental condition is M_2/M_1 = 0.04. The experimental results obtained under these conditions show that the jet is deflected along a circular Coanda surface with a constant momentum ratio. It is also confirmed that the jet continues to adhere to the wall surface after deflection due to the Coanda effect. Subsequently, when the momentum ratio M_2/M_1 was increased as a parameter, the jet deflection became smaller. This result is similar to that of Kobayashi et al. [1], indicating that fluid thrust vectorization has an extreme value of the momentum ratio that deflects the jet significantly.

These results show the possibility of controlling a wide range of jet flow directions by adjusting the momentum ratio of the primary jet to the secondary flow when a coanda surface is applied to one side of the slot outlet.

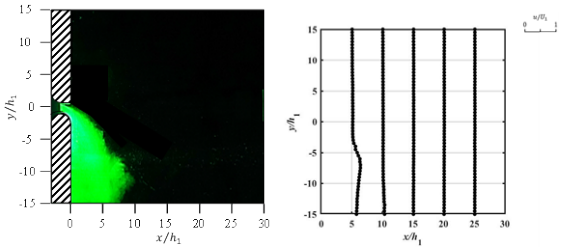

Fig. 1. Flow visualization and time-averaged velocity distribution under the condition of $M_2/M_1 = 0.04$ ($h_1 = 1.0 \times 10^{-2}$ m, $h_2 = 2.0 \times 10^{-3}$ m, $U_1 = 10.0$ m/s, $U_2 = 5.5$ m/s)

References:

[1] R. Kobayashi, Y. Watanabe, Y. Tamanoi, K. Nishibe, D. Kang, K. Sato, “Jet vectoring using secondary Coanda synthetic jets”, Bulletin of the JSME, Mechanical Engineering Journal, Vol. 7, No. 5 (2020).

[2] H. Tezuka, Q. Zhang, K. Nishibe, K Sato, “Flow-Direction Control of Primary Jets near a Wall Boundary using Secondary Flow with a Coanda Surface”, 12th TSME-International Conference on Mechanical Engineering 2022, Phuket, Thailand and Online, (2022).

[3] Mason, M. S. and Crowther, W. J., “Fluidic thrust vectoring of low observable aircraft,” CEAS Aerospace Aerodynamic Research Conference, Cambridge UK, (2002).

[4] Al-Asady, A., and Abdullah, A.M., “Fluidics thrust vectoring using co-flow method”. Al-Nahrain Journal for Engineering Sciences, Vol. 20, No. 1 (2017), pp. 5-18.

2023 International Symposium on Advanced Technology (ISAT-22)
Tainan City, Taiwan, October 19-20, 2023

Investigation of the thermosensitive mechanism in the interface of TiO_2/Cu_2O thin-film temperature sensors

Reika Miyajima*, Ichiro Takano**

*Department of Electrical and Electronic Engineering, Graduate School of Engineering, Kogakuin University, Tokyo, Japan
E-mail: cm23067@g.kogakuin.jp
**Department of Electrical and Electronic Engineering, Faculty of Engineering, Kogakuin University, Tokyo, Japan
E-mail: ct97912@ns.kogakuin.ac.jp

Abstract

In recent years, the applications of temperature sensors have expanded rapidly with the demand for IoT, and most of them are used in the field of consumer electronics. In general, chip-type NTC thermistors are the most widely used temperature sensors. On the other hand, in order to improve responsiveness to temperature changes, there is an increasing demand for thin film temperature sensors with as small a volume as possible. Our previous studies have shown that the interface of films has a significant effect on the thermosensitivity of pn-junction in oxide semiconductors. In this study, thin films with different copper oxide structures were fabricated by changing an input power of Cu_2O formation on TiO_2/Cu_2O multilayer thin films. To improve the sensitivity of TiO_2/Cu_2O thin-film temperature sensors, the thermosensitive mechanism of the interface was investigated.

Experimental procedure

A multi-process coating system (BC5146, ULVAC) was used for film deposition and the TiO_2 and Cu_2O layers were deposited by reactive sputtering. The deposition conditions are shown in Table 1. The temperature characteristics were measured by the two-terminal method using a table-top muffle furnace at temperatures ranging from 20 to 100 °C. The B constant, which represents the sensitivity of sensors, was calculated from the temperature and film resistance. The crystal structure was analyzed using a thin-film X-ray diffractometer (XRD: Rigaku Co., Ltd. Smart Lab.) at an angle of incidence of 0.4°. Depth profiles were measured by Auger electron spectroscopy (AES: JEOL JAMP-9500) to determine the atomic distribution around the interface of TiO_2 and Cu_2O layers in the films. As for the semiconductor properties, Mobility and carrier concentration were measured using a Hall effect measurement system (HMS-3000, ECOPIA).

Table 1 Film deposition conditions

Thin film	TiO_2	Cu_2O
Substrate	Glass (Eagle XG)	
Base pressure [Pa]	8.0×10^{-6}	
Film thickness [nm]	100	100
O_2 flow rate [sccm]	1.5	10
Ar flow rate [sccm]	20	15
Input power [W]	100	15, 20, 25 30, 40
Substrate heating temperature [℃]	300	250

Results and Discussion

Figure 1 shows the semiconductor properties of only the Cu_2O layer fabricated with different input powers of Cu_2O sputtering. Resistivity gradually decreased with an input power and reached a minimum value at 30 W, while the TiO_2/Cu_2O multilayer thin film showed the lowest resistance at 40 W. The trend of mobility with an input power was similar to that of resistivity. On the other hand, the carrier concentration showed the highest value at 30 W, but the B constant was a low value at 1400 K. The carrier density at 25 W with 3000 K in the B constant, was equivalent to that at 40 W with 1400 K.

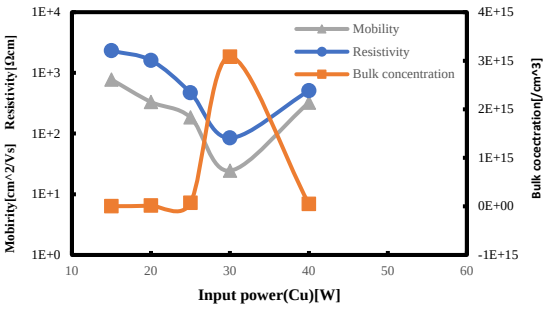

Fig. 1 Semiconductor properties of the Cu_2O layer

Summary

In this study, in order to investigate the influence of the interface of TiO_2/Cu_2O multilayer thin films, Cu_2O layers were fabricated at different Cu input powers and evaluated about temperature characteristics, crystal structures, depth profiles, and semiconductor properties. AES measurements revealed that Cu diffusion was observed around the interface as the input power for Cu_2O layer fabrication increased.

References

[1] H. Yamamoto, M. Takada, H. Nagai, *Ceramic functional films and their applications*, **1**, 143−149 (1998).

2023 International Symposium on Advanced Technology (ISAT-22)
Tainan City, Taiwan, October 19-20, 2023

Development of Accelerated Calendar-life Evaluation Method for Lithium-Sulfur Batteries

Kento Okanishi [a], Uran Tsunoda [a], Masayoshi Watanabe [b] and Shiro Seki [a]

[a] Graduate school of applied chemistry and chemical engineering, Kogakuin University, Tokyo, Japan
[b] Yokohama National University, Kanagawa, Japan
E-mail: bm22011@g.kogakuin.jp

Abstract

Lithium-sulfur(Li-S) batteries are attracting attention as high-capacity batteries. However, dissolution of reaction intermediates into the electrolyte is recognized as one of the issues for practical application. In order to solve this problem, sulfolane (SL)-based highly concentrated electrolyte has been reported. In this study, storage tests of Li-S batteries were carried out using this electrolyte with each temperature and state of charge(SOC).

Li-S batteries have been expected as one of the next-generation secondary batteries. The major advantages of Li-S batteries are their high theoretical capacity of elemental sulfur (S_8,1,672 $mAhg^{-1}$) as positive electrode active material which is derived from multi-step electron transfer reactions. On the other hand, S_8-based positive electrodes easily dissolve into conventional organic electrolyte solution as reaction intermediates of Li_2S_x ($2<x<8$), which is recognized as major cause of capacity loss factor. In order to solve this problem, solvate ionic liquid and sulfolane (SL)-based highly concentrated electrolyte has been investigated as Li_2S_x low-soluble electrolytes[1]. This electrolyte system should be effective for practical application of LiSB from long cycle performances. However, there have been no reports that focus on a mid to long-term life evaluation method specifically for Li-S batteries. In this study, storage tests of Li-S coin cells were carried out at each temperature and state of charge (SOC) for the establishment of accelerated calendar evaluation method.

S_8 (active material):Ketjen Black (KB: conductive additive):Titanium Black (TiB: additive) = 24:8:1 (wt.%) were mixed and heat-treated under Ar atmosphere at 428 K. Slurry of S_8/KB/Ti:CMC:SBR = 96.5:1.5:2 (wt.%) was prepared by adding binder solution (CMC:SBR), and was applied onto carbon-coated Al foil[2]. The obtained sheet was dried and punched into φ16 mm diameter disks for use as S_8 positive electrode. S_8 positive electrode, Li metal negative electrode, and electrolyte (HFE(diluent) : SL(solvent) : LiTFSA(electrolyte salt) = 4:2:1) were sealed in 2032-type coin cell to fabricate Li-S batteries(more than 200). The charge-discharge test for 3 cycles was carried out at 303 K as a pre-cycle to confirm the initial capacity of prepared cells. The cells were selected basis on several conditions, and the SOC were adjusted to 0, 30, 50, 70, and 100%, respectively, and storage tests were carried out at 303, 313, 323, and 333 K. Stored cells were performed charge-discharge tests every month (28 to 30 days).

Fig.1 shows the capacity retention after 20 months of storage in each SOC at 303.2 K, which is calculated from the discharge capacities of initial and after-storage tests. In particular, the cells stored at SOC70% exhibited a relatively noticeable cell degradation. While higher SOC tends to cause faster degradation in general-purpose LIBs[3], the results suggest that the trend may be different for Li-S batteries. Therefore, improvement of stability at charged state was expected in the case of Li-S batteries. Since the charge-discharge curves around 7 months(≒ 200 days) showed irregular redox-shuttle-like trends, it is necessary to examine the validity of storage degradation in particular.

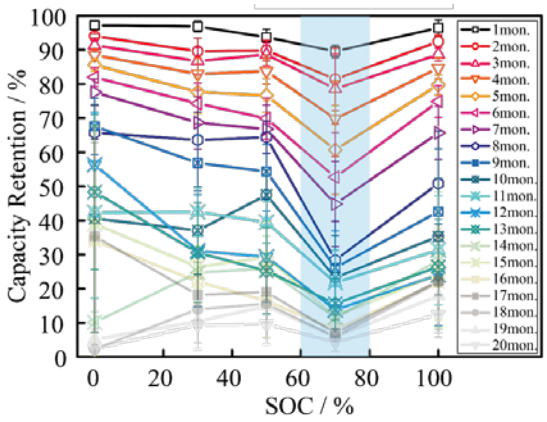

Fig. 1. Capacity retention after 20 months storage test in each SOC at 303.2 K.

On the day of the presentation, the results of d*V*/d*Q* analysis of charge-discharge curves will be presented to evaluate the validity of degradation by storage tests.

References:

[1] M. Yanagi, *et. al., J. Electrochem. Soc.* **167**, 070531 (2020).
[2] J. Liu, *et. al., Sustain. Energy Fuels*, **5**, 1821 (2021).
[3] M. Dubarry *et. al., Curr. Opin. Electrochem.* **9**, 106 (2018).

BEHAVIOR OF SYNTHETIC JET PRODUCED BY DOUBLE SLOTS

M. Takano[1]*, M. Katano[2], K. Nishibe[3], and K. Sato[4]

[1] Mechanical Engineering Program in the Graduate School of Engineering, Kogakuin University
E-mail: am23037@ns.kogakuin.ac.jp
[2] Mechanical Systems Engineering, Kogakuin University, Tokyo, Japan
E-mail: a220026@ns.kogakuin.ac.jp
[3] Department of Mechanical Engineering, Tokyo City University, Tokyo, Japan
E-mail: knishibe@tcu.ac.jp
[4] Department of Mechanical System Engineering, Kogakuin University, Tokyo, Japan
E-mail: at12164@ns.kogakuin.ac.jp

Abstract
In recent years, synthetic jets, which have been garnering increasing attention, have mostly been generated using single slots. The behavior of synthetic jets generated using multiple slots has not been widely discussed. In this study, we elucidated the behavior of synthetic jets generated using two slots. Control of the jet structure was achieved through time-averaged velocity distributions.

Steady-state continuous jets have been widely applied for flow control across various fields. In recent years, synthetic jets have garnered attention as alternatives to steady-state continuous jets, and researchers have been progressively elucidating the flow characteristics of synthetic jets [1]-[5].In particular, Nishibe and colleagues [1] reported that there were no significant differences in the properties between a continuous jet and a synthetic jet in the far downflow region of the synthetic jet.

However, it should be noted that conventional synthetic jets have mostly been generated using single slots [4-5], and the behavior of synthetic jets generated with multiple slots has not been widely discussed up to this point.

In this study, we attempted to elucidate the behavior of synthetic jets generated with the simplest configuration of multiple slots, specifically using two slots. We primarily discussed experimental results obtained under the condition of a slot spacing of 1 mm. Furthermore, some of the experimental results were compared with numerical simulations to validate their accuracy.

In this experiment, synthetic jets were generated by amplifying two waveforms generated by a pulse generator and driving two independent speakers with them.

The slot widths were each 3.0 mm. For flow visualization, liquid paraffin (Kanto Chemical Cat. No. 32033-00) was applied to Nichrome wires, and white smoke was generated by controlling the voltage using a transformer (Yamabishi Electric S-130-10). Subsequently, laser light was directed using a KATO KOKEN PIV Laser G1000, and the flow was captured using a SONY ZV-1 camera.−To measure the time-averaged velocity distribution, a hot-wire anemometer (KANOMAX IHW-100/7000 Series/Smart CTA7250), an I-type probe (KANOMAX 0251R-T5), a probe support (KANOMAX 4G0103), and a traverse system (Central Precision ALS-230-C2P) were employed.−Furthermore, for numerical simulations, ANSYS 2021 R1 with Fluent (ANSYS, Inc.) was utilized. The turbulence model chosen was the standard k-epsilon model, and numerical calculations were performed assuming two-dimensional, incompressible viscous flow. The mesh consisted of approximately 200,000 elements.

Figure 1 illustrates the time-averaged velocity distribution of the flow field under the conditions of a velocity $U_0 = 6.0[m/s]$ and a dimensionless frequency $f^* = 1.67 \times 10^{-2}$ ($f = 20[Hz]$). In this configuration, the total slot width for the two slots is 6 mm, but there is a 1 mm gap in the center. It is evident from the figure that the jet is spreading as it progresses downstream.

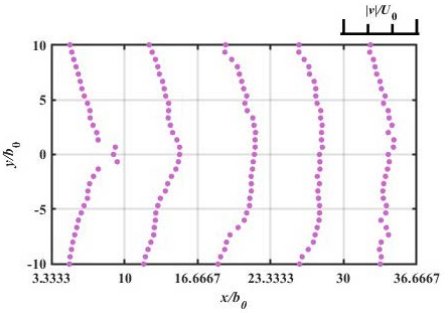

Fig. 1. Typical flow pattern

Furthermore, it is possible to investigate the influence of phase difference on the jet structure by independently controlling each synthetic jet.

References:
[1] Nishibe, K., Fujita, Y., Sato, K., and Yokota, K., 2014, “Study on the fundamental flow characteristics of synthetic jets (Behavior of free synthetic jets),” Journal of Fluid Science and Technology, Vol. 9, No. 1, pp. 1–12.
[2] Koso, T., and Morita, M., 2014, “Effects of Stroke and Reynolds Number on Characteristics of Circular Synthetic Jets,” J. Fluid. Sci. Tech., 9(2), pp. 1–15.

[3] Koso, T., Matsuda, S., Masuda, H., and Akahoshi, T., 2014, “Effect of Stroke on Structure of Vortex Ring Array in Circular Synthetic Jets,” J. Fluid. Sci. Tech., 9(3), pp. 1–11.
[4] T, ITO., K, NISHIBE., K, SATO., and D, KANG., 2022 “INFLUENCE OF ASYMMETRIC PROTRUSION-SHAPED SLOTS ON SYNTHETIC JETS” The 32nd International Symposium on Transport Phenomena.
[5] Ito, T., Miyachi, Y., Nishibe, K., and Sato, K., 2022, “INFLUENCE OF RECTANGULAR PROTRUSION-SHAPED SLOT ON FLOW CHARACTERISTICS OF SYNTHETIC JETS” The 7th international Conference on Jets, Wakes and Separated Flow.

Semiconductor Properties of Ti-doped ZnO Transparent Conductive Thin Films

Naoya Utsu*, Ichiro Takano**

*Department of Electrical and Electronic Engineering, Graduate School of Engineering,
Kogakuin University, Tokyo, Japan
E-mail: cm23008@g.kogakuin.jp
**Department of Electrical and Electronic Engineering, School of Engineering,
Kogakuin University, Tokyo, Japan
E-mail: ct97912@ns.kogakuin.ac.jp

Abstract

Oxide semiconductors such as ITO are the mainstream transparent conductive films used in liquid crystal displays or other devices. However, there is a need for an alternative material that exhibits the same performance as ITO because indium is a rare metal with limited production areas. In this study, we focused on ZnO which is one of the transparent oxides, and investigated the optimum conditions for transparency and electrical resistivity by doping Ti. The optimal Ti-doping condition for both transmittance and resistivity was obtained at 3.9 at.%.

1. Introduction

Transparent conductive films are widely used in touch panels and liquid crystal displays. Transparent conductive films are thin films which have visible light transmittance of 80 % or more and electrical resistivity of 10^{-3} Ωcm or less, and oxide semiconductors such as indium tin oxide (ITO) are currently the mainstream. However, as indium (In) is a rare metal with limited production areas, its stable supply is limited and its price fluctuates significantly.[1] Therefore, there is a need for an alternative material that offers the same performance as ITO.

In this study, we focused on zinc (Zn), which is 400 times more abundant than the rare metal In (Clark's number) and has the same amount of resources as tin (Sn). Another reason is that the transparent conductivity of its oxide, namely zinc oxide (ZnO), is comparable to that of ITO.[1] ZnO has n-type semiconductor properties and is expected to be highly functional when doped with impurities. The authors focused on titanium (Ti) as a doping element because of its transparency despite its high resistance as an oxide. There have been several reports on the improvement of transparency and electrical conductivity by doping Ti, although the methods are different.[2] In this study, we measured the optical transmittance and electrical resistivity of ZnO doped with Ti and investigated the relationship between the mobility and carrier concentration as a semiconductor.

2. Experimental Methods

2.1 Film Deposition Methods

The experimental method utilized by us has two steps. The first step uses film deposition equipment. We fabricated thin films using a multi-process coating system. It is based on the principle of reactive sputtering. This principle is that Argon ions collide at high speed with the target. Sputtering particles ejected from the target combine with the oxygen of the atmosphere gas to form oxide thin films. These deposit to the glass substrate forming thin films. The sample substrates were micro slide glasses (15 x 10 mm in a size) and silicon plates, that were ultrasonically cleaned with ethanol for 10 minutes. The oxide thin films were deposited by reactive sputtering using the multi-process coating system (BC5146, ULVAC Corp.). The deposition conditions are shown in Table 1. The deposition conditions were Zn sputtering input power of 20 W with an Ar gas flow rate of 20 sccm and an O_2 gas flow rate of 5 sccm to obtain a film thickness of 100 nm. The amounts of Ti doping were determined by the sputtering rate of Ti, so the sputtering rate of Zn was fixed, and the input power of Ti was varied.

Table 1 Film Deposition Condition

Thin-film name	ZnO-Ti doped
Substrate	Glass / Silicon
Pressure [Pa]	$< 1.0\times10^{-5}$
Film thickness [nm]	100
Zn input power [W]	20
Ti input power [W]	100 to 180
Ar flow rate [sccm]	20
O_2 flow rate [sccm]	5
Deposition temperature [℃]	Room temperature (25 to 30℃)

2.2 Evaluation Methods

The second step involves evaluation methods from five points. First, the amount of Ti doping in the prepared samples was measured using an energy dispersive X-ray fluorescence analyzer (EDX-7000/8000, Shimadzu Corp.). Next, for optical properties, transmittance was measured using a UV-visible spectrophotometer (UV-2550, Shimadzu

Corp.). After that, for electrical properties, voltage and electrical current were measured using a four-point probe (RG-5, NPS Corp.) with a pin spacing of 1.0 mm; then the resistivity of deposited samples was calculated. The resistivity ρ is expressed by the following equation (1) with the voltage value as V, the electrical current value as I, the film thickness as t, and the correction factor as Fr.

$$\rho = \frac{\pi}{\ln 2} \cdot \frac{V}{I} t \cdot F_r \quad (1)$$

Mobility and carrier concentration were measured using a Hall effect analyzer (HMS-3000, ECOPiA). Conductivity σ is expressed by the following equation (2) with the electron charge as q, mobility as μ_e, and carrier concentration as n.

$$\sigma = q\mu_e n \quad (2)$$

Finally, crystal structure analysis was performed by X-ray diffraction (SmartLab, Rigaku Co., Ltd.) at an X-ray incidence angle of 0.4 degrees.

3. Experimental Results

Figure 1 shows the light transmittance for Ti-doping ratio. With Ti-doping into ZnO, the optical transmittance in the visible light region increases and can be maintained at 80 %. Figure 2 shows the electrical resistivity for the Ti-doped ratio. In addition, figure 3 shows the mobility and carrier concentration. In 3.9 at.% of the Ti-doped ratio, the electrical resistivity was found to be 1.03×10^{-1} Ωcm (mobility: 2.85 cm^2/Vs, carrier concentration: -2.49×10^{19} cm^{-3}), the lowest among the other doping levels. The decrease in resistivity was attributed to the decrease in carrier concentration and increase in mobility because of the effect of Ti as a dopant in the oxygen vacancies of ZnO.

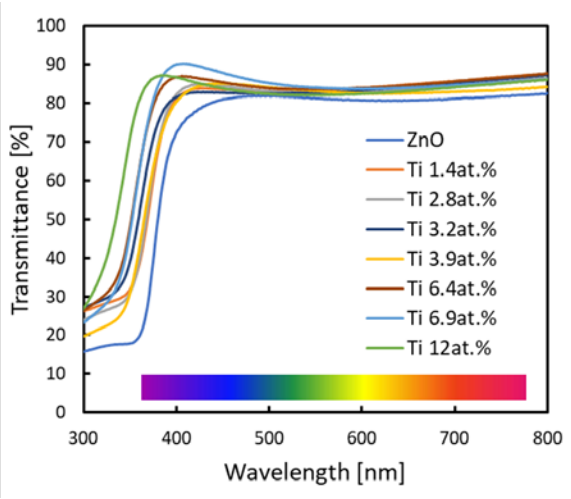

Figure 1 Light transmittance for the Ti-doped ratio

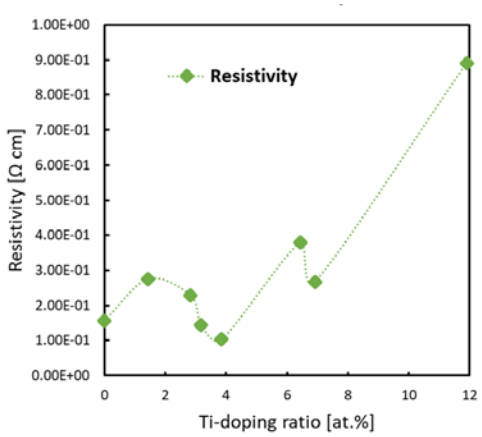

Figure 2 Electrical resistivity for the Ti-doped ratio

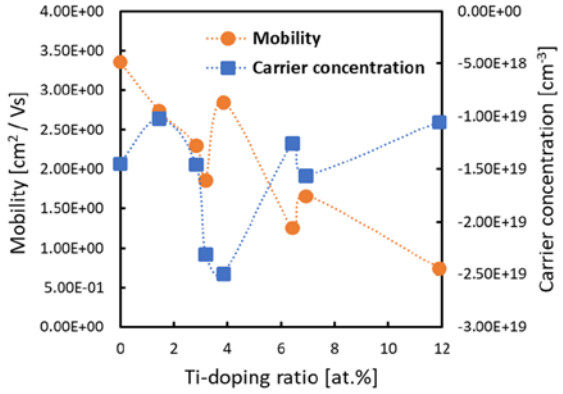

Figure 3 Mobility and carrier concentration for the Ti-doped ratio

4. Conclusion

In this study, Ti-doped ZnO thin films were prepared by reactive sputtering of Zn and Ti in an oxygen atmosphere. Ti-doping of ZnO resulted in better optical transmittance than ZnO. On the other hand, the lowest resistivity: 1.03×10^{-1} Ωcm (mobility: 2.85 cm^2/Vs, carrier concentration: -2.49×10^{19} cm^{-3}) was obtained at 3.9 at.% in Ti-doping. In the future, the results will be compared with those obtained by annealing in an oxygen atmosphere (heating temperature: 100°C) after film deposition in order to further reduce of the resistivity. In addition, the change in band gap with respect to the amount of Ti doping will also be investigated.

References:

[1] Maki, Kunisuke et al. *Technology of Transparent Conductive Films, Revised 2nd Edition*, Japan Society for the Promotion of Science, Committee on Transparent Oxide Optical and Electronic Materials No. 166, Ohmsha, (2008) pp.10-21,113-115,171-172.

[2] J.J.Lu, Y.M.Lu, S.I.Tasi, T.L.Hsiung, H.P.Wang, L.Y.Jang., "Conductivity enhancement and semiconductor–metal transition in Ti-doped ZnO

films", Optical Materials, Volume 29, Issue11, (2007) pp.1548-1552.

Entrainment Characteristics of Plane Jets Passing Over Tow-Dimensional Flat Plates

Kota Ishiwata[1], Koichi Nishibe [2] and Kotaro Sato[3]

[1]Mechanical Engineering Program in the Graduate School of Engineering, Kogakuin University, 2665-1 Nakano-cho, Hachioji-shi, Tokyo 192-0015, Japan
E-mail: am23008@ns.kogakuin.ac.jp
[2]Department of Mechanical Engineering, Tokyo City University, 1-28-1 Tamatsuzumi, Setagaya-ku, Tokyo 158-8557, Japan
[3]Department of Mechanical System Engineering, Kogakuin University, 2665-1 Nakano-cho, Hachioji-shi, Tokyo 192-0015, Japan

Abstract

In this study, the behavior and entrainment of jets passing over a two-dimensional plate row with multiple partition plates were discussed based on numerical analysis results. The trend of the entrainment amount depending on the length of the partition plates under some conditions was elucidated.

Research on jets has been active, and many studies have been conducted [2]. Jet flow research is wide-ranging, and jet flow behavior has been elucidated from a variety of perspectives, showing that secondary jets can control jet flow direction [2]. In recent years, ventilation technology has also attracted attention due to the influence of the Covid19 epidemic and beyond [1]. If directional control of jets is realized, efficient ventilation would be possible even in enclosed spaces. However, there is insufficient research on the behavior of jets and entrainment by two-dimensional flat plate rows. In this study, a two-dimensional flat plate array was reproduced by installing multiple partition plates, assuming ventilation in a partitioned and confined space such as the interior of an express train or a high-speed bus. Jet stream behavior and entrainment were investigated.

The study used a simple model and was performed numerically. The software used was ANSYS Fluent (ANSYS Inc.). The analysis domain was approximately 3.0×10^{-1} [m] in length and 2.0×10^{-1} [m] in width. For the boundary conditions, the upper part of the analysis area was set to constant total pressure, the slot outlet and suction slot areas were set to inlet, and the partition plate area and other areas were set to wall. The representative velocity is 3.0 [m/s], and the jet is ejected from the slot outlet. At the same time, it is suctioned from the suction slot at 3.0[m/s]. The basic slot width is 5 [mm], and the offset ratio was kept constant at 14. The distance from the center of the slot exit to the bottom of the partition plate is 70 [mm]. The main parameter of this study is the length of the partition plate, and the analysis was attempted in the range of 0 to 60 [mm]. The main result was that over the range of this study, the amount of entrainment did not change and no particular differences in entrainment were observed when the partition plates were longer than a certain length. It is possible that the wide spacing of the partition plates and the fact that the direction of travel of the jet did not change significantly in this experiment did not cause significant differences in entrainment volume.

References:

[1] Sowoo Park, Younhee Choi, Doosam Song, Eun Kyung Kim, 2021, " Natural ventilation strategy and related issues to prevent coronavirus disease 2019 (COVID-19) airborne transmission in a school building" Science of The Total Environment Volume 789, 1 October 2021, 147764

[2] Qiang ZHANG, Yu TAMANOI, Donghyuk KANG, Koichi NISHIBE, Kazuhiko YOKOTA, Kotaro SATO, 2023, "Influence of Amplitude of Excited Secondary Flow on the Direction of Jets" (https://doi.org/10.2322/tjsass.66.37)

Elucidation of the behavior of synthetic jets impinging on the flat plate

Michiya Yasumiba[1], Koichi Nishibe[2], and Kotaro Sato[3]

[1]Mechanical Engineering Program in the Graduate School of Engineering, Kogakuin University, Tokyo, Japan
[2]Department of Mechanical Engineering, Tokyo City University, Tokyo, Japan
[3]Department of Mechanical System Engineering, Kogakuin University, Tokyo, Japan
E-mail: am22068@ns.kogakuin.ac.jp

Abstract

The behavior of synthetic jets impinging on a flat plate of constant length was investigated. The flow field was visualized by numerical analysis, and continuous jets and synthetic jets were compared. When the distance of the slot-to-plate were relatively small, there was a difference between the flow fields of the continuous jet and the synthetic jet. In addition, it was observed that the behavior of the vortex between the slot and plate depended on the dimensionless stroke.

In recent years, impinging jets[1] has been demanded miniaturization of cooling systems, the use of synthetic jets with a simple driving principle in place of continuous jets is gaining momentum[2],[3]. In particular, cooling of precision devices such as electronic devices[2] requires a localized jet impinging on a target heat source. Bazdidi-Therani et al.[4] reported that for impinging synthetic jets, when the jet-plate distance is relatively small, a circulating vortex is formed between the jet and the plate. However, the formation mechanism of the circulation vortex remains unclear. In this study, a plate (rectangular body) of a fixed length was placed downstream of the synthetic jet, and changes in the vortex structure of the synthetic jet were observed by changing the relative distance between the slot and the plate.

Figure 1 shows a time-averaged dimensionless velocity contour plot obtained by numerical analysis for a slot-to-plate distance $x_w/b_0 = 2$. Under the conditions, the values of the continuous jet and synthetic jet representative of velocities U_{c0}, U_{s0}, slot width b_0, and plate length s_w, respectively, are constant. When $x_w/b_0 = 2$, (i) Continuous jet is traveling in the y-axis downstream as a wall jet after impinging on the plate. On the other hand, for synthetic jet of (ii) $L_0 = 90$, a large vortex is observed downstream in the y-axis downstream after impinging on the plate, and for (iii) $L_0 = 15$, it is confirmed that a very small circulating vortex is formed between the slot-to-plate. Therefore, it is clear that the behavior of the flow field of the synthetic jet between the slot and the plate under the under the conditions depends on the dimensionless stroke.

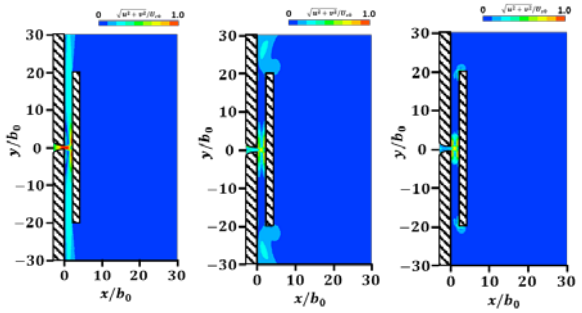

(i) Continuous Jet | (ii) $L_0 = 90$ ($f = 10$ Hz) | (ii) $L_0 = 15$ ($f = 60$ Hz)

Fig. 1. Flow field of continuous and synthetic jets from computational fluid dynamics (CFD).

[$\boldsymbol{U_{c0} = U_{s0} = 4.5\ \mathrm{m/s}, b_0 = 5.0 \times 10^{-3}\ \mathrm{m}}$, $\boldsymbol{s_w/b_0 = 40,\ x_w/b_0 = 2}$]

References:

[1] Kanamori, A, Hiwada, M, Senaha, I, Oyakawa, K. Effect of orifice configuration on flow behavior and impingement heat transfer. *The Japan Society of Mechanical Engineers Essay Collection (Part B)*, **77**(775), 456-464 (2011). (in Japanese).

[2] Gopal, K., Kean, C. A., Rajnish, N. S: a review. Contents lists available at ScienceDirect: Synthetic jet impingement heat transfer enhancement, *Applied Thermal Engineering*, **149**, 1305–1323 (2019).

[3] Yasumiba, M., Nishibe, K., Kang, D., Sato, K. Flow Characteristics of Two-Dimensional Plane Impinging Synthetic Jets. *Interdisciplinary Conference on Mechanics, Computers and Electrics (ICMECE 2022)*, (2022).

[4] Bazdidi-Tehrani, F., Karami, M., Jahromi, M. Unsteady flow and heat transfer analysis of an impinging synthetic jet. *Springer, Heat Mass Transfer*, **47**, 1363–1373 (2011).

Influence of TiO2 film thickness variation on photocatalytic properties of TiO2/Ti-Cu-O photocatalysts

Ritsuki. Kakizawa*, Ichiro. Takano**

*Department of Electrical and Electronic Engineering, Graduate School of Engineering,
Kogakuin University, Tokyo, Japan
E-mail: cm23016@ns.kogakuinac.jp
**Department of Electrical and Electronic Engineering, Faculty of Engineering,
Kogakuin University, Tokyo, Japan
E-mail: ct97912@ns.kogakuin.ac.jp

Abstract

TiO_2 photocatalyst has been improved effect to use several methods such as impurity dope. In this research, we focused on the thin film photocatalyst which was inserted Ti-Cu-O layer under TiO2 layer. TiO2 layer thickness changed from 0nm to 400nm. As a result, TiO2 layer thickness have an influence on photocatalyst property; 300nm has the highest ability.

Soler energy has been researched the purpose of improvement environment of earth. It is excepted making hydrogen-energy and organic-energy from water and CO_2.[1] TiO_2 is known as the photocatalyst which is found photochemical reaction the earliest of other materials. Therefore, TiO_2 is improved photocatalyst property by various methods such as doped impurity.[2] In addition, multilayer thin film photocatalyst which made CuO and TiO_2 layers showed higher effect than only TiO_2.[3] In this laboratory, CuO layer was changed to mixed TiO_2 and CuO layer; it calls Ti-Cu-O layer. Cu diffused from Ti-Cu-O layer to surface of TiO_2 layer. In this research, TiO_2 thin film thickness was changed from 0nm to 400nm, so I investigated influence of the property of photocatalyst, and the amount of Cu on the surface.

The film deposition process used a Multi-process Coating System (BC5146, ULVAC Corp.). The sample substrates were Non-Alkali grass (EagleXG); the size is 15 × 9mm. Table.1 shows the film deposition conditions. In this experiment, TiO_2 layer was changed the film thickness to 0, 10, 50, 100, 200, 250, 300, 350 and 400nm.

Table.1 Film Deposition Condition

Thin film	TiO_2	Ti-Cu-O
Substrate	Glass (EagleXG)	
Pressure [Pa]	5×10^{-6}	
Thickness [nm]	0~400	100
Ti target input power [W]	100	
CuO target input power [W]	-	90
O_2 flow rate [sccm]	1.5	
Ar flow rate [sccm]	20	
Substrate temperature [℃]	430	

I evaluated three points. First, the crystal structure of the samples was measured using an X-ray diffractometer (Smart Lab, Rigaku Co. Ltd.). Next, the property of photocatalyst was measured using 10ppm methylene-blue (Cat. No. 25249-30, KANTO CHEMICAL CO., INC.) aqueous solution; this solution is become transparent by photocatalyst when sunlight radiate from the sunlamp to photocatalyst, so transmittance of the solution evaluated photocatalyst property. Transmittance of the solution was measured using a UV-vis spectrophotometer (UV-2550, SHIMADZU Corp.) Finally, the surface chemical analysis was measured using an X-ray Photoelectron Spectroscopy (JPS9030, JEOL).

Figure.1 shows photocatalyst property and the amount of Cu on the surface. The sample of TiO_2 film thickness 300nm is the most effective of photocatalyst. In addition, photocatalyst efficient increases and the amount of Cu on the surface decreases with thickness of TiO_2 layer of the thickness from 0 to 200nm, but there is a no correlation between TiO_2 thickness and the amount of Cu of TiO_2 layer of the thickness from 200 to 400nm. In the thickness from 250 to 350nm, Cu on the surface prove influence photocatalyst property.

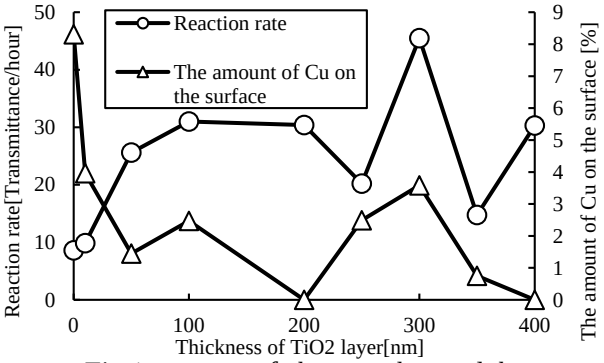

Fig.1 property of photocatalyst and the amount of Cu

In this study, we studied photocatalyst property when TiO_2 layer was changed the thickness. As a result, the sample of 300nm is the highest photocatalytic effect. In addition, Cu on the surface was suggested influence of the effect.

References

[1] T. Kubota, K. Doumen. Energy Conversation Photocatalyst, 2017. p.1~13
[2] N. Meng, L. Michael, L. Dennis, K. Sumathy; Renewable and Sustainable Energy Reviews, **11**, 401-425(2007)
[3] K. Takeda, I. Takano, JFS 148th lecture series, 06B-27, 58 (2022.9.6)

Three-dimensional Residual Stress Estimation of a Resistance Spot-welded Plate using the Eigenstrain Theory and X-ray Diffraction

Kensei Miyoshi*, Toshinori Tanaka, and Masaru Ogawa

Department of Mechanical Engineering, Graduate School of Kogakuin University, Tokyo, Japan
E-mail: am22064@ns,kogakuin.ac.jp

Abstract

Resistance spot welding is used in automotive manufacturing. However, the relatively large welding residual stresses generated during welding affect the fatigue life. Remaining life prediction of a vehicle body is possible if the three-dimensional residual stress distribution could be non-destructively evaluated on site. The X-ray diffraction method currently used can only non-destructively evaluate the surface residual stresses. The neutron diffraction method can be used to non-destructively evaluate the internal residual stresses, but it cannot be used in the field. In this study, a three-dimensional residual stress estimation method using X-ray diffraction and eigenstrain theory to estimate the three-dimensional residual stress distribution in resistance spot welding materials and evaluate its evaluation accuracy. Also, methods to improve the estimation accuracy of this method are discussed.

Introduction

Spot welding is a widely used in the manufacture of automobile bodies and home appliances. The residual stresses generated during welding affects the fatigue life of product. Individual differences in the residual stress are relatively large, so non-destructive method for evaluating three-dimensional residual stress is required. Currently, X-ray diffraction and neutron diffraction methods are used to evaluate residual stress. However, the X-ray diffraction method can only measure the surface, and the neutron diffraction method is only available in special facilities, making on-site measurements difficult. In this study, the surface elastic strains are measured by X-ray diffraction and the three-dimensional residual stresses are estimated based on the eigenstrain theory[1]~[3]. The three-dimensional residual stresses are estimated from obtained eigenstrain by finite element analysis. The estimation accuracy of this method for actual welded plates is evaluated and inverse problem analysis methods to improve the estimation accuracy are discussed.

Theory

The relationship between the surface elastic strain $\{\varepsilon\}$ and the three-dimensional eigenstrain $\{\varepsilon^*\}$ can be expressed as follows[2]:

$$\{\varepsilon\} = [R]\{\varepsilon^*\} \quad (1)$$

$[R]$ is the elastic response matrix that relates the surface elastic strain and three-dimensional eigenstrains, and it depends on the Young's modulus, Poisson's ratio, and geometry of the structure. Therefore, the inverse analysis for estimating the three-dimensional eigenstrain from the surface elastic strain can be expressed as follows:

$$\{\varepsilon^*\} = [R]^{-1}\{\varepsilon\} \quad (2)$$

When determining three-dimensional eigenstrains using surface elastic strains, the number of unknowns is relatively large in relation to the number of measurements. Therefore, there is a method to reduce the number of unknowns by approximating the unknowns by functions that takes into account the distribution trend of eigenstrain[4]. In this study, the eigenstrain distribution in the radial direction from the welding point was approximated by a Chebyshev polynomial multiplied by a Gaussian function. A parameter α was introduced to express the eigenstrain distribution in the thickness direction and the approximation was made by the following equation.

$$T_n(r) \times f(r) = \cos(nt) \times \frac{1}{\sqrt{2\pi}\frac{d}{3}} \exp\left(-\frac{r^2 + \alpha\left(\frac{T}{2} - z\right)^2}{2 \times \left(\frac{d}{3}\right)^2} \right) \quad (3)$$

Where n is the number of functions used in the approximation. The parameter d indicates the range of existence of the solution, which corresponds to the 3σ range of the Gaussian function. The eigenstrains of the r-, θ-, and z-directional components were approximated by n+1 functions of order 0 to n, respectively. In this study, the values of n, d, and α were optimized by the response surface method using the difference between the estimated and measured elastic strain on surface (hereinafter referred to as the residual norm) as the objective function.

Experimental material and methods

As shown in Fig. 1, a resistance spot weld was applied to the center of a single disc of 240 mm diameter ferritic stainless steel SUS430. The thickness of the plate was 4 mm. In this study, the estimation accuracy of this method was evaluated by comparing the estimated residual stresses on the bottom surface (z = 0 mm) with the values directly measured by the X-

ray diffraction. Measurements with the X-ray diffractometer to estimate eigenstrains were taken on the top surface (z = 4 mm) at intervals of 0.4 mm from the welding point (r = 0 mm) to 20 mm and at intervals of 10 mm after 20 mm, at θ = 30°, 60°, 90°, 120°, 150°, and 180°. At each measurement point, the elastic strain of the radial and circumferential components were measured.

Fig. 1 Resistance spot-welded disc made of ferritic stainless steel SUS430.

Results and discussion

The measured and the esitimated residual stresses at the bottom surface (z = 0 mm) are shown in Fig. 2. As the generated eigenstrains and residual stresses are relatively uniform in the circumferential direction, the measured values were calculated by averaging the residual stress distributions in the r-direction for different circumferential directions. First, the parameters were optimised for values of n up to 5, with the smallest residual norm at n = 5. As shown by the blue dotted line in Fig. 2, the results show that the residual norm can be estimated with good accuracy at a relatively large distance from the weld point, but the estimation accuracy near the weld is poorer, and the evaluation is on the dangerous side. When the range of n was examined up to 15, the residual stress distribution with the smallest residual norm at n = 12 improved the accuracy of the estimation near the weld, as shown by the pink dashed line in Fig. 2. However, the finite element model used in this study was not able to correctly simulate the plane stress state at the surface, resulting in errors in the physical quantities at the surface of the welded material. Therefore, the analysis needs to be carried out under more realistic conditions.

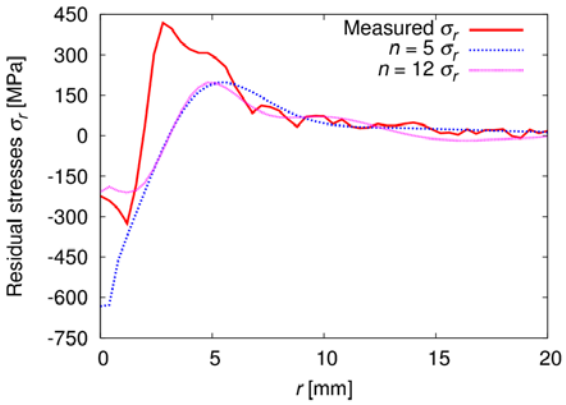

Fig. 2 Comparison of measured and estimated radial residual stresses on the bottom surface.

Conclusion

In this study, a three-dimensional residual stress estimation method using the X-ray diffraction and the eigenstrain theory was applied to an actual spot-welded plate to evaluate the estimation accuracy. Eigensrains were approximated by a Chebyshev polynomial multiplied by a Gaussian function to reduce unknown parameters. Estimation was performed by optimising the number and shape of approximation functions. As a result, the estimation accuracy was improved to increase the order of Chebyshev polynomial. However, the accuracy of the finite element model is insufficient, and improvements to the finite element model are needed for reliable estimation.

Acknowledgements

This work is supported by Japan Keirin Autorace (JKA).

References:

[1] Korsunsky, A. M., Butterworth-Heinemann, (2017).
[2] Ogawa, M., The Japan Society of Mechanical Engineers, **80**, No. 815 (2014).
[3] Ogawa, M., Ishii, T. and Furusato, S., The Society of Materials Science, Japan, **64**, No. 11 (2011), pp. 932-939.
[4] Yukio Ueda., Ning Xu Ma., Japan Welding Society, **11**, No.1(1993), pp. 189-195.

LCCO₂ Evaluation and Proposal of the Measures for Environmental Impact Reduction focusing on the Material Manufacturing, Fabrication, and Construction on site Phases of Steel-framed Buildings in Japan

First A. Takuto Kobayashi, Second B. Masaki Tamura,
Third C. Kenji Yamaoka, and Fourth D. Kazuaki Miyagawa

Department of architecture, Kogakuin University, Tokyo, Japan
E-mail: db20132@ns.kogakuin.ac.jp

Abstract
Carbon dioxide emissions are regarded as the main cause of global warming, which is now a serious problem in the world. This paper describes the calculation of the total amount of carbon dioxide emitted during the actual construction of buildings and the methods that can be used to reduce carbon dioxide emissions.

1. Introduction
The earth in which we live is currently experiencing a variety of abnormal weather events, such as localized heavy rainfall and record-breaking heat waves, and the natural disasters resulting from these events are becoming more serious in many parts of the world. One of the causes of this is the problem of global warming, which is caused by the release of large amounts of greenhouse gases into the atmosphere. Carbon dioxide (CO_2) accounts for the largest proportion of these greenhouse gases. It goes without saying that this substance is caused by the economy and other human activities, but since it is said that about one-third of the current emissions in Japan are related to buildings, it is essential for the building industry to work on reducing emissions of this substance. In the life cycle (LC) of a building, the operational phase accounts for a large proportion of emissions from the temporal perspective of long-term use, but it is important for the building industry to work to reduce CO_2 emissions in the construction phase, which is the phase before the operational phase. Therefore, this study investigates and understands the current status of carbon dioxide emissions from building construction, and based on this, examines methods that can be effective in curbing emissions of the same substance from various perspectives.

2. CO_2 emissions during the construction phase of steel-framed buildings

2.1 Calculation method for CO_2 emissions during material production and transportation
Regarding CO_2 emissions during the construction of a building, we first took an actual building and clarified its construction scale and material input. The basic information and details of the subject building are shown in Table 1. Then, we proceed with the calculation using the specific information of this building and the general CO_2 emission intensity. Among the LC of a building, we focused particularly on the stages from material production to construction. The calculation of the current amount and the study of methods to reduce emissions are conducted using the procedures shown in Table 2.

Table 2. Research Items and Contents.

1.Hearing	Data on CO_2 emissions intensity of steel products
2.Setting	System Boundary Scope Setting
3.Gathering	Assembling information on the subject building
4.Calculation	Total current emissions of CO_2 a. Manufacturing phase of building materials b. Transportation stage of building materials c. Construction phase on site
5.Comparison	Analyze calculated values and results
6.Simulation	Case Study for methods to reduce CO_2 emissions

Table 1. Overview of steel-framed warehouse construction to calculate CO_2 emissions during construction.

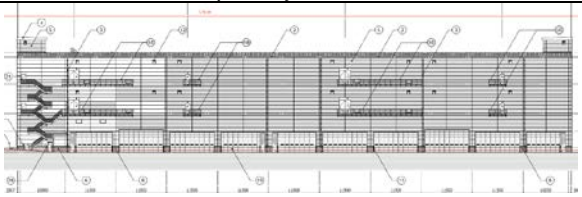
North side elevation view

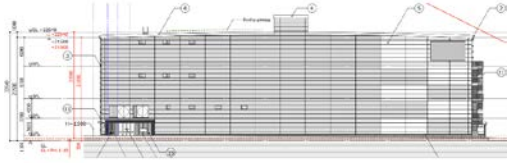
East side elevation view

Location		Hiratsuka City, Kanagawa Prefecture, Japan	
Main applications		Warehouses engaged in the logistics business	
Total floor area [m²]	29,606.53	**Floor-area ratio [%]**	194.81
Building area [m²]	9,666.57	**Building-to-land ratio [%]**	64.34
Fundamental structure	**Superstructure**	**Pillars and Beams**	Steel frame
		Floor	QL Deck/Fab Deck
	Substructure	**Foundation**	Reinforced concrete
		Piles	Ready-made pile

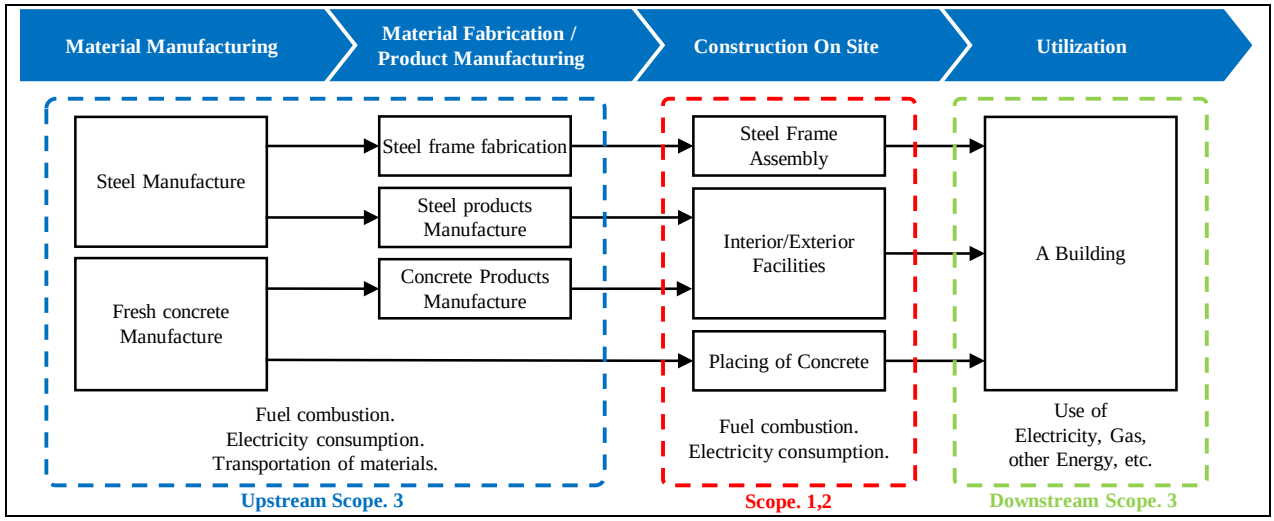

Fig. 1. Conceptual diagram of system boundary.

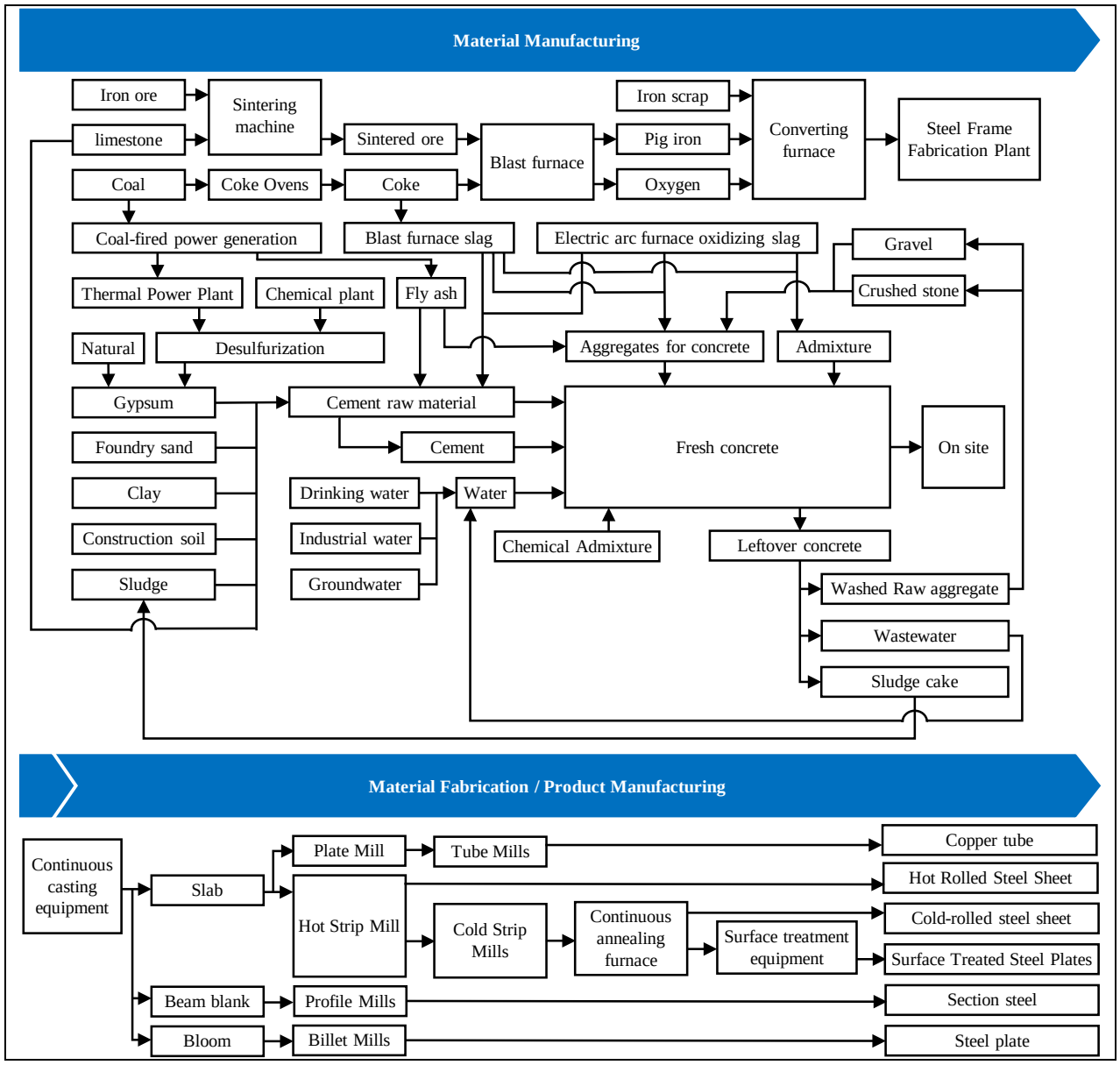

Fig. 2. Detailed diagram of Upstream Scope 3.

Table 3. CO_2 emissions intensity regarding the manufacturing and transportation stages of materials.

Item	Value	Authority
Ordinary Portland	0.77 [kg-CO_2/kg]	Japan Concrete Institute
Blast Furnace Cement Class A	0.66 [kg-CO_2/kg]	
Blast Furnace Cement Class B	0.45 [kg-CO_2/kg]	
Blast Furnace Cement Class C	0.30 [kg-CO_2/kg]	
10t Agitator Truck	0.25 [kg-CO_2/m^3km]	
10t Truck	0.18 [kg-CO_2/tkm]	
Fresh Concrete	0.32 [t-CO_2/m^3]	Industrial Relations Table
Steel Pipe	2.40 [t-CO_2/t]	
Glass Wool	2.69 [kg-CO_2/kg]	
Rebar	752.75 [g-CO_2/kg]	The Japan Iron and Steel Federation
Steel Plate	856.69 [g-CO_2/kg]	
Shaped Steel	874.20 [g-CO_2/kg]	
Hot Dip Galvanized Steel Plate	1063.99 [g-CO_2/kg]	

2.2 Amount of CO_2 emitted in the material manufacturing stage (Upstream Scope.3)

(1) Emission from reinforced concrete used in foundations

The total quantity of ready-mixed concrete is 9,479 [m^3]. By multiplying that quantity by the CO_2 emissions intensity value of raw concrete, the amount of carbon dioxide emitted from the raw concrete used can be calculated.

995[t] of rebar is used. The CO_2 emission of the rebar is obtained by using the CO_2 emission intensity of the rebar to that value.

(2) Emission from steel materials used in the superstructure

Steel frame members include beam materials such as H-beams and square steel tubes, and column materials. The total CO_2 emissions of steel frame materials can be calculated by using the CO_2 emissions intensity of each steel frame member.

(3) Emission from precast piles

Since a pile is composed of four types of parts that are combined to form one pile, the emissions of each part were first determined in order to get the CO_2 emissions of all 96 piles. Then, the emissions of each type of pile were calculated by summing the emissions of the four specified types of parts.

(4) Emission from deck plates

Fab decking and composite decking are shown as emissions of steel plate and rebar only, not including the already required emissions of ready-mixed concrete.

(5) Emission from roofs

As shown in Figure 5, it consists of 0.8[mm] galvalume steel plate, 100[mm] glass wool, and 0.6[mm] galvalume steel plate in a three-layer folded half structure.

(6) Emission from exterior walls

The CO_2 emissions of the exterior wall material were calculated using information on the materials and thicknesses of that product from the exterior wall manufacturer's catalog.

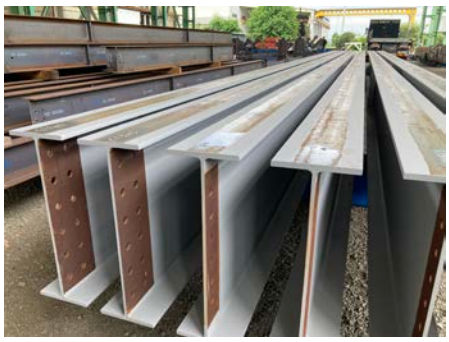

Fig. 3. Steel frame used for superstructure.

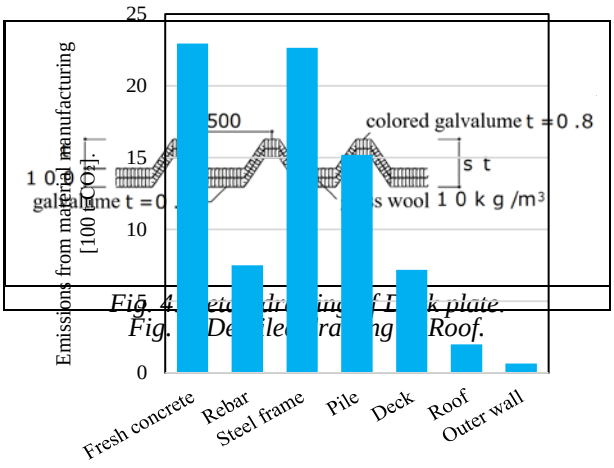

Fig. 4. [illegible] of Deck plate.
Fig. [illegible] Roof.

Fig. 6. Calculated amount of CO_2 emitted in material manufacturing.

(7) Emission in the fabrication of steel frame components

The main processes in a processing plant for steel members include purchasing crude steel, bolt drilling, cutting, end machining, and welding. The calculation of CO_2 emissions from these processes is based on the power consumption associated with the operation of the plant's machinery.

As of September 2023, we have not received any data related to these processes from the processing plants that we visited, and we plan to begin calculating CO_2 emissions from processing as soon as we are able to obtain such data.

2.3 Amount of CO_2 emitted in the material transportation stage

The CO_2 emissions of fresh concrete are larger per distance due to the difference in weight used. However, since the distance of transportation for rebar and steel frame materials is very large, when both weight and distance are taken into account, the emissions are greater for rebar and steel frame than for fresh concrete.

Figure 8 shows the loading of steel-frame members that have finished processing onto a transportation vehicle. if a large number of materials can be loaded at once when loading members that are about 12 [m] long and uneven, transportation time can be reduced, energy can be saved, and CO_2 emissions related to transportation can be curbed. The loading will significantly change the efficiency of the transportation of materials to the site and the degree of environmental impact during the transportation phase.

Table 4. Machining process for steel components.


a. Crude steel


b. Machining of bolt drilling


c. Sandblasted surface


d. Manual welding work

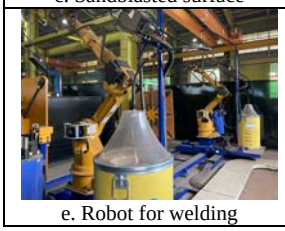
e. Robot for welding

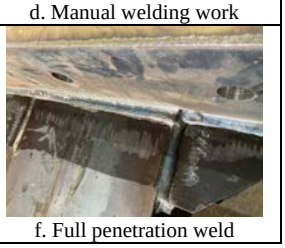
f. Full penetration weld

Table 5. Calculated value of CO_2 emissions during the transportation stage of materials.

Material	Quantity		Transport Distance [km]	Vehicles	Emissions [kg-CO_2]
Ready-mixed concrete	9,479	[m³]	5	Agitator	11,991
Rebar	955.106	[t]	400	10ton truck	68.004
Steel frame	2596.149	[t]	500	10ton Trailer	231,057
Piles	2901.302	[t]	200		103,286
Deck	922.018	[t]	70		11,488
				Total Emissions	425,826

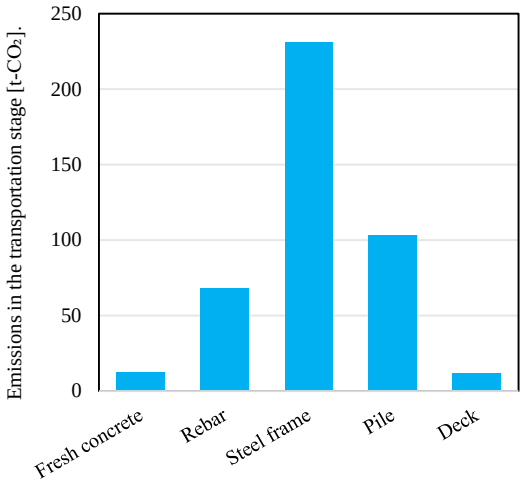

Fig. 7. Calculated amount of CO_2 emitted during transportation of materials.

Fig. 8. View of loading processed steel frame components.

2.4 Comparison for CO_2 emissions of building frame materials and exterior materials

The percentage of CO_2 emissions in the manufacture of each material determined above is represented in Figure 9. Fresh concrete and steel frame members, which are used in large quantities, accounted for a large percentage, followed by piles, reinforcing bars and deck plates, and roofing and exterior wall materials, in that order. The building frame materials from ready-mixed concrete to deck plates accounted for 96.6 percent of the total CO_2 emissions, while emissions from exterior materials were only 3.39 percent. Therefore, it can be said that most of the CO_2 emitted in the construction of a building from the manufacture of its materials comes from the building frame materials.

2.5 Comparison for CO_2 emissions of upper and lower structural parts of buildings

Figure 11 shows a graph comparing CO_2 emissions from materials used in the superstructure with those from materials used in the substructure.

The sum of the CO_2 emissions from the fresh concrete and rebar used in the foundation is slightly higher than that of the steel frame material in the superstructure, plus about 1,500 [t] more from the piles. As for the piles, more than half of their emissions are derived from concrete, so that, in effect, most of the CO_2 emissions of the substructure can be considered to be from concrete.

On the other hand, in the superstructure, the ratio of emissions from exterior materials such as roofing and exterior wall materials is very small among those added on top of the steel frame materials, and the floor deck is the second largest emission area in the superstructure after the steel frame materials. After steel framing, floor decking is the second largest superstructure in terms of emissions, and this varies with the size of the floor area. Considering that the subject building is a warehouse building for logistics, it is necessary to ensure that the floor area is above a certain level and that spans are skipped. The large floor area can be expected to increase CO_2 emissions to some extent. Beams play the most important role in achieving the skipped span, but at the same time, the floor itself must be able to support a larger load. This requires an increase in the thickness of the floor, which in turn increases the amount of concrete used. In fact, the 3,479 [m³] of concrete used in floor decks is by far the largest amount of concrete compared to other materials, and more CO_2 is emitted from that concrete. Reinforcing steel in the floor deck emitted half as much CO_2 as concrete.

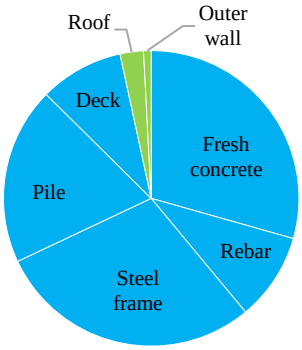

Fig. 9. CO_2 emission ratio of building frame and exterior materials.

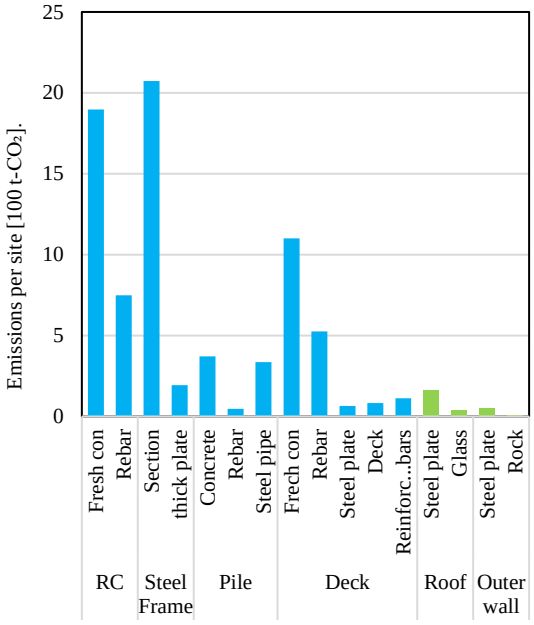

Fig. 10. Calculated value of CO_2 emissions by constituent material for each part (up-S.3).

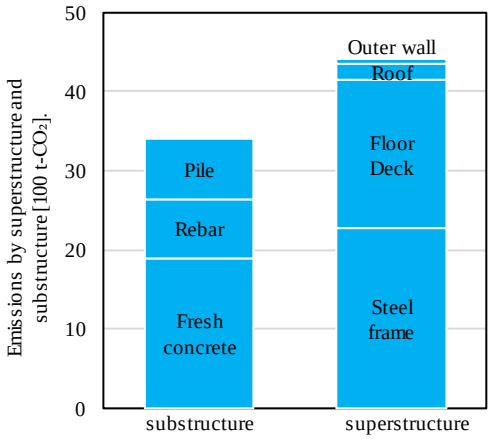

Fig. 11. Total CO_2 emissions from superstructure and substructure.

2.6 Comparison for CO_2 emissions in material production and transportation

Figure 12 shows the CO_2 emissions during the manufacture of the frame and exterior materials and the transportation of these materials.

About 7,800[t] of CO_2 is emitted in the manufacturing of materials, and about 400[t] of CO_2 is emitted in their transportation stage. In other words, of the CO_2 emitted from the production of materials at the plant to their transportation to the site, transportation accounts for only about 5 percent, and about 95 percent is accounted for by the manufacturing stage.

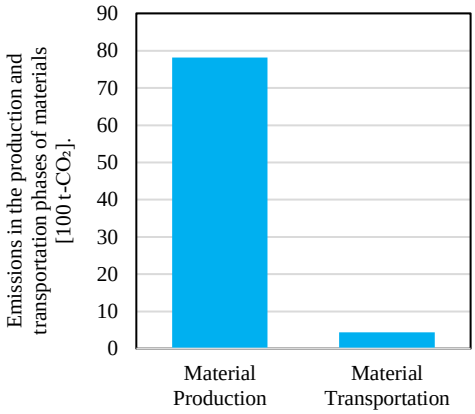

Fig. 12. Calculated value of CO_2 emissions in material production and material transportation.

3. Study for CO_2 emission reduction effect by material replacement

As mentioned above, the stage of building materials from manufacturing to transportation that emits the largest amount of CO_2 is the manufacturing of materials. Furthermore, since most of the CO_2 emissions are emitted from structural materials, priority is given to reducing these emissions. As a first effort, a simulation was conducted to replace the type of cement used in concrete with one that has a smaller environmental impact. The material properties of each type of cement are taken into account.

The cement used in the fresh concrete was replaced from ordinary Portland cement to blast furnace cement type B. Due to the characteristic of blast-furnace cement of delayed onset of strength, it was used in areas of abandoned formwork and in areas where little or no strength was required to be secured. Since concrete made of blast-furnace cement is superior to that made of ordinary Portland cement in terms of durability, blast-furnace cement was used for the earthen floor, which is affected by external forces such as trucks being brought into the building. From the viewpoint of design, blast-furnace cement was used in areas exposed to the surface because of its resistance to cracking on the concrete surface.

Other aspects to be considered include cost, technology, and distribution, but cost and distribution are not considered important in this study.

This case study is still in the research stage, and we plan to examine methods of CO_2 reduction by simulating various cases in the future.

4. Summary

From the above, it was found that the production of frame materials accounts for the largest proportion of CO_2 emissions in building construction. In addition, since the amount of frame materials used is large, their weight is larger than that of exterior materials, and the amount of CO_2 emitted during transportation is likely to increase accordingly.

By replacing the materials used in the building frame with materials that have a smaller environmental impact, it will be possible to significantly reduce the CO_2 emissions of the entire building.

Furthermore, for the building targeted in this study, the emissions from the substructure were larger than those from the superstructure because it is a warehouse building used for logistics and a low-rise building with a large floor area. This means that the ratio of emissions from the superstructure to the substructure changes with the height of the floors.

With regard to the transportation of materials, more efficient loading that allows more materials to be transported at one time can reduce CO_2 emissions associated with transportation.

Acknowledgements

This research is a collaboration between Kogakuin University and JFE Civil in 2023, and we would like to thank Mr. Kamura of JFE Civil and Kajikei Tekko for their cooperation.

References

[1] Ministry of the Environment: Greenhouse gas emissions in FY2020 (preliminary figures)
[2] JCI: Environmental text of concrete (draft) [revised version]
[3] JISF: LCI Data Collection
[4] Architectural Institute of Japan, Committee on the Global Environment, Subcommittee on LCA Guidelines
LCA Guidelines for Buildings (Draft) - Focusing on LCCO₂ for the Prevention of Global Warming -, 1998, 11
(Draft) LCA Guidelines for Buildings - Focusing on LCCO₂ for Preventing Global Warming, 1998, 11

2023 International Symposium on Advanced Technology (ISAT-22)
Tainan City, Taiwan, October 19-20, 2023

Automatic Exploration Method for Identification of Multiple Radiation Sources

Yurika TAKAHASHI* and Hanwool WOO

Department of Mechanical Engineering, Kogakuin University, Tokyo, Japan
E-mail: am23039@ns.kogakuin.ac.jp

Abstract

This study proposes an automatic exploration method using a mobile robot for unknown multiple radiation sources. The proposed method autonomously determines the next measurement point based on the obtained data from a directional gamma-ray detector. Through simulation experiments, it is demonstrated that the proposed method can autonomously generate an inspection path and accurately identify multiple radiation sources.

1. Introduction

It is necessary to grasp the distribution of radiation sources in advance for human workers who conduct tasks close to radiation sources such as decommissioning the Fukushima Daiichi Nuclear Power Plants. However, there is a risk of radiation exposure when human workers conduct the inspection to grasp the distribution of radiation sources. To solve this problem, an approach using a mobile robot equipped with a gamma-ray detector to estimate the distribution of radiation sources while moving autonomously has been proposed. Kim et al. measured the number and direction of incoming gamma rays at unit time from a directional gamma-ray detector and used Maximum Likelihood Expectation Maximization (MLEM) to reconstruct them [1]. However, the measurement points were predefined and no mention was made of path generation. Kishimoto et al. measured the number and direction of incident gamma rays at unit time using a directional gamma-ray detector. They used principal component analysis to plan the exploration path [2]. However, this method cannot be applied to the exploration for unknown radiation sources since the method has the limitation that the intensity of the radiation source should be known. In actual exploration missions, it is difficult to know the intensity of a radiation source in advance. Consequently, an automatic exploration method is strongly required for identifying radiation sources.

This paper proposes an automatic exploration method to generate moving paths and identify multiple radiation sources even if the intensity of the radiation sources is unknown. The proposed method applies a law that the number of incident gamma rays per unit of time is inversely proportional to the square of the distance between the radiation source and the detector. A novel index which depends on only the distance between the radiation source and the detector is proposed, and it leads to grasp the distance to the source. Hence, it is possible to generate an exploration path that approaches and encloses the radiation source up to a certain distance even if the radiation intensity is unknown. Moreover, this paper discusses an exploration procedure to identify multiple radiation sources using the proposed index.

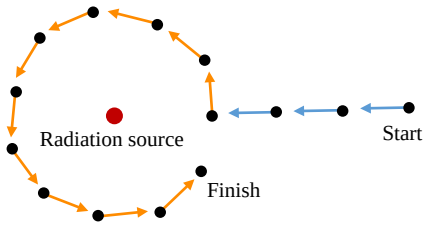

Fig. 1. Designed path for autonomous exploration.

Based on the obtained data from the gamma-ray detector, the distance to the radiation source can be estimated. Then, the exploration can be performed in order starting from the closest radiation source to the current position of the robot.

2. Proposed Method

2.1 Radiation Measurement

There are several types of radiation, including alpha, beta, and gamma rays. Among them, the gamma rays have the most muscular penetrating power through objects. Radiation detectors can be divided into two categories: non-directional and directional detectors. Non-directional detectors acquire the number of incident rays emitted from a radiation source. In contrast, directional detectors acquire the direction of incident radiation and the number of incident rays. The radiation suitable for the mission depends on the mission, and detectors have been developed to meet the purpose. In this study, directional gamma-ray detectors are assumed to be used to locate the position of the radiation source based on the direction of incidence of the source . Specifically, Compton cameras[3] and gamma cameras can be used.

The exploration path to localize the radiation source should be close enough to the radiation source to encircle it, as shown in Fig. 1. The closer the distance between the radiation source and the gamma detector, the greater the number of incoming gamma rays per unit time and the higher the measurement efficiency. Therefore, the robot first moves in the direction where the radiation source can be present to shorten the measurement time. The gamma rays measured by the detector are projected using the simple back projection method. Although the

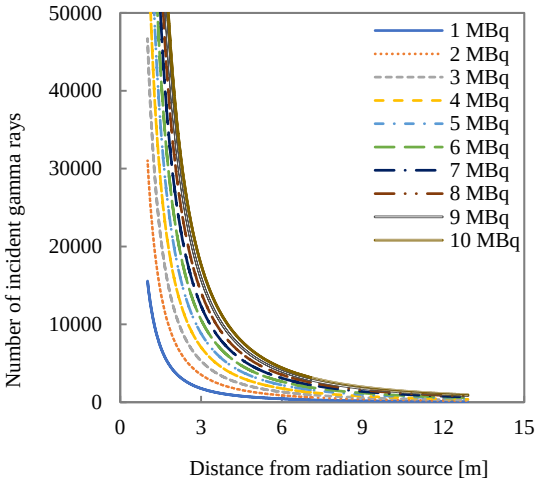

Fig. 2. Number of incident gamma rays vs distance from radiation source.

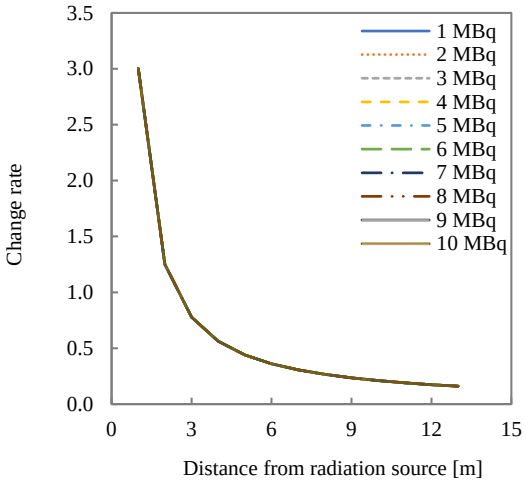

Fig. 3. Change rate vs distance from radiation source.

directional detector can determine the direction of incidence of gamma rays, it cannot acquire depth information. Therefore, measurement from multiple directions is required to locate the radiation source, and the robot must move to surround the radiation source.

2.2 Characteristics of Incident Gamma Rays

As radiation spreads in all directions, the number of incident gamma rays in unit time is inversely proportional to the square of the distance from the radiation source. Assuming a spherical radiation source in a flat space, the radiation intensity is G, and the distance from the detector to the source is r, the number of incident gamma rays per unit time and unit area, N, can be obtained as follows.

$$N = G/4\pi r^2 \tag{1}$$

Furthermore, if the area of the detector is S, the number of incident gamma rays n detected by the detector per unit time is expressed as follows.

$$n = SN = GS/4\pi r^2 \tag{2}$$

This paper focuses on the law that the number of incident rays is inversely proportional to the square of the distance from the radiation source and defines a novel index necessary for generating the exploration path.

Kishimoto et al. performed a principal component analysis to generate the exploration path [2]. Then, the direction of incidence of gamma rays was set as the first principal component, and the perpendicular direction to it was set as the second principal component. The robot's movement was used to generate the path generation so that it would move toward the first principal component and approach the radiation source until it reached a certain intensity and then move toward the second principal component and surround the radiation source once it exceeded the index. As this criterion index was determined based on the known intensity of the radiation source, this paper derives an index independent of the intensity of the radiation source.

2.3 Novel Index for Path Planning

In Eq. (2), the relationship between the number of incident gamma rays and the distance r between the detector and the radiation source is shown in Fig. 2, as the intensity of the radiation source G varies from 1 MBq to 10 MBq. The slope obtained by integrating Eq. (2) is challenging to use as an indicator since it depends on the intensity of the radiation source. Therefore, the change rate is derived from the number of incident gamma rays. If the number of incident gamma rays closer to the radiation source is $n(r_i)$, the number of incident gamma rays at the previous measurement point is $n(r_{i-1})$, and the following equation expresses the change rate α.

$$\alpha = \{n(r_i) - n(r_{i-1})\}/n(r_{i-1}) \tag{3}$$

Substituting and transforming Eq. (2), we obtain the following equation.

$$\alpha = ({r_{i-1}}^2/{r_i}^2) - 1 \tag{4}$$

Figure 3 shows the relationship between the change rate α and the distance r between the detector and the radiation source for a robot taking measurements at 1.0 m intervals. Equation (4) shows that the change rate α can be expressed only in terms of the distance r from the detector to the radiation source. The distance r is the distance from the detector to the radiation source, and it can be used in the case of a straight line moving toward the radiation source at regular intervals.

Equation (4) shows that the distance r from the detector to the radiation source is expressed by the change rate α. From this, the distance r from the detector to the radiation source can be estimated from

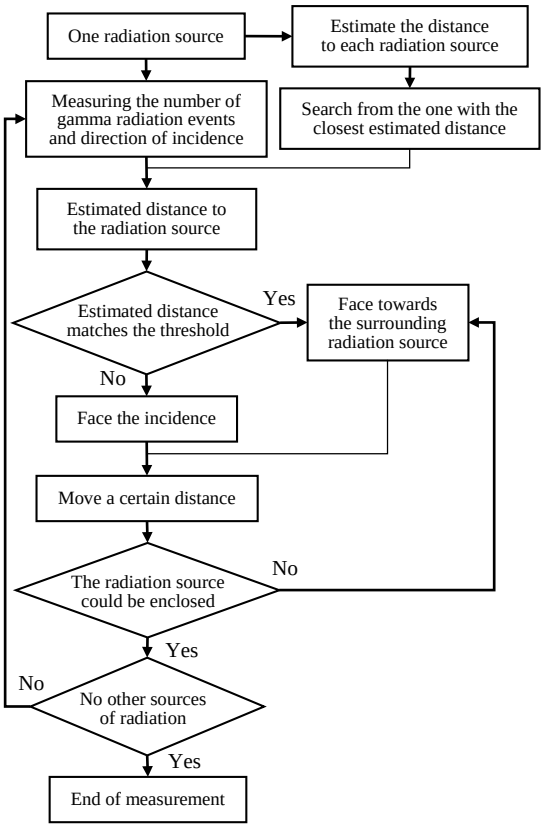

Fig. 4. Flowchart of path planning method.

the change rate α. If the distance advanced between measurement points $i-1$ and i is l, the distance to the radiation source at the measurement point can be expressed as $r_{i-1} = r_i + l$. Substituting this into Eq. (4) and transforming it, r_i can be expressed as

$$r_i = \left(1 + \sqrt{1+\alpha}\right) l/\alpha \qquad (5)$$

Therefore, the change rate α can be calculated from the incident number n measured by the detector, and this change rate α can be used to estimate the distance r from the current position to the radiation source. Since the change rate α is not affected by the intensity of the radiation source, the estimated distance r to the radiation source can be used as an indicator to determine the direction of movement in route generation using principal component analysis, even when the intensity of the radiation source is unknown.

2.4 Path Planning Method with Novel Index

In this study, the path planning is based on the estimated distance to the radiation source presented in Section 2.3. A flowchart of the proposed method is shown in Fig. 4. First, the number of gamma rays and the direction of incidence are measured for a certain time using directional gamma-ray detectors. The incident gamma rays are depicted on a map using the simple back projection method. The rate of change is calculated based on the measured data and the distance to the radiation source is estimated from the rate of change. When the estimated distance is greater than a threshold value, the orientation of the robot is rotated in the direction of the incident gamma radiation. When the estimated distance matches the threshold value, rotate the orientation of the robot in the direction surrounding the radiation source. The robot moves a certain distance in the direction it is facing. When the radiation source is completely surrounded after the movement, the measurement is completed When there are no other radiation sources. When the source is not enclosed, or when there is another source of radiation, the number of gamma radiation events and the direction of incidence are measured again. Once the radiation source is sufficiently close, the path encircling the radiation source is taken and the location of the radiation source is determined.

When there are multiple radiation sources, the distance to the source is first estimated by taking two measurements toward the direction of incidence of each radiation source. The estimated distances to the radiation sources are compared, and the search is performed in order from the radiation source closest to the current position to reduce the measurement time. When several radiation sources are located in the same direction, there is a risk that the searcher may get too close to the radiation source and contaminate it after the measurement of one source is finished. Therefore, the measurement is carried out again after a certain distance away from the measured radiation source.

3. Results

3.1 Experimental Setup

When the estimated distance to the radiation source was more than 5 m, the data was moved at 3 m intervals from the acquired data in the direction of incidence in order to reduce the search time. When the estimated distance to the radiation source was less than 5 m, the movement distance was reduced to 1 m intervals. The robot stopped for 300 s at each measurement point to acquire the gamma radiation. The goal of our exploration system is that the source location can be identified within 2 m. If the localization is successfully completed, the retrieval system heads to the location and performs the task. Consequently, the inspection robot switched to encircling the source when the distance to the source was within 2 m range. The size of the map was set to 16 m × 16 m, and the environment was free of obstacles. The distribution of the measured gamma rays was visualized and drawn so that the pixel color becomes darker the greater the number of measurements. Simulations were performed for single and multiple radiation sources, varying the intensity of the radiation sources and varying the position of the radiation sources.

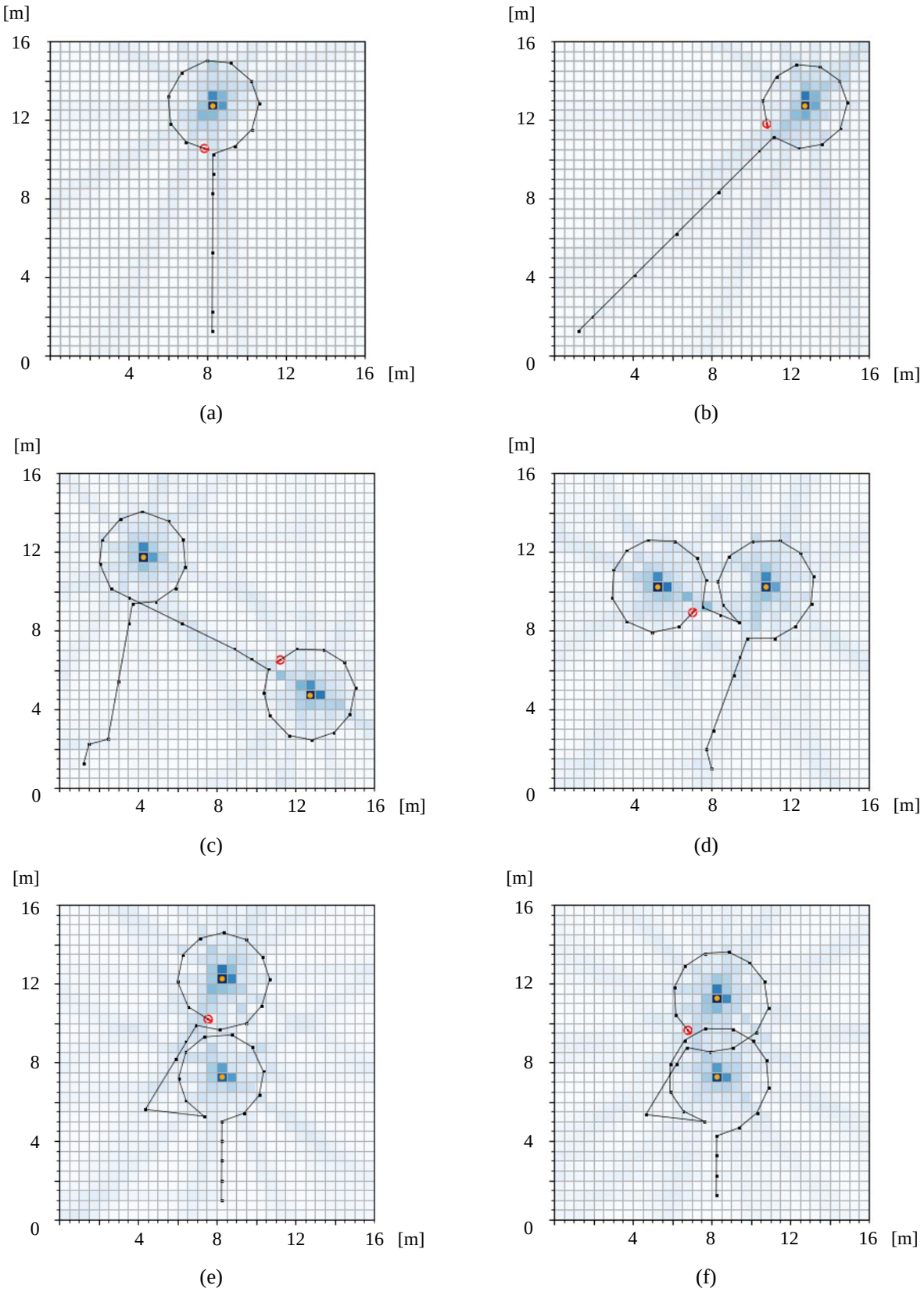

Fig. 5. Simulation results: (a) intensity of the radiation source is 10 MBq, (b) the radiation source is positioned at 45° anticlockwise as viewed from the robot, (c) intensity of the radiation source is 1 MBq and 5 MBq, (d) two radiation sources located horizontally, and the distance between the sources is 6 m, (e) two radiation sources located vertically, and the distance between the sources is 5 m, (f) the distance between the sources is 4 m.

3.2 Exploration Results for Single Source

For the case of varying the intensity of one radiation source, the intensity of the radiation source was varied every 1 MBq, 5 MBq, and 10 MBq. Figure 5 (a) shows the distribution of pathways and gamma rays produced for a radiation source intensity of 1 MBq. The black line represents the generated path and the black dots on the line are the measurement points. It can be seen from Fig. 5 (a) that the distance travelled could be switched based on the estimated distance to the radiation source. For all radiation source intensities, the pixel number with the densest gamma-ray distribution corresponds to the pixel number of the radiation source, confirming the validity of the proposed method.

The case of changing the position of one radiation source was compared by changing the position of the radiation source in each of the seven directions viewed by the robot. The intensity of the radiation source was set to 1 MBq. Figure 5 (b) shows the distribution of pathways and gamma rays produced for the radiation source is positioned at 45 deg anticlockwise as viewed from the robot. In all cases, the pixel number of the radiation source with the most profound gamma-ray distribution matched the pixel number of the radiation source, confirming the effectiveness of the proposed method.

3.3 Exploration Results for Multiple Sources

For the two radiation source intensity cases, the intensity of the radiation source varied between 1 MBq and 5 MBq and 5 MBq and 10 MBq. Figure 5 (c) shows the distribution of pathways and gamma rays produced for radiation source intensities of 1 MBq and 5 MBq. Figure 5 (c) confirms that the distance estimation was first made towards each radiation source and the search was conducted from the closer radiation source. For all radiation source intensities, the pixel number with the densest gamma-ray distribution corresponds to the pixel number of the radiation source, confirming the validity of the proposed method.

Comparisons were made for the cases where the two radiation sources are located vertically and in a straight line as viewed by the robot, varying the distance between the radiation sources. The intensity of the radiation sources was set to 1 MBq. Figure 5 (d) shows the distribution of pathways and gamma rays produced for the radiation sources are vertically positioned, and the distance between the sources is 6 m. Figure 5 (e), (f) shows the distribution of pathways and gamma rays produced for the radiation sources are located in a straight line, and the distance between the sources is 5 m, and 4 m. It can be seen from Figure 5 (f) that the search area of each radiation source overlaps when the radiation sources are closely spaced. When the distance between the two radiation sources was more than 4 m, the darkest pixel number in the gamma-ray distribution matched the pixel number of the radiation source, confirming the effectiveness of the proposed method. On the other hand, when the distance between the two radiation sources was less than 4 m, the path generation did not work well because it was too close to the other radiation source. Since the search process in this study was conducted in the order of the nearest radiation sources, a path generation method that considers the case where the radiation sources are close to each other is necessary.

4. Conclusions

In this paper, we have developed a system for autonomously generating a path for estimating the location of a radiation source using a mobile robot, even when the source's intensity is unknown. The change rate was derived from the number of incident gamma rays, and it was confirmed that the change rate is constant regardless of the intensity of the radiation source. The distance to the radiation source was estimated from the change rate, and an index was determined.

Simulations were performed for single and multiple radiation sources, varying the intensity of the radiation source and varying the location of the radiation source. In the case of a single radiation source, the proposed method effectively identifies the location of the radiation source when the intensity of the radiation source is varied and when the location of the radiation source is varied.

In the case of multiple radiation sources with different radiation source intensities, the location of the radiation source can be identified, confirming that the proposed method is effective. In this study, the search was performed starting from the nearest radiation source, so when the position of the radiation sources was changed, the search could not be performed considering the other radiation source if the radiation sources were close to each other. Therefore, a route generation method is needed to consider the case where multiple radiation sources are clustered together.

References

[1] D. Kim, H. Woo, Y. Ji, Y. Tamura, A. Yamashita, H. Asama, *IEEE/SICE International Symposium on System Integration (SII)*, 444-449 (2017)
[2] T. Kishimoto, H. Woo, R. Komatsu, Y. Tamura, H. Tomita, K. Shimazoe, A. Yamashita, H. Asama, *Applied Sciences*, **11**, 4707 (2021)
[3] K. Uema, H. Tomita, K. Kanamori, T. Takahashi, T. Iguchi, J. Hori, T. Matsumoto, T. Shimoyama, J. Kawarabayashi, *JPS Conf*, **24**, 011016 (2019)

Development and basic property evaluation of mortar for 3D printer using sea shells waste with blue carbon fixation properties

Natsuka HOSODA[*1], Kikuno IGUCHI[*1], Masaki TAMURA[*2], Tetsuya SASAKI[*3], Takashi SAITO[*3], Ryota OZEKI[*3], Taichi YAMAMOTO[*3], Ayano KOSEKI[*3]

Department of Architecture, Kogakuin University, Tokyo, Japan
E-mail: db20294@g.kogakuin.jp

1. Introduction

As the movement to achieve a carbon-neutral society by 2050 gains momentum worldwide, development of new environmentally friendly materials using blue carbon, which is attracting attention as a carbon-neutral material following green carbon and white carbon, is underway[1)2)3)]. Blue carbon is carbon that is absorbed and stored in the marine environment by the function of marine organisms. It is defined by the 2009 United Nations Environment Programe (UNEP) report "BLUE CARBON"[4)].

This study focuses on scallop shells, one of the blue carbon resources. First, we will investigate the occurrence of shells and the current status of their recycling, and then conduct an evaluation test of the basic properties of mortar using scallop shell powder, which is discharged in the process of crushing scallop shell.

2. Survey of current scallop shell resources

2.1 Occurrence of scallop shells

One of the blue carbon resources is scallop shells, which are made of calcium carbonate from dissolved CO2 in the ocean. Figure 1 a), b), c), and d) show the process of processing scallop shells into shell sand. Discarded scallop shells can be recycled by transporting them to an intermediate treatment plant, curing them, and crushing them into smaller pieces. Figure 2 shows the percentage of scallops farmed and caught annually. Hokkaido and Aomori Prefecture account for 90% of the total amount farmed, while Hokkaido accounts for almost 100% of the total catch. In addition, Figure 3 a), b), and c) shows scallop catch M_0, shell generation M_1, and shell unutilized M_2 and their distribution in 12 regions of Hokkaido and Aomori Prefecture. It can be seen that in areas where there is a constant catch, shells are generated as fishery waste at industrial waste treatment plants in the same areas. On the other hand, there are still many unutilized shells, so it is necessary to consider how to use these resources in the future. The average percentage of scallop shells to total scallops was 52%, and M_2 was calculated from Equation (1).

$$M_2=0.52\times M_0-M_1 \ldots (1)$$

a) Landing of scallops farmed for 3 or 4 years

b) Separation process of scallops at a seafood processing plant

c) Transportation to intermediate treatment plant by 10t truck

d) Sedimentation curing and organic decomposition

Fig. 1. Conversion of scallop shells into blue carbon resources

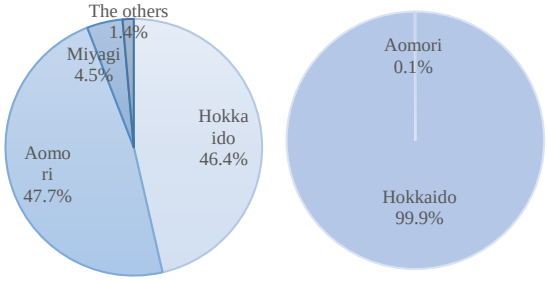

a) Aquaculture (160,000 t) *b) Catch (350,000 t)*

Fig. 2. Scallops Annual aquaculture and catch ratio (2021)

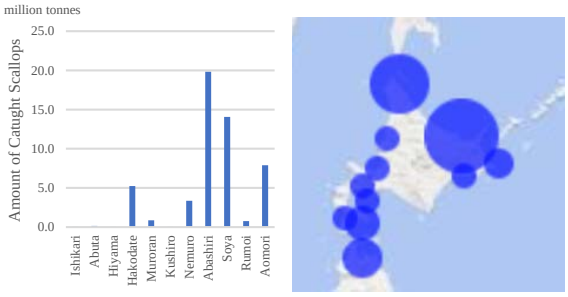

a) Caught Scallops M0 and its distribution map

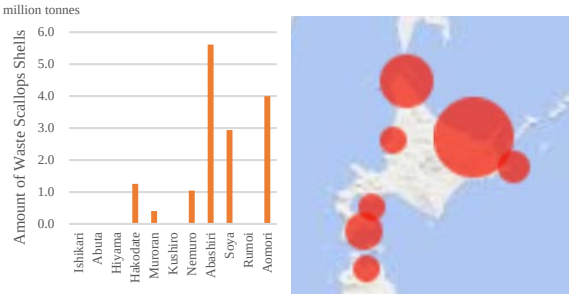

b) Wasted Scallop shells M1 and its distribution map

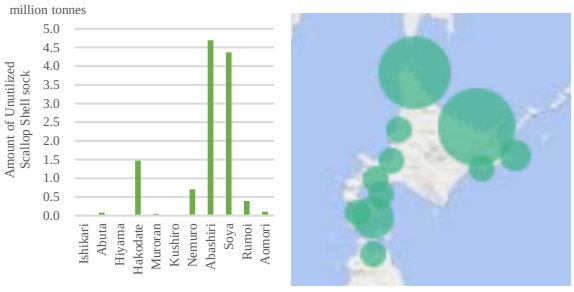

c) Unutilized scallop shell stock M2 and its distribution map

Fig. 3. Scallop and blue carbon stocks in 12 regions of Hokkaido and Aomori Prefecture

2.2 Potential of scallop shells as an environmental resource

Table 1 shows the applications of recycled products using scallop shells, and Figures 4 a) and b) show the percentage of Hokkaido's specified procurement items as defined under the Green Purchasing Law and the percentage of products using scallop shell sand among them. Scallop shell sand is used in a wide range of products, including construction and civil engineering materials, fertilizers, and stationery, indicating its versatility for reuse. Hokkaido has established a system called "Hokkaido Certified Recycled Products" (hereinafter, this is called "HCRP"). This is an action to certify recycled products with certain environmentally friendly standards manufactured using recyclable resources generated in Hokkaido as specified procurement items under the Hokkaido Green Purchasing Basic Policy and to promote their use. Ten products using scallop shells are included in the 116 HCRP for 2021, which is expected to lead to further expansion of scallop shell use in the future.

Table 1. Applications of products using scallop shells in Hokkaido

Applications of products using scallop shells	
stationery	choke
fertilizer	Calcium carbonate fertilizer
non-slip material	Non-slip material for cattle barns, Bedding for raising livestock, deicer salt
abrasives	Blast Cleaning Material
Civil engineering materials	Concrete aggregate and soil conditioner for civil engineering, Ground drainage
Architectural interior materials	plastering materials for interior
Architectural exterior materials	Wall materials, exterior insulation systems, exterior plastering materials

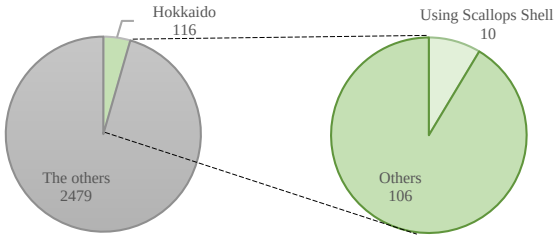

a) Number of Hokkaido shares among national specified procurement items

b) Number of products using scallop shell sand among HCRP

Fig. 4. The number of Hokkaido's specified procurement items

3. Interview survey at processing plant of scallop shell sand

3.1 Plant inspection

A survey of intermediate processors in Hokkaido was conducted in March 2023 with the aim of converting scallop shells to blue carbon. Figure 5 shows a scallop shell processing plant located in Shibetsu, Hokkaido. This plant focused early on the effective use of scallop shells, which were discharged as industrial waste in the Nemuro, and processed them into animal calcium materials. Scallop shells are purchased for a fee from a fish processing plant near the plant as unused marine resources. First, shells that have been sedimented and cured outdoors are dried by a counter-current heating dryer, and then dust and sand attached to the shells are removed using a bag filter and sand remover. The shells are then crushed by a super sander and sifted by a horizontal vibrator to produce sand with a grain size of 2.5 mm or less. At this time, oversized shells are returned and crushed again by the super sander. After passing through the sifter, the shell powder is crushed again in the super mill, and then sorted into various particle sizes by the eco-separator. Finally, the scallop powder with a particle size of 6 is sucked up by a bag filter, packed in bags for each size, stored, and shipped. Scallop shells are crushed into smaller pieces in stages by primary and secondary crushing, and classified into several types of particle sizes (0.25 mm to 2.5 mm). Therefore, the size and quantity of shell sand that can be produced per day is limited.

3.2 Challenges for the Intermediate Treatment Industry

When intermediate processors received scallop shells, they used to collect them as industrial waste in accordance with the Waste Disposal and Public Cleaning Law, but now they purchase them from producers for a fee as unused marine resources. Therefore, it is essential to increase the demand for processed products in order for intermediate processors to generate sales. In addition, although there are many scallop shells left on the beaches of Hokkaido, there are few intermediate treatment plants that have primary and secondary crushing facilities and efficient classification processes to process them. In the future, when aiming to improve the productivity of scallop shell sand, it can be said that it is necessary to improve social capital facilities using subsidies related to the promotion of carbon cycle.

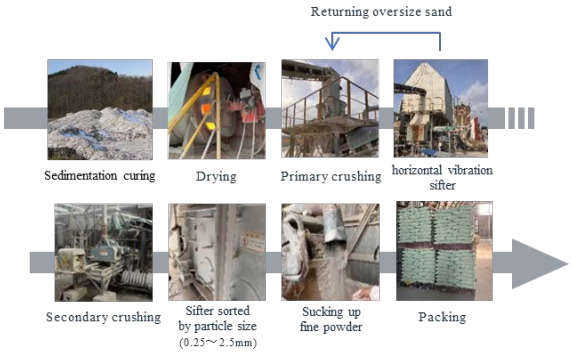

Fig. 5. Processing plant of scallop shell sand

4. Basic property evaluation of mortar for 3D printer

4.1 Experimental Policy

In this study, basic property evaluation tests of mortar using scallop shell fines will be conducted for the application of 3DP construction. Mortar specimens were prepared from two types of scallop shell fines produced at different factories, and three types of strength tests were conducted: compression, shear, and bending. Compare the properties of conventional mortar and scallop-shell-fines mortar, and discuss issues for 3DP construction tests.

4.2 Used Materials and Experimental Contents

Table 3 a) and b) show details of two types of scallop shell fines and shell sand produced in Hokkaido, Table 4 lists the materials used for scallop-shell-fines mortar, Table 5 shows the mortar formulations, and Table 6 shows the test lists and its contents. There are two types of scallop shell fines, SH and SB, with the most appropriate particle size for 3DP mortar. Mortar specimens H1-H3 and B1-B3 were prepared using these fine grains, and mortar specimens N1-N3 of normal formulation were also prepared. A total of nine specimens were used in the foundation property evaluation tests.

Table 3. Details of scallop shell fines and sand

	Class	Size		Class	Size
SH	Small Grain	1.0～2.0 ㎜	SB	3号	1.2～2.5 ㎜
	Ground	0.5～1.0 ㎜		4号	0.6～1.2 ㎜
	Fine	0.2～0.5 ㎜		5号	0.25～0.6 ㎜
	Fine Powder	0.2 ㎜ under		6号	0.25 ㎜ under

a) Particle size standard of scallop shell fines (SH and SB)

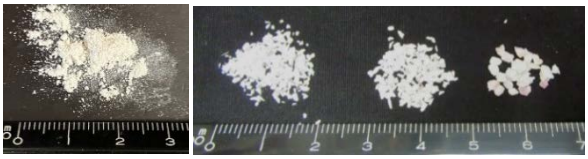

b) Scallop shell fines by particle size (left: fines, right: sand)

Table 4. Used materials

Materials	Sign	Details of materials	Contents
Water	W	Tap water	—
binder	C	Ordinary Portland cement	Density 3.16g/cm^3
	Ad1	Inorganic admixture 1	Density 2.3g/cm^3
	Ad2	Inorganic admixture 2	Density 2.2g/cm^3
Fines	S	Fine aggregate for 3DP	Density 2.63g/cm^3
	SH	Scallop shell fines (0.2-0.5 mm)	Density 2.62g/cm^3
	SB	Scallop shell fines (0.25-0.6 mm)	Density 2.62g/cm^3
chemical admixture	F	PP fiber (Class A, I, less than 15 mm)	JIS A 6208
	M	Superplasticizer	Polycarboxylic Acid Ether compounds

Note) Density of fines is the surface dry density.

Table 5. Mortar formulation for 3DP (kg/m^3)

Sign	W	C+Ad1+Ad2	S	SH	SB	F	M (C×%)
N	365	1143	796	-	-	2	0.3
H	365	1143	239	557	-	2	0.5 + 0.5
B	365	1143	239	-	557	2	0.7 + 0.2

Table 6. Experiment list and its contents

Experiment	Method and Contents	The conditions of an experiment
Compression strength (N/mm^2)	Prismatic specimen (40mm×40mm×160mm) Age 28 days	
Shear strength (N/mm^2)	Prismatic specimen (40mm×40mm×160mm) Age 28 days	
Bending strength (N/mm^2)	Prismatic specimen (40mm×40mm×160mm) Age 28 days	

4.3 Fresh properties of scallop-shell-fine mortar

Figure 6 a), b), and c) show the slump, mortar flow, and fresh properties of the scallop-shell-fine mortar. Compared to the normally formulated mortar N for 3DP, both H and B are within a certain slump range. Therefore, the scallop-shell-fine mortar retains the autonomous stability required for mortar for 3DP. This is considered to be due to the characteristics of the shape of scallop shell fines[1)-3)]. In addition, it is assumed that the mortar retains the same rheological properties (viscosity and yield value) as the normal formulation N, since the mortar has not flowed down significantly in the 15-hit flow. The unit volume mass was reduced by an average of 2.3% and the air content was increased by an average of 2%. This is assumed to be due to the fact that the shape of the scallop fines was flat and sharply angled compared to that of the plaster sand fines, resulting in more fine void areas than in the ordinary Formulation N. Therefore, the scallop-shell-fines mortar was considered to have a level of freshness properties that could be used equally with the normally formulated mortar N for 3DP.

4.4 Mechanical properties of scallop-shell-fines mortar

Figure 7 a), b), c), and d) show the results of each strength test, the density of the mortar and its standard deviation. For compression strength, B was slightly lower than the strength of N, but for H, the strength was equivalent to N. The shear and bending strengths of H and B were also higher than those of N. This can be attributed to the flat and sharply angled shape of the scallop fines compared to that of the plaster sand fines, which easily ensures mechanical meshing with the cement[1)-3)]. On the other hand, the density is below N in both cases, and further improvement is needed to increase the strength.

4.5 Application to 3D printer construction

Based on the above, we will test a 3D printer construction using scallop shell mortar. The mortar will be extruded from the nozzle of the 3D printer and stacked from bottom to top. In this stacked construction, it is important that the fluid mortar does not drop down due to gravity. In that regard, scallop-shell fines mortar retains the autonomous stability that comes from the scallop shell fine shape, so the mortar does not drop down easily. We will examine modeling that can be fabricated with 3D printer by taking advantage of these characteristics. Figure 8 a), b), and c) show an example of 3DP mortar under study for trial production based on this formulation. Since this is a stacked construction method, the construction surface is based on such a border. The moderate autonomous stability of the mortar is important not only in terms of structure but also in terms of design.

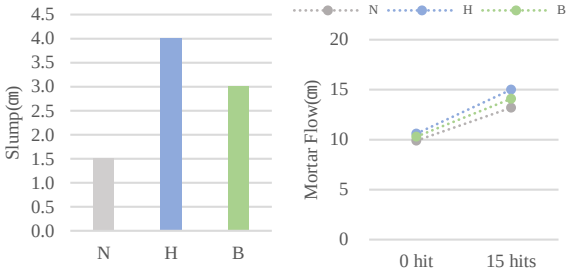

a) Mortar Slump *b) Mortar Flow*

	Slump (cm)	0 hit	15 hits	Unit volume mass (kg/m^3)	Air content (%)	Bleeding	Temperature (°C)	Chloride (kg/m^3)	Mixing time (s)
N	1.5	9.9	13.2	2150	-	No	20	0.02	60+30
H	4.0	10.6	15.0	2109	1.67	No	20	0.07	60+60
B	3.0	10.3	14.1	2093	2.40	No	20	0.08	60+60+30

c) Freshness Properties

Fig.6. Freshness Properties of scallop-shell-fines mortar

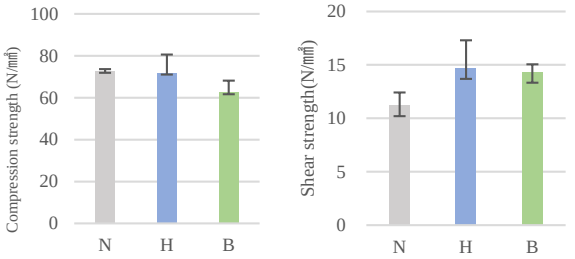

a) Compression strength *b) Shear strength*

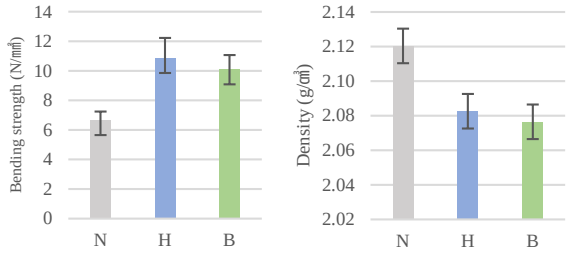

c) Bending strength *d) Density*

Fig. 7. Mechanical properties and density of each mortar

a) Fresh scallop-shell- mortar

b) Construction of mortar by 3DP

c) Stacked area with small deformation

Fig. 8. Mortar prototypes by 3DP

5. Conclusion

The following knowledges were obtained in this study.

1) Scallop shell waste, which can be collected mainly in the Hokkaido region, is expected to have resource productivity as a blue carbon fixation material.
2) The fresh properties of the scallop-shell-fines mortar tend to be slightly softer than the actual formulation, but it retains a certain degree of autonomous stability and rheological properties required for 3DP mortars.
3) Scallop-shell-fines mortars are expected to have compressive strength comparable to that of ordinary formulations and shear and flexural strength greater than those of ordinary formulations due to the mechanical meshing1)-3) provided by the shape characteristics of the scallop shell fines.

Acknowledgements

This research was conducted in collaboration with Takahashi Curtain Wall Industrial Co and Hokkaido Yuga Corporation, Bisshel Corporation, Polyuse Corporation, Aimori Corporation, and some engineers provided generous cooperation.

Affiliation

*1 Undergraduate student,Kogakuin Univ.
*2 Prof.School of Architecture.Kogakuin Univ.
*3 Takahashi Curtain Wall Corporation

References:

[1] Komuro, Tamura, Fundamental Mechanical Properties of Mortar Mixed with Carbon-Fixing Marine Biological Shells, Proceedings of the Japan Concrete Institute, Vol.33, No.1307, 2011.6
[2] Komuro, Tamura, Investigation of carbon neutrality of reinforced concrete buildings using carbon-fixing marine biological shells, Technical Report of the Architectural Institute of Japan, No. 40, pp. 841-846, 2012,10
[3] Sasaki et, Development of PCa concrete materials using marine bio-shell wastes with carbon fixation properties, Part 1-3, Annual Report of the Architectural Institute of Japan, 2022.9
[4] United Nations, United Nations Environment Program (UNEP), Attachment13-k, 07/14/2017
[5] Hosoda, Development Of Precast Concrete Members Using Blue Carbon-Fixing Marine Shell Waste (Part1 Basic Properties of Mortar Using Scallop Shell Sand Powder for 3D Printer), Proceedings of the Annual Conference of the Architectural Finishing Institute of Japan, 2023.10

Phase Control of Copper Oxides by Changing Temperatures and Gas Types in Growth of Mist CVD

N. Sugita, S. Yoshida, H. Nagai, T. Onuma, T. Honda, and T. Yamaguchi

Department of Electrical Engineering and Electronics, Kogakuin University, Japan
E-mail: cm23041@ns.kogakuin.ac.jp

Abstract

Phase control of copper oxides was investigated by changing growth temperatures and gas types in the growth by mist CVD method. In the films grown using O_2 gas, single phase of Cu_2O and CuO was obtained at low growth temperature of 300-400℃ and high growth temperature of 800℃, respectively. In the case of N_2 gas, single phase of Cu_2O was also obtained at low growth temperature of 300℃. However, the formation of Cu was dominantly observed at high growth temperature.

Copper oxides, involving Cu_2O and CuO, have attracted attention as p-type oxide-semiconductors. Cu_2O is a p-type oxide semiconductor with a direct bandgap of 2.0-2.1 eV. This has high absorption coefficient in the visible light region, and the conductivity is relatively easy to control among transition metal oxides. Therefore, it is expected to be applied to devices such as solar cells. CuO also shows p-type oxide semiconductor with an indirect bandgap of 1.4-1.7 eV[1,2,3].

Generally, the phase of copper oxide is easy to be changed on the conditions of temperature and oxygen partial pressure in the growth atmosphere[4]. It has been reported that many of the methods of growing copper oxide result in a combined growth of Cu_2O and CuO[5]. We have grown copper oxide films by mist chemical vapor deposition (Mist CVD) method. There are few reports on the growth of copper oxides using Mist CVD[6].

In this study, the phase control of copper oxide was studied by changing growth temperatures and gas types in the growth of mist CVD.

Copper oxide films were grown by Mist CVD on (0001) α-Al_2O_3 substrates. $Cu(C_5H_7O_2)_2$ and $C_2H_8N_2$ were used as source materials. A 100 mL of the solution was atomized using a 2.4 MHz ultrasonic transducer, and the mist was transported by a carrier gas to the substrate. The growth temperature was varied between 300 and 800°C. Oxygen or nitrogen was used as a carrier gas.

The results of XRD measurements in the samples grown with diffrent tempetatures and carrier gases are shown in Fig. 1. The formed phase of copper oxide is surmmarized in Fig. 2. In the films grown using O_2 gas, single phase of Cu_2O and CuO films was obtained at low growth temperatures of 300-400℃ and high growth temperature of 800℃, respectively. In the case of N_2 gas, single phase of Cu_2O was obtained at low growth temperatures of 300℃. At high growth tempeature, however, the formation of Cu was dominantly observed. From these results, growth temperatures and gas types are important for phase control in the Mist CVD growth of copper oxide.

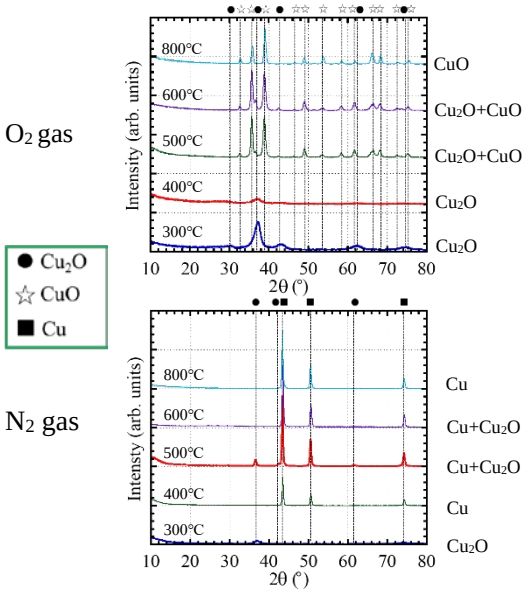

Fig. 1. XRD patterns of copper oxide grown at various temperatures with O_2 and N_2 gases.

Table 1. Phase of cooper oxide at various temperatures with O_2 and N_2 gases.

	300°C	400°C	500°C	600°C	800°C
O_2	Cu_2O	Cu_2O	CuO+ Cu_2O	CuO+ Cu_2O	CuO
N_2	Cu_2O	Cu	Cu+ Cu_2O	Cu+ Cu_2O	Cu

Reference

[1] F. L. Weichman, Phys. Rev. **117**, 998 (1960).
[2] C. Malerba *et al.*, Sol. Energy Mater. Sol. Cells **95**, 2848 (2011).
[3] S. Suda, I. Soc. Inorg. Mater, Japan **5**, 415 (1998).
[4] J. Xue, R. Dieckmann, J. Phys. Chem. Solids, **51**, 1263 (1990).
[5] A.A. Ogwu *et al.*, Acta Mater. **53,** 5151(2005).
[6] T. Ikenoue *et al.*, Appl. Phys. Express **12**, 055509 (2019).

Dynamic Behavior of Two Cavitation Bubbles Induced near a Rigid Boundary

First Y. KUBOTA[1], Second D. KANG[2], Third A. KIYAMA[2] and Fourth K. SATO [1]

[1] Department of Mechanical Engineering, Kogakuin University
2665-1 Nakano-cho, Hachioji-shi, Tokyo 192-0015, Japan
[2] Department of Mechanical Engineering, Saitama University
255 Shimo-ohkubo, Sakura-ku, Saitama-shi, Saitama 338-8570, Japan
E-mail: am22024@ns.kogakuin.ac.jp

Abstract

This study focused on the interaction between two cavitation bubbles near a rigid wall surface. The bubbles were generated by discharge with electrodes in a tank of sufficient size. The images were taken with a high-speed camera using a halogen lamp as a light source. In addition to the experiment two numerical methods, the boundary element method and the VOF method, were used to compare the numerical results with the experimental results. The mutual interference of cavitation bubbles under the wall surface is classified.

In recent years, there have been attempts to actively utilize cavitation bubble exercise in the medical and life science fields [1-2]. Fong et al. reported the effect of bubble position and time parameters on the mutual interference between two very close sized bubbles [3]. Tomita and Sato investigated the characteristics of the bubble shape and pulse jet in the range where the two bubbles show strong mutual interference [4]. However, there are still many unanswered questions about the motion of cavitation bubbles due to their short characteristic time and the complexity of the phenomenon.–In particular, the mutual interference of multiple bubbles near a rigid wall surface is closely related to erosion and is of great engineering importance, yet the mechanism is not well understood because of its complex non-spherical motion.

In this study, the mutual interference between two cavitation bubbles near a rigid body surface was investigated through experiments and numerical calculations.

In the experiments, cavitation bubbles are generated by local evapor-ation in the liquid by applying a voltage of 110 V DC with a pulse width of 100 μm. the experiment is performed in a sufficiently large glass aquarium (W=600 mm x D=295 mm x H=360 mm) filled with tap water. The rigid wall is suspended from the top of the tank by an acrylic disk Its position can be adjusted in the vertical (y) axis by a stage equipped with a micrometer head.–Bubble behavior was captured by a high-speed camera (Fotron FASTCAM-MAX 120K) using a halogen lamp as a light source.

Two methods, the Boundary Element and the VOF method, were applied to the numerical calculations and compared with the experimental results. For the VOF method, Fluent in ANSYS was used.

The experimental results show the coordinates of the bubble surface on the axes obtained from the coma diagram and the transition of the coordinates of its midpoint.

In the behavior of two cavitation bubbles generated at infinity, it is known that the jet is generated mainly in the direction that the two cavitation bubbles attract or repel each other. However, near the wall surface, a change in the mutual interference of the bubbles is observed. One particularly characteristic behavior is a change in the direction of midpoint movement of the bubbles on one side. Because the cavitation bubble on the wall side is smaller, the first bubble that collapses moves toward the other bubble. The other bubble then also collapses, but this time the earlier collapsed bubble moves toward the wall. The behavior below the wall is classified according to the ratio of the distance from the wall to the bubble to the size of the bubble.

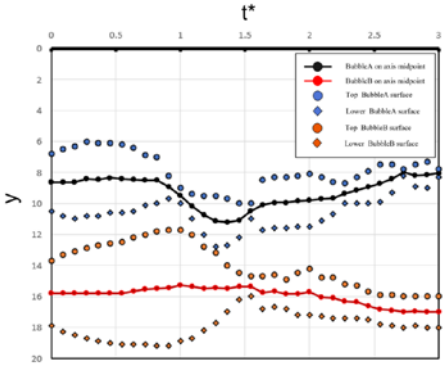

Fig.1 Changes in bubble surface and movement of bubble midpoint on axiso of $R^* = 0.63$, $l_{m,B}{}^* = 2.69$ ($R_A = 1.30$, $R_B = 2.05$, $l_{m,B} = 9.0$)

References:

[1] Sankin, G. N., Yuan, F. and Zhong, P. (2010): “Pulsating Tandem Microbubble for Localized and Directional Single Cell Membrane Poration”. Physical Review Letters, Vol. 105, pp. 078-101

[2] Hernot, S., Kilbanov, A.L. (2008) “Microbubbles in ultrasound-triggered drug and gene delivery. Adv Drug Deliv Rev, Vol. 60, Issue, 10, pp. 1153-1166

[3] Fong, S. W., Adhikari, D., Klaseboer, E. & Khoo, B. C. 2009, Interactions of multiple spark-generated bubbles with phase differences. *Exp. Fluids* **46**, pp.705–724.

[4] Tomita, Y. and Sato, K., Pulsed jets driven by two interacting cavitation bubbles produced at different times. J. Fluid Mech, 819, 2017, pp.465-493.

The Development and Achievement of Contactless Transport Stage with Acoustic Levitation Technology

Yu-Ting Chen, and Sheng-He Wang*

Department of Biotechnology and Food Technology, Southern Taiwan University of Science and Technology, Tainan, Taiwan
E-mail: *Sunhur0315@stust.edu.tw*

Abstract

Recently, depend on the evolution of science and technology, the miniaturization of each industrial manufacturing processes was been developed for the thin plates or non-rigid and fragile materials, such as wafers, liquid crystal panels, food, or drugs, etc. In the miniaturized manufacturing process, because the mechanical contact by the clamping jaws was necessary, the surface of the component is easy to damage during the gripping and handling process. In particularly, the dust particle can be generated by the friction of the mechanical contact, which may be resulted in the short circuit of the wafer/panel or the blockage of the machining tool. To resolve aforementioned problems, in this paper, a standing wave type of contactless acoustic levitation technology is proposed to achieve a contactless transport stage. Based on the transient simulation analysis of the ultrasonic field, the position of each ultrasonic source on the standing wave node can be estimated to ensure the accuracy of the suspension position. Finally, in order to achieve non-contact movement, multiple standing wave acoustic fields are established in the horizontal direction, and it is proved that by controlling the phase of each ultrasonic source, the standing wave pressure distribution can be accurately adjusted to obtain the phase offset relationship of each ultrasonic source. By designing the phase and frequency control technology of the ultrasonic driving voltage through the ultrasonic source architecture array, the node position of the standing wave in the ultrasonic field can be adjusted and controlled, thereby improving the limitations of the acoustic levitation technology, which can only stably levitate at the node position. Because the acoustic levitation technology is not restricted to certain materials and shapes, the designed contactless transport stage can be applied in the miniaturized manufacturing process without the dust particle generation.

Keywords: Ultrasonic standing wave, Acoustic levitation technology, Contactless transport stage

1. The horizontal array of acoustic levitation strusture

The acoustic floating structure proposed in this paper is in the form of a horizontal array. Through the ultrasonic field generated by the mutual coupling of two ultrasonic sound sources in the horizontal direction, and through the phase difference (time difference) of different ultrasonic waves, the two nodes in the horizontal direction are After the fusion occurs, the suspended object can be transferred from one node to another node in the horizontal direction, realizing acoustic floating non-contact displacement technology in the horizontal direction.

To achieve the conditions for generating standing waves, the principle of wave superposition must be used to continuously increase the sound pressure after continuous reflection and interference of sound waves. Finally, when the sound pressure can offset the gravity of the object, the object will be able to float. The ultrasonic actuator designed by High Frequency Drive is used in the laboratory to drive two ultrasonic actuators and set up on a simulated acoustic levitation experimental platform set up in the laboratory. Figure 1 shows the experimental platform where the developed ultrasonic actuator is installed on a simulated acoustic levitation platform. The previously designed ultrasonic actuator is used to change the sound pressure distribution of the coupled standing wave ultrasonic field. Since experiments are conducted with multiple sets of different ultrasonic actuators, and the resonance frequency of each ultrasonic actuator is different, the design needs to be flexible enough to be adjusted step by step according to different parameters. In the laboratory, The ultrasonic actuator fixing frame installed on the simulated acoustic levitation experimental platform is designed using light curing technology. The upper and lower parts of the ring in the middle of the ultrasonic actuator are locked with screws, nuts and washers respectively. According to different The resonant frequency can be adjusted by adjusting the distance between the upper reflector and the distance between the two ultrasonic sound sources, which can be moved and observed while driving.

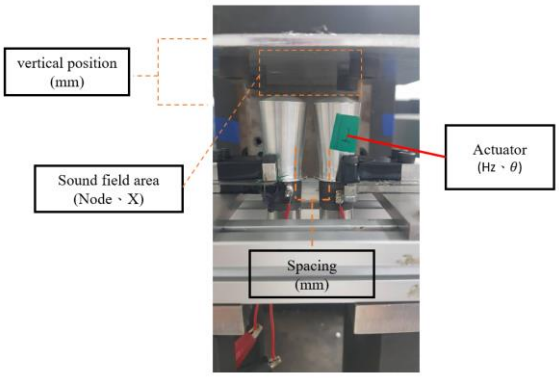

Fig. 1. Contactless transport stage Architecture by Acoustic Levitation Technology

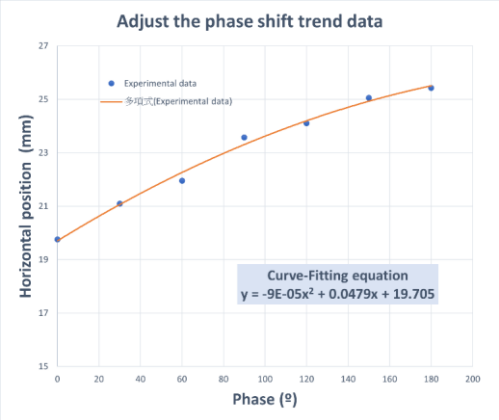

Fig. 2. Phase adjustment and suspension position relationship diagram

2. Measurement result

In order to drive the ultrasonic actuator to produce high-frequency vibration, two ultrasonic actuators drive 35.041 KHz to achieve the conditions for standing wave generation. Therefore, the hardware test structure in Figure 1 is used for experiments, and the suspended object is selected to be less than 3 mm in diameter. Styrofoam balls. From the experimental results, it is known that the resonance frequency measured by the impedance analyzer and the output of 35 KHz to the two drivers can achieve the effect of generating a standing wave sound field and suspending it between the two ultrasonic actuators.

In order to verify that the position of the standing wave node can be controlled through the phase control node offset, the phase change function in the dual-channel high-frequency signal generator is used to change the phase from 0 degrees, 30 degrees, 60 degrees, 90 degrees, and 120 degrees respectively. , 150 degrees, and 180 degrees, sequentially change and record the movement trend of the Styrofoam ball, and the movement trend chart of the suspended object through the phase change, as shown in Figure 2.

It can be seen from the figure that as the phase difference of the actuators on both sides is adjusted, when the phase difference increases, the suspended position of the Styrofoam ball will tend to move to the right, which proves that the standing wave node changes the phase by driving two sound sources. At the same time, the nodes will be offset, causing the suspended objects to shift horizontally. In addition, the linear increasing relationship can be calculated through the curve fitting method, and the floating position value can be estimated, which can be used to measure the phase in practical applications. The curve fitting method is expressed in the formula (1).

$$y = 9e - 05x^2 + 0.0479x + 19.705 \qquad (1)$$

References:

[1] "Ultrasonics | Physics, Sound Waves & Applications | Britannica" https://www.britannica.com/science/ultrasonics.

[2] "Acoustic Analysis - an overview | ScienceDirect Topics." https://www.sciencedirect.com/topics/medicine-and-dentistry/acoustic-analysis.

[3] Florian Puci, Miroslav Husak, "Magnetically Levitated and Guided Systems," Advances in Science, Technology and Engineering Systems Journal Vol. 2, No. 3, pp. 241-244, 2017.

[4] F. Molteni, "Metrological characterization of a cycle ergometer to optimise the cycling induced by FES on patients with stroke," Medical Engineering & Physics, vol. 32, no. 4, pp. 339-348, 2010.

[5] T. Otsuka and T. Nakane, "Ultrasonic levitation for liquid droplet," Japanese Journal of Applied Physics, Vol. 41, pp. 3259–3260, 2002

[6] 樂桂冬、張金鐸、王仁乾，壓電換能器和換能器陣，北京大學出版社，2005.

[7] 王聖禾，非接觸式超音波聲浮夾持系統之設計與分析，成功大學機械工程學系博士論文，2011。

[8] Electronics and Applications, 2015, Switzerland.

Developement And Achievement of An Intelligent Safety System for Robot Arm Operation Based on Vision Learning Technology

Wei Fu, Kuo, Sheng He, Wang*

Department of Biotechnology and Food Technology, Southern Taiwan University of Science and Technology, Tainan, Taiwan
E-mail: *Sunhur0315@stust.edu.tw*

Abstract

Depend on the development of Industrial 4.0 and Artificial Intelligence (AI) technologies, to increase the manufacturing efficiency, the automatic robot arm technologies were widely applied in current industrial production factory. To achieve more complex and flexible manufacturing process, the human–robot collaboration (HRC) technologies was developed to become as a collaborative robot. However, during the human–robot collaboration working process, operator should be necessary to enter the robotic working area to collaborating work, such as repairing or maintaining operation. However, the impact accidents may be occurred during the robot arm working process. Therefore, in this paper, a safety monitoring technology of robot arm was built by proposed computer vision detection method, which can monitor the working intrusion of robot arm from the human hand or obstacle through webcam. The hand landmarks detection was built based on the AI detection software of Mediapipe Framework. The shape of human hand can be framed and utilized to calculate the distance between the robot arm and the hand landmarks by OpenCV. Finally, the operating safety mechanism was defined, which the robot arm will be stop immediately when the human hand enters into the working area. From the experimental testing result, the proposed intelligent safety monitoring method demonstrated the high efficiency that the response time from hand detection to machine stop at around 35-80 milliseconds.

Keywords: Computer Vision Detection, Robot Arm Safety, Human–Robot Collaboration

1. The Identification Methodology

Due to the limitation of image vision along with the shooting range of the mobile device and multi types of the machine to be recognized in AR environment, according to Niall O' Mahony et al. mentioned in "Deep Learning vs. Traditional Computer Vision" [6], the ordinary traditional image recognition method needs to filter the characteristic through artificial, after that, perform a model training with Big-Data, the traditional computer vision workflow usually takes a lot of time, finally leads to impact the quality and efficiency of production line.

Most of the recognition objects of AR are identified by the outline of the main body of the object, which leads to an increase in the complexity of the use environment and identification. Therefore, this paper overcomes and optimizes it by identifying the characteristics of the object. Use several features of objects as labels for deep learning, the recognized algorithm will not fail to recognize due to occlusion or the inability to obtain the overall outline of the subject. For example, when we see a flower, we will discrimination of the flower characteristics (or features, like shape, color, appearance, etc.).

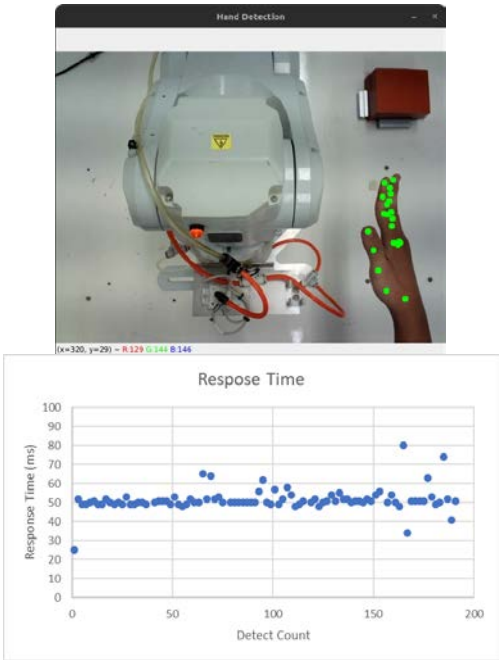

Fig. 1. The result of the Hand Detection response

References:

[1] S. Lu.; J. Berger.; Lan, E. I.; J. Schilp.; Chang, P. *System of Robot Learning from Multi-Modal Demonstration and Natural Language Instruction. Procedia CIRP*. 2022, 107, 914-919.

[2] V. Chunduru.; D. Romit N. S.; M. Roy.; J. Schilp.; Rajeevlochana G. Chittawadigi. *Hand Tracking in 3D Space using MediaPipe and PnP*

Method for Intuitive Control of Virtual Globe. R10-HTC. 2021, 1-6.

[3] M. Ciccarelli.; A. Papetti.; C. Scoccia.; G. Menchi.; L. Mostarda;. G. Palmieri;. M. Germani.; *A system to improve the physical ergonomics in Human-Robot Collaboration. Procedia Computer Science*. 2022, 200, 689–698.

[4] Y. Quiñonez.; C. Lizarraga.; R. Aguayo. *Machine Learning solutions with MediaPipe. CIMPS*. 2022, 107, 212-215.

[5] P. Padhi.; D. M. Das. *Hand Gesture Recognition using DenseNet201-Mediapipe Hybrid Modelling. ICACRS*. 2022, 978, 995-999.

MICROSTRIP GRID ARRAY WITH TWO ELEMENTS FOR WLAN 5.8GHz BAND

Bing-Hong Cai and Wen-Shan Chen*

Department of Electronic Engineering, Southern Taiwan University of Science and Technology, Tainan, Taiwan
E-mail: mb130204@stust.edu.tw, chenws@stust.edu.tw*

Abstract

A 1×2 microstrip grid array for WLAN 5.8 GHz application is proposed. The antennas and feed network are printed on FR4 substrate with loss tangent of 0.0245, dielectric coefficient of 4.4, and thickness of 1.6 mm. The overall dimensions of the design are 230 mm × 50 mm × 1.6 mm. The design uses a 50-ohm SMA feed for excitation and feed network to excite the antennas. By proper adjusting the dimensions of radiating elements and the feed network, an array design at 5.8GHz band could be obtained. Based on simulations and experimental measurements, this array can be used to the WLAN 5.8 GHz band. It exhibits a radiation pattern concentrated primarily in the positive Z-direction and an average simulated efficiency of over 25%, and a simulated gain ranging from 6.9 to 7.7dBi. The design with good performances is a good candidate for wireless application at 5.8GHz.

I. INTRODUCTION

For most wireless applications, higher gain antennas are good for applications, because they can increase the transmission distance. Array is a promising method to increase the gain of design. There are some papers [1-5] of increasing the gain having published. In ref. [1], an array with two elements with two slotted slots was proposed. The gain of the array increased to 7.7dBi. Fractal antennas with star chain arrangement were presented in ref. [2]. The arrangement increases the gain when the size is also compact. The Grid array antenna [3] with 13 rectangular rings for dual-band application was proposed. The design has a gain of 13.6dBi at low band and a gain of -0.6dBi at high band. Multibeam Grid array antenna[4] was presented. The design of grid array antenna with different feed position changed the radiation beam.

In the paper, a design of array with two elements will be proposed. The element with three meshes is a simplified grid array antenna. Adding the feed network, a design for 5.8GHz band and good gain will be achieved.

II. ANTENNA DESIGN AND RESULTS

Fig. 1 shows the overall view of the array. The overall size of the array is 230 × 50 × 1.6 mm^3. The element of the array is shown in Fig. 2. The element is a 3-mesh grid array, which is a simplified version of grid array. The geometry of the antenna array is also shown in Fig. 3. The microstrip feed network is used to excite the array. The dimensions of the array are also listed in Table 1. The array is implemented in a 1.6mm thickness FR4 substrate with a permittivity of 4.4 and loss tangent of 0.0245. The simulation and measurement S11 of the array is demonstrated in Fig. 4. The simulated results of the array are obtained by HFSS.

From the results in Fig. 4, the obtained bandwidth of the array fits the band of 5.8GHz (5.725－5.825GHz). The bandwidth is defined the S11 less than -10dB. The simulated S11 with different length of W5 is plot in Fig. 5. The change of W5 is also changing the spacing of the elements. It can be observed that the length of W5 will affect the impedance match and bandwidth. The simulated current density of the array at 5.75GHz is plotted in Fig. 6. The same phase in the radiation part of the array is shown. It is expected that the array is suitable excited. Fig. plots the simulated radiation patterns of the proposed array. The radiation pattern directed at +z direction, and the radiation beam is also concentrated to +z direction. The simulated antenna gain of the array is shown in Fig. 7. The radiation gain of the array is ranging of 6.9 to7.7dBi. The array with good gain and radiation pattern.

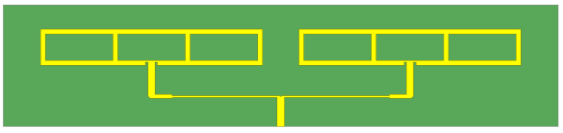

Fig. 1. Overall view of the Antenna array

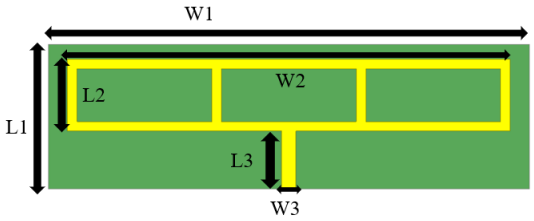

Fig. 2. Antenna geometry

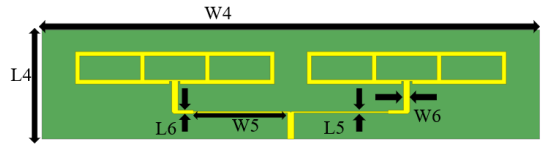

Fig. 3. Geometry of the antenna array

Table 1. Dimensions of the antenna array

Parameters	W1	W2	W3	W4
Unit (mm)	100	92	3	230
Parameters	W5	W6		
Unit (mm)	43.5	3		
Parameters	L1	L2	L3	L4
Unit (mm)	30	15	12	50
Parameters	L5	L6		
Unit (mm)	0.7	1.6		

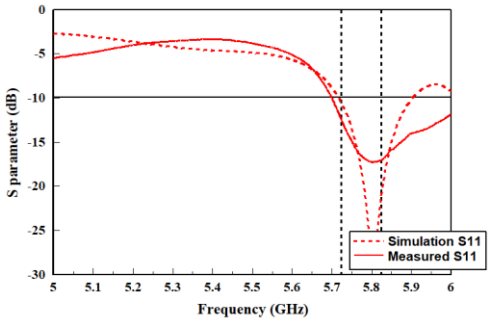

Fig. 4. Measured and simulated S11 for the proposed array.

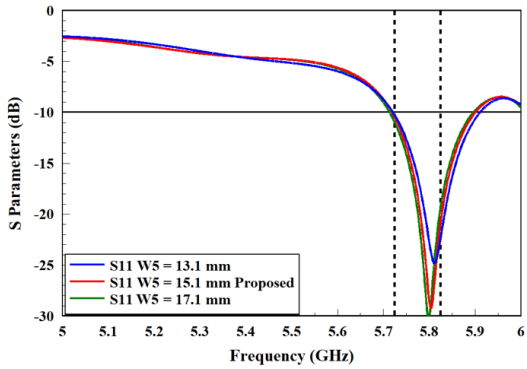

Fig.5. Simulated S11 of the array with the different length of W5

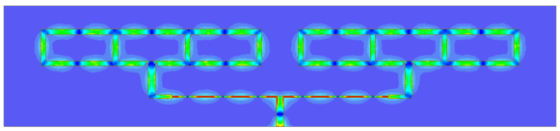

Fig.6. Simulated current at 5.75GHz

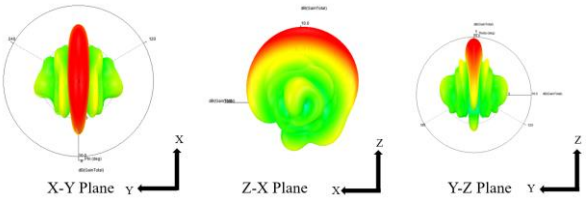

Fig.7. 3D field diagram of the proposed antenna at 5.75GHz

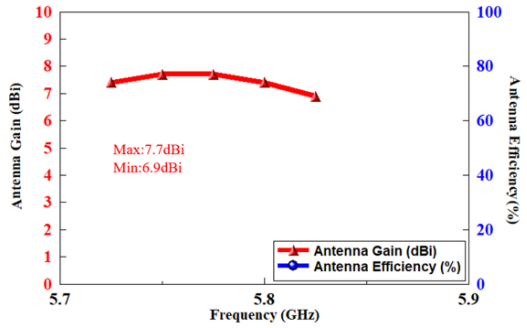

Fig. 8. Simulated antenna gain of the proposed array.

III. CONCLUSION

A 1 x 2 antenna array of grid array elements operating at 5.8GHz band has been proposed. A simplified grid configuration is adopted as the element for array design. By proper choosing the feed network to excite the array. From the results of the array, the array can be used to the band of 5.8GHz (5.725 –5.825GHz). The simulated gain and radiation pattern can be applied to WLAN 5.8GHz systems.

References:

[1] P. S. Naik and H. G. Virani, "1×4 Microstrip Patch Slotted Array Antenna for 5G C-Band Access Point Application," 2020 International Conference on Electronics and Sustainable Communication Systems (ICESC), Coimbatore, India, 2020, pp. 641-644.
[2] R. Somvadee, A. Namsang, R. Lerdwanittip and P. Chomtong, "A dual-band star chain fractal CPW antenna for LTE and RF altimeter systems," 2016 International Symposium on Antennas and Propagation (ISAP), Okinawa, Japan, 2016, pp. 1072-1073.
[3] G. Xu, H. Luan, H. -L. Peng, Y. -P. Zhang and W. -Y. Yin, "A Microstrip Grid Array Antenna for Dual Band Applications," 2018 IEEE International Symposium on Antennas and Propagation & USNC/URSI National Radio Science Meeting, Boston, MA, USA, 2018, pp. 667-668.
[4] J. Duan and S. Sun, "A Multi-Beam Grid Array Antenna with Multi-Port Excitations," *2018 Cross Strait Quad-Regional Radio Science and Wireless Technology Conference (CSQRWC)*, Xuzhou, China, 2018, pp. 1-2

Antennas on Smart Watch for GPS/BT/Wi-Fi 6E Applications

Yong-Zhi Su and Wen-Shan Chen*

Department of Electronic Engineering, Southern Taiwan University of Science and Technology, Tainan, Taiwan
E-mail: mb130109@stust.edu.tw, chenws@stust.edu.tw

Abstract

The paper proposes a design of antennas for GPS/BT/ Wi-Fi 6E on smart watch devices. The overall size of the design is 40 × 40 × 5.4mm^3. In the design, IFA (Inverted-F Antenna) is adopted. This design is design to achieve the bands of GPS (Global Positioning System), BT (Bluetooth), WLAN2.4GHz, WLAN5.2GHz, WLAN5.8GHz and Wi-Fi 6E 6GHz. Moreover, the design with three inductors is used to shorten the resonant length of operating modes. There are two antennas designed at Wi-Fi 6E 6GHz band acted as MIMO (Multi-Input Multi-Output) antenna design, and this arrangement can improve the transmission rate. From the results, the design can cover the bands of GPS, BT, WLAN2.4GHz, WLAN5.2GHz, WLAN5.8GHz and Wi-Fi 6E 6GHz. The design with small antennas and broadband effect is suitable for GPS/BT/Wi-Fi 6E applications on smart watch devices.

I. INTRODUCTION

Smart watch is more and more popular used in recently years. Adding functions in smart watch is also expected. In the same time, antennas in smart watch should be added [1, 2]. Wi-Fi 6E has been released, and a new frequency band of W-Fi 6E at 6GHz band (5.925 – 7.125 GHz) can be used to enable faster transmission speed. Some antenna designs [3-6] for Wi-Fi 6E band have been published recently. In ref. [3], a MIMO antenna design is with a pairs of coupled-fed monopole/loop antenna with a conjoined section for Wi-Fi 6E laptop computer applications. In ref. [4], a conformal and yet highly compact Wi-Fi 6E antenna is proposed for laptop applications. In ref. [5], a planar inverted-F antenna (PIFA) is designed for the WLAN band (2.4 / 5 GHz) and Wi-Fi 6E 6GHz band (5.925–7.125GHz) is proposed for laptop computer applications. In ref. [6], a design of MIMO antennas consists of a monopole antenna with a rectangular patch, inverted-E, and asymmetrical T-shaped strip to generate 5G Sub-6 GHz and Wi-Fi 6E frequency bands. However, there is less paper for smart watch at Wi-Fi 6E bands.

In the paper, a design for smart watch at 2.4/5GHz bands and utilizes Wi-Fi 6E 6GHz to enable fast transmission speed will be proposed. The design uses four antennas to achieve the operating bands of WLAN 2.4GHz/5.2/5.8GHz and Wi-Fi 6E 6GHz bands. The two antennas in the design act as MIMO antennas operating at 5.2/5.8GHz and Wi-Fi 6E 6GHz bands. The design with multi-bands would be suitable for wearable devices.

II. ANTENNA DESIGNS

Fig. 10 shows the overall view of the antenna design on the smart watch. The overall size of the design is 40 × 40 × 5.4mm^3. The design is implemented on an FR4 substrate with a thickness of 0.4mm, relative permittivity of 4.4, and loss tangent of 0.024 S/m. The antennas are fed by 50 ohm mini-coaxial cables. There are four antennas in the design with a 30 × 30mm^2 ground plane. Fig. 2 shows the geometry of (a) GPS antenna (Ant. 1), (b) WLAN 2.4GHz/BT antenna (Ant. 2), and (c)WLAN5.2/5.8GHz/ Wi-Fi 6E 6GHz (Ant. 3, and Ant. 4).

Fig. 2(a) shows the geometry of GPS antenna (Ant. 1), and the main resonant path of the IFA is added a 6.8nH inductor to effectively reduce the antenna resonance frequency. This GPS antenna can excite at a lower frequency mode while the same antenna size is maintained, and it is with less influence on antenna gain and efficiency simultaneously. Fig. 2(b) shows the geometry of the WLAN2.4GHz/BT antenna (Ant. 2). The antenna design added two inductors (6.8nH, 4.9nH) at the different paths on the antenna. The inductor of 6.8nH was added to the main path of IFA to shorten the antenna path. The inductor of 4.9nH was added to the short circuit path of the IFA to achieve the impedance match. Fig. 2(c) shows the geometry of WLAN5.2/5.8GHz/Wi-Fi 6E 6GHz bands (Ant. 3 and Ant.4). The two antennas (Ant. 3 and Ant. 4) are MIMO antennas that can enhance the transmission rate. The main paths of the IFA of antenna 3 and 4 are used of exciting the modes at WLAN 5GHz, while the left slot is used to excite the mode of Wi-Fi 6E 6GHz band. Two open-slots on the ground plane are used to reduce the mutual coupling between Ant. 3 and Ant. 4, lead to the design with good isolation. The dimensions of the design are also listed in Table 1.Table 1.

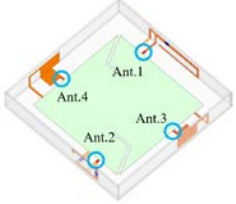

Fig. 1. Overall view of the antenna design on smart watch.

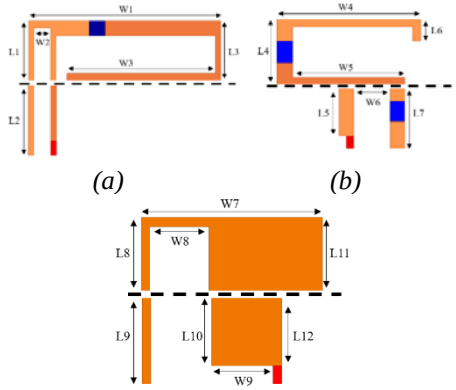

(a) *(b)*

(c)

Fig. 2. Geometry of (a) GPS antenna (Ant.1), (b) WLAN 2.4GHz/BT antenna (Ant.2), and (c)WLAN5.2/5.8GHz /Wi-Fi 6E 6GHz (Ant. 3, and Ant. 4).

Table 1. Detailed Dimensions of The Proposed design

Parameter	W1	W2	W3	W4	W5	W6
Unit(mm)	17.5	1.5	13.5	9	7	2.5
Parameter	W7	W8	W9			
Unit(mm)	10.7	3.5	3.5			
Parameter	L1	L2	L3	L4	L5	L6
Unit(mm)	4	4.6	4	4.5	3.6	1.5
Parameter	L7	L8	L9	L10	L11	L12
Unit(mm)	4.6	4	4.6	3.6	4	3.6

III. RESULT AND DISSGUSSION

The simulated results of the design was simulated by HFSS (High Frequency Structure Simulation) software. Fig. 3 shows the measured and simulated S11 and S22 of the design. Fig. 4 shows the simulated and measured S33 and S44 of the design. In Fig. 3, the bandwidth defined on -6dB of the Ant.1, can be applied to GPS band. The bandwidth defined on -10dB of Ant. 2 can be applied to WLAN2.4GHz and BT applications. Fig. 4 shows the S33 and SS44 of the design. The bandwidth defined on -8dB can be applied to WLAN5GHz and Wi-Fi 6E 6GHz bands. Fig. 5 shows the Sij (when i is not equal to j, and i, j =1 - 4) of the design. From the results, the Sij of the design are all less then -10dB, which can be used for applications.

Fig. 6 — 9 show the simulated gains and efficiencies of the design. In Fig. 6, the simulated gain of the Ant. 1 (GPS) is ranging from 1.2 to 1.3dBi, and the efficiency is about 80%. In Fig. 7, the simulated gain of the Ant. 2 (WLAN2.4GHz/BT) is ranging from 1.51 — 1.57dBi, and the simulated efficiency is about 87%. Fig. 8 and Fig. 9 show the simulated gain and efficiency at WLAN 5.2GHz, WLAN 5.8GHz, and Wi-Fi 6E 6GHz bands separately. The gain of the design at WLAN 5.2GHz band is ranging from 2—2.2dBi, and the efficiency is ranging from 83 to 84%. The gain of the design at WLAN 5.8GHz band is about 2.5dBi, and the efficiency is ranging from 84 to 85%. In Fig. 9, the antenna gain of the design is ranging from 1.9 to 2.4dBi, and efficiency is ranging from 82 to 84%.

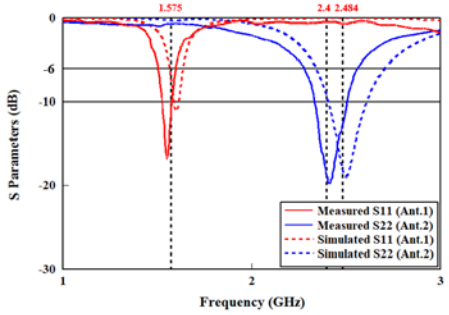

Fig. 3. Measured and simulated S11 and S22 of the design (Ant.1 and Ant. 2).

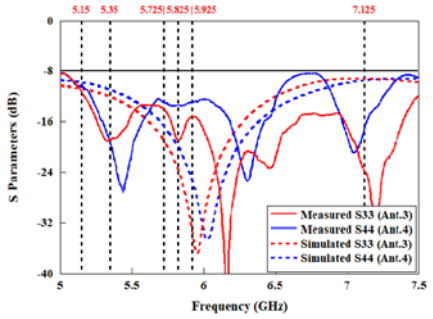

Fig. 4. Measured and simulated S33 and S44 of the design(Ant. 3 and Ant. 4).

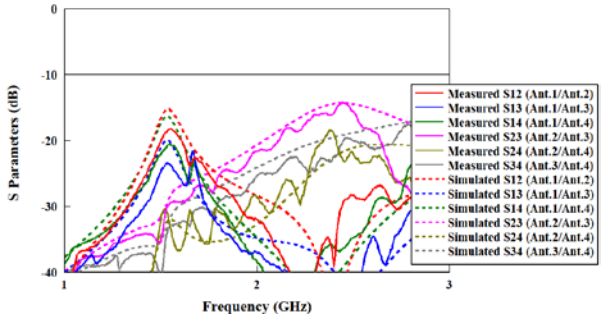

(a)

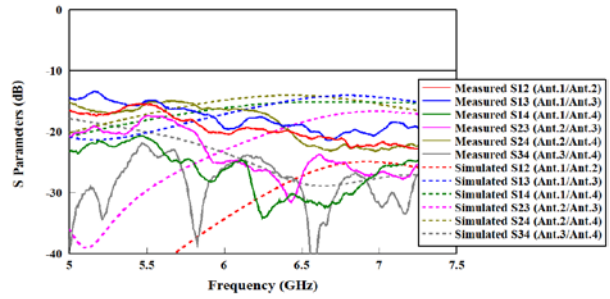

(b)

Fig. 5. Measured and simulated Sij (when i is not equal to j) of the design.

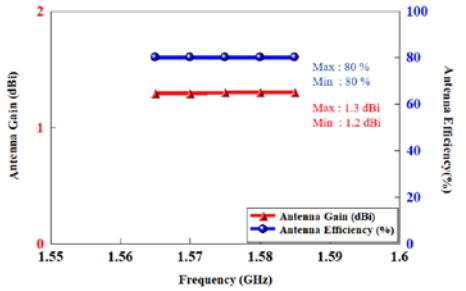

Fig. 6. Simulated gain and efficiency of the design at GPS band (Port 1).

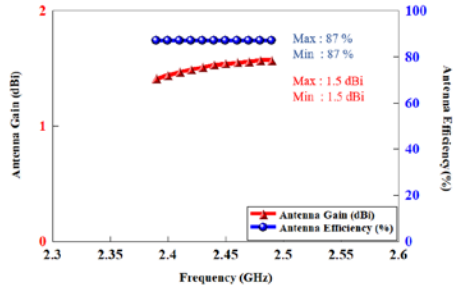

Fig. 7. Simulated gain and efficiency of the design at WLAN 2.4GHz/BT bands (Port 2).

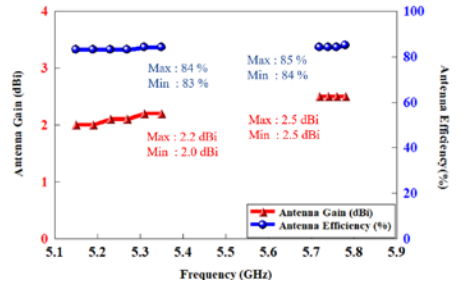

Fig. 8. Simulated gain and efficiency of the design at WLAN 5.2/5.8GHz bands (Port 3).

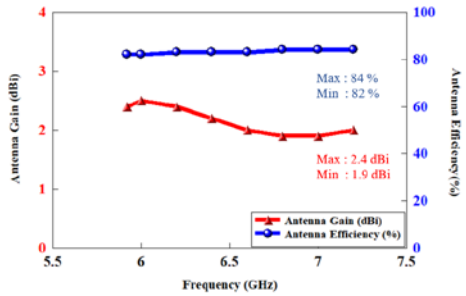

Fig. 9. Simulated gain and efficiency of the design at Wi-Fi 6E 6GHz band (Port 3).

IV. CONCLUSION

A design of four antennas for smart watch application has been proposed. The design is design for GPS/WLAN5.2/5.8GHz/Wi-Fi 6E 6GHz bands. The use of IFA structure is adopted in the design. The two antennas are used for MIMO antennas for WLAN5.2/5.8GHz/Wi-Fi 6E 6GHz bands to increase transmission rate. From the results, the design can cover the bands of WLAN5.2/5.8GHz/Wi-Fi 6E 6GHz. And the radiation performances of the design are all good for applications. The design with multi-band operation and good radiations can be applied to applications in smart watch devices.

References:

[1] H. -S. Huang, H. -L. Su, S. -L. Chen, "Multiband antennas for GPS/GSM1800/Bluetooth/Wi-Fi smart watch applications," *2017 IEEE International Conference on Computational Electromagnetics (ICCEM)*, pp. 352-354, 2017.

[2] Wen-Shan Chen, Guan-Quan Lin, Wen-Hsiu Hsu, "WLAN MIMO antennas with a GPS antenna for smart watch applications," 2017 International Workshop on Electromagnetics: Applications and Student Innovation Competition, pp. 89-90, 2017.

[3] S. -W. Su, D. P. Yusuf, F. -H. Chu, "Conjoined, Wi-Fi 6E MIMO Antennas for Laptops," 2021 International Symposium on Antennas and Propagation (ISAP), pp. 1-2, 2021.

[4] M. I. Magray and S. -W. Su, "Conformal and Highly Compact Wi-Fi 6E Antenna for Laptop Applications," 2022 Asia-Pacific Microwave Conference (APMC), pp. 536-538, 2022.

[5] C. -Y. -D. Sim et al., "A PIFA Design with WLAN and Wi-Fi 6E Band for Laptop Computer Applications," 2022 IEEE International Symposium on Antennas and Propagation and USNC-URSI Radio Science Meeting (AP-S/URSI), pp. 1808-1809, 2022.

[6] C. -Y. -D. Sim, V. Dhasarathan, T. K. Tran, J. Kulkarni, B. A. Garner, Y. Li, "Mutual Coupling Reduction in Dual-Band MIMO Antenna Using Parasitic Dollar-Shaped Structure for Modern Wireless Communication," in IEEE Access, vol. 11, pp. 5617-5628, 2023.

532nm Green Laser Annealing for Improving the Physical Properties of ITO/Ag/ITO and AZO/Ag/AZO Transparent Conducting Electrodes

Manikandan Rajendran[1†], Keh-Moh Lin[1*], Wen-Tse Hsiao[2]

[1]Department of Mechanical Engineering, Southern Taiwan University of Science and Technology, Tainan 71005, Taiwan.
[2]Instrument Technology Research Center, National Applied Research Laboratories, Hsinchu 30076, Taiwan.
[†]Presenter: **Manikandan Rajendran**
[*]Corresponding author's e-mail: kemo@stust.edu.tw

Abstract

Transparent conducting ITO/Ag/ITO and AZO/Ag/AZO electrodes were fabricated using RF magnetron sputtering at room temperature. To improve the optical, electrical, and structural properties of the electrode, the films were annealed with a 532nm green laser. The optical, electrical, and structural characteristics of the electrode were examined using the UV-Vis spectrophotometer, four-point probe station, and XRD analysis. In this work, the high optical transmittance of 84% and 82% and very low electrical resistivity of 6.9 Ω/sq and 6.3 Ω/sq were attained at ITO/Ag/ITO and AZO/Ag/AZO electrodes, respectively, after laser annealing. The middle Ag layer's crystallite size significantly increased during laser annealing, according to the XRD examination. After laser annealing, the Haacke index increased from ϕ Vis ≅ 20 × 10^{-3} Ω^{-1} to ϕ Vis ≅ 24 × 10^{-3} Ω^{-1}. These findings suggested that the laser annealing effect and annealing parameters have a substantial impact on the improvements in the optical, electrical, and structural characteristics of the highly conducting ITO/Ag/ITO and AZO/Ag/AZO electrodes. We also achieved significant enhancements in the physical properties of the electrode after laser annealing.

Keywords: 532nm laser annealing, Sputtering, TCO electrodes.

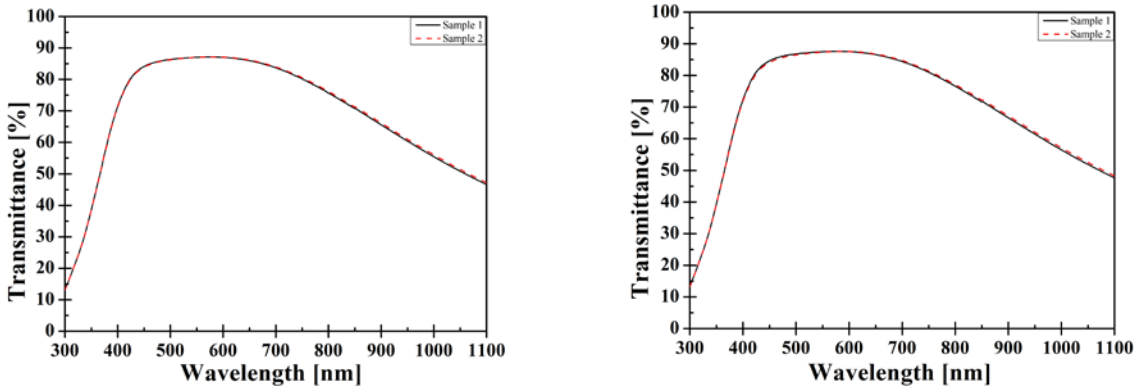

Fig.1. (Left) Transmittance spectra of as-deposited sample, (Right) Transmittance spectra of laser annealed sample. (Set-3: ITO/Ag/ITO)

Acknowledgment:

Financial support was granted in part by the Ministry of Science and Technology of Taiwan R.O.C under MOST 110-2622-E-218-006 and MOST 111-2221-E-218-015.

References:

[1] Junichi Nomoto, Iwao Yamaguchi, Tomohiko Nakajima, Yasuhito Matsubayashi, Thin Solid Films 698 (2020) 137867.
[2] Wen-Tse Hsiao, Shih-Feng Tseng, Chien-Kai Chung, Donyau Chiang, Kuo-Cheng Huang, Keh-Moh Lin, Liang-Yan Li, Ming-Fei Chen, *Optics & Laser Technology* 68 (2015) 41–47.

2023 International Symposium on Advanced Technology (ISAT-22)
Tainan City, Taiwan, October 19-20, 2023

The effect of the drying methods on the texture properties of banana

Quoc Thien Pham[1], Pawan Rajput[2], Sheng-En Lu[2], Yu-Hsuan Huang[2], Cheng-Hsuan Chiang[2], Nai-Shang Liou[2]

[1]HUTECH University, Ho Chi Minh, Vietnam

[2]Department of Mechanical Engineering, Southern Taiwan University of Science and Technology, Taiwan

E-mail: nliou@stust.edu.tw

Abstract

In this study, the best different drying methods of banana were subjected to two different drying methods, and the effect of the drying method (oven drying and vacuum drying) on the textural characteristics and fresh banana were compared. The results show that different drying methods will increase the hardness, fracture, gumminess, and chewiness of banana samples and decrease the cohesiveness, springiness, and resilience to varying degrees. The flavor content of the active substance is most significant in vacuum freeze drying compared to oven drying. At last, there was no shrinkage in the fruit in the vacuum drying method and it maintained good hardness, fracture, gumminess, and chewiness. With comprehensive texture characteristics and changes in properties, vacuum freeze drying is more efficient for the drying and processing of banana fruit. Understanding the effect of drying methods on banana texture is crucial for optimizing the drying process and meeting consumer expectations.

Keywords: Drying methods, oven drying, vacuum drying, TPA (Textural Profile Analysis).

Introduction

Bananas are among the most widely consumed fruits globally, cherished for their delightful taste, nutritional value, and convenience. This study shows the different drying methods of banana samples and the texture properties of the final product. Textural is a critical attribute of the food product, as it directly affects the sensory experience. Therefore, understanding how different drying techniques affect the properties of dried bananas is essential for producers and consumers. Currently, the commonly used drying methods for fruits are oven drying, vacuum drying, and so on. Oven drying is a method of using heat when the wet material is in the oven. The vacuum drying of food means that the frozen water in the food is sublimated and removed under the condition of low temperature and low pressure below the triple point of water [1]. These drying methods have their advantages and disadvantages. This paper studies the two most common drying methods: how oven and vacuum drying affect the texture properties (hardness, fracture, springiness, cohesiveness, gumminess, resilience, chewiness) and active ingredients.

Result and discussion

Fig1. shows the detailed overview and the textural properties in the different methods of drying state. Fig.1 (a) hardness, (b) fracture ability, (c) cohesiveness. Fig.2 (a) springiness, (b) gumminess, (c) chewiness. The results are that in the oven banana there is an increase of the hardness by 2290.81%, fracture ability by 621.526%, gumminess by 11699.1%, and chewiness by 11060%. On the other hand, the results in the vacuum drying are, there is an increase in hardness by 1930.64%, fracture ability by 2100.12%, gumminess by 2917.12%, and chewiness by 1384.48% and there is a decrease in the cohesiveness and springiness by 6.99% and 44.8104% respectively.

Fresh banana

Texture properties Fresh bananas, used as a control group in this study, served as the benchmark for comparing the effects of drying methods. They exhibited the typical texture associated with ripe bananas, characterized by a soft and chewy consistency.

Oven drying

Texture Properties: The bananas subjected to oven drying exhibited distinct texture properties. The texture analysis revealed that oven-dried bananas had a higher hardness value than fresh bananas.

Vacuum drying

Texture properties: Vacuum-dried bananas maintained a softer and chewier texture, resembling fresh bananas' texture. As a result, vacuum-dried bananas retained their original softness and were less brittle than oven-dried ones.

Conclusion

In this study, we conducted a comprehensive investigation into the effects of two distinct drying methods, namely oven drying and vacuum drying, on the texture properties of bananas. Texture is a critical attribute in the sensory evaluation of fruit. The results of our research provide valuable insights into how these drying techniques impact the texture properties of bananas. Vacuum drying involves lower temperatures and reduced exposure to oxygen, which helps retain the fruit's natural moisture content and softness. As a result, vacuum-dried bananas exhibit a softer, chewier texture, which is closer to the fresh fruit.

References

[1] L. Qian, L. Yongbin, S. Keying, L. Simei, Z. Shiming, L. Ruiting, Effect of drying methods on the texture properties and active ingredients in Longan flesh et al.2021

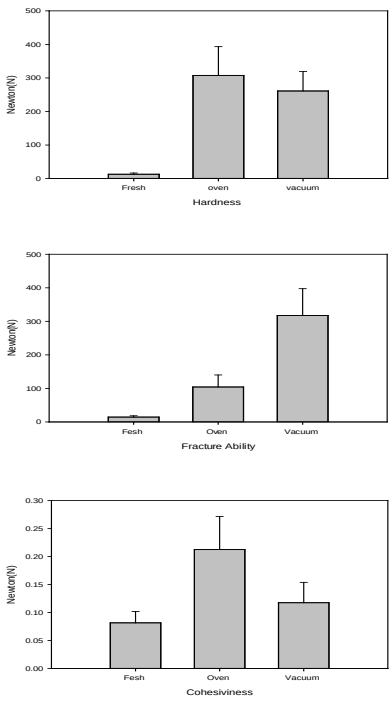

Figure 1: Drying properties comparison of fresh, oven, and vacuum banana samples. (a) Hardness, (b) fracture ability, and (c) cohesiveness.

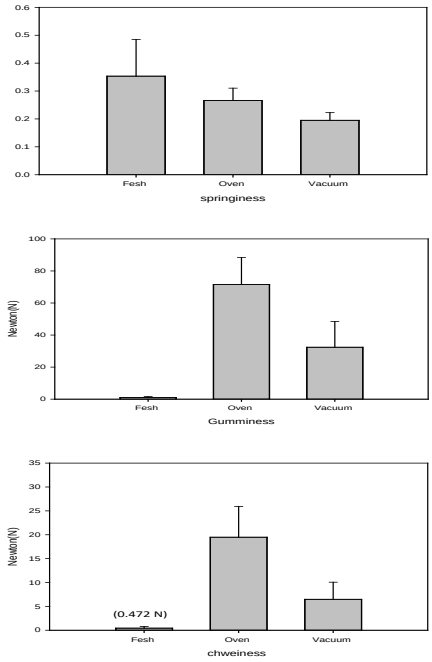

Figure 2: Drying properties comparison of fresh, oven, and vacuum banana samples. (a)springiness (b)gumminess, and (c) chewiness.

Image-based Classification and Analysis of Hospital Dishes for Nutritional Monitoring and Personalized Care

Yao-Lin Zhang 1†, Wen Yao She2 and Yu-Sheng Lin1*

[1] Department of Mechanical Engineering, Southern Taiwan University of Science and Technology, Tainan, Taiwan
[2] Department of Mechanical Engineering, National Kaohsiung University of Science and Technology, Kaohsiung, Taiwan
E-mail: yushenglin@stust.edu.tw

Abstract
The trend towards medical digitization and personalization is a significant development in the healthcare industry. This trend encompasses various care, treatment, and tracking processes in both hospital and home settings. One critical aspect of patient care is the regulation of nutritional intake through diet. However, monitoring the quantity of intake can be challenging due to time and environmental constraints, which can lead to inadequate recording. The use of machines to mimic the observations of dietitians and record the types and portions of food consumed could potentially alleviate the workload of dietitians and enhance personalized care for patients. In this study, we aim to analyze a hospital menu in Taiwan through image preprocessing techniques.

Over the past few years, the healthcare industry has undergone a significant transformation as a result of the increasing trend towards digitization and personalization. This shift has brought about a range of developments in care, treatment, and monitoring practices, both within hospital settings and in patients' homes. One crucial aspect of patient care is the regulation of nutritional intake through dietary measures. However, accurately monitoring the quantity of food consumed can present challenges due to time constraints and environmental factors, often resulting in incomplete documentation. The potential solution lies in leveraging machine technology to replicate the observations made by dietitians, enabling the recording of food types and portion sizes [1]. This approach has the potential to alleviate the workload of dietitians and further enhance the provision of personalized care to patients. In this study, we aim to analyze a hospital menu in Taiwan using image preprocessing techniques.

Regarding the experimental procedure shown in Fig 1, the initial phase involved the collection and filtration of dietary data obtained from the hospital. Image segmentation techniques were employed to identify and categorize 107 distinct dishes present in the dataset. Subsequently, in order to gain insights into the color composition of the dishes, RGB and grayscale histogram analyses were performed. This step could help clean the data to identify any outliers or abnormal values that may exist within the dataset [2]. Likewise, box plots, RGB histograms, and grayscale value histograms were utilized to effectively detect and remove such anomalies. To further distinguish the similarity of each dishes, K-means analysis [3] was employed to investigate the distribution patterns. By clustering the dishes, it was possible to identify commonalities and variations among the different types of dishes.

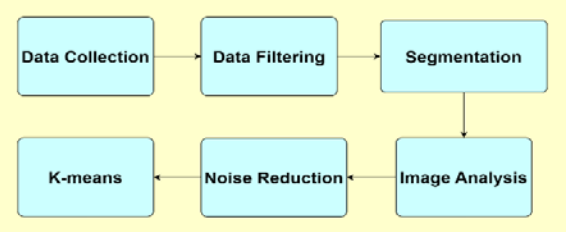

Fig. 1. Experimental procedure.

Fig 2 shows the color analysis between two dishes as examples. The photo of meats is constantly brighter than the photo of vegetables. It can be seen that much higher intensity on low grayscaled pixels color of vegetable. In Fig 3, the results of K-Means can be divided into 5 groups. It can be observed that dishes closer in hue to lighter colors tend to have their distributions around the 180-200 range in the R, G, B values. Dishes with brighter colors, like meat and bean sprouts, typically fall around the value of 100 for all three RGB values. Dark green vegetables and darker dishes, such as water spinach and stir-fried sea cucumbers, are located in the 0-60 range. From the K-means clustering results, it's evident that meats and similar foods have a more uniform color distribution, leaning towards brighter hues. In contrast, green vegetables tend to skew towards darker colors. This method can generally differentiate green vegetables from meats, but for dishes like cabbage, which leans more towards white, the aforementioned approach may not be suitable.

The study concludes that K-Means and color analysis can effectively help categorize the Taiwanese hospital dishes based on color.

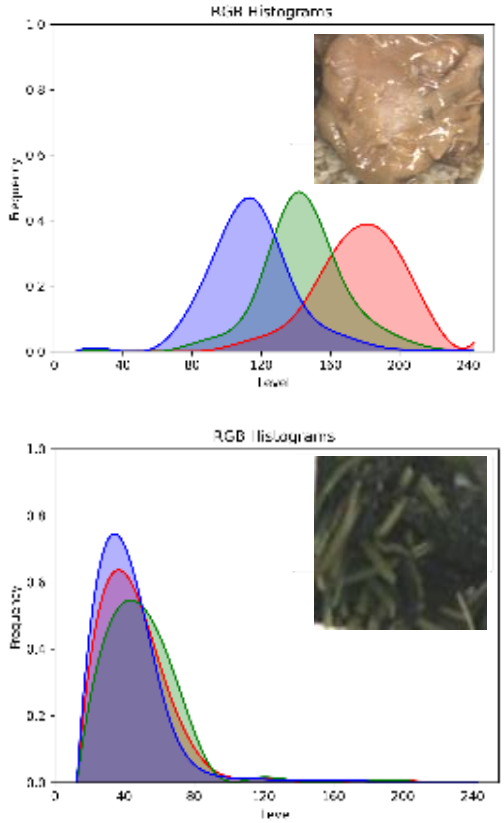

Fig. 2. Color distribution of Meats (Left) and Vegetables (Right).

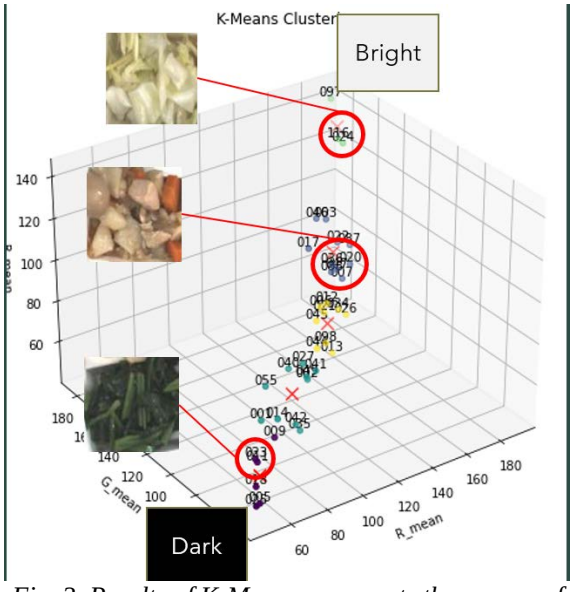

Fig. 3. Results of K-Means represents the groups of different dishes.

References:

[1] NTUH Hsin-Chu Branch," Nutrition room" from: https://www.hch.gov.tw/?aid=626&pid=62&page_name=detail&iid=750

[2] Basar, S., Ali, M., Ochoa-Ruiz, G., Zareei, M., Waheed, A., Adnan, A. "Unsupervised color image segmentation: A case of RGB histogram based K-means clustering initialization". PLOS ONE, 2020.

[3] Lingeswari, S., Gomathi, P.M., & Kailasam, S.P. A Study Of Tomato Fruit Disease Detection Using Rgb Color Thresholding And K-Means Clustering. Ijcsmc, Vol. 10

Using Discrete Cosine Transform for Automated Pattern Recognition

Kai-Hsien Chen, Zheng-Quan Wang, Ming-Hua Chen, and Gwo-Jiun Horng*

Department of Computer Science and Information Engineering, Southern Taiwan University of Science and Technology, Tainan, Taiwan
*E-mail: grojium@stust.edu.tw

Abstract

Due to the rapid development of artificial intelligence technology nowadays, when it comes to image recognition, most people immediately train artificial intelligence models to complete image recognition. However, training artificial intelligence models requires a considerable amount of hardware resources. If only simple image recognition results need to be achieved, it may be less necessary to use such a hardware resource consuming method. Nowadays, with the gradual expansion of memory space, people can have a large amount of image data at the same time but cannot quickly find similar images.

This study implements an image search system using the discrete cosine transform algorithm, which can quickly search for similar images in many images. Users can take pictures through mobile apps, and through the image recognition system in this study, similar images can be quickly searched for, and corresponding image information can be returned to the mobile app for display.

The subsystems used in this study include a dataset subsystem, a user subsystem, and an image matching subsystem. The dataset subsystem performs discrete cosine transform and hash value conversion on the card images of the dataset, and pre stores the hash value after the conversion to save program execution time. After the user takes the identification card to be identified, the image data is transmitted to the dataset subsystem. After undergoing discrete cosine transformation and converting the hash value, the numerical value is sent to the image comparison subsystem for Hamming distance comparison with the pre stored data in the dataset. After comparison, the image name of the card with the shortest Hamming distance will be returned to the dataset subsystem, which will then transmit the relevant data of the card back to the user.

When using the device lens to capture images, it can automatically detect the direction of the image and transmit the image to the computer application program. It can search for the corresponding card number in the dataset (with approximately 38000 images). In most normal environments (with normal lighting, angles, and no severe reflections), the accuracy rate is relatively high (around 70% to 90%), and even in noisy and dimly lit environments, it can work normally. And it can complete the search within 0.5 to 2.5 seconds to ensure a user experience, allowing users to obtain the required card information when using this app. easily and quickly.

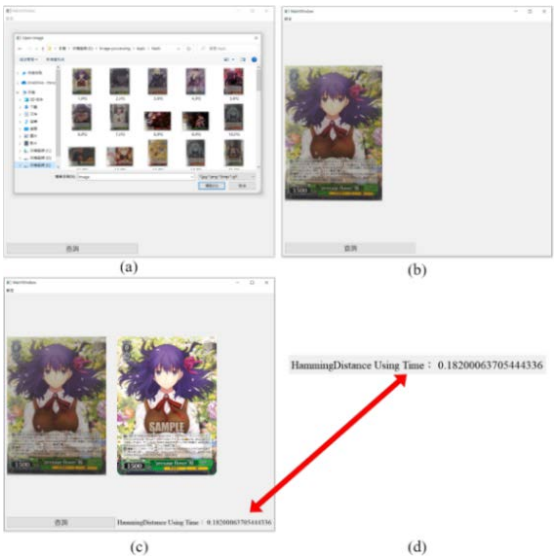

Fig. 1. Picture comparison expected results.

References:

[1] "Region of interest- Wikipedia." https://en.wikipedia.org/wiki/Region_of_interest(accessed May 28, 2022).
[2] " OpenCV: Canny Edge Detection." https://docs.opencv.org/4.x/da/d22/tutorial_py_canny.html(accessed May 28, 2022).
[3] "Qt for Python " https://doc.qt.io/qtforpython/ (accessed May 29, 2022)
[4] "scipy.fftpack.dct ", https://docs.scipy.org/doc/scipy/reference/generated/scipy.fftpack.dct.html (accessed May 20, 2022)
[5] "How to detect an octagonal shape in Python and OpenCV", https://stackoverflow.com/questions/60177653/how-to-detect-an-octagonal-shape-in-python-and-opencv(accessed May 20, 2022)
[6] "OpenCV–more on contours #2" https://chtseng.wordpress.com/2016/12/05/opencv-more-on-contours-2/(accessed May 20, 2022)

Application of Face Image Recognition in Sleep-deprived Driving Warning System

Yen-Yu Chen, Huai-Wen Hsu, and Gwo-Jiun Horng*

Department of Computer Science and Information Engineering, Southern Taiwan University of Science and Technology, Tainan, Taiwan
*E-mail: grojium@stust.edu.tw

Abstract

In recent years, the proportion of Sleep-deprived driving caused by land transportation has been rising, which has become a social problem of concern. Sleep-deprived driving not only endangers the safety of the driver, but also may cause danger to other road users. We have found that fatigue detection functions are mostly included in new cars, while old cars cannot be equipped with similar functions due to insufficient intelligence. We have developed a detection system that is simple to use, easy to install, and can be used if it is plugged in, without being limited by the usage field, and has a reliable API interface. This research uses the facial recognition function to obtain facial feature points, calculates specific feature points, and concludes that when the driver enters the state of Sleep-deprived driving, or when the driver has dangerous driving, the wearable device will remind the driver of the appropriate rest or stop the dangerous driving as soon as possible, and if it is possible to intervene in the auto drive system when the situation is unavoidable, And remind other pedestrians through devices such as the vehicle's dual flashing lights or speakers.

This study is divided into three parts, including the main processor, wearable devices, and vehicle control. The main processor uses Jetson nano as the processing core to process camera control, Edge computing and communication functions, and controls wearable devices and vehicles through Wi Fi or wired interfaces.

After obtaining data on the eyes, top of the nose, left and right cheeks, and facial midline in this study, the predicted values of fatigue can be obtained by calculating the proportion of the eyes to the fatigue. This data has a consistently high value, and the time for the eye proportion to maintain a high value is calculated. When this time reaches the preset trigger value, the wearable device alarm and the automatic driving intervention function will be triggered.

Figure 1. Driver driving normally

Figure 2. The driver continues to close their eyes

Figure 3. Dual flashing lights on and vehicle braking activated

In addition to obtaining eye values, this study also applied different filtering methods to this value. The waveform with high values is effectively calculated. Through the average filtering method, this study can better achieve the planned goal of judging the eyes. This study also tests whether the combination function of truck simulator and vehicle is normal and feasible. Figures 1 to 4 show the simulator test diagram.

Figure 4. Vehicle completely stopped

References:

[1] C. Xiang, S. Li, "Time-varying Regularity Exploration and Regulation Practice of Driving Fatigue," 2021 6th International Conference on Transportation Information and Safety (ICTIS), Wuhan, China, 2021, pp. 1587-1590, doi: 10.1109/ICTIS54573.2021.9798575.

[2] W. Hailin, L. Hanhui and S. Zhumei, "Fatigue Driving Detection System Design Based on Driving Behavior," 2010 International Conference on Optoelectronics and Image Processing, Haikou, China, 2010, pp. 549-552, doi: 10.1109/ICOIP.2010.101.

[3] F. Zhang and F. Dai, "Research and Application of Fatigue Driving Monitoring and Emergency Treatment," 2017 International Conference on Computer Technology, Electronics and Communication, Dalian, China, 2017, pp. 1072-1075, doi: 10.1109/ICCTEC.2017.00235.

[4] L. Zeng, Y. Wang, Q. Han, K. Zhou, L. Ye and Y. Long, "Driving Fatigue Detection Combining Face Features with Physiological Information," 2021 7th IEEE International Conference on Network Intelligence and Digital Content (IC-

NIDC), Beijing, China, 2021, pp. 138-142, doi: 10.1109/IC-NIDC54101.2021.9660529.

Development of a Bluetooth-Based Rehabilitation Ball and Its Corresponding Interactive Games

Jeng-Han Li, Yu-Chin Lin, Wei-Ting Hou, Tien-Yu Hsu, Yu-Xiang Hong, and You-Cheng Kang

Department of Electrical Engineering, Southern Taiwan University of Science and Technology, Tainan, Taiwan
E-mail: jenghanli@stust.edu.tw

Abstract

The rehabilitation process is usually very long-time and boring; thus, many rehabilitation patients often interrupt their rehabilitation exercises for this reason, which reduces the effect of treatment. This paper develops a rehabilitation ball with Bluetooth communication module as its core of the system. The system is equipped with pressure sensors to sense the strength of the grip force, then the Bluetooth communication can transmit the relevant sensing information to mobile phones or tablets for the control of interactive games. We also design an interactive game in Android OS environment for the developed rehabilitation ball. Since the system developed in this paper is intended for the elder people, the designed game will be as simple and easy to use as possible. So that, patients can wave their arms and grasp their palms according to the game situation. The Bluetooth-based rehabilitation ball and the corresponding interactive game developed in this paper can make the rehabilitation process no longer boring, reduce the resistance of the elderly to rehabilitation medical treatment, and make the elderly willing to increase the time and frequency of use to achieve the goals of rehabilitation. effect.

Figure 1 shows the photos of the appearance and internal components of the designed rehabilitation ball. We use a foam baseball as the main body of the rehabilitation ball, and hollow out the interior to install the relevant sensors, main control board, Bluetooth transmission module and lithium battery.

Figure 2 shows the game screen we created by using App Inventor software. The program of the game is that the rehabilitator holds the rehabilitation ball. When the little dinosaur approaches the obstacle, one holds the rehabilitation ball tightly and controls the little dinosaur to jump through the obstacle. If the jumping is successful, one will get extra points. If he encounters the obstacle, the game. would be terminated. Through simple games, boring rehabilitation activities can be made lively and interesting, improving the rehabilitation patients' willingness to participate in rehabilitation and the effectiveness of rehabilitation.

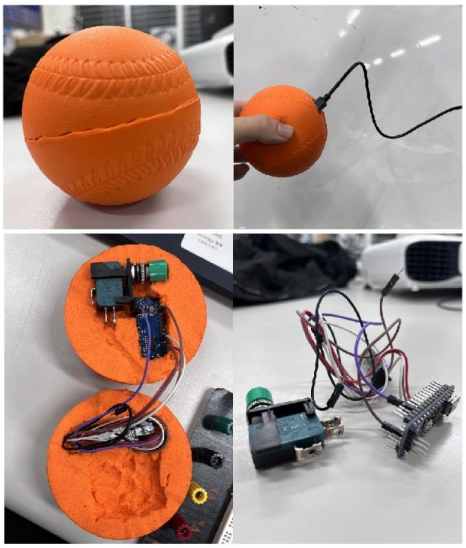

Figure 1. Physical photos of the designed rehabilitation ball

Figure 2. Actual screen of the designed interactive game

References:

[1] Irene Kuo, Discussion on product design for elderly users, 2019. Link：https://medium.com/@irenekuo_70917/%E6%9B%B8%E6%91%98-%E9%AB%98%E9%BD%A1%E4%BD%BF%E7%94%A8%E8%80%85%E7%94%A2%E5%93%81%E8%A8%AD%E8%A8%88%E4%B9%8B%E6%8E%A2%E8%A8%8E-d3600175ef72

[2] Siang-Jyun Jheng, Development of a customizable visual feedback device for upper limb rehabilitation, Master Dissertation of National Yang Ming University, 2014.

[3] Han-Lin Li, Development and application of active and passive hand rehabilitation equipment with game interaction design and wearable physiological sensor monitoring system, Master Dissertation of Kun Shan University, 2021.

A Study on a Vision Transformer Model with Squeeze-and-Excitation Blocks for a Generative Adversarial Network Model

Tatsuhiko Ikeda* and Hidetoshi Saito

Graduate School of Engineering, Kogakuin University, Tokyo, Japan
E-mail: cm22005@g.kogakuin.jp

Abstract

The Transformer is well known as a novel neural network (deep learning) architecture for natural-language understanding (natural language processing) which provides a machine learning-based service to build natural language into apps, bots, and IoT devices, etc. Moreover, the Transformer has been applied in order to solve various vision tasks recently. For example, The *Vision Transformer* (ViT) is the first computer vision model using the Transformer architecture for image classification tasks at large scale. In this research, we propose a new modified ViT using *Squeeze-and-Excitation* (SE) blocks for improving the quality and increasing diversity of *Generative Adversarial Network* (GAN) generated images.

1. Introduction

An SE network can be generated by simply stacking a collection of SE blocks[1]. Each SE block is introduced as an architectural unit designed to improve the representational power of a network by enabling it to perform dynamic channel-wise feature recalibration. In this research, we consider that improving the accuracy of the discriminator in a GAN leads directly to generate a high-quality image with an appropriate resolution. The discriminator plays the role of a classifier and tries to distinguish real data from the data created by the generator. Hence, we expect that the discriminator using a ViT with SE blocks to improve the performance of a GAN model based on the quality and diversity of the generated synthetic images.

2. Proposed Vision Transformer Model

We propose a following ViT encoder shown in Fig. 1. At first, we change the multi-head attention layers to the SE block layers in the original Transformer encoder[2]. Secondly, we replace two full connected convolution layers by a single *Convolutional Neural Network* (CNN) layer in all residual connections. Our proposed ViT model (vit.SE) uses the above encoder.

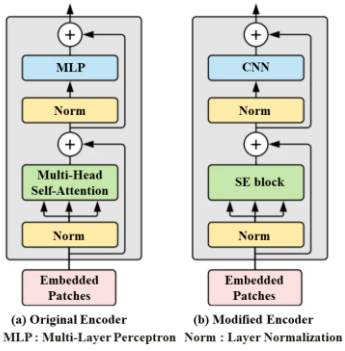

Fig. 1. Vision Transformer Encoder.

3. Evaluation and Simulation Methods

We construct a new GAN model using both the generator of the Self-attention GAN model[3] and the discriminator including the our proposed ViT model. Our proposed GAN model is compared with the other modified GAN model[4]. If we evaluate each GAN model, the GAN generated images are evaluated by using following three evaluation indices as *Fréchet Inception Distance* (FID), *Kernel Inception Distance* (KID) and *Iteration Speed* (it/s, iteration per second). In simulation, we obtain all evaluation parameters and loss functions for each model within 50 epochs under the condition of a batch size equal to 32. We select an optimum image based on subjective visual inspection which has best diversity and quality after 30 epochs. If we decide the optimum image, we can record the number of epochs, the FID score and the KID score and the number of iterations every second at that time (itr/s). The generating dataset from each GAN model is created by using "102 Category Flower Dataset" consisting of 102 flower categories as real dataset with 8,192 items of image data[5].

4. Simulation Results

Table 1 shows the evaluation results for both of GAN models. From Table 1, the quality and diversity indices of achieve the 25.5 and 15.3 percent improvements in KID and FID scores, respectively. From the view of reducing in the amount of calculation for discrimination, calculation speed index achieves the 59.0 percent improvement in iter/s.

Table 1. Evaluation results for ViT models.

GAN model	Conventional[4]	Proposed
ViT model in the discriminator	ViT	vit.SE
Epochs	50	48
FID score	124	105
KID score	0.0857	0.0637
iter/s	1.66	2.64

5. Conclusion

In this research, the modified GAN model using SE blocks is proposed and each performance is evaluated.

References:

[1] https://ieeexplore.ieee.org/document/8578843.
[2] https://doi.org/10.48550/arXiv.2010.11929.
[3] https://arxiv.org/abs/1805.08318.
[4] T. Ikeda and H. Saito, ISAT-21, EEEL7., 2022.
[5] 102 Category Flower Dataset, https://www.robots.ox.ac.uk/~vgg/data/flowers/102/.

2023 International Symposium on Advanced Technology (ISAT-22)
Tainan City, Taiwan, October 19-20, 2023

Measuring Facial Sway Using the Front Camera of a Smartphone

Shunki SUZUKI and Hisaya TANAKA

Department of Information Design, School of Informatics, Kogakuin University, Japan, Tokyo
E-mail: jx20143@ns.kogakuin.ac.jp

Abstract

This study conducts basic research aimed at measuring a person's level of concentration using the front-facing camera of a smartphone. To facilitate the measurement, an application was developed to capture facial information such as tilt, blink, and eye angle. In this study, we investigated errors related to head movement. When comparing the angle errors with optical motion capture as a reference, smartphones showed an error of approximately ±1.2 degrees. As a result, it was found that Facial Sway can be measured with sufficient accuracy to estimate concentration levels.

Introduction

In recent years, the assessment of human concentration and drowsiness has become increasingly critical in scenarios such as driving assistance, lectures, and remote work. Recent research includes studies employing methods like estimating concentration levels using brainwave data [1] and predicting actions requiring concentration using acceleration sensors [2]. However, these measurements often require dedicated equipment and the inconvenience of device attachment remains a challenge. Consequently, there is growing interest in methods that utilize relatively straightforward indicators, such as eye movement and posture, to estimate drowsiness and concentration. As an example, one approach for estimating posture is through the use of external cameras that measure the body's posture using Kinect. This method has shown a significant correlation with behavior and levels of concentration [3]. Moreover, it has been found that facial sways and saccadic eye movements are delayed when concentration diminishes [4]. Therefore, facial sways are considered to be a crucial factor in indicating concentration levels. A study of ours [5] used a facial estimation technique called Mediapipe to detect blinks and estimate drowsiness. By incorporating facial sway indicators into this research, we anticipate achieving more precise estimations. However, a challenge remains in verifying the accuracy of facial sway estimations using the front-facing camera of smartphones. Therefore, the development of an application capable of measuring facial sway, eye angles, and eyelid movements using a smartphone's front-facing camera was undertaken in this study, with the specific aim of calculating the error in measuring facial sway results.

Measuring Facial sways

In this study, ARKit, provided by Apple, was used to validate the facial sways. In this study, optical motion capture values were used as the standard, and the differences were compared with values measured using a smartphone. We developed an application that operates on an iOS to obtain the values measured on the smartphone. Fig. 1 shows a diagram of the developed application, with the left side representing a front-facing facial position and the right side illustrating a tilted facial orientation. The techniques employed are detailed in Fig. 2, where the values acquired with ARKit are transformed into angles using affine transformations and Euler angles. In addition, to measure the error caused by wearing glasses, the difference between wearing and not wearing glasses, was verified, as depicted in Fig. 3. Moreover, previous research [4] relied on the times when facial sways occurred and saccades were initiated for estimation. Therefore, on this basis, we assume that if significant differences emerge between facial sways in motion and static, there is sufficient precision to conduct experiments to estimate concentration levels from facial sways.

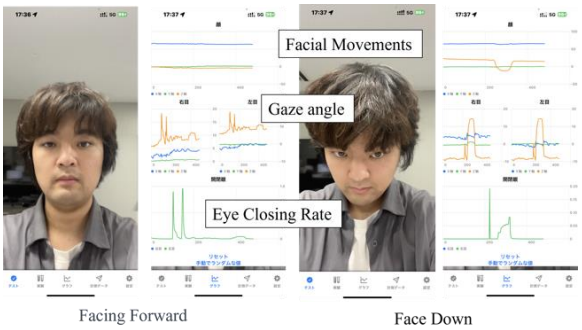

Fig.1 Facial sway measurement application

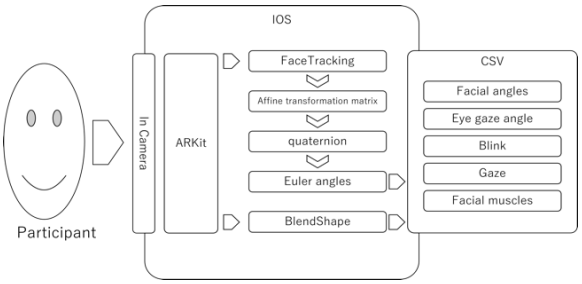

Fig.2 Diagram of facial expression measurement system using front camera

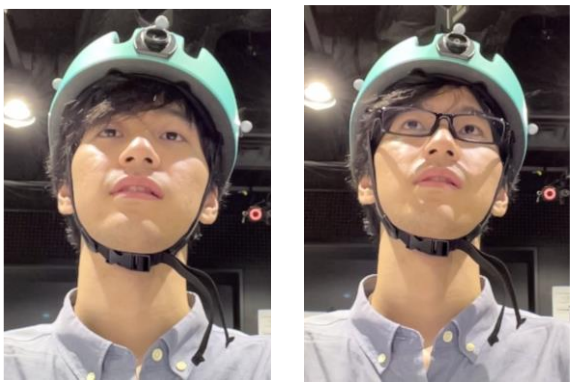

Fig.3 Photos of Participants with and without glasses

Experimentation

To measure facial sways, subjects were instructed to perform specific exercises, and the measurements obtained from motion capture (60 Hz) and those from the smartphone were compared. Verification was performed concurrently during static periods with and without glasses. Four healthy individuals, aged 22–23 years, participated in the experiments. Optical motion capture was used to estimate facial sways, utilizing the MAC3D System developed by the Motion Analysis Corporation and distributed by nac Image Technology. The A-axis reference was established using axis reference gauges produced using a 3D printer. The validation application used was an Apple iPhone 13 Pro Max. In terms of the experimental procedure, after initiating the recording on each measurement device, the participants synchronized their movements by nodding. Subsequently, they performed head movements in the following directions: up and down, left and right, diagonal, clockwise, and counterclockwise. They were then asked to remain still for 10 s, during which the changes in the stationary state were captured. Furthermore, to measure variations in errors due to the presence or absence of glasses, measurements were performed when wearing and not wearing glasses, regardless of their usual usage. For data processing in the experiment, a t-distribution was used to calculate a confidence interval of 0.0001% (99.999%) for each measurement frame, resulting in the computation of the measurement errors. Equation (1) is used for calculations, where x_i represents individual measurement values, and $\bar{x}$ signifies the mean value.

$$\mu_X = \sqrt{\frac{1}{n}\sum_{n=1}^{n}(x_i - \bar{x})^2} \times t\_value(p,n) \quad \ldots(1)$$
$$p: 0.99999 \quad n: number\ of\ frames$$

The t-value corresponds to a 99.999% confidence interval with degrees of freedom equal to the frame count of each data point. Taking the square root of the sum of these values allows for the calculation of the error range, which was verified on based on the differences in motion from the previous frame. This study was conducted in accordance with the Ethical Review of Human Subjects Research, Psychobiometrics for Novel Interface Development (Approval No.: 2021-A-28).

Experimental Result

Graphs depicting the measurements during the actual movements are shown in Fig. 4. Table 1 lists the errors under movement and static conditions. Table 2 compares the results with and without glasses. During motion, the X- and Y-axes exhibited deviations of approximately ±1.212° and ±1.154°, respectively, whereas the Z-axis exhibited a slightly higher deviation of approximately ±1.493°. Furthermore, when comparing the cases with and without glasses, the former resulted in larger errors of approximately ±0.2° for the X- and Y-axes and approximately ±0.4° for the Z-axis. In the static state, the Y-axis exhibited the highest precision with deviations of approximately ±0.122°. The other axes exhibit deviations of approximately ±1.5°. Regarding the static state, no significant differences were observed between wearing and not wearing the glasses.

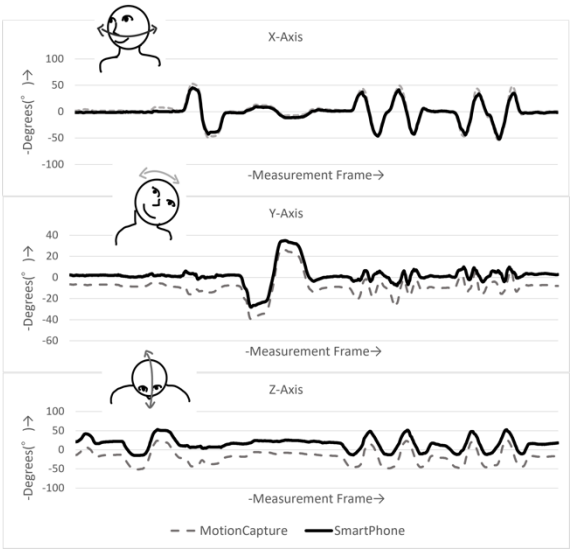

Fig.4 Example of accuracy verification using optical motion capture

Table1. Errors during moving and static

	μ_X	μ_Y	μ_Z
Moving	±1.212°	±1.154°	±1.493°
Static	±0.159°	±0.122°	±0.154°

Table2. Errors when comparing between wearing and not wearing glasses

	Wearing glasses	μ_X	μ_Y	μ_Z
Moving	**On**	±1.341°	±1.340°	±1.740°
	Off	±1.107°	±0.992°	±1.280°
Static	**On**	±0.175°	±0.131°	±0.158°
	Off	±0.147°	±0.116°	±0.152°

Discussion

Table 1 shows that the errors during motion are less than ±1.5°, which is significantly below the required level of ±3°. This suggests that measurements can be achieved at a similar angular velocity to optical motion capture. Furthermore, a comparison between the motion and static states shows that the static state has a smaller error than the motion state. This suggests that the accuracy is sufficient to discriminate between the operating and stationary states. This observation suggests that there exists a level of precision sufficient to discriminate between states of activity and repose. However, the error along the Z-axis is larger than that along the other axes. This could be attributed to the distortion in the depth direction, which makes it difficult to accurately estimate the positions of the eyes and nose, resulting in significant distortion in angle estimation. Although the X- and Y-axes allow for a clear measurement of the eyes and nose from the camera's perspective, which makes facial recognition straightforward, the Z-axis experiences significant distortion in the depth direction, making it difficult to accurately measure the nose and eyes from the camera's viewpoint, thereby complicating the estimation process. In addition, the reason for the approximately ±0.2° larger error when wearing glasses may be attributed not only to the distortion in the depth direction, but also to the fact that features such as the eyes may be obscured by glasses, making estimation more challenging.

Conclusion

When comparing the results of facial sways between ARKit and optical motion capture, we found an error of approximately ±1.2° for the X- and Y-axes, and approximately ±1.5° for the Z-axis. Furthermore, wearing glasses resulted in an increased error of approximately ±0.2° compared with that when not wearing glasses. In addition, in the static state, there was no significant difference in the error between wearing and not wearing the glasses. These findings indicate that facial sways can be measured with sufficient accuracy to estimate the concentration levels. The facial sway technology employed in this study can be used to measure the concentration and assess drowsiness in practical applications.

References:

[1] R. Nagase, et al. "Design and Implementation of a Remote Communication Partner's Concentration Measurement System Using Brainwave Signals" (in Japan), *The 79th National Conference of the Information Processing Society of Japan*, 4U-01 IPSJ (2017).

[2] T. Hamatani, et al. "Exploration of Concentration Sensing Method Combining Various Sensors" (in Japan), *IPSJ SIG Technical Report*, 2025-MBL-77 10 (2015).

[3] S. Kamei, "Estimation of Degree of Concentration Based on Behavior Analysis in Learning" (in Japan), *Graduate School Research Annual Report - Faculty of Science and Engineering,* 45 (2015).

[4] A. Doshi, M.M. Trivedi, "Head and Eye Gaze Dynamics During Visual Attention Shifts in Complex Environments", *Journal of Vision*, **12**(2):9 (2012).

[5] Y, Koshi, "Improving the Accuracy of Driver Drowsiness Grading System using MediaPipe" (in Japan), *Human Interface Society*,-SIG-ACI-31, **25**(2) (2022).

2023 International Symposium on Advanced Technology (ISAT-22)
Tainan City, Taiwan, October 19-20, 2023

Nonhazardous Extraction of Gold from Electronic Waste

Miku Yoshizawa [1,*] and Tomohide Takami [2,*]

[1] Department of Environmental Chemistry and Chemical Engineering, School of Advanced Engineering, Kogakuin University, Tokyo, Japan
[2] Division of Liberal Arts, Center for Promotion of Higher Education, Kogakuin University, Tokyo, Japan

E-mail: s320073@ns.kogakuin.ac.jp, takami@cc.kogakuin.ac.jp

Abstract

Gold is a precious metal with unique properties, and the usual method of recovery involves the use of hazardous aqua regia. Therefore, the development of a safe recovery method of gold without the use of aqua regia is highly anticipated in environmental chemistry. Here, we demonstrate the recovery of gold from electronic waste using alternating current (AC) bipolar electrochemical electrolysis.

A cell phone contains approximately 48 mg of gold, which is equivalent to the amount obtained by mining 52.8 kg of ore [1]. If it were possible to recover gold from all the used mobile phones discarded in Japan each year, it would yield approximately eight billion yen worth of gold [1].

Typically, aqua regia is used in the extraction and recovery of gold [2], which can produce harmful chlorine gas during the recovery process. Furthermore, aqua regia is classified as a hazardous substance under the Poisonous and Deleterious Substances Control Act [3] due to its extremely strong oxidizing properties, which can cause severe chemical burns upon skin contact. On the other hand, our research laboratory has found that the use of alkaline halides or seawater electrolysis can dissolve gold [4]. In this study, we have developed a method to recover gold without the use of hazardous substances such as aqua regia or strong acids.

We performed electrolysis using alternating current bipolar electrodes. Unlike conventional electrodes, which are defined as positive and negative to control current flow, bipolar electrodes take advantage of their close proximity, allowing them to cancel each other out, resulting in highly selective current flow to specific areas [5]. Figure 1 shows a schematic of the apparatus used in this study. Carbon rods were used as electrodes. We used a bidirectional AC generator (GW INSTEK AFG-2005), which is capable of generating various waveforms and amplitudes of electrical signals. The generated AC signal was amplified using a bipolar power supply (NF BP4610), and the amplified 200 Hz and 60 V AC was applied between the carbon electrodes. The applied AC was monitored with a current-voltage meter (ADCMT 7352E). We confirmed that the electrolysis of gold resulted in the generation of tetrachloroauric acid. In addition, when electronic components such as gold-plated crimp terminals and round pins were used as samples and subjected to electrolysis as shown in Fig. 2, it was confirmed that gold was dissolved in the process.

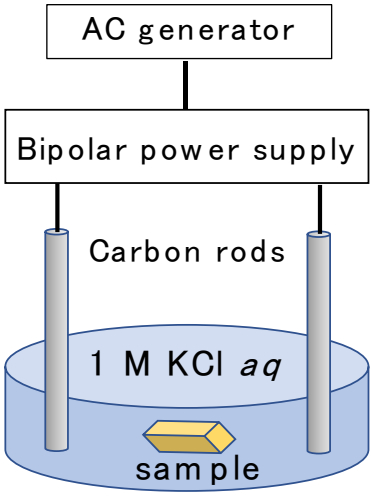

Fig. 1. Schematics of bipolar AC electrolysis apparatus used in this study.

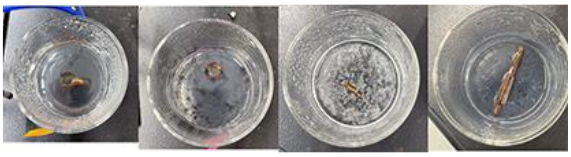

Fig. 2. Various electronic component waste used as samples to extract and recover gold.

However, with the current maximum voltage (60 V) and power (900 W) of the bipolar power supply, it is not possible to apply sufficient potential to the samples to dissolve gold. The process was limited to dissolving approximately 0.1 g of gold from 1 g in 10 minutes. Therefore, the use of a higher voltage and power source would be required to advance this study. In addition, we plan to replace the carbon rods with plates to apply a homogeneous electrical file to the sample.

References:

[1] Ministry of the Environment, Japan, "White Paper on Environment, Material-Cycle Society and Biodiversity" (in Japanese) 2012. https://www.env.go.jp/policy/hakusyo/h24/html/hj12010403.html

[2] R. Sousa, M. J. Regufe, A. Fiúza, M. M. Leite, and A. Futuro, *Extract. Indust. Soc*., **9**, 101018 (2022).

[3] The National Institute of Health Sciences (NIHS), "Poisonous and Deleterious Substances Control Law", http://www.nihs.go.jp/law/ dokugeki/eng_ dokugeki.html (in Japanese)

[4] K. Oya, K. Aoshika, M. Ageishi, H. Magara, S. Ogawa, Y. Takakuwa, and T. Takami, *Chem Lett.*, **50**, 191–194 (2021).

[5] S. E. Fosdick, K. N. Knust, K. Scida, and R. M. Crooks, *Angew. Chem. Int. Ed*., **52**, 10438–10456 (2013).

Enhancing Trust in Human-Machine Collaboration: An Analysis of Contributing Factors to Transportation Accidents

Kazuma Shirakawa and Daigo Misaki*

Department of Mechanical Engineering, Kogakuin University, Japan, Tokyo
E-mail: am22034@g.kogakuin.jp

Abstract

This study investigates human-error accidents in the aviation, railway, and marine sectors, particularly amid increasing automation. Through an analysis of 40 Japanese and 6 Taiwanese cases, we employed text mining to identify recurring accident themes. Our research emphasizes communication barriers between humans and machines, identifying potential trust-building avenues. These findings are crucial for bettering industry-wide collaboration and addressing prevalent issues in human-machine interfaces. Furthermore, the research stresses the importance of considering cultural and linguistic differences in system designs, emphasizing the role of trust in modern human-machine interactions.

Introduction

Examining the factors behind communication errors between humans and machines in human-error-induced accidents can build trust in collaborative settings and autonomous driving environments. This analysis can also shed light on human decision-making traits. Luo et al. utilized text mining to study incident reports from Chinese construction sites, pinpointing a lack of safety training as a critical factor [1]. In contrast, Lee et al. created a system for therapists and AI to engage and decide collaboratively. Their results showcased heightened performance, igniting discussions on the advantages of collaborative human-AI systems in bolstering accurate decisions by leveraging each other's strengths [2]. Moreover, Awad et al. found, through their experiments with the Moral Machine, that cultural nuances shape ethical choices [3]. These studies employ text mining to investigate accident causes, explore human-AI collaborative potentials, and evaluate culture-influenced decision-making.

However, comprehensive research spanning multiple domains and design perspectives on accident causes still needs to be expanded. Contemporary challenges in societies advancing in human-AI collaboration warrant deeper discussions. Understanding how humans depend on various factors and decide in collaborative scenarios with machines and AI is still nascent. Thus, this study seeks to discern accident patterns and variations, considering the potential impact of cultural and societal backdrops on accident causes. We aim to integrate this understanding into reshaping collaborations between humans and machines, emphasizing trust and reliability.

Methods

Our research analyzed 40 accident cases attributed to human error in aviation, railways, and marine transportation, as made public by the Japan Transport Safety Board. We also studied six similar cases from the Taiwan Transportation Safety Board. Utilizing word clouds and co-occurrence networks, we aimed to grasp these incidents' broader picture and context. We further examined commonalities, discrepancies, and contributory factors to these accidents, considering modern societal challenges linked to each cause.

Our approach started with identifying relevant accident cases in aviation, railways, and marine transportation by searching keywords like "human error" and "human factors" on governmental websites. These cases were archived as PDF files on Google Drive, followed by a text analysis conducted using Python. We employed the "word cloud" library post-text extraction to visualize through word clouds. We incorporated libraries compatible with Japanese characters to handle Japanese fonts in the PDFs.

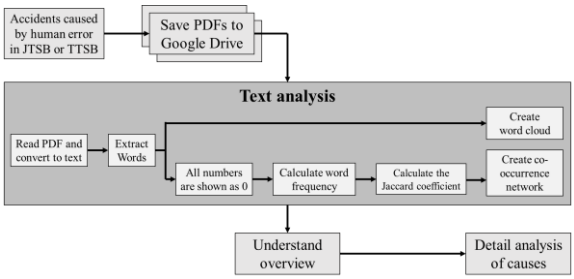

Fig. 1. Workflow diagram for text analysis.

For co-occurrence networks, we structured the extracted terms (number representations were set to zero), gauged word frequencies, computed Jaccard coefficients, and clustered associated terms. The visualizations were crafted using the "networkx" library, tailored to each accident case. We meticulously studied the interrelations between various factors, often not immediately evident in the standalone text, offering insight into intricate interactions between humans and machines. In parallel, we weighed the implications of our findings in the context of prevailing societal challenges. This analysis process is depicted in Figure 1.

Results

Figures 2 and 3 showcase word clouds derived

from JTSB and TTSB accident data, respectively. Meanwhile, Figures 4 and 5 present the co-occurrence networks related to these accidents. A cursory glance at these visuals offers insights into the general landscape and root causes of the casualties.

Within the word clouds, more prominent text elements typically represent facets directly pertinent to the accidents. From the co-occurrence networks, we can ascertain the interrelationships of these facets and their importance in the context of the particular accidents.

From Figure 2, "回転翼航空機" refers to helicopters, and "つり下げ輸送中における物件の落下" signifies the dropping of cargo during transport. In summary, Figure 2 indicates that it is a helicopter accident involving the dropping of cargo.

Figure 4 employs the same accident case as Figure 2. The section enclosed by the red frame in Figure 4 provides a detailed description of the aircraft involved in the accident. The portion enclosed by the blue frame represents the factors contributing to the accident, where "スイッチ" denotes a switch, and "開閉" indicates the act of opening and closing. It is evident that an error in the operation of the switch played a part in the accident's cause. The section enclosed by the black frame primarily outlines areas for future improvement.

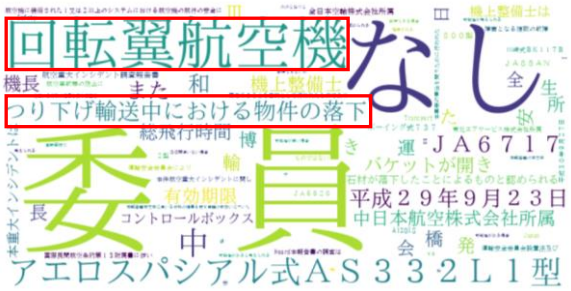

Fig. 2. Word cloud of accident cases in one JTSB (Japan Transport Safety Board) data [4].

Fig. 3. Word cloud of accident cases in one TTSB (Taiwan Transportation Safety Board) data [5].

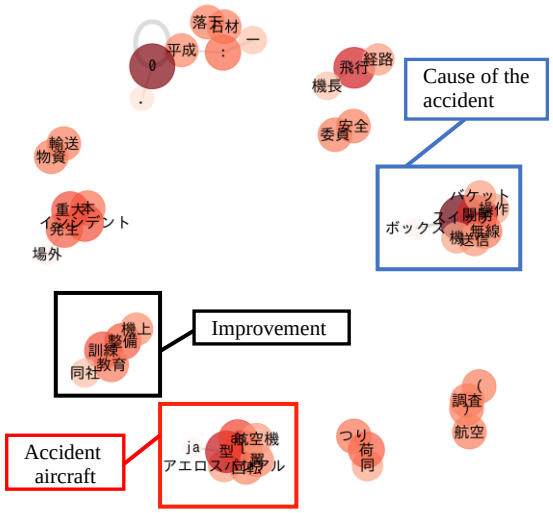

Fig. 4. Co-occurrence network of accident cases in one JTSB data [4].

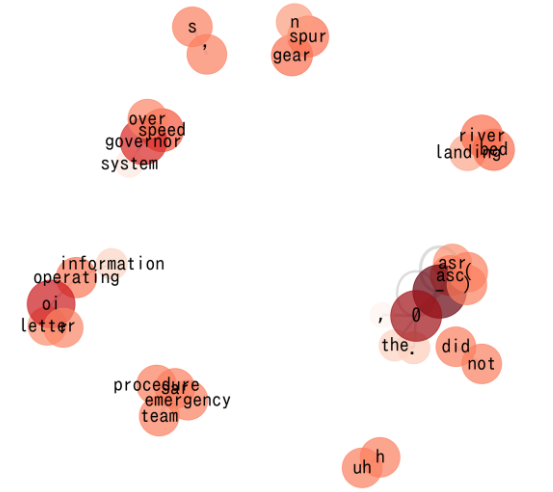

Fig. 5. Co-occurrence network of accident cases in one TTSB data [5].

Discussion

First, First, we discuss the analysis results from the Japanese data (JTSB). In aviation, human communication errors were prevalent. Railway accidents often stemmed from time pressures, whereas marine incidents frequently highlighted an overreliance on past experiences. These distinctions may reflect the varying adoption levels of autonomous technologies across sectors. The aviation industry, characterized by extensive automation, leans heavily on machinery for decisions, which could explain the predominance of human-to-human communication errors over human-to-machine miscommunications.

On the other hand, the marine sector, less enveloped in automation, manifests accidents where human biases and overconfidence are evident. This suggests a more hesitant trust in machinery,

culminating in mistakes grounded in past experiences. Paradoxically, heightened automation in aviation might engender accidents from novice supervisors and inter-human misunderstandings.

Subsequently, we delve into the Taiwanese data (TTSB) results. Notably, numerous errors are traced back to linguistic disparities. When juxtaposed with Japanese cases, the influence of cultural nuances appeared more pronounced in the Taiwanese context. Nevertheless, it's pivotal to acknowledge the data constraints – our analysis hinged on website-available data, which is quantitatively limited. Comprehensive research employing a more expansive dataset is imperative. Figure 6 contrasts the accident causations between JTSB and TTSB datasets.

	Japan(JTSB)	Taiwan(TTSB)
Aviation	**Communication errors between people** are high. (6/16) **Overreliance on experience errors are few.** (1/16)	Mistakes due to **language differences** in the manual. (2/3)
Railway	**There are many mistakes related to time.** (7/8)	Mistakes due to differences in **cultural backgrounds.**
Marine	There are many mistakes **due to attention elsewhere or Overreliance on experience.** (7/13)	Mistakes due to differences in **cultural backgrounds.**

Fig. 6. Typical characteristics from the accident investigation reports by Japan Transport Safety Board (JTSB) and Taiwan Transportation Safety Board (TTSB).

Conclusions

In this study, we conducted a text analysis of accident cases caused by human errors in the aviation, railway, and marine sectors. We examined the characteristics of accident causes specific to each field, their potential connection to contemporary societal issues, and explored the factors contributing to causes that vary by country. Through the analysis of accident cases involving human error using text mining, it has become evident that identifying elements that enhance trust between individuals, as well as between humans and machines, is essential. Furthermore, we believe that in the evolving society, creating systems and environments that take into account cultural and linguistic differences is of paramount importance.

In the future, we will conduct experiments aimed at uncovering elements that enhance reliability in settings involving human-machine collaboration and within the context of autonomous driving, taking into account the characteristics of accident causes resulting from the differences in context identified in this study. Subsequently, we will propose appropriate decision-making approaches for emergencies in a collaborative society with AI.

References:

[1] X. Luo, Q. Liu, Z. Qiu, *Frontiers in Built Environment*(2021).

[2] Lee, M. H., Siewiorek, D. P., Smailagic, A., Bernardino, A., Bermúdez i Badia, S., *Proceedings of the 2021 CHI conference on human factors in computing systems. 2021*., 1-14(2021).

[3] E. Awad, S. Dsouza, R. Kim, J. Henrich, A. Shariff, J. Bonnefon, I. Rahwan, *Nature*, 563(7729), 59-64(2018).

[4] “運輸安全委員会 (Japan Transport Safety Board).” MLIT 国土交通省, www.mlit.go.jp/jtsb/. Accessed 16 Sept. 2023.

[5] Taiwan Transportation Safety Board, www.ttsb.gov.tw/english/. Accessed 12 Sept. 2023.

Demand Forecasting of Bus Ridership in Sightseeing Areas with Considering both Passenger Convenience and Business Profitability

Ibuki.Enomoto, Yoshio.Miki

Kogakuin University of Technology & Engineering, Tokyo, Japan
E-mail: jx20040@ns.kogakuin.ac.jp

Abstract

In this study, we aimed to balance the profitability of the bus business and the convenience of passengers, while complying with Japanese law. To this end, a model of the number of passengers was developed and evaluated.

Introduction

The bus business in Japan is facing a variety of problems, including changing lifestyles, declining ridership due to an aging population, rising fuel prices, and crew shortages. In order to maintain and improve transportation services as public transportation, cooperation with local communities and the use of IT technology are being considered[1]. On the other hand, the financial efficiency of bus businesses often results in a reduction in the number of services and the elimination of routes, thereby compromising convenience for users. In Japan, the Road Transport Law[2] and Passenger Vehicle Transportation Business Law[3] restrict the operation of bus routes, and bus operators are required to operate according to a timetable and cannot freely establish routes and times. In addition, any changes to the operation plan must be notified to the ministry in advance, and crews must be arranged. Therefore, it is difficult to operate according to fluctuations in demand, and this makes the bus business unprofitable.

In this study, demand forecasting is conducted with the aim of achieving both passenger convenience and business profitability. In this study, "both passenger convenience and business profitability" refers to a state in which operating costs are reduced by operating in response to fluctuations in demand, and both supply and demand are in balance. The goal is to enable highly accurate demand forecasting in advance, which will enable appropriate crew arrangements and changes to the operation plan.

Methods

Nishi-Tokyo Bus Co. provided us with several years of boarding and alighting data for each bus stop, which we used as the basis for our demand forecasting. The forecasted areas were Akiruno City, Hinode Town, and Hinohara Village, where there were many natural tourist attractions. These areas had a large number of hikers, and they were characterized by the fact that they used different stops for their outbound and return trips, and that their destinations vary depending on the season. Therefore, current demand forecasting relied on human experience and intuition. The model was created by performing multiple regression analysis based on data such as dates, days of the week, and weather conditions.

Results

The model was created using data from a bus stop in Juurigi, Akiruno City, Tokyo[4], and its validity was verified. Barbecue pits, campgrounds, and hiking trails are scattered around this bus stop[5].

Data from April 1, 2015 to December 31, 2018 were used to create the model, and data from January 1, 2019 to December 31, 2019 were used to validate the model. Note that data from March 24, 2017 to March 31, 2017 were treated as missing values. The model was based on a 14-day moving average of measured data, with corrections based on the day of the week and weather conditions.

The model is shown below.

$$F = Fp + Ec \quad (1)$$

$$Ec = Db * Ev_{-1} \quad (2)$$

$$Ev_{-1} = M_{-1} - Fp_{-1} \quad (3)$$

$$Fp = D + W + Mavg \quad (4)$$

$$W = Ma * \{Max.temp.(℃)\} + Mi * \{Min.temp(℃)\} + P * \{precipitation(mm)\} \quad (5)$$

$$D = \sum_{i=1}^{7} b_i d_i + b_8 d_8 \quad (6)$$

F : Forecasts
Fp : Preliminary forecast
Ec : Error correction value
Db : day-before error coefficient
Ev : Error value
M : Measured value
D : Day-of-week correction value
W : Weather Correction Value
Mavg : 14-day moving average of measured value
Ma : Max. temperature coefficient
Mi : Min. temperature coefficient
P : Precipitation coefficient
b_i: i-th day of the week coefficient.
d_i: If the i-th day of the week applicable, then $d_i = 1$, if not, $d_i = 0$
Monday be the first day of the week, $i = 1$, and thereafter in order, $i = 7$ for Sundays. Also, $i = 8$ for holidays.

Figure 1 and Table 1 below show the verification results.

Table 1. Forecast error per hour

Forecast error per hour	Error (people)
Average	0.9
Maximum	7.4
Minimum	0.0

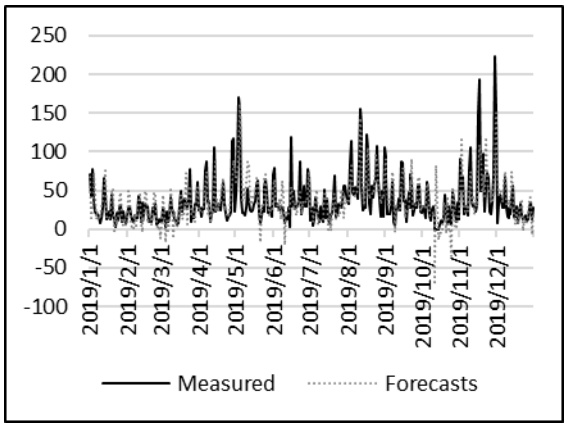

Fig. 1. Comparison of measured and predicted values

The coefficient of determination was $R^2 = 0.5427$. The average forecast error per hour was 0.9 persons.

Regarding the profitability of the bus business, the capacity of a medium-sized bus is 60 passengers[6], and the forecast error is much less than the capacity of it, so we believe that the bus service can be operated appropriately to meet the demand. On the other hand, for passenger convenience, there is room for improvement in the model equation and mechanism, since forecasts may be off on days that differ significantly from the norm, such as major holidays and seasonal events.

Conclusion

In this study, we developed and evaluated a ridership forecasting model to support efficient operation planning, aiming for both user convenience and business profitability.

Demand forecasting in response to seasonal events, application to other stops, and the development of a system that receives real-time demand from passengers on the day of the event and uses this data for forecasting are future research topics.

In addition, It is also necessary to verify whether the use of this demand forecast will lead to a reduction in operating costs.

References:

[1] Nihon Bus Association, “Business Plan for FY2023”, Nihon Bus Association, (Retrieved September 9, 2023, https://www.bus.or.jp)

[2] “The Road Transport Law”, e-Gov Portal, (Retrieved September 13, 2023, https://elaws.e-gov.go.jp)

[3] “Passenger Vehicle Transportation Business Law”, e-Gov Portal, (Retrieved September 13, 2023, https://elaws.e-gov.go.jp)

[4] Nishi-Tokyo Bus Co.,”PDF for printing route map”, Nishi-Tokyo Bus Co., (Retrieved September 12, 2023, https://www.nisitokyobus.co.jp）

[5] Nishi-Tokyo Bus Co.,”Selected Hikes by Nishi-Tokyo Bus”, Nishi-Tokyo Bus Co., (Retrieved September 13, 2023, https://www.nisitokyobus.co.jp)

[6] Hino Motors, Ltd., “Lineup | Hino Blue Ribbon HINO RAINBOW | Hino Motors, Ltd.”, Hino Motors, Ltd., (Retrieved September 13, 2023, https://www.hino.co.jp)

Diversity Experience using the Human Augmentation and impact on Design

First Samu Hong, and Second Daigo Misaki*

Department of Engineering, Kogakuin University of Mechanical Engineering, Tokyo, Japan
E-mail: am22026@ns.kogakuin.ac.jp

Abstract

Human Augmentation research project aims to use technology to enhance human abilities. One of them, research on Supernumerary Robotic Fingers shows that adding a sixth finger to the hand not only improves physical function but also generates a sense of bodily ownership, as if the hand were an integral part of the body. We focus on designers with a novel experience of left-handedness and helps to reduce unconscious biases by promoting an understanding of left-handedness, even among right-handed designers. First, we developed Supernumerary Robotic Finger, and subjects put the Robotic finger on their left hand. In the experiment, Subjects designed products for left-handedness, and the results showed that the group that experienced left-handedness with the robotic finger designed better and also had greater awareness of left-handedness than the group that was given no suggestions. In this study, we discuss experiments on left-handed experiences and left-handed product design using the Supernumerary Robotic Finger.

Introduction

Diversity and Inclusion (D&I) denote endeavors directed towards shaping a society that venerates diversity and integrates disparate values and abilities, thereby engendering innovation and the genesis of novel worth. This vision ensures that each individual assumes an active role and discovers their place.[1] Particular emphasis is allocated to marginalized constituencies, including the LGBTQ community, various ethnicities, and individuals with disabilities. However, numerous products and services are primarily designed with the majority in mind, often leaving minorities bereft of equitable and fair opportunities. This stems from a lack of interest and understanding of minority perspectives. According to a 2021 survey by the Nippon Foundation, prejudice and discrimination against socially marginalized individuals remain pervasive in Japanese society. However, the 2020 Tokyo Paralympics appear to have gradually increased the positive perception of D&I. Therefore, engaging with and fostering understanding of minorities is essential for problem-solving. In this study, we focused on handedness as a readily relatable and easily experiential minority issue for Japanese students and analyzed the design process accordingly. In Japan, it is said that 90% of the population is right-handed, while approximately 10% is left-handed. Human augmentation techniques will be harnessed to scrutinize the left-handed experience and its ramifications on product design.

Human Augmentation

Human Augmentation is technology that can work in harmony with humans in ways that enrich lives, enhance the human experience, and promote sustainable progress for the benefit of people. In recent years, Human Augmentation research extends not only virtual domains, but also the body of reality. Kohei Umezawa's research on Supernumerary Robotic Finger [3] showed that the inclusion of a sixth digit to the hand not only enhances physical functionality but also imparts a profound sense of corporeal ownership, as though the hand were an intrinsic facet of the user's corporeal entity. Body augmentation not only bolsters physiological faculties but also exerts a profound influence on consciousness. Changing consciousness has a huge impact on designers. For instance, "Hand Morph"[4] research shows that exposure to the exoskeleton of a child's hand can modulate perceptions, the objects feel larger. In an experiment aimed at designing a trumpet for children, interaction with a child's hand imbued the designers with increased confidence in their creative process. In this study, we incorporate the left-handedness experience into the design process through the meticulous recreation of the left hand, employing the Supernumerary Robotic Finger as a surrogate mother digit, thereby facilitating the envisioning of the left-handed perspective.

Diversity Experiences

In this study, we propose incorporating minority experiences into the Human-Centered Design (HCD) process. HCD is an approach that focuses on user needs to enhance usability. Situation comprehension is deemed most crucial in HCD. By integrating minority experiences at this stage, we surmise that a deeper understanding of users could be achieved, potentially eliminating inequalities for minorities in products and services. We developed Robotic finger, and another experiment to observe and verify the impact of experiencing different perspectives on design..

Robotic Finger development

I developed Robotic Finger. The robot has one degree of freedom (DOF), and operates with two joints by a servo motor. Made of acrylonitrile butadiene styrene (ABS) plastic. The servo motor employed is the KRS3301 from Kondo Kagaku, whose rotary motion is conveyed to the flexible

component via tensioned wires. M5-StickC is employed to govern the servo motor, inducing a bend of approximately 45 degrees when the integrated bending sensor registers a voltage below 0.7V. The bending sensor is affixed to the thumb and serves as the control mechanism for the robotic finger, eliminating the necessity for conventional grasping movements. The Supernumerary Robotic Finger is affixed to the fifth digit of the right hand, thereby assuming the role of the preeminent mother digit. Positioned upon the ball of the right hand, the Supernumerary Robotic Finger metamorphoses the hand's morphology into an analogous configuration to the left hand, thereby enabling experimental investigations.

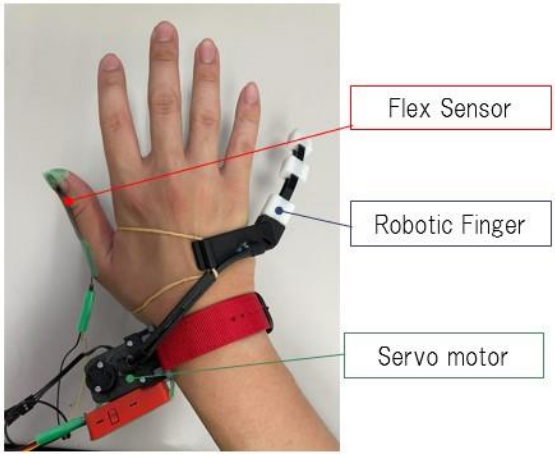

Fig.3. Robotic Finger

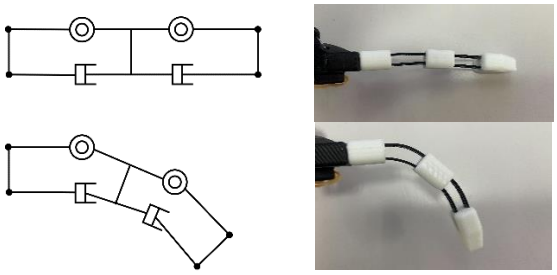

(a)Link Model *(b)Picture*

Fig.4. Robotic Finger mechanism

Experiment

In the course of the experiment, the subjects iteratively reconfigured the calipers: initially without explicit instructions, and subsequently, following a division into three distinct groups. Group1 interacted with the calipers without any prior guidelines (with limited contact during the initial design phase). Group2 was furnished solely with didactic materials in elucidating the concept of left-handedness, while the Group3 leveraged the calipers as didactic tools for expounding the notion of caliper left-handedness. Group3 received the Supernumerary Robotic Finger and was instructed to engage with the calipers as if they were left-handed. Subsequent to each group completing two design iterations, evaluations of the designs and awareness levels were conducted. It was anticipated that the third group employing the Supernumerary Robotic Finger would manifest a more profound understanding of mirror-image motions. The culmination of the study witnessed the administration of a questionnaire to the third group, aimed at ascertaining the appropriateness of the left-handed experiential process facilitated by the Robotic Finger.

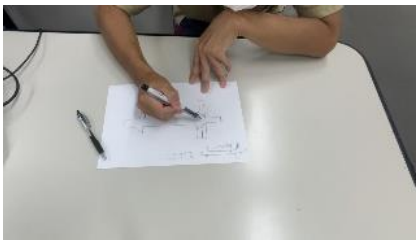

(c)Design step(1st)

(d)Design process step

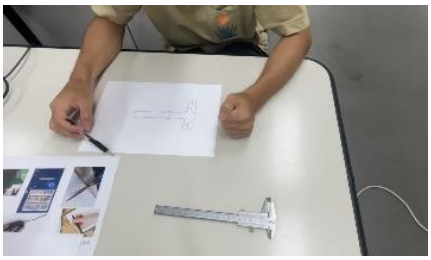

(e)Redesign step(2nd)

Fig.5.Experiment step

Eveluation are three. First, a comparison was made between the first and second designs. Subjects were interviewed and asked what ideas they generated. In particular, groups 2 and 3, which involved left-handers, were asked how they envisioned left-handers using the product.Second, subjects then completed the three questions. The questions used a rubric evaluation. They self-rated their design quality(Q1), confidence in their design(Q2), and awareness of the left-handedness(Q3) on a 4-point scale. Finally, subjects using the robotic finger completed the four questions. Sense of Ownership(Q4), Sence of Agency(Q5)[5], increased physical function(Q6), and left-handedness reproduction(Q7) were rated on a 7-point Likert scale.

Q. The design is best for the user

- ○User-friendly for both left- and right-handedness
- ○User-friendly for left-handedness
- ○User-friendly for left-handedness to use with right hand or both hands, or manage to use it with the left hand
- ○User-friendly for right-handedness only

(f) Q1.Design evaluation question

Q. Feel confident in your own design

○Can present confidently to a large audience (especially left-handed people)

○Can present confidently to groups of several people

○Can present this design only to acquaintances, family members, etc.

○I am not confident in this design

(g) Q2.Confidence question

Q. Conscious of the design of the theme

○During the design process, I was always conscious of the left-handedness use

○When starting the design, I was conscious of the left-handedness use

○I was conscious for myself or any other person to use

○I designed without being conscious of anything

(h)Q3.Conscious question

Q4. Additional fingers feel like my body

Q5.Feel in control of additional finger

Q6.The additional finger helped increase my grip strength

Q7.Feel as if my right-hand became left-hand

(i)Q4-Q7 questions

Fig.6.Questions list

Result and Discussion

Engineering students aged 23-24 years conducted the experiment. Group1 is subjects A and B:using calipers during design. Group2 is subjects C and D:explained about left-handedness with paper documents during design. Group3 is subjects E and F: experience left-handedness with Robot Finger during design. The results of Q1, Q2, and Q3 in Tables 1, 2, and 3;-using rubric ratings on a 4-point scale from 1 to 4, and the results of Q4-Q7 in Table 4 using Likert scales on a 7-point scale from 0 to 6. The larger the number is better the rating.

Table 1.Q1 Result about design evaluation

Q1	Group 1		Group2		Group3	
	A	B	C	D	E	F
1st	1	1	2	2	2	1
2nd	4	1	2	4	4	4

Table 2.Q2 Result about confidence

Q2	Group 1		Group2		Group3	
	A	B	C	D	E	F
1st	2	3	2	3	3	2
2nd	4	2	3	3	4	4

Table 3.Q3 Result about conscious

Q3	Group 1		Group2		Group3	
	A	B	C	D	E	F
1st	2	1	1	4	2	2
2nd	3	2	3	4	4	4

Table 4.Q4-Q7 Result about Robot Finger Impressions

	Q4	Q5	Q6	Q7
E	2	4	2	2
F	4	5	0	5

Q1: Design evaluation, subject B in Group1 is lower than the other groups. In the interview, he said he had forgotten about left-handedness. Subject A noticed that he was left-handed. Subject C in Group2 did not consider using the device with the left hand. It can be seen that Group3 had a large increase in evaluation compared to the other groups and the first time.

Q2: Confidence, Subject C in Group 2 seemed a little less confident, even though he took left-handedness into consideration. Group 3, on the other hand, gave the highest confidence rating.

Q3: Conscious, Groups 2 and 3 showed greater awareness of left-handedness.

Conclusion

Without diversity explanation(Group1) designs exhibited a conspicuous absence of considerations for left-handedness or manifested an insufficiency in addressing such considerations. Conversely, explained about left-handedness with paper documents(Group2) evidenced a profusion of deliberations regarding left-handedness, albeit many of the designs were characterized by unjustness. Experience left-handedness with Robot Finger(Group3) presented a plethora of designs that substantiated their suitability for left-handed users.

Diversity experience or an explanation can change attitudes, the experience may be more concrete in understanding and being closer to minorities. In addition, many of the actual designs for left-handed people were symmetrical, but there was a difference in the number of symmetrical elements between explained group and Robotic Finger group, Robotic finger group having more symmetrical elements. Even when symmetrical, whether or not the orientation of letters and numbers was taken into account did not produce a clear difference in design evaluation.

References:

[1] 2021 “Survey of Attitudes Toward Diversity and Inclusion.”,THE NIPPON FOUNDATION, https://www.nippon-foundation.or.jp/who/news/pr/2021/20211130-64961.html, 15 Sep 2023.

[2] Kurokawa Toshiaki, Design Thinking Education in Universities and Graduate Schools. Research Center for Science and Technology Trends, National Institute of Science and Technology Policy, 2012.

[3] Umezawa, K., Suzuki, Y., Ganesh, G. *et al.* Bodily ownership of an independent supernumerary limb: an exploratory study. *Sci Rep* 12, 2339 (2022).

[4] Nishida, Jun and Matsuda, Soichiro *et al*, Ziwei and Suzuki, Kenji and Lopes, Pedro, HandMorph: A Passive Exoskeleton That Miniaturizes Grasp, 2020, 9781450375146, Association for Computing Machinery, New York, NY, USA,

[5] Braun Niclas, Debener Stefan et al, “The Senses of Agency and Ownership: A Review”, Frontiers in Psychology,vol 9,(2018)
[6] Daigo Misaki, Sam Hong, Miyu Inoue,Analyzing the Effectiveness of Diversity Experiences in the Classroom for Design Education, Extended Abstract of Clive L. Dym Mudd Design Workshop XIII,(2023)

Adapting Design Thinking to engineering education in the Asian context

Daigo Misaki*

Faculty of Engineering Department of Mechanical Systems Engineering, Kogakuin University, Tokyo, Japan
E-mail: misaki@cc.kogakuin.ac.jp

Abstract

In recent years, design thinking has gained traction in educational and corporate environments across Japan and other Asian countries. Beyond traditional engineering product design, its application extends to web services and urban planning. This paper introduces our research on adapting Design Thinking, rooted in Stanford University, to engineering education on the Asian context, factoring in regional cultural nuances.

Introduction

As illustrated in Fig. 1, design thinking offers a holistic approach to problem-solving by seamlessly merging technological and business aspects with a human-focused lens. A multidisciplinary team is crucial to materialize this approach, encompassing experts from fields like design, social science, business, and engineering. This diversity ensures that any specific expertise bias doesn't constrain decisions. The team's core objective becomes the identification and resolution of underlying user needs. This is achieved by harnessing divergent thinking to envision many innovative solutions and convergent thinking to zero in on particular answers.

However, despite its burgeoning popularity, the design thinking approach is not without its criticisms and challenges. Lee Vinsel notably emphasizes the pitfalls in innovation training services stemming from misconceptions about design thinking[1]. One primary concern is the superficial adoption by engineering educators. Viewing design thinking as a panacea or a swift solution is a grave oversight. The characteristics often associated with design thinking in specific cultural hubs, like Silicon Valley's spirited approach, are not its defining elements. Crafting a robust design curriculum goes beyond merely mirroring successful initiatives such as Stanford's d.school and ME310[2]; it demands a deep understanding and customization of the institution's unique ecosystem.

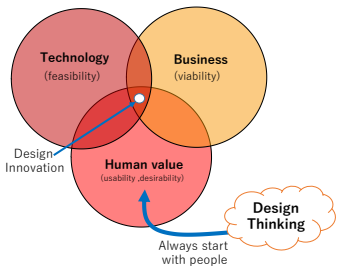

Fig. 1. Human Centered Design

Framework for engineering education with design thinking [3]

The learning framework for design thinking and engineering was proposed by Beckman [4] and Figueiredo [5]. In our study, we applied it to the framework of design thinking-related subjects for the Mechanical Systems Engineering department at Kogakuin University as show in Fig. 2. The vertical axis shows theory and practice. In contrast, the horizontal axis shows science and art. In addition to the conventional framework of design education composed of engineering design lectures, as shown in the right frame of Fig. 1, design thinking lectures were applied, as shown in the lower half. Regarding the design thinking lectures, two subjects, "mechatronics basic exercises" and "design engineering," as well as seminars and graduate courses, were assigned to each area (Design and Production).

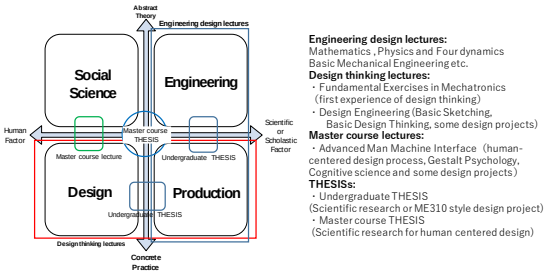

Fig. 2. Proposed framework for engineering education with design thinking

Comparing Creativity in Western and Eastern Cultures

In our study, we particularly emphasize the role of cultural context as shown in Fig.3 when introducing design thinking education, especially within Asian engineering education. A member of our research group has been actively adapting and applying design thinking methodologies to educate engineers and scholars in China [6]. Central to effective design thinking instruction in varying cultural milieus is a profound, empathetic grasp of the cultural nuances spanning from broad societal norms to individual psychological tendencies. Recognizing the characteristics of the Chinese research team, for instance, we portrayed design thinking as a methodical process equipped with a robust toolkit.

Additionally, we developed instructional aids tailored for more reserved Chinese participants. Adapting design thinking to a novel culture extends beyond mere linguistic translations; it necessitates understanding and integrating local cultural values and recalibrating objectives, goals, and specific methodologies to align with that particular cultural framework.

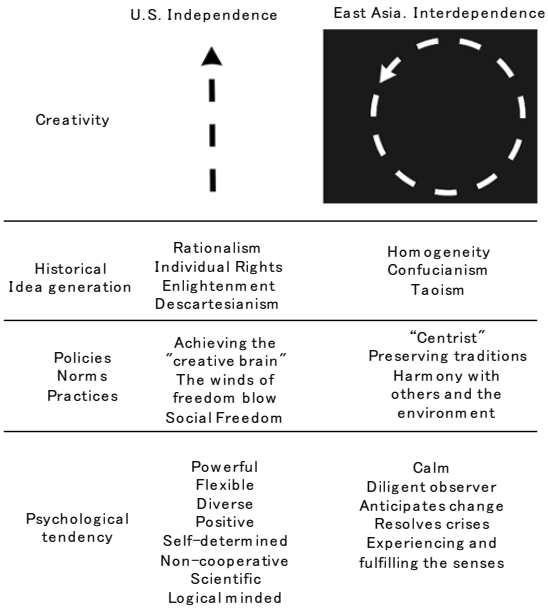

Fig. 3. Comparison of Western and Eastern cultures regarding Creativity [7]

Diverse Experiences in the Classroom for Design Education

The understanding of circumstances through the human-centered design process is an integral part of design education and research proposals. Numerous educational institutions have adopted design thinking education as an effective pedagogical methodology to encourage non-designers to undertake the design process. Various approaches have been used to understand user context, including observations, interviews, and experiential learning. As shown in Figure 4, empathizing with the user's issues (pain points) is a quintessential approach, but students often fail to empathize sufficiently because of an unconscious bias. [8] Design Thinking emphasizes the Human-Centered Design (HCD) process, beginning with empathy for the user. As illustrated in Figure 3, respecting diversity is crucial. While the West showcases creativity by deviating from tradition and embracing change, the East embodies creativity through simplicity and uniformity. We are presently exploring case studies and research to understand how experiences of diversity can benefit design education.

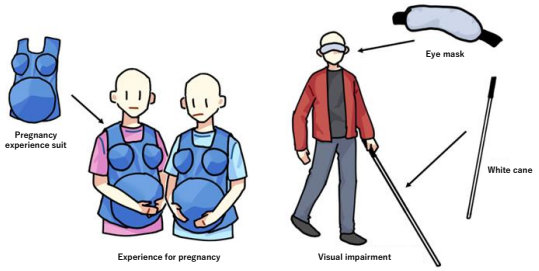

Fig. 4. Diversity Experience for Design

Conclusions

This paper presents a case study on integrating design thinking into engineering education in Asia. It underscores the importance of collaborative efforts in both education and research, firmly rooted in theoretical study. Establishing partnerships with universities participating in ISAT-22 is crucial for advancing our design education initiative.

References:

[1] Vinsel, L. Design Thinking Is a Boondoggle. Retrieved April 22, 2019, from https://www.chronicle.com/article/Design-Thinking-Is-a/243472,(2018)

[2] Carleton, T., and L. Leifer. "Stanford's ME310 course as an evolution of engineering design." Proceedings of the 19th CIRP design conference–Competitive design. Cranfield University Press, 2009.

[3] Daigo Misaki, Akito Sekiguchi and Xiao Ge: Embedding Design Thinking into Traditional Japanese Engineering Design Education, Extended Abstract 05 2019, Clive L. Dym Mudd Design Workshop XI, (2019)

[4] Beckman, Sara L., and Michael Barry. "Innovation as a learning process: Embedding design thinking." California management review 50.1: pp.25-56.(2007)

[5] Figueiredo, Antonio Dias de. "Toward an epistemology of engineering." (2008).

[6] Ge, X. & Maisch, B. Industrial Design Thinking at Siemens Corporate Technology, China. In Design Thinking for Innovation(pp. 165-181). Springer International Publishing. (2016).

[7] DaigoMisaki and Xiao Ge,Design Thinking for Engineering Education"工学教育におけるデザイン思考の活用". July 2019; Journal of the Japan Society for Precision Engineering 85(7):636-639,(in Japanese)

[8] Daigo Misaki, Sam Hong, Miyu Inoue,Analyzing the Effectiveness of Diversity Experiences in the Classroom for Design Education, Extended Abstract of Clive L. Dym Mudd Design Workshop XIII,(2023)

Relation between composition ratio and electrical properties in MgNiZnO films prepared by RF magnetron sputtering

A. Ishikawa[1,*], M. Murayama[1], T. Akiba[1], T. Yamaguchi,[1] T. Honda,[1]
K. Sasaki,[2] A. Kuramata,[2] and T. Onuma[1]

[1] Department of Electrical Engineering and Electronics, Graduate School of Engineering, Kogakuin University, Hachioji, Tokyo, Japan
[2] Novel Crystal Technology, Inc., Sayama, Saitama, Japan
*E-mail: cm22006@g.kogakuin.jp

Abstract

MgNiZnO thin films were deposited by RF magnetron sputtering. All the films were confirmed to show a p-type conductivity. Both MgO and ZnO increased the resistivity, and the resistivity mostly depended on the Ni composition which was determined by the the area ratio of the target.

To realize a decarbonized society, ultra-high volta ge power devices are required. β-gallium oxide (β-Ga $_2O_3$) is attracting attention as a new candidate ultra-wi degap material to replace Si, which is currently the m ainstream material [1]. However, p-type doping is dif ficult to achieve. Integration of ultra-widegap p-type l ayers is essential for further improvements in device performance. We have been focusing on nickel oxide (NiO), which has a rocksalt structure with a bandgap energy of 3.7 eV, and it shows intrinsic p-type condu ctivity. A NiO/β-Ga_2O_3 heterojunction showed excell ent rectifying current-voltage characteristics [2]. Mag nesium oxide (MgO) has a rocksalt structure with a b andgap energy of 7.7 eV, and it is expected to reduce the valence band offset at the NiO/β-Ga_2O_3 interface by alloying with MgO [3]. Zinc oxide (ZnO) has a w urtzite structure, and it showed p-type conductivity b y doping with nitrogen [4]. Behind this background, we have been focusing on MgNiZnO alloys to enhanc e functionality as a new p-type ultra-widegap materia l. In this study, MgZnNiO films were deposited on sa pphire substrates by RF magnetron sputtering, and rel ation between composition ratio and electrical propert ies were clarified.

The films were deposited by RF magnetron sputte ring (Canon-Anelva: L-332-FH) at an ambient temper ature. A 99.9 mol% purity NiO target and substrate h older were set with a distance of 3 cm. The films wer e deposited simultaneously on c-plane sapphire and q uartz substrates at an ambient temperature. To alloy with MgO and ZnO, the NiO target was co-sputtered with 0 to 5 pieces of 10×10 mm^2 square-shaped 99.9 % purity MgO substrates and 0 to 7 pieces of ϕ=10 m m round-shaped 99.99% purity ZnO pellets, which w ere placed on the target. RF power and oxygen flow r ate were fixed at 150 W and 5 sccm, respectively. Sp uttering pressure was fixed at 0.75 Pa. Resistivity ρ w as determined by four-point probe method at room te mperature. Mg, Ni, and Zn compositions were quantif ied by energy dispersive X-ray spectrometry. Carrier type was determined by the Seebeck effect measurem ent.

A total of eighteen samples were prepared, and a relation between numbers of MgO substrates and ZnO pellets and solid-state composition ratios are summaried in Table 1. Configuration diagrams of MgO substrates and ZnO pellets on NiO target are shown in Fig. 1. As shown in Table 1, composition ratio was well controlled by changing in the numbers of substrate and pellet. Resistivites ρ are plotted as a function of Ni composition in MgNiZnO films in Fig. 2. All the films were confirmed to show a p-type conductivity by the Seebeck effect measurement. As shown, the resistivity increased monotonically by alloying with MgO and ZnO. Furthermore, the resistivities in all the series of samples, i.e., MgNiO (MgO: 0, 1, 2, 3, 4, 5, and 6), MgNiZnO (MgO: 0, 1, 3, and 5, ZnO: 3), MgNiZnO (MgO: 0, 1, 3, and 5, ZnO: 5), and MgNiZnO (MgO: 0, 1, 3, and 5, ZnO: 7) increased with almost the same increment rate with the Ni composition. The results suggest that both MgO and ZnO increased the resistivity, and the resistivity mostly depends on the Ni composition, which is determined by the the area ratio of the target.

In summary, MgNiZnO films were deposited on sapphire substrates by RF magnetron sputtering. All the films were confirmed to show a p-type conductivity. Both MgO and ZnO increased the resistivity, and the resistivity mostly depended on the Ni composition which was determined by the the area ratio of the target.

The authors would like to thank Prof. S. Aikawa for his help with the sputtering equipment.

References:

[1] M. Higashiwaki *et al*., Semicond. Sci. Technol. **31**, 034001 (2016).
[2] Y. Kokubun *et al*., Appl. Phys. Express **9**, 091101 (2016).
[3] M. Murayama *et al*., IWGO4, (2022), Pos 1-41.
[4] A. Tsukazaki *et al*., Nature Mater. **4**, 42 (2005).

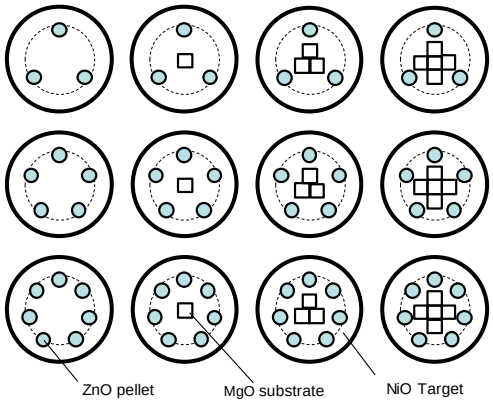

Fig. 1. Configuration diagrams of MgO substrates (squares) and ZnO pellets (circles) on NiO target in MgNiZnO deposition.

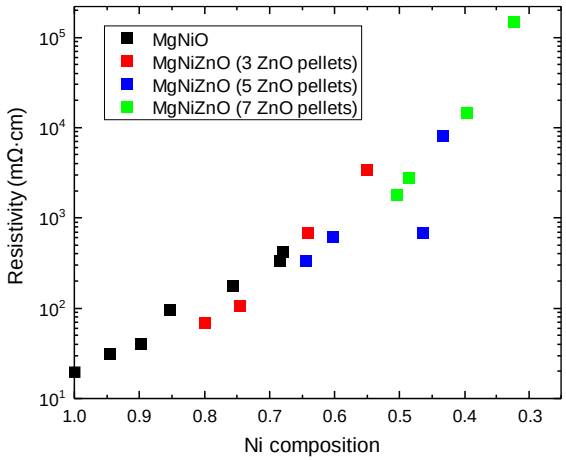

Fig. 2. Resistivities of MgNiO and MgNiZnO films at room temperature as a function of Ni composition.

Table 1. Relation between numbers of MgO substrates and ZnO pellets and composition ratios in MgNiO and MgNiZnO films.

MgO	ZnO	Composition ratio
1	0	$Mg_{0.05}Ni_{0.95}O$
2	0	$Mg_{0.10}Ni_{0.90}O$
3	0	$Mg_{0.15}Ni_{0.85}O$
4	0	$Mg_{0.24}Ni_{0.76}O$
5	0	$Mg_{0.32}Ni_{0.68}O$
6	0	$Mg_{0.32}Ni_{0.68}O$
0	3	$Ni_{0.80}Zn_{0.20}O$
1	3	$Mg_{0.06}Ni_{0.75}Zn_{0.19}O$
3	3	$Mg_{0.18}Ni_{0.64}Zn_{0.18}O$
5	3	$Mg_{0.28}Ni_{0.55}Zn_{0.17}O$
0	5	$Ni_{0.65}Zn_{0.35}O$
1	5	$Mg_{0.05}Ni_{0.60}Zn_{0.35}O$
3	5	$Mg_{0.16}Ni_{0.46}Zn_{0.38}O$
5	5	$Mg_{0.26}Ni_{0.43}Zn_{0.31}O$
0	7	$Ni_{0.50}Zn_{0.50}O$
1	7	$Mg_{0.06}Ni_{0.49}Zn_{0.45}O$
3	7	$Mg_{0.17}Ni_{0.40}Zn_{0.43}O$
5	7	$Mg_{0.27}Ni_{0.32}Zn_{0.41}O$

Optical transitions in rocksalt-structured MgZnO based metal-semiconductor-metal-type VUV sensor

H. Kusaka[1,*], K. Ogawa[1], T. Mitomi[1], K. Kaneko[2], T. Yamaguchi[1], T. Honda[1], S. Fujita[3], and T. Onuma[1]

[1]Department of Electrical Engineering and Electronics,
Graduate School of Engineering, Kogakuin University, Tokyo, Japan
[2] Research Organization of Science and Technology, Ritsumeikan University, Shiga, Japan
[3] Office of Society-Academia Collaboration for Innovation, Kyoto University, Kyoto, Japan
*E-mail: cm22020@ns.kogakuin.ac.jp

Abstract

Photocurrent spectra were measured for rocksalt-structured (RS) MgZnO films to evaluate the optical transitions in the VUV spectral range. The films were grown on (100) MgO substrates by mist chemical vapor deposition method. The responsivities increased around 6.64 eV, 7.16 eV, and 7.24 eV for the films with molar ratios of Mg to Zn source precursors of 90:10, 95:5, and 98:2, respectively. The Mg composition dependency in the photocurrent spectra suggested band conduction of photoexcited carriers.

Rocksalt-structured (RS) MgZnO alloys are good candidates for deep UV and vacuum UV emitters. Their absorption edge has been determined by the transmittance measurements, [1-3] but undesired sub-bandgap absorption in the MgO substrate has prevented the determination in the wavelength range below 190 nm. Therefore, in this study, we measured the photocurrent spectra for the RS-MgZnO films to evaluate the optical transitions in the VUV spectral range.

690 nm, 860 nm, and 1270 nm-thick RS-MgZnO films were grown on (100) MgO substrates by the mist chemical vapor deposition method. The molar ratios of Mg to Zn source precursors were set to 90:10, 95:5, and 98:2. For the photocurrent measurement, a metal-semiconductor-metal (MSM) type photodetector was fabricated by forming a Ni/Ti/Au comb electrode. Photocurrent spectra were measured using a monochromatic light from deuterium lamp. The optical path was purged with nitrogen gas [3,4].

The photocurrent was spectrally divided by the excitation power to extract the photoresponsivity. Figiure 1 shows the responsivity spectra at 300 K. The applied external bias was 10 V. As indicated by the arrows in the figure, the responsivities increases around 6.64 eV, 7.16 eV, and 7.24 eV for the films with [Mg]:[Zn]=90:10, 95:5, and 98:2, respectively. The values are slightly smaller than the previously reported bandgap enegies: 6.9±0.1 eV at x=0.90, 7.4±0.1 eV at x=0.95, and 7.5±0.1 eV at x=0.98 for RS-$Mg_xZn_{1-x}O$ [5]. The results may imply excsitence of a tail state. And. the higher energy shift with increasing the Mg composition may imply band conduction of photoexcited carriers.

In summary, photocurrent spectra were measured for th RS-MgZnO films. The responsivities increases around 6.64 eV, 7.16 eV, and 7.24 eV for the films with [Mg]:[Zn]=90:10, 95:5, and 98:2, respectively. The Mg composition dependency in the photocurrent spectra suggested band conduction of photoexcited carriers.

This work was supported, in part, by Grants-in-Aid for Scientific Research Nos. 20H00246 and 22K04952 from MEXT, Japan.

References:

[1] T. Onuma *et al.*, Appl. Phys. Lett. **113**, 061903 (2018). [2] M. Ono *et al.*, J. Appl. Phys. **125**, 225108 (2019). [3] T. Onuma *et al.*, J. Appl. Phys. **134**, 025102 (2023). [4] T. Onuma *et al.*, Appl. Phys. Lett. **119**, 132105 (2021). [5] T. Takeuchi *et al.*, J. Appl. Phys. **94**, 7336 (2003).

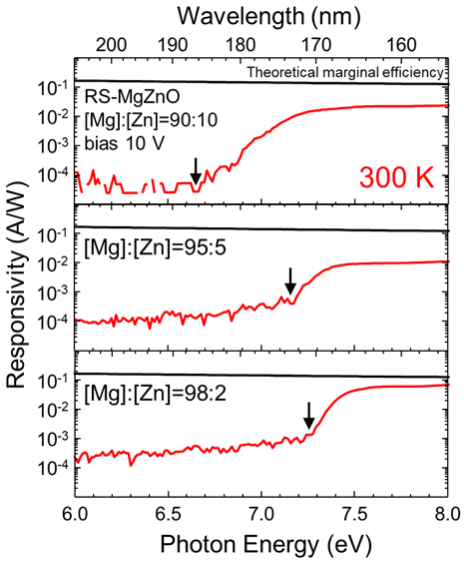

Fig. 1. Responsivity spectra of RS-MgZnO with [Mg]:[Zn] of 90:10, 95:5 and 98:2 at

Positive Preparation and Electrochemical Characterization Containing Highly-Concentrated Electrolyte for High Performance Clay-Type All-Solid-State Batteries.

Keigo Suzuki, Takaaki Ichikawa, Rintaro Mogi and Shiro Seki

Department of School of Advanced Engineering, Kogakuin University, Tokyo, Japan
E-mail: s320204@g.kogakuin.jp

Abstract

Clay-type all-solid-state batteries are expected to simplify the process, improve battery safety, energy density and battery longevity characteristics. In this study, a clay-type all-solid-state battery composed with a high-concentration electrolyte was fabricated and evaluated to constant-current charge-discharge tests, and the results of electrochemical characterization were presented. Clay-type all-solid-state batteries were successfully fabricated, however, further improvements are required, such as optimizing battery fabrication methods and material composition ratios.

In recent years, high-concentration electrolytes, in which the concentration of lithium salts is higher than that of conventional electrolytes, have been reported as one way to improve the performance of lithium-ion batteries[1]. High concentrations of electrolyte have been reported to improve thermal stability and significantly extend the effective potential window. Ensuring safety is an extremely important issue for the future improvement of lithium-ion batteries to larger sizes and application fields. However, lithium-ion batteries are obtaine organic solvents, which may cause ignition due to leakage. Clay-type all-solid-state batteries are attracting attention new battery systems. Clay-type all-solid-state batteries are characterized by simplification of the process and thicker electrode film layer, which are expected to improve battery safety, energy density, battery life and other properties. In this study, fabrication process of a clay-type all-solid-state battery were investigated with high-performance lithium-ion conductive path formation by using a highly concentrated electrolyte with a high lithium-ion transporter number, and the electrochemical properties were also evaluated.

All experiments were conducted in a glow box under an inert Ar atmosphere. Electrode clays were prepared for the positive electrode by mixing $LiFePO_4$ and AB, LiTFSA and EC in a composition ratio of 1:4 (58.7:3.9:37.4 (wt%), respectively. The prepared electrode clay was spread onto Al foil to prepare a positive electrode sheet, which was then punched into ϕ16. LiTFSA+4EC electrolyte and polyether macromonomer (P(EO/PO)) were mixed at 80:20 (wt%), photo-crosslinking initiator DMPA was added, heated and stirred at 313K. The resulting solution was adjusted to a thickness of 1 mm between glass plates and UV irradiated for 5 min to produce a solid electrolyte membrane. A coin cell was prepared using the prepared electrode and solid electrolyte membrane and Li as the negative electrode, and constant current charge-discharge tests were conducted at 303K, C-rate 0.05, theoretical capacity 170 mAh g^{-1}, upper voltage limit 3.5 V, current value 349 μA cm^{-2} for apparent electrode area 2.01 cm^{-2} and active material weight 41.1 mg cm^{-2} respectively.

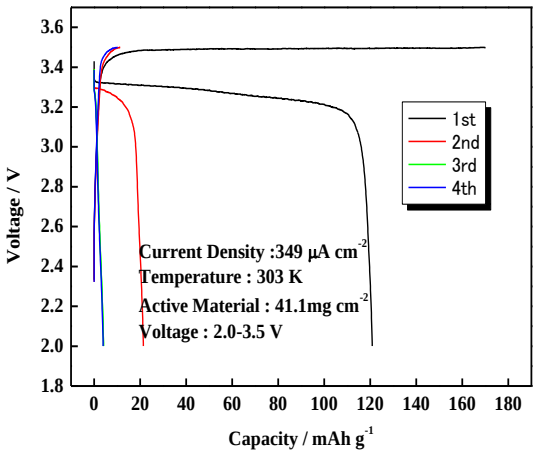

Fig. 1 Charge-discharge curve of clay-type all solid state batteries

Fig. 1 shows the charge-discharge profile of the fabricated clay-type all-solid-state battery. Compared to the theoretical capacity of 170 mAh g^{-1}, sufficient discharge capacity of 120 mAh g^{-1} was observed only first cycle and the calculated coulombic efficiency was approximately 71%. In addition, from the second cycle onwards, the favolable charge-discharge profiles were not obtained compared with the case of first cycle. In this case, upper voltage limit was set at 3.5 V, and the cell could easily approach the upper voltage accroding to the resistance increase. Proposed composition of LiFePO4, AB and LiTFSA+4EC electrolyte enabled to the sufficient clay for positive electrode. In conclusion, prepared clay-type all-solid-state batteries operated the basically charge-discharge behavior. In presentation, we will detained results for various preparation conditions.

Reference:

[1] Y. Yamada, A. Yamada,
J.Electrochem.Soc.,162(14), A2406-A2423 (2015).

2023 International Symposium on Advanced Technology (ISAT-22)
Tainan City, Taiwan, October 19-20, 2023

An Objective Method to Compare CT Data of Normal and Malformed Cochlea

Yuta Miura[1], Taku Ito[2], Takeshi Tsutsumi[2], and Yutaka Fukuoka[1]

[1]Department of Electrical and Electronic Engineering, Kogakuin University, Tokyo, Japan
[2]Department of Otolaryngology, Tokyo Medical and Dental University, Tokyo, Japan
E-mail: cm23065@g.kogakuin.jp, fukuoka@cc.kogakuin.ac.jp

Abstract

Pendred syndrome is caused by SLC26A4 gene mutation, and it is reported that about 80% of cases have enlarged vestibular canal. However, the exact structure of the cochlea malformation of a Pendred syndrome patient has not been determined. In this study, we proposed a method to compare normal and malformed cochlea structures in a plane determined using anatomical structures. We then applied the proposed method to cochlea images obtained from a genetically engineered model mouse of Pendred syndrome and a wild type mouse. The measured area of the vestibular canal in the genetically engineered mouse was about 1.7 times larger than that in the wild type.

Pendred syndrome, whose symptoms include bilateral hearing loss and recurrent dizziness, is caused by SLC26A4 gene mutation, and it is often reported that about 80% of cases have enlarged vestibular canal in the inner ear and Mondini type malformation in the cochlea [1]. However, the exact structure of the cochlea malformation of a Pendred syndrome patient and its mechanism have not yet been elucidated. Hence, the authors aim to develop an analysis method of cochlea structure. As a first step, we proposed a method to compare normal and malformed cochlea structures in a plane determined using anatomical structures.

Using a micro-CT, cochlea images were obtained from a genetically engineered model mouse of Pendred syndrome and a wild type mouse. Then, the 3 dimensional structure of the cochlea in each mouse was manually extracted using Image-J. After Li method was applied for binarization of the images, the center of gravity in each binarized image was determined. Based on the centers of gravity of the images in each mouse, an approximate line was identified using the primary component analysis [2]. Another anatomical structure, the head of stapes, was used to determine a plane. The cochlea structure on the plane was compared in the genetically engineered mouse and the wild type. Finally, the area of scala vestibuli and cochlear duct was determined using polygonal approximation. The approximation was carried out five times using different initial values because the result might be influenced by the initial value.

Figure 1 illustrates the cochlea structure in the genetically engineered mouse whereas Fig. 2 illustrates the cochlea structure in the wild type. In each figure, (a) and (b) show results by the polygonal approximation with different initial values. As shown in Figs. 1 and 2, the scala vestibuli and cochlear duct (blue area) in the genetically engineered mouse was enlarged. The blue area was chosen for analysis because it was markedly different for both mice. When comparing (a) and (b) in each figure, the blue areas had slightly different values depending on the initial values.

Table 1 compares the average number of pixels in the blue areas for both mice at the five different initial values. As shown in the table, the area in the malformed cochlea (genetically engineered mouse) was about 1.7 times larger than that in the wild type. The standard deviation over the five trials was about 130 pixels in both mice, indicating that the results from the polygonal approximation varied depending on the initial values.

The results in Figs. 1 and 2 and Table 1 demonstrate that the proposed method is promising for analyzing the structure of malformed and normal cochlea. In particular, the plane determined using the anatomical features was useful to compare the corresponding structures (scala vestibuli and cochlear duct in this study) in both mice. If an inadequate plane (for example, a plane determined without anatomical features) is used for analysis, a direct comparison between the resultant cross sections could be impossible.

There exist some rooms for further improvement of the proposed method. First, the polygonal approximation should be more accurate because the determined polygonal in Figs. 1 and 2 indicated that there were some errors on the boundary regions. As noted above, the initial value in the polygonal approximation has significant influence on the accuracy. In addition, some parameters such as the number of vertices and the maximum internal angle are used for the polygonal approximation. In this paper, the parameters were determined through a try and error process. An automatic method to determine the parameters and the initial value is desirable.

In the future, we are planning to develop a method which can analyze structural differences in three dimensions between the Mondini-type malformation and the wild type cochlea to elucidate the pathophysiology of the malformation.

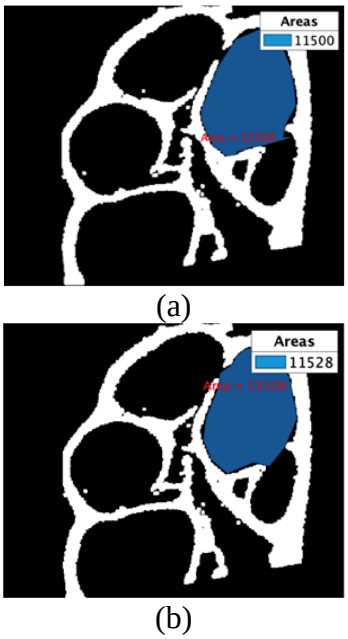

(a)

(b)

Fig. 1. Cochlea structure of the genetically engineered mouse. (a) and (b) show results obtained with different initial values.

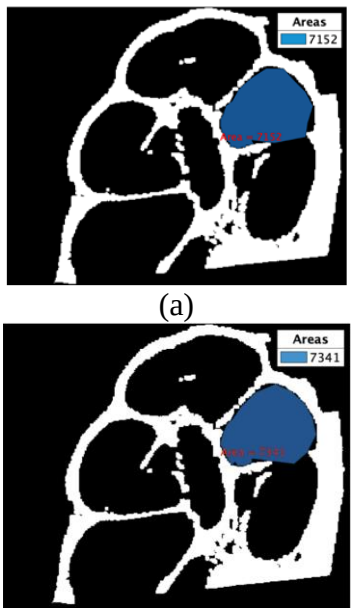

(a)

(b)

Fig. 2. Cochlea structure of the wild type mouse. (a) and (b) show results obtained with different initial values.

Table 1. Average area of the scala vestibuli and cochlear duct in both mice over the five different initial values.

	Genetically engineered	**Wild type**
Area (#pixels)	12599.9±136.3	7364.2±124.9

References:

[1] L. Sennaroglu, I Saatci, *Laryngoscope*, **112**, 2230−2241 (2002).

[2] H. Akatsuka, J. Hara, H. Watanabe, *IPSJ SIG Tech Report*, **AVM104**, #3 (2019) (in Japanese).

Evaluation Methods for Learning Attitude Using Head Sway Assessment System

Hiroki Horiuchi*1 *2 and Hisaya Tanaka*1

*1 Graduate School of Kogakuin University, Tokyo, Japan
*2 Kanagawa Prefectural Yokohama Shuyukan High School, Kanagawa, Japan
E-mail: ed22001@ns.kogakuin.ac.jp

Abstract

We propose a system for the quantitative evaluation of the proactive attitude toward learning by evaluating students' concentration using biometric data. Verification was performed on both the system evaluation based on Head Sway and the teacher evaluation based on videos of students' efforts during learning. The agreement rate between the system and teacher evaluation was 50.0%, and the difference in evaluation within ±1 range was 85.7%. This indicates that 85.7% of the students were evaluated at the same level as teachers' evaluations of students' learning based on close observation.

1. Introduction

During class, teachers cannot see every student in the classroom. However, teachers must evaluate all students. Japan's MEXT has stated that one of the evaluation perspectives is to assess the "Proactive attitude toward learning" [1]. The attitude toward learning tends to be a subjective assessment by teachers. The appropriate evaluation of students is to fairly and quantitatively assess students whom teachers have not seen. Quantitative evaluation reduces the teachers' amount of evaluation work, which in turn leads to a change in the way they work. If students can visualize their own efforts, they can reflect on their learning methods and adjust their learning [2]. To solve these issues quantitatively, our research focuses on biometric data [3]. Our research has utilized blink rate and Head Sway to calculate system ratings of "Proactive attitude toward learning" [4][5]. The number of students who agreed with the teachers' ratings was 40.91%, and 95.45% were within the ±1 rating difference ratings <1 rating, which means that many students could give a system rating within a satisfactory range. However, only one school model is represented by these results. This study examined whether our evaluation model could be implemented in additional schools. The results showed that 50.0% of the students agreed with the assessment of the system and 85.7% of the students fell within the ±1 range. This suggests that the system can be used in different schools.

2. Grade Evaluation by Head Sway

Head movement was measured by a gyro sensor on the EEG instrument. The evaluation was based not on a "comfortable posture" but on a "posture that enables sustained learning" To ensure that the evaluation takes into account actual learning situations, thresholds for posture evaluation have been set based on posture demonstrations by five current high school teachers [5]. The evaluations are calculated on a 5-grade evaluation scale and verified by comparison with the teachers' evaluations. Trends in Head Sway are investigated for each rating, and representative data are shown in Figure 1: Grade 4 and Grade 3 have less movement, while Grade 4 and Grade 4 have more movement; Grade 5 has more movement, and Grade 4 and Grade 3 have more movement; Grade 4 and Grade 4 have more movement, and Grade 4 and Grade 4 have more movement; Grade 4 and Grade 3 have less movement, while Grade 4 and Grade 4 have more movement; and Grade 4 and Grade 4 have more movement, and Grade 4 and Grade 4 have more movement.

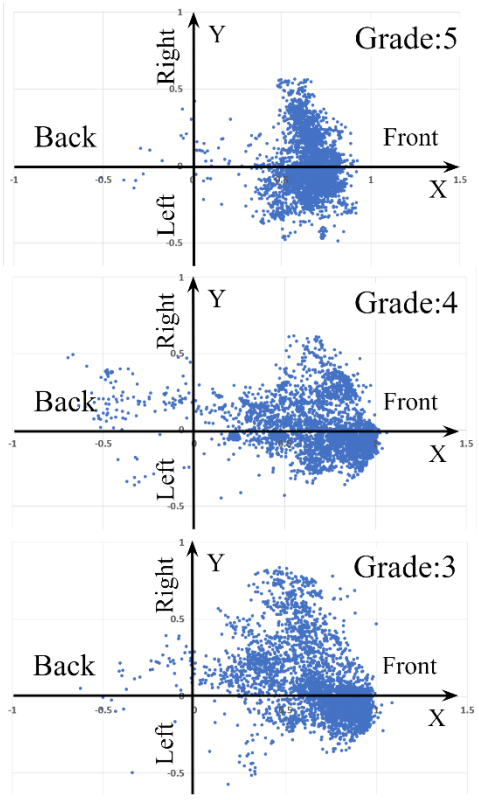

Fig 1 Trends in head movement by learning evaluation (Grade 5: Excellent , Grade 4: Great , Grade 3: Good , Grade 2: Poor , Grade 1: Unsatisfactory)

3.Experiment Environment

The experiment was carried out in Kanagawa, Japan, with 16 secondary school students (14 of whom had valid data). The experiment was conducted in accordance with "Biometric Measurements for Quantitative Learning Attitude Assessment (2022-A-26)" a research ethics review for human subjects at Kogakuin University. The equipment used was Good Brain's Muse2 as an EEG measuring device and the smartphone application "Mind Monitor" as an application that outputs the Muse2's biometric data in CSV format.

The work task was the same for all participants. Participants were asked to solve 600 elementary school-level arithmetic problems on "KeisanMondai.com" for 20 minutes.

The video was taken while the students worked on the tasks(Fig 2). The students were filmed from the side and the teachers evaluated their attitude toward the task after the experiment was completed.

Fig 2 A portion of the experiment. Even when the teacher is not looking, evaluations are conducted

4. System Evaluation and Teacher Evaluation

The attitudes of the students toward learning using the system developed in this study were evaluated on a 5-point scale. Figure 3 depicts a schematic representation of this system.

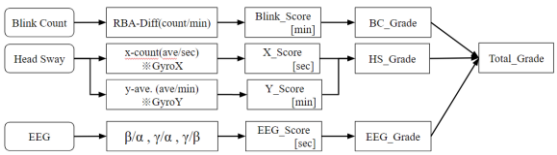

Fig. 3 Overall diagram of the evaluation method of this system

We compared the video of this experiment to the five-point rating visually assessed by the teacher. The rate of agreement between system evaluation and teacher evaluation was 50.0%, and the difference in evaluation within ±1 was 85.7% (Table 1).

Table 1 Differences between the evaluation of the system based on head movement and the evaluation of the teacher based on video

[Head Sway] Video evaluation	Teacher/System Evaluation Difference ±0 match					50.0%
	Teacher/System Evaluation Difference within ±1					85.7%
	System Evaluation(SE)					
Grade		1	2	3	4	5
Teacher Evaluation (TE)	1	0	0	0	0	0
	2	0	0	0	0	0
	3	0	0	0	0	0
	4	0	0	0	1	3
	5	0	0	2	2	6

5. Conclusion

This system is a quantitative evaluation of "Proactive attitude toward learning" in Japan, and it was developed at a high school other than the one that assisted us with this experiment. In this experiment, 85.7% of students fell within the 1 range of the system evaluation and teacher evaluation, so it is possible to objectively determine whether students are making progress in their self-study even without the help of teachers. This provides a quantitative and fair indicator to assess learning during self-study time and long vacations. Additionally, it was suggested that the indicator could be utilized in various schools.

References:

[1] Ministry of Education, Culture, Sports, Science and Technology, Japan. About the ideal form of learning evaluation. 2015. https://www.mext.go.jp/b_menu/shingi/chukyo/chukyo3/siryo/attach/1364317.htm (Accessed September 14, 2023)

[2] Ministry of Education, Culture, Sports, Science and Technology, Japan. Qualities and abilities that we aim to develop, as well as optimal individual learning and collaborative learning. https://www.mext.go.jp/a_menu/shotou/new-cs/senseiouen/mext_01491.html (Accessed September 14, 2023)

[3] Objective assessment of self-Study attitude of high school students using bio-signal measurement - Relationship between blinking and learning contents-, Hiroki Horiuchi, Hisaya Tanaka, AROB 28th 2023 8th International Symposium on BioComplexity, OS13-3

[4] Concentration evaluation based on blinks of eyes, Hiroki Horiuchi, Hisaya Tanaka, ISASE 2023, PM-2B, C000020ET

[5] Using biometric technology objective evaluation of self-study attitude of high school students - Relationship between Head Sway and Learning Content, Hiroki Horiuchi, Hisaya Tanaka, ET2022-80

A proposal of a method to get recommendations for unknown different fields from known preference information

Ami. Ehara, Yoshio. Miki
Kogakuin University of Technology and Engineering
E-mail: j320402@g.kogakuin.jp

Abstract

We examined the basic technology for a service that analyzes user's preferences based on their action history and matches their input information with their preferences in other fields that we don't own, thereby clarifying user's preferences between different fields and reading out appropriate recommendations to them. In terms of popularity, we considered that the rankings in which popularity increases with popularity in the power-law distribution have similar structures among the top ranked items in each field and that they are related to each other even if they are in different fields. So, we expressed the preference trends between different fields from the data of a confectionery specialty store and Tokyo Disneyland and confirmed whether the preference trends in different fields follow a power-law distribution.

1. Introduction

Recently, Recommendation systems that provide appropriate recommendations as a service by reading customers consumption behavior and action history such as route search are becoming common. However, not all information in the world is publicly available and there are many cases in which the information needed to make recommendations such as the user's attributes, action history and product information [1] isn't in the public domain. In this research, we propose a method that analyzes user's preferences based on their action history and associates their input information and their preferences in other fields that we don't own, thereby clarifying user's preferences between different fields and reading out appropriate recommendations to them. This IT service will make it possible to provide recommendations even in fields where we don't have the user's information.

2. Method and Discussion

In the method of this research, we think that recommendations on how to use attractions of Tokyo Disneyland, for which we have some understanding of preference patterns ourselves, should be determined based on customer behavior that can be extracted from the ID-POS data of a confectionery specialty store stored in our laboratory.

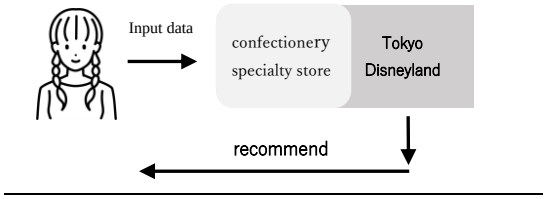

Fig. 1 System chart

2.1.1 Background of the occurrences of power-law distribution

It is empirically described that product sales ranking and national income have a Pareto distribution, which is a kind of power-law distribution [2]. The Pareto distribution has almost the same shape even in different fields, so it isn't just a law discovered by experience, but it implies that some mathematical model is hidden behind the distribution. In fact, there are some models that have defined the mechanism by which power-law distribution is produced. For example, the BA algorithm is a mechanism where more branches are concentrated at nodes with the large number of branches and the probability of adding a branch to the BA algorithm is proportional to the number of branches already connected. Consequently, the number of branches at the final node is power-law distribution and the popular ones are expected to be popular. In this popularity perspective, it could be considered that the rankings in which popularity increases with popularity in the power-law distribution, there is a similar mechanism between the top ranked items in each field and these items are related to each other even if they are in different fields.

2.1.2 How to determine the power-law distribution

The mathematical basic form of power-law distribution is expressed as "$y = bx^{-a}$". Taking the logarithm of both sides of the above equation, "$\log y = -a\log x + \log b$", double logarithmic chart are straight downward slopes and the power exponent is the inclination [3].

2.2 Expression of preference trends

The ID-POS data is used to calculate the weight of preference which is the connection between products for a customer and the products that are commonly preferred by many customers are aggregated as purchasing trends. If both the preference of a

confectionery specialty store and the preference of the field to be recommended are scale-free like the BA model, they will have the same shape. By mapping the nodes of these graphs in the order of the number of connected branches, it would be possible to match the preference trends of different fields. The subjective preference patterns for Tokyo Disneyland in this research were obtained from the attraction's wait time data of randomly selected from July 23, 2023 to August 30, 2023. Attractions with longer wait times have the ability to pull in more customers and means that the number of connected branches in the graph is higher.

3. Results and Discussion

These histograms represent the connections between products for a given customer based on ID-POS data from a confectionery specialty store and the average waiting time for each attraction from the data of them. In Figure 2 and 3, the curves show a gently growing base toward a larger value on horizontal axis. In the first class in Figure 2, there are about 1,600,000 frequencies and the number of frequencies decreases rapidly in the subsequent class. This suggests that the distribution of data is highly biased and that a large amount of data is concentrated in the first class.

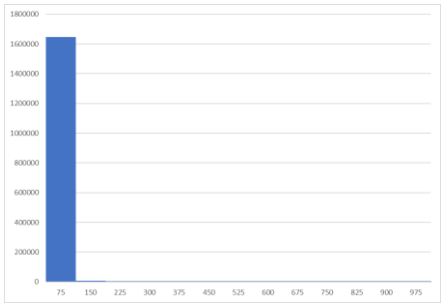

Fig. 2 Histogram of a Confectionery Specialty store

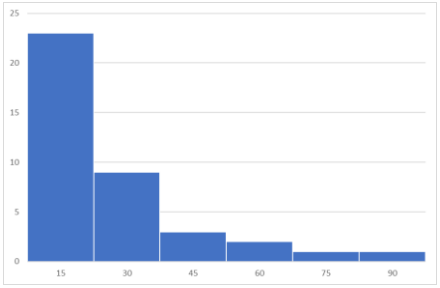

Fig. 3 Histogram of waiting times for attractions

Figure 4 and 5 are double logarithmic charts of the histograms of Figure 2 and 3. It could be read that the distributions of both are almost linear. It was found that the popularity of the products of a confectionery specialty store and the popularity of the attractions of Tokyo Disneyland respectively follow a power-law distribution. It is highly possible to associate the preference trends in different fields with each other like a confectionery specialty store and Tokyo Disneyland.

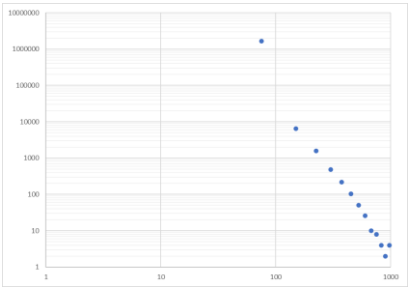

Fig. 4 Double logarithmic graph of a confectionery specialty store

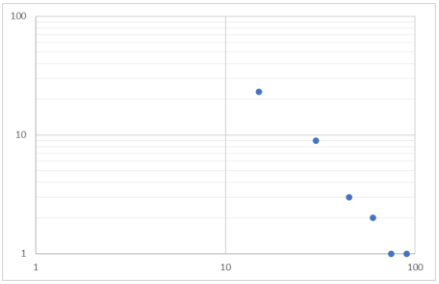

Fig. 5 Double logarithmic graph of waiting times for attractions

Table 1 shows the product names of a confectionery specialty store and the names of the attractions in Tokyo Disneyland in order of the number of connected branches, namely, their popularity. It means that users who purchased "strawberry shortcake" at a confectionery specialty store should be recommended the attraction "Enchanted Tale of Beauty and the Beast" at Tokyo Disneyland and users who bought "Japanese chestnut Mont Blanc" should be suggested "Splash Mountain".

Table 1 Most popular in each field(ascending)

Product Name	Attraction's Name
strawberry shortcake	Enchanted Tale of Beauty and the Beast
Japanese chestnut Mont Blanc	Splash Mountain
escargot（single）	The Happy Ride with Baymax

4. Conclusions

In this research, we analyzed the preferences of users of a confectionery specialty store by analyzing their spending behavior and compared them with the preferences of Tokyo Disneyland's attractions for which we don't have data from the users directly. By doing so, we proposed a method to get recommendations for unknown different fields from known preference information. In terms of popularity, we believe that there is a similar mechanism between the top ranks of each field in the power-law distribution and that they are related to each other even if they are in different categories. We focused on the similarities of the distribution and hypothesized that the ranking of major tastes and preferences in different fields would be approximately the same. We found that both the preference for products of a confectionery specialty store and the preference for attractions at Tokyo Disneyland have a power-law distribution and that these preference trends could be matched. If it is possible to correlate the preferences of different fields, it would be possible to provide recommendation even when user's direct information isn't available. To confirm the validity of the above, we would like to conduct a large number of questionnaires that ask about both preferences.

At this time, the method is simple: it is recommended if the same rank is obtained at the method level. However, it is necessary to examine the necessity of changing the recommendation depending on the shape of the distribution.

References:

[1] "What is a recommendation engine? Easy-to-understand explanation of its definition, how to make it, and how to choose it". Kyozon. 2023/08/02. (https://kyozon.net/list/what-is-recommendation-engine/)

[2] "Explaining the Pareto principle using familiar examples! Introducing actual usage, precautions, and recommended books". makeshop. 2023/08/07. (https://www.makeshop.jp/main/know-how/knowledge/pareto.html)

[3] Umeno Yoshio. "The Feature and Mathematical Principle of the Powerlaw Distribution", "Transactions of mathematical education for Kosen and University Vol.26 No.1",2020/3,76

Forming and Mechanical Properties of Thin Porous Metals

Haruto Tada* and Masanori Shiomi

Graduate School of Engineering, Kogakuin University, Tokyo, Japan
E-mail: am22040@ns.kogakuin.ac.jp

Abstract

In order to enhance the porous metals for applications in sports and leisure, fabrication processes of thin porous metals by the powder metallurgy route are considered. The solid skin layer on the surface of the thin porous metals or a sandwich structure with thin solid sheets could be a key point to maintain the strength.

Introduction

Porous metals have many pores inside and are expected to be used for the functional applications such as shock absorbers, heat exchangers and sound insulations because of their mechanical, thermal and sound properties [1]. Blocks and round bars of porous metals are practically produced, and then complicated shapes of porous metals are formed through secondary processing. In order to enhance the porous metals for the wide applications in sports and leisure, a simple fabricating process of thin parts like a gear is desirable. In this paper, forming of thin porous metals is conducted.

Fabrication of porous metals

Manufacturing processes of porous metals are basically divided into two processes: melt route and powder metallurgy route [2]. In the melt route, gas or a foaming agent such as TiH_2 is added into the molten metal to make pores, and the blocks of the porous metals are fabricated after cooling. It is suitable for the mass production of porous metals of large-sized blocks. However, porous metals of thin-plate shapes are made by secondary processing, such as machining, which is a more time-consuming and expensive process.

In the powder metallurgy route, powder mixture of metal and foaming agent is compacted into the solid, and then the foamable solid is heated and foamed in a furnace to become porous metals. Another process of this route is that metal powder is mixed with space holder for making pores instead of a foaming agent and compacted into the solid. The compacted solid including space holder is sintered in a furnace, and then the space holder is removed from the sintered solid so as to be porous form. The powder metallurgy route can be used to make complicated shapes by using dies.

To fabricate thin porous metals, in this paper, two processes are considered. One process is that metal powder mixed with NaCl powder as a space holder is compacted with dies to form a thin sheet and sintered in a furnace. The NaCl powder is removed from the sintered sheet. It is suitable to control the shape and size of porous metals. The other process is that metal powder is mixed with a foaming agent and formed a thin sheet by compaction. The compacted sheet is heated and foamed to be porous. It is preferable to keep the strength of the thin porous metals because solid skin layer is formed on the surface which tends to be stronger than porous form.

Properties of porous metals

The drawback of porous metals is the reduction of strength, because lightweight and strength are in a trade-off relationship. Thin components are often subjected to bending loads. The load in three-point bending test of porous aluminum is shown in Fig. 1 as an example. The bending load increases at first and gradually decreases after the peak with the increase of stroke. The maximum stress at fracture is less than 1 MPa, which is much lower than that of the solid state. To maintain the strength of porous metals, it is preferable to form a solid skin layer on the surface or to use a sandwich structure with thin solid sheets.

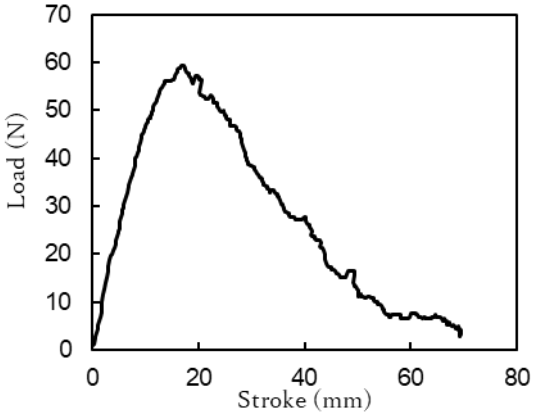

Fig. 1. Load in three-point bending test of porous aluminum.

Conclusion

Two forming processes for thin porous metals are conducted and the mechanical properties will be examined in the future work.

References:

[1] J. Banhart, Metal Foams: Production and Stability, *Advanced Engineering Materials*, **8**, 781−794 (2006).

[2] J. Banhart, Manufacture, characterisation and application of cellular metals and metal foams, *Progress in Materials Science*, **46** (6), 559−632 (2001).

Improvement of photoelectric conversion efficiency of Cu_XO/TiO_2 thin film solar cells

Shunta Endo*, Ichiro Takano**

*Electrical engineering and electronics, Graduate school of engineering, Kogakuin university, Tokyo, Japan
E-mail: cm23009@g.kogakuin.jp
**Department of electrical and electronic engineering, School of engineering, Kogakuin university, Tokyo, Japan
E-mail: ct97912@ns.kogakuin.ac.jp

Abstract

In this study, laminated oxide solar cells with a Cu_XO and TiO_2 layer deposited by reactive sputtering were fabricated. Deposition conditions and electrode structures were investigated to improve the photoelectric conversion efficiency. As a result, the highest photoelectric conversion efficiency was obtained by the sample with a Cu_2O layer of a film thickness of 300 nm at an input power of 45 W.

The use of solar cells is advancing as countermeasure against global warming. Most of the solar cells in the market are silicon solar cells, but new materials such as oxide solar cells are being developed from the viewpoint of securing resources and reducing manufacturing energy. In our previous studies, the photoelectric conversion efficiency of Cu_2O/TiO_2 or $CuO/Cu_2O/TiO_2$ thin film solar cells based on pn junctions of CuO, Cu_2O, and TiO_2 were investigated. In this study, an input power of Cu sputtering was varied to fabricate a Cu_XO layer with different structures and the photoelectric conversion efficiency was investigated.

The multi-process coating system (BC5146, ULVAC Co.) was used for film deposition. FTO-deposited glass (16 × 16 mm) was used as the sample substrate. After ultrasonic cleaning with ethanol for 10 minutes, the sample was treated with Ar plasma for cleaning. The deposition conditions of Cu_XO, CuO, and TiO_2 thin films are shown in Table 1.

Table 1 Deposition conditions

Oxide film	TiO_2	Cu_XO	CuO
Substrate	Glass with an FTO film (16×16mm)		
Base pressure [Pa]	$<1.0\times10^{-5}$		
Substrate heating temperature [℃]	300	250	250
Target	Ti	Cu	CuO
Ar flow rate [sccm]	20.0	15.0	20.0
O_2 flow rate [sccm]	1.5	10.0	0
Input power [W]	100	30~45	200
Film thickness [nm]	300	150, 300	150

The crystal structures were analyzed by thin-film X-ray diffraction (XRD: Rigaku Co., Ltd., SmartLab) at an X-ray incidence angle of 0.4°. Optical properties were measured by UV-visible spectrophotometer (UV-2550, Shimadzu Co.), and J-V characteristics were measured by a solar simulator (HAL-320, Asahi Spectroscopy Co., Ltd.) using an artificial solar lamp with irradiation intensity of 100 mW/cm^2 and an electronic load device.

Figure 1 shows the J-V characteristics of Cu_2O/TiO_2 and $CuO/Cu_2O/TiO_2$ thin film solar cells. On the crystal structure, the CuO peak decreased and the Cu peak increased with an input power of Cu sputtering. On the photoelectric conversion efficiency, the Cu_XO/TiO_2 thin film with an input power of 45 W showed the highest value of 7.3×10^{-3} %. These results indicate that the Cu in the Cu_XO layer decreased the internal resistance and increased the short-circuit current density. The $CuO/Cu_2O/TiO_2$ thin film exhibited the highest open circuit voltage at 40 W in an input power, possibly due to increase of resistance caused by the CuO layer.

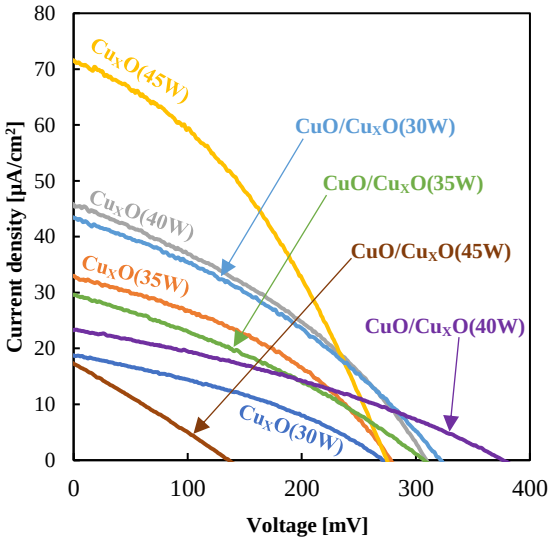

Fig. 1 J-V characteristics for various input powers of Cu sputtering.

In this study, the Cu_2O/TiO_2 thin film with an input power of 45 W showed the highest photovoltaic conversion efficiency. The effect of the total thickness and thickness ratio (CuO/Cu_2O) of the p-type layer on the photovoltaic conversion efficiency will be investigated in the future.

References

[1] M. Ichimura, *Introduction to Solar Cells*, p.88 (2012).

HCl-assisted Mist CVD Growth and Electrical Properties of α-In_2O_3 Films Using Various In-based Materials

T. Yamamoto, A. Taguchi, R. Yamada, H. Nagai, T. Onuma, T. Honda, and T. Yamaguchi

Department of Electronic Engineering and Electronics, Graduate School of Engineering, Kogakuin University, Japan
E-mail: cm22046@ns.kogakuin.ac.jp

Abstract

α-In_2O_3 films were grown using various In-based materials ($In(acac)_3$, In_2O_3 powder, $InCl_3$ powder and metal In) by HCl-assisted Mist Chemical Vapor Deposition (Mist CVD), and the growth mechanism and electrical properties of α-In_2O_3 were investigated. The results clearly indicate that the Cl^- concentration in the solution affects the growth rate of α-In_2O_3 in all In-based materials. The increased growth rate resulted in the improvement of electrical properties, except for the sample grown with $In(acac)_3$.

Corundum-structured indium oxide (α-In_2O_3) with a band gap of 3.7 eV is expected to be applied to power switching field-effect transistors[1]. The α-In_2O_3 films can be reproducibly grown by Mist chemical vapor deposition (Mist CVD). In the mist CVD method, HCl has been typically used to dissolve In-based powders in deionized water. We found that HCl affected not only to dissolve In-based materials, but also to control structural and electrical properties of In_2O_3[2]. As an In-based material, $In(C_5H_7O_2)_3$ ($In(acac)_3$) has been typically used for the growth of α-In_2O_3[1]. We recently reported that α-In_2O_3 films with superior electrical properties (carrier concentration of ~10^{17} cm^{-3} and Hall mobility of ~200 cm^2/Vs) were successfully grown using carbon-free In_2O_3 powder, instead of $In(acac)_3$[3,4]. However, the growth mechanisms in the Mist CVD growth of α-In_2O_3 have not been fully understood yet. The understanding of growth mechanism is expected to result in the realization of α-In_2O_3 films with further superior electrical properties. In this study, we discuss the growth mechanisms through the results of HCl-assisted Mist CVD growth of α-In_2O_3 using various In-based materials. We also discuss the electrical properties of the obtained α-In_2O_3 films.

In_2O_3 thin films were grown at 550°C for 1 hour by Mist CVD on (0001)α-Al_2O_3 substrates. $In(acac)_3$, In_2O_3 powder, indium chloride ($InCl_3$), and In metal were used as In-based materials. Each of source In-based material was dissolved by HCl in deionized water. The molar concentration of Cl^- in the solution was varied between 0.82 and 2.3 mol/L, while that of In^{3+} was fixed at 0.10 mol/L. For the $InCl_3$ solution, the molar concentration of Cl^- was calculated involving not only HCl but also source material of $InCl_3$. The obtained α-In_2O_3 films were characterized by Scanning Electron Microscopy (SEM) for film thickness measurements and by Hall effect for electrical property measurement.

Figure 1 shows the relationship between Cl^- concentration in the solution and film thickness of In_2O_3. We clearly found for all In-based materials that the film thickness increased with increasing Cl^- concentration in the solution. Higher growth rate was observed only in $In(acac)_3$, despite using the same molar concentration of In. When the Cl^- concentration was small, it was observed that polycrystals of In_2O_3 tended to grow, as shown in open symbols in less than 1.0 mol/L of Fig. 1. This was similar tendency as previous report[2]. We believe that these phenomena mentioned above can be explained by Langmuir model[5].

Figure 2 shows the relationship between Hall mobility and carrier concentration in the grown In_2O_3 films using various In-based materials. The electrical properties were improved (lower carrier concentration and higher Hall mobility) with increasing film thickness, except in the films grown using $In(acac)_3$. These results suggest that the growth rate basically affects the electrical properties of α-In_2O_3 films. Among In-based materials, only $In(acac)_3$ involves carbon. Therefore, carbon involved in the source material affects one of crucial issues in the electrical properties of α-In_2O_3. In the presentation, the detailed results of electrical properties will be described with the discussion of growth mechanism, mentioned above.

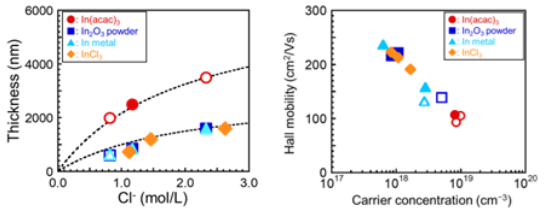

(Close symbol: single phase film, Open symbol: polycrystalline film, Broken lines: guide for the eye.)

Fig. 1. (left) Relationship between Cl^- concentration in the solution and film thickness of In_2O_3.
Fig. 2. (right) Relationship between Hall mobility and carrier concentration in grown In_2O_3 films using various In-based materials.

[1] K. Kaneko *et al.*, Appl. Phys. Express **8**, 095503(2015).
[2] T. Yamaguchi *et al*., Appl. Phys. Express **13**, 075504 (2020).
[3] A. Taguchi *et al*., Phys. Status Solidi B **259**, 2100414 (2021).
[4] A. Taguchi *et al*., Jpn. J. Appl. Phys. **62** SF1023 (2023).
[5] A. Sekiguchi, Dr. Thesis, Aoyama gakuin university, Kanagawa (2016).

Sn-doped α-Ga_2O_3 Films Grown Using Sn Source Solutions with Different Aging Times and Their Electrical Properties

Ko. Yamada[1], T. Yamamoto[1], R. Yamada[1], Ka. Yamada[1], H. Nagai[1, 2], S. Aikawa[1, 3], T. Onuma[1, 2], T. Honda[1, 2], and T. Yamaguchi[1, 2]

1. Department of Electrical Engineering and Electronics, Graduate School of Engineering, Kogakuin University, Tokyo, Japan
2. Department of Applied Physics, School of Advanced Engineering, Kogakuin University, Tokyo, Japan
3. Department of Electrical and Electronic Engineering, School of Engineering, Kogakuin University, Tokyo, Japan

E-mail: cm23072@ns.kogakuin.ac.jp

Abstract

Sn-doped α-Ga_2O_3 was grown with different aging times of Sn source solutions by Mist CVD. With increasing aging time, the Sn source solution was yellowish. The electrical conductivity was confirmed only in the sample grown with the aging time of 0 days, while other films grown with aging times between 10 and 30 days showed high resistivity.

SiC and GaN have been currently used in power Schottky barrier diodes (SBD). Ga_2O_3 has a higher Baliga's figure of merit than Si, SiC, and GaN, making it a promising alternative material for SBD applications[1]. Ga_2O_3 is a wide bandgap oxide semiconductor having six polymorphs. Among them, corundum-structured Ga_2O_3 (α-Ga_2O_3) is the material with the largest bandgap energy of 5.3-5.6 eV[2]. While low on-resistance and high breakdown voltage are expected because of its large bandgap energy, it is very difficult to obtain conductivity. We have focused on Sn doping in α-Ga_2O_3 to control conductivity. α-Ga_2O_3 can be reproducibly grown by Mist chemical vapor deposition (Mist CVD)[3].

Mist CVD is a solution-based growth method. It has advantages of simple equipment configuration and mass production. In the growth by Mist CVD, the source solution is typically prepared by dissolving source metal powder in deionized water involving a small amount of hydrochloric acid. The source solution is atomized by an ultrasonic transducer and the atomized particles are transported by a carrier gas to a reaction furnace, where thermal decomposition reaction occurs[4].

One of the problems in the growth by Mist CVD is the stability of source solution. We accidentally observed the change of Sn source solution by leaving it for a long time. It is feared that the change of solution also affects the grown film. In this study, Sn-doped α-Ga_2O_3 thin films were grown using Sn source solutions with different aging times by Mist CVD. The electrical properties of the grown films were also investigated.

To prepare Ga source solution, 0.05 mol of Ga acetylacetone $Ga(acac)_3$ was dissolved in 0.09 mol/L HCl solution. The Sn source solution was also prepared by dissolving 0.05 mol of tin (II) chloride hydrate $SnCl_2 \cdot 2H_2O$ in 0.05 mol/L HCl solution. The aging times of Sn solutions were varied between 0 and 30 days. For the growth of Sn-doped Ga_2O_3, the 99.5 mol% of Ga solution and 0.5 mol% of Sn solutions with different aging times were mixed. Using these solutions, Sn-doped Ga_2O_3 films were grown at 460°C for 1 hour by Mist CVD on (0001)α-Al_2O_3 substrates. N_2 was used as carrier gas and dilution gas with flow rates of 3.0 L/min. and 0.5 L/min., respectively. The I-V measurement was used as an electrical evaluation of the grown films.

Figure 1 shows the color change of Sn solution with different aging times. With increasing aging times, the solution was yellowish. This suggested that there was a change in the solution with aging variation.

The electrical conductivity was confirmed only in the sample grown with the aging time of 0 days, although this has a nonlinear I-V characteristics, as shown in Fig. 2. Other films grown with aging times between 10 and 30 days showed high resistivity. This result suggests that the change in the source solution affects the grown films. The change of the resistance in the grown films would be one of the distinct features.

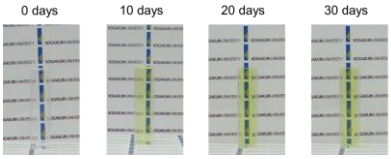

Fig.1 Color change of Sn source solution with different aging times.

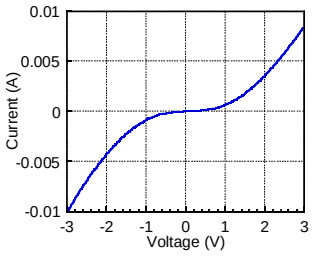

Fig. 2 I-V characteristics of thin films Grown with 0 days aging time of Sn source solution.

References:

[1] Y. Oshima *et al.*, Appl. Phys. Lett. **121**, 260501 (2022).
[2] A. Segura *et al.*, Phys. Rev. Materials. **1**, 024604 (2017).
[3] D. Shinohara and S. Fujita, Jpn. J. Appl. Phys. **47**, 7311 (2008).
[4] T. Kawaharamura, Kyoto University Graduate School Doctoral Thesis (2008).

Research on UIUX Evaluation using Heart Rate Variability of Wearable Devices

Kota Yamamoto[1,a] and Daigo Misaki[1,b]

[1]Graduate School of Engineering, Kogakuin University, Tokyo, Japan
[a]am22072@ns.kogakuin.ac.jp, [b]misaki@cc.kogakuin.ac.jp

Abstract

As research on UIUX is gaining importance, a challenge exists with UIUX evaluation methods being subjective and time-consuming to yield results. Our study proposes an efficient UIUX evaluation method leveraging wearable devices to address this issue. We achieved rapid and objective UIUX evaluations through empirical experiments by analyzing heart rate variability using wearable devices.

INTRODUCTION

In Recently, there has been a growing societal emphasis on evaluating UI and UX. In today's digital landscape, user experience directly impacts the success of companies and products. Providing users with intuitive and satisfying UIUX is essential for differentiation in a highly competitive market. However, traditional evaluation methods have been subjective and time-consuming [1]. In this study, we address this challenge by utilizing wearable devices to analyze heart rate variability, enabling rapid and objective UIUX evaluations.

METHODOLOGY

This study utilized the wearable device Apple Watch and employed a heart rate monitoring application designed for the Apple Watch. Through this application, we collected users' electrocardiogram (ECG) data, which was then used to analyze heart rate variability (HRV). Heart Rate Variability (HRV) refers to the phenomenon where the heart rate varies over time, reflecting the activity of the autonomic nervous system. The autonomic nervous system regulates various bodily functions, including the stress response. Specifically, we employed the HRV metric known as SDNN (Standard Deviation of NN intervals), which is calculated according to Formula (1). The number of data points for RRI is denoted as N, and the value of the i-th RRI is xi. SDNN values are typically higher during relaxed states and lower during periods of stress [2]. The primary focus of this experiment was on the UIUX of websites, where we aimed to explore the relationship between UIUX quality and users' physiological responses. As a part of our methodology, users were asked to interact with a website with a 'BadUIUX' design, and their electrocardiogram data was recorded before and after this interaction. Subsequently, we conducted UIUX evaluations.

EXPERIMENT

In the experiment, we referred to BadUIUX, developed by a Belgian software company, and created a BadUIUX website for use in the study [3]. The distinctive features of BadUIUX included a blue background with green text, unconventional placement of the confirm and return buttons, and difficulty discerning the next button compared to conventional layouts. The BadUIUX website we created is shown in Figure 1. In this study, we developed an objective UIUX evaluation method using Apple Watch and heart rate variability analysis. We also verified its usefulness through experimentation.

$$(1) \quad SDNN = \sqrt{\frac{1}{N}\sum_{i=1}^{N}(x_i - \bar{x})^2}$$

Fig. 1. BadUIUX website screen

RESULTS AND DISCUSSION

We had 7 participants interact with a BadUIUX website. We depict the experimental setup in Figure 2. Additionally, Figure 3 displays the heart rate variability SDNN values before and after user interactions. As a result, among the group of participants excluding the two smokers, all five individuals showed a decrease in SDNN values, suggesting the possibility of experiencing stress. The data for smokers includes subjects F and E, where the SDNN values have increased. Therefore, decreasing SDNN values was observed in evaluating the Bad

UIUX website. Conversely, in the case of smokers, it is believed that the impact of smoking on the autonomic nervous system was reflected in the heart rate variability values [4].

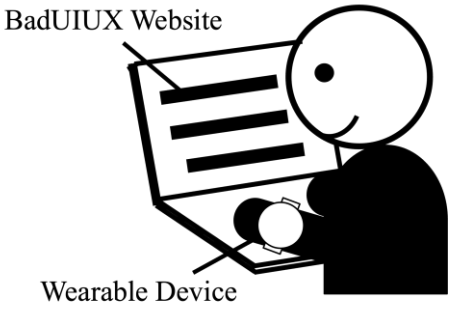

Fig. 2. The experimental process of interacting with the BadUIUX website.

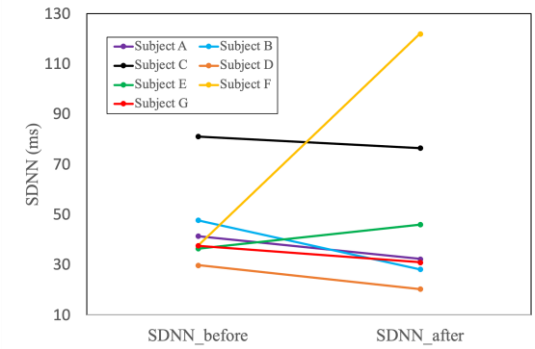

Fig. 3. Comparison of SDNN of heart rate variability

CONCLUSION

In this experiment, we evaluated BadUX caused by BadUI. However, in the future, we plan to conduct experiments even with a BadUI that results in a GoodUX website. BadUI will involve content similar to that used in this experiment but with difficult-to-read color schemes and inconvenient button placements. On the other hand, for GoodUX, we intend to insert questions that pique the user's interest and incorporate backgrounds or images that align with the user's preferences.

References:

[1] Mancini Gerhana, Yana Aditia, et al. "Heuristic and Webuse Method to Evaluate UI/UX of Faculty Website." 2022 10th International Conference on Cyber and IT Service Management (CITSM). IEEE, 2022.

[2] Machado, Arthur Viana, et al. "Association between distinct coping styles and heart rate variability changes to an acute psychosocial stress task." Scientific Reports 11.1 (2021): 24025.

[3] “UserInyerface”. Verhaert Digital Inovation. https://userinyerface.com/index.html,(2023-9-16)

[4] Murgia, Federico, et al. "Effects of smoking status, history and intensity on heart rate variability in the general population: The CHRIS study." PloS one 14.4 (2019): e0215053.

Study on high-speed growth of β-Ga_2O_3 by Mist CVD method

M. Sugitani[1], T. Yamaguchi[1,2], K. Sasaki[3], A. Kuramata[3], T. Honda[1,2], and T. Onuma[1,2]

[1] Department of Electrical Engineering and Electronics, Graduate School of Engineering, Kogakuin University, Tokyo, Japan
[2] Department of Applied Physics, School of Advanced Engineering, Kogakuin University, Tokyo, Japan
[3] Novel Crystal Technology, Inc.
*E-mail: cm23042@ns.kogakuin.ac.jp

Abstract

In this study, we aimed at high-speed growth of β-Ga_2O_3 by Mist CVD method focusing on metal source concentration and source feed rate. The film thickness of samples grown on (010) and (001)β-Ga_2O_3 substrates were confirmed to be about 12.4 μm and 13.4 μm, respectively. Growth rates exceeding 10 μm/h were obtained regardless of the substrate.

We are focusing on β-gallium oxide (β-Ga_2O_3), which is thermodynamically stable and can produce large-diameter and high-quality single-crystal substrates by the melt growth method[1]. Vertical Schottky barrier diode (SBD) has been demonstrated using the halide vapor phase epitaxy (HVPE)-grown homoepitaxial film as its drift layer. In the SBDs, device performance is improved by depositing a thick, high-quality and low carrier concentration undoped layer [2]. For the growth of β-Ga_2O_3, we are using the mist chemical vapor deposition (Mist CVD) method, which is a simple and energy-efficient deposition technique[3]. Although a high-speed homoepitaxial growth of β-Ga_2O_3 has been demonstrated for the Mist CVD method[4], the reported growth rate of 3.2 μm/h is still lower than the other methods, such as the HVPE or metalorganic vapor phase epitaxy (MOVPE). Behind this background, high-speed Mist CVD growth of β-Ga_2O_3 is investigated in terms of metal precursor source concentrations and source supply rate.

β-Ga_2O_3 films were grown by mist CVD. $Ga(C_5H_7O_2)_3$ [$Ga(acac)_3$] was used as the source precursor. The $Ga(acac)_3$ concentration was varied between 0.1 and 0.3 mol/L, in which the HCl concentration was varied between 1.2 and 3.6 mol/L. The growth process was carried out at 800°C. One to three ultrasonic transducers were employed to atomize the source solution. The growth period lasted for 60 minutes. We optimized the source precursor concentration and source feed rate to achieve high-speed β-Ga_2O_3 growth on (0001) α-Al_2O_3 substrates. Following the optimized conditions for high-speed growth, we conducted β-Ga_2O_3 growth on (010) and (001) β-Ga_2O_3 substrates.

Growth rates for the homoepitaxial films were determined from the weight difference of the bulk substrate before and after epitaxial growth. As shown in Fig. 1, the values are 12.4 and 13.4 μm for the films grown on (010) and (001) β-Ga_2O_3 substrates, respectively. Figure 2 shows the XRD θ-2θ patterns of samples grown on (010) and (001) β-Ga_2O_3 substrates. We confirmed that the peaks corresponding to the substrate's orientation dominate for both samples. For the film grown on (010) β-Ga_2O_3 substrate, we also observed the presence of peaks originating from $\bar{2}04$ and $\bar{2}21$. For the film grown on (001) β-Ga_2O_3 substrate, we confirmed the presence of diffraction peaks originating from 110. Although polycrystallinity is still remaining in the homoepitaxial layers, we achieved high grow rate exceeding 10 μm/h regardless of the substrate orientation. At present, the polycrystallinity is attributed to the temperature drop at the sample surface under the large source supply rate. Results for the preliminary studies toward high-speed growth of β-Ga_2O_3 on (0001) α-Al_2O_3 substrates will be included at the presentation.

In summary, we investigated the high-speed growth of β-Ga_2O_3 using the Mist CVD method. One hour growth yielded thicknesses of 12.4 and 13.4 μm for the films grown on the (010) and (001) β-Ga_2O_3 substrates, respectively. Growth rate exceeding 10 μm/h was achieved successfully, regardless of the substrate orientation. The results indicated achievement of high-speed growth of β-Ga_2O_3.

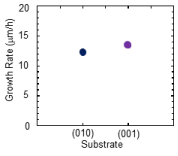

Fig. 1 Film thickness of samples grown on (010) and (001)β-Ga_2O_3 substrates.

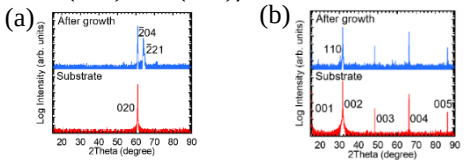

Fig. 2 XRD θ-2θ patterns of samples grown on (a) (010) and (b) (001) β-Ga_2O_3 substrates.

References:

1) A. Kuramata *et al.*, Jpn. J. Appl. Phys. **55** 1202A2 (2016).
2) K. Sasaki *et al.*, Appl. Phys. Express **10**, 124201 (2017).
3) T. Kawaharamura, Dr. Thesis, Faculty of Engineering, Kyoto Univ., Kyoto (2008).
4) H. Nishinaka *et al.*, Mater. Sci. Semicond. Process. **128** 105732 (2021).

Realization of Cathodoluminescence in 190 nm Wavelength Range in Rocksalt-Structured MgZnO Films Grown by Mist Chemical Vapor Deposition

Kotaro Ogawa[1],*, Wataru Kosaka[1], Hiroya Kusaka[1], Yuichi Ota[2], Tomohiro Yamaguchi[1], Tohru Honda[1], Kentaro Kaneko[3], Shizuo Fujita[4], and Takeyoshi Onuma[1]

[1] Department of Electrical Engineering and Electronics, Graduate School of Engineering, Kogakuin University, 2665-1 Nakano, Hachioji, Tokyo 192-0015, Japan
[2] Tokyo Metropolitan Industrial Technology Research Institute, 2-4-10 Aomi, Koto-ku, Tokyo, 135-0064, Japan
[3] Research Organization of Science and Technology, Ritsumeikan University, 1-1-1 Noji-Higashi, Kusatsu, Shiga 525-8577, Japan
[4] Office of Society-Academia Collaboration for Innovation, Kyoto University, Yoshidahonmachi, Sakyo-ku, Kyoto, Kyoto 606-8501, Japan
*E-mail: k-ogawa@cc.kogakuin.ac.jp

Abstract

Rocksalt-structured $Mg_xZn_{1-x}O$ films with x=0.65-0.97 were grown on MgO (100) substrate by mist chemical vapor deposition method. By employing post-growth slow-cooling to suppress thermal stress, small full width at half maximum (FWHM) values of 61-202 arcsec were achieved for 200 diffraction peak in θ-2θ X-ray diffraction profiles. FWHM values in XRC for 200 diffraction were 48 to 317 arcsec, in which the smallest one was even smaller than that of MgO substrate of 57 arcsec. Cathodoluminescence spectra showed near-band-edge emission peaks in 190 nm spectral range for MgO molar fraction x≥0.92 at 300 K.

1. Introduction

Vacuum ultraviolet (VUV) and deep ultraviolet (DUV) lights have important roles in various applications such as virus sterilization, water treatment, lithography process, and so on. However, most commercially available light sources in the shorter wavelength range are discharge-type lamps or lasers. Therefore, development of ultrawide-bandgap (UWBG) semiconductor-based far-UV emitters will be a technical breakthrough since their energy consumption is expected to be drastically reduced.

Rocksalt-structured (RS) MgZnO alloys are expcted as candidate materials for the DUV and VUV light emitters. The $Mg_xZn_{1-x}O$ alloys with MgO molar fraction x>0.6 have rocksalt structure as a thermodynamically stable phase [1]. Bandgap energy (E_g) can be tuned from 2.45 eV for RS-ZnO [2] to 7.7 eV for MgO [3-5] by varying x. Theoretical calculation predicted that RS-$Mg_xZn_{1-x}O$ alloys are direct bandgap for x>0.5 if Mg and Zn atoms are uniformly distributed in the alloys [6].

Our group has reported growths of atomically flat single crystalline RS-$Mg_xZn_{1-x}O$ films on MgO (100) substrates by the mist chemical vapor deposition (mist CVD) method and observation of DUV cathodoluminescence (CL) peak in 199-250 nm spectral range [7-12]. However, large Stokes-like shift, which is defined as the energy difference between E_g and CL peak energy, was observed as large as 0.7-0.9 eV [8,10,12]. Exact origin of the Stokes-like shift is unknown at present. But, formation of Zn-related isoelectronic trapped-hole centers may be a cause of the large Stokes-like shift[12]. Therefore, decrease in the trapping centers by growing homogeneous RS-$Mg_xZn_{1-x}O$ alloys is indispensable to realize near-band-edge (NBE) emission in 190 nm spectral range.

Although the lattice mismatch between RS-ZnO (a=0.42766 nm) [13] and MgO (a=0.42128 nm) is very small (1.5%), difference in the thermal expansion coefficients of RS-ZnO (α=4.7-6.2×10^{-5} K^{-1}) [14] and MgO (α=10.5-15.0×10^{-6} K^{-1}) [15] is large. Since large difference in the thermal expansion coefficient generally induces thermal stress during the growth of epitaxial films, thermal management is essential. Growth of RS-$Mg_xZn_{1-x}O$ film on the MgO substrate is expected to be suffered from in-plane tensile stress. In this study, we focus on thermal management during the cooling process in the mist CVD growths of RS-$Mg_xZn_{1-x}O$ epitaxial films on MgO (100) substrates.

2. Experiment

RS-$Mg_xZn_{1-x}O$ epitaxial films were grown on MgO (100) substrates by the hot-wall-type mist CVD as shown in Fig. 1. $Mg(CH_3COO)_2 \cdot 4H_2O$ and $Zn(CH_3COO)_2 \cdot 2H_2O$ were dissolved in a mixed solution of deionized water and acetic acid (4:1 in volume). Total concentration of the source precursors in the solvent was fixed at 0.01 mol/L, and the molar ratio of magnesium ($[Mg]^L$ = [Mg]/([Mg]+[Zn])) was varied in the range from 0.6 to 0.97. Oxygen gas was used as a carrier and a dilution gas with flow rates of 4.0 and 0.5 L/min, respectively. Temperature sequence is shown in Fig. 2. Temperature first increased with a heating-rate of +20°C/min. After 1-hour-growth at 700°C, the mist generation was stopped, and the temperature decreased slowly with a natural cooling rate with maintaining the oxygen gas flow until the temperature dropped to 300°C, and the slow-cooling was further conducted in an air atmosphere until the temperature dropped to 100°C. Averaged cooling rates were -10°C /min and -1.67°C /min for the temperature ranges of 700-300°C and 300-100°C, respectively. The films were evaluated by spectroscopic ellipsometry, X-ray diffraction (XRD), and CL measurements. CL measurements was conducted using a custom-built VUV spectroscopy system, in which the optical path was filled with nitrogen gas [8,10,12].

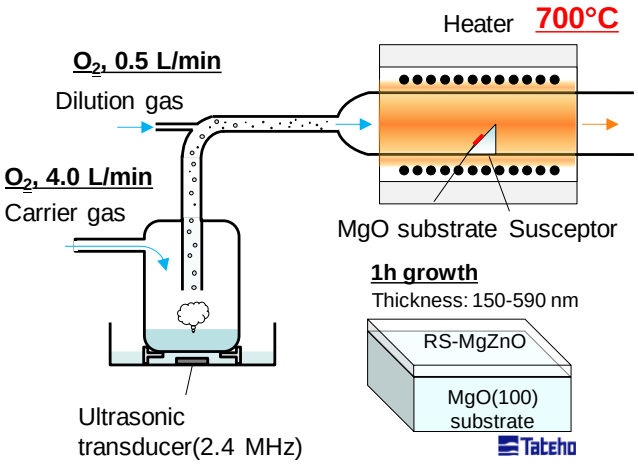

Fig. 1. The schematic diagram of Mist CVD system.

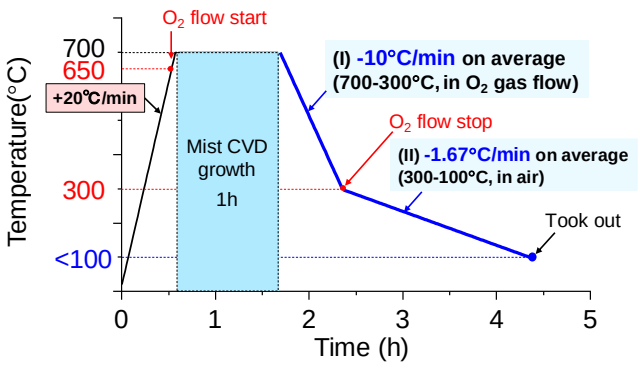

Fig. 2. Temperature sequence in the growth of RS-$Mg_xZn_{1-x}O$ films on MgO (100) substrates using post-growth slow cooling process.

3. Results and Discussion

Film thickness was evaluated by the spectroscopic ellipsometry measurements. As shown in Fig. 3, values decreased from 590 nm to 150 nm with decreasing $[Mg]^L$. XRD θ-2θ profiles near 200 diffraction peaks of the RS-$Mg_xZn_{1-x}O$ films are shown in Fig. 3. The x values are determined by the X-ray reciprocal space mapping (RSM) measurements (data not shown). As we decreased $[Mg]^L$ from 0.97 to 0.6, diffraction peak monotonically shifted from 2θ=42.91° to 2θ=42.69° by reflecting a larger ionic radius of Zn than that of Mg. All the films, except for $[Mg]^L$=0.97, apparently show the Laue oscillation, and the results imply that the films have smooth surface and interface. Full width at half maximum (FWHM) value (Δ2θ) was 25 arcsec for the substrate, and the values increased from 61 to 202 arcsec with decreasing x. Note that the values for x=0.92-0.97 were extracted by fitting analyses using the Voigt function. Though the difference in film thickness should be considered, FWHM values in XRC for the 200 diffraction peak increased from 48 to 317 arcsec with decreasing x. The smallest one was even smaller than that of MgO substrate of 57 arcsec. CL spectra of RS-$Mg_xZn_{1-x}O$ films at 300K are shown in Fig. 4. All the spectra showed NBE emission in 190 nm spectral range, and the peak energies showed monotonical increase with x. The Stokes-like shift was found to be reduced as low as 0.1-0.2 eV.

4. Conclusion

Rocksalt-structured RS-$Mg_xZn_{1-x}O$ films with x=0.65-0.97 were grown on MgO (100) substrate by the mist CVD method. Post-growth slow-cooling process was employed to suppress thermal stress in RS-$Mg_xZn_{1-x}O$ films. The small FWHM values in θ-2θ and XRC for 200 diffraction profiles were achieved. It is implied that the alloy compositional fluctuation and mosaicity in the RS-$Mg_xZn_{1-x}O$ alloys were reduced. As a result, reduction of the Stokes-like shift realized observation of the NBE emission peaks in 190 nm spectral range for $x \geqq 0.92$ at 300 K.

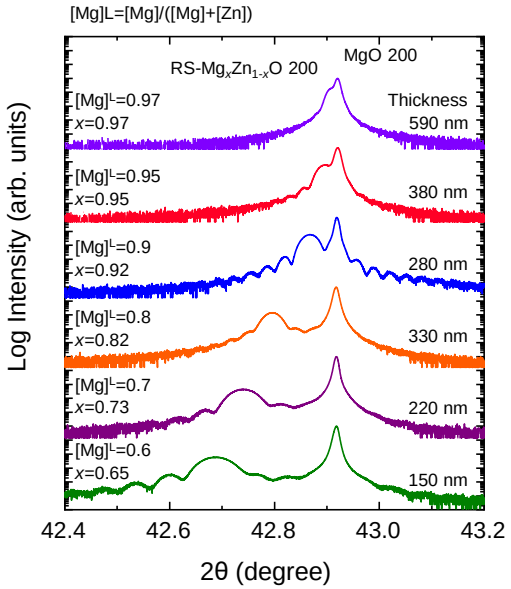

Fig. 3. XRD θ-2θ profiles near 200 diffraction peaks of RS-$Mg_xZn_{1-x}O$ films grown on MgO (100)

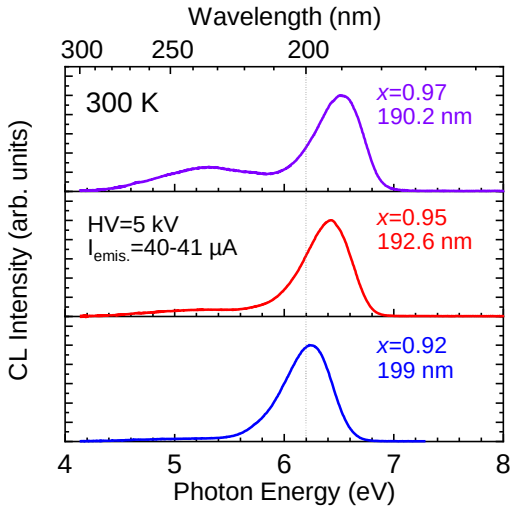

Fig. 4. CL spectra at 300 K for RS-$Mg_xZn_{1-x}O$ films grown on MgO (100) substrates.

Acknowledgement

This work was supported in part by Grants-in-Aid for Scientific Research Nos. 20H00246 and 22K04952 from MEXT, Japan.

References

[1] I. Takeuchi *et al*., J. Appl. Phys. **94**, 7336 (2003).
[2] A. Segura *et al*., Appl. Phys. Lett. **83**, 278 (2003).
[3] D. M. Roessler and W. C. Walker, Phys. Rev. Lett. **17**, 319 (1966), and Phys. Rev. **159**, 733 (1967).
[4] R. C. Whited and W. C. Walker, Phys. Rev. Lett. **22**, 1428 (1969).
[5] T. Onuma *et al*., Appl. Phys. Lett. **119**, 132105 (2021).
[6] I. Gorczyca *et al*., Phys. Rev. B **101**, 245202 (2020).
[7] K. Kaneko *et al*., Appl. Phys. Express **9**, 111102 (2016).
[8] T. Onuma *et al*., Appl. Phys. Lett. **113**, 061903 (2018).
[9] K. Kaneko *et al*., J. Electron. Mater. **47**, 4356 (2018).
[10] M. Ono *et al*., J. Appl. Phys. **125**, 225108 (2019).
[11] K. Ishii *et al*., Appl. Phys. Express **12**, 052011 (2019).
[12] T. Onuma *et al*., J. Appl. Phys. 134, 025102 (2023).
[13] M. C. Wen, *et al*., J. Cryst. Growth **477**, 169 (2017).
[14] F. Decremps *et al*., Europhys. Lett. **51**, 268 (2000).
[15] G. K. White and O. L. Anderson, J. Appl. Phys. **37**, 430 (1966).

Proposal for Teaching Methods of Programmatic Thinking in the Field of Programming Education

Masato.Tasaki, Yoshio.Miki

Kogakuin University of Technology and Engineering
Email:jx20167@ns.kogakuin.ac.jp

Abstract

In Japan, education in Programmatic Thinking is provided as training in thinking skills that are necessary after entering the workforce. However, the content of such education does not differ greatly from that of programming education. In this study, we propose a method of making programming thinking education materials by adding a thinking part of problem definition to Computational Thinking (CT) and Operations Research (OR) materials. In this presentation, we explain an example of extending the problem definition of the traveling salesman problem.

1. INTRODUCTION

In Japan, programming education has started in elementary education from the 2020 school year. The purpose of this education is to help students make more appropriate and effective utilization of computers in order to live in the future society, and to develop a "programmatic thinking," which is universally demanded throughout permanently, no matter what job they are hired for[1]. To learn a programmatic thinking, students will not only be able to perform routine tasks in society, but will also be able to use their own minds to organize and find solutions to ambiguous problems that have not been standardized or verbalized.

However, most of the content of the classes is related to robot programming and computer programming, and education on "programmatic thinking" for living in the future society is still insufficient.

Currently, The CT, OR, and algorithm examples, such as order/reordering, number guessing, and shortest path problems, are used in classes as teaching materials for programmatic thinking.

The purpose of this research is to propose a method of making algorithmic teaching materials such as CT and OR, which are treated as examples of programmatic thinking, into programmatic thinking teaching materials by adding a thinking part of problem definition to them.

2. METHODS

In conventional programming education, programmatic thinking is expressed in terms of five items: decomposition, combination, simulation, abstraction, and generalization, and it is said that by developing these basic skills, thinking and, eventually, coding skills can also be cultivated. These five items are based on CT, which also encompasses solution methods such as algorithms and OR[1]. As mentioned in Chapter 1, in order to solve ambiguous problems that have not been formulated or verbalized, it is first necessary to define the problem precisely. However, the problem definitions of CT and OR examples are implied, it is necessary to clarify the problem definitions such as goals and constraints. Here, goals refers to the numerical values to be optimized, the state of affairs, and the conditions for termination. Constraints refer to constraints on the means, quantities, and actions that may be used.

As mentioned above, example problems for algorithms such as CT and OR already have prerequisites. Therefore, we will use these examples to change the problem definition to examples that allow us to think. The following is a description of the steps involved in creating an example.

- First, implicitly ask the pupils to solve an standard example problem.
- Then, the implicitly defined preconditions of the solved example are given, as well as new and different preconditions for solving the new example.
- By defining new preconditions, make them aware that there are various alternative ways to solve the problem under different conditions.
- Repeat the cycle of asking pupils to come up with new preconditions and presenting their own solutions to the preconditions they have defined.

According to the general rules of the curriculum guidelines[1], programming thinking is

> the ability to think logically about what combinations of movements are necessary to realize a series of activities one intends, how to combine the symbols corresponding to each movement, and how to improve the combinations of symbols to get closer to the intended activities.

The authors thought that this ability can be developed by creating example problems that

consider multiple goals or constraints in defining the problem. In the next chapter, detailed examples will be explained.

3. EXAMPLE : TRAVELING SALESMAN PROBLEM

The traveling salesman problem is such a problem that Given a list of cities and the distances between each pair of cities, what is the shortest possible route that visits each city exactly once and returns to the origin city?[2]

Usually, the departure and return points are same, and all cities specified need to be visited in the shortest possible route. Considering that the objective is to visit each point and do business, it is not necessary to visit all stores in a single day or to do everything by oneself. By modifying the goals and constraints as necessary, the authors thought pupils can produce multiple examples on their own and develop the ability to think flexibly.

Figure 1 below shows an example of the traveling salesman problem. In this example, the starting and ending points are Nishi-Shinjuku Elementary School, with the Tokyo Metropolitan Government Office, Kogakuin University, Nishi-Shinjuku 5-chome Station, the New National Theatre, and Bunka Gakuen University as the visiting points.

Most people will probably follow the following route: Nishi-Shinjuku Elementary School → New National Theater → Bunka Gakuen University → Kogakuin University → Tokyo Metropolitan Government Office → Nishi-Shinjuku 5-chome Station → Nishi-Shinjuku Elementary School.

Next, the goals, constraints, and other prerequisites of the example problem to be solved are explained to the pupils. In the case of this example, the goals and constraints are as follows.

Goals : Both starting and ending points are Nishi-Shinjuku Elementary School.

Constrains : The pupils must follow the shortest route and visit all the facilities in a cycle.

The pupils are made aware that these conditions are valid for a traveling salesman problem, but are implicitly presented as preconditions.

Next, the following conditions are presented in order to show that other conditions exist, and that for these conditions, other solutions exist than those described above.

Goals : The starting point is Nishi-Shinjuku Elementary School.

Constraints : It is possible to split the visit into two. The facility can be visited by either person.

The return point can be different from the starting point, so that the pupils can return directly from the last stop, or take a route that could not be taken by one group by having two groups.

After that, as already mentioned, the cycle is repeated by asking the pupils to think of new preconditions and to present their own solutions to those preconditions.

4. CONCLUSION

In this paper, the authors proposed a teaching material for programmatic thinking. Ten fourth-, fifth-, and sixth-grade pupils of Nishi-Shinjuku Elementary School in Shinjuku City were given the example of the traveling salesman problem discussed in this paper. First, it was found that the example of the standard traveling salesman problem was acceptable to the elementary school students by explaining the rules of the problem. After the pupils solved the standard traveling salesman problem, we presented a new premise: instead of one person visiting around, two people should visit around. This was also solved without difficulty.

However, most elementary school pupils spent most of their time thinking alone, rather than cooperating with each other. The ability to talk cooperatively toward the solution of a project is very important. In the future, the authors would like to develop examples that can be solved cooperatively.

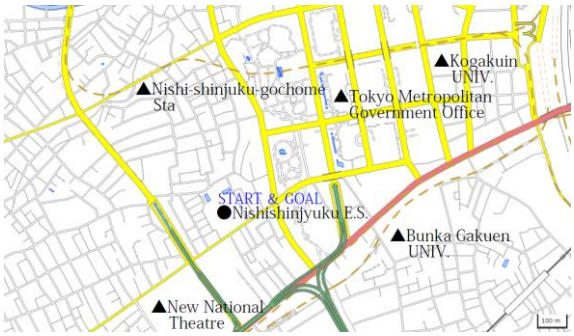

Fig. 1. Example of the traveling salesman problem

5. REFERENCES

[1] Ministry of Education, Culture, Sports, Science and Technology, [Regarding the ideal form of programming education at the elementary school level (summary of discussions)] Syogakko dankai ni okeru programming kyoiku no arikata ni tsuite (giron no torimatome) (in Japanese), 2016.

[2]"Traveling salesman ploblem", WIKIPEDIA,WIKIPEDIA,https://en.wikipedia.org/wiki/Travelling_salesman_problem, 16 Sep 2023.

Evaluation of ZnO thin film on Ar plasma treated CNF

Kai Ishikawa*, Ichiro Takano**

Department of Electrical and Electronic Engineering, Kogakuin University, Tokyo, Japan
E-mail: cm23005@g.kogakuin.jp *, ct97912@ns.kogakuin.ac.jp **

Abstract

We have attempted to apply cellulose nanofiber CNF (Oji Holdings Co., Ltd.), a plant-derived material that is currently attracting attention in various fields, as a substrate for flexible transparent conductive films, which are expected to expand in the future. When ZnO thin film was deposited on untreated CNF substrate, cracks were observed in the ZnO thin film. Ar plasma treatment suppressed the cracks in the ZnO thin film observed on the untreated CNF substrate.This is due to the change in surface chemistry state and the surface etching caused by the Ar plasma treatment in which improved adhesion. Ar plasma treatment not only modified the surface of the CNF substrate, but also affected the crystal structure of the ZnO thin film on the CNF substrate. These results demonstrate the effectiveness of ar plasma treatment in surface modification of CNF substrates and bring us closer to future applications in flexible devices.

Introduction

Soil and ocean pollution have become serious problems in the global environment and are pressing issues for mankind. Against this backdrop, the development of eco-materials has been remarkable, and environmentally friendly plant-derived materials have been attracting attention. In this study, cellulose nanofiber (CNF), a plant-derived material that is attracting attention in the field of advanced materials, was subjected to surface treatment with Ar plasma with the aim of applying it to various fields. The CNF used in this study (Oji Holdings Co., Ltd.) has a transmittance in the visible light range comparable to that of glass substrates, and is expected to be applied as a substrate for flexible transparent conductive films, which are expected to expand in the future.

To use polymers as device substrates, the adhesion between the polymer and metal film must be improved because it affects reliability and preformance. Surface modification is effective in improving adhesion between the substrate and metal, and various methods are available, but to date there have been few reports on surface modification of CNF substrates. In this experiment, when ZnO thin film was deposited on untreated CNF substrate, cracks were observed in the ZnO thin film. Such cracks must be prevented if the CNF is to be applied as a device substrate.

In this study, Ar plasma treatment was used for surface modification of CNF substrates. The purpose of this study is to investigate the effect of Ar plasma treatment on CNF substrates and to deposit ZnO thin films without cracks.

Experimental Methods

Ar plasma treatment and magnetron sputtering were performed using a multi-process coating system. The substrate used in this experiment was a sheet of CNF (Thickness:70[μm]) were treated by Ar plasma. Ar plasma conditions are included in the following ranges: Input Power (50[w]), Pressure (5.0×10^{-5} [Pa]), Ar flow flow (5[sccm]), and Time (0~240[s]).

After Ar plasma treated, ZnO films were deposited on plasma treated CNF substrates by RF sputtering magnetron. ZnO films (Thickness:50[nm]) were deposited by sputtering an Zn target (99.9% purity) under an oxygen atmosphere. Magnetron Sputtering conditions are included in the following ranges: Input Power (20[w]), Pressure (5.0×10^{-5} [Pa]), Ar flow flow (20[sccm]), and O_2 flow flow (5[sccm]).

The surface chemical state of CNF before deposition was evaluated by X-ray photoelectron spectroscopy (XPS, KRATOS ULTRA2, Shimadzu Co., Ltd.). The wettability evaluation was measured by water contact angle measurement (DM-300, Kyowa Co., Ltd.). The surface roughness of untreated and plasma treated CNF were measured by the atomic force microscopy (AFM, OLS4500, OLYMPUS) with scanning range 10 × 10 μm. The crystal structure of the ZnO thin film was evaluated using X-ray diffraction. (XRD, High quality XG M18CE-Mac Science Co.Ltd).

Results and Discussion

3.1 The surface states of ZnO thin film

Fig.1 shows the surface states of ZnO thin film on untreated CNF(a) and Ar plasma treated CNF(b). Cracks were formed on ZnO thin film on untreated CNF. Cracks have been reported to occur when metal oxides are deposited on polymer substrates [1]. This is due to the high film hardness of the metal oxide and the stress generated during deposition [2]. ZnO thin film as a metal oxide may have been hard and therefore inflexible to slight deformation of the CNF substrate. Heat is also generated when thin films are deposited on the substrate. This causes a difference in

the coefficient of thermal expansion between the substrate and the thin film, which generates internal stress called thermal stress in the thin film. Cracks are thought to be caused by these. On the other hand, no cracks were observed in the ZnO thin film on ar plasma treated CNF. This is thought to be related to the improved adhesion between the CNF and ZnO thin films due to surface modification by Ar plasma, and ZnO thin films without cracks were formed on the CNF substrate even at room temperature. In order to investigate the cause of this prevention of cracking, the CNF surface chemical condition was observed before deposition.

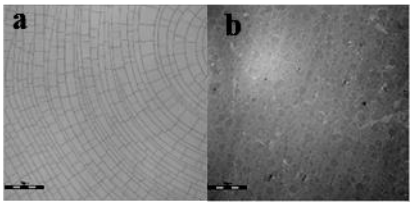

Fig.1 The surface states of ZnO thin film on (a) untreated CNF, (b)Ar plasma treated (240s) CNF.

3.2 XPS analysis

Before deposition, the chemical state of the CNF substrates surface was determined by XPS. Fig.2 shows the C1s spectra of untreated CNF and Ar plasma treated CNF. C-O (286.5 eV) bonds were dominant in the untreated CNF, but C-O bonds decreased and C-C(C-H) (285.0 eV) and C=O (288.1 eV) bonds increased with Ar plasma treatment time [3]. C-C(C-H) crosslinked structures were formed on the CNF surface by Ar plasma treatment. Ar plasma treated is sufficient to break chemical bonds, leaving free radicals at or near the surface. These radicals can react only with other surface radicals or by chain transfer reactions [4].

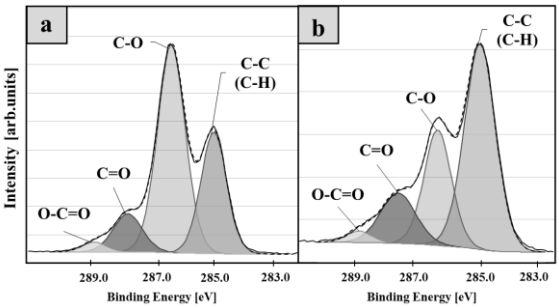

Fig.2 C1s XPS spectra (a) untreated CNF, (b)Ar plasma treated (240s) CNF.

3.3 Contact angle and AFM analysis

Contact angle measurement was performed for wettability evaluation. The contact angle of untreated CNF was 67.7°, while the contact angle of water after Ar plasma treatment (240s) was 34.0°, indicating that the contact angle became more hydrophilic. The contact angle was almost constant after 40s. This decrease in contact angle is due to the increase in the polar C=O bond and the increase in surface free energy due to the C-C(C-H) crosslink structure caused by Ar plasma, resulting in an increase in hydrophilicity. Furthermore, due to the etching effect of Ar plasma, the surface roughness (Sa) of the untreated CNF was 4.76nm, while the surface roughness of the Ar plasma treated CNF was 6.11nm.

3.4 XRD analysis

The diffraction peaks of the ZnO thin film on the Glass substrate were clearly observed. On the other hand, for the CNF substrate, the overall number of peaks decreased, and only the peak on the ZnO (002) plane was observed after Ar plasma treatment. The results show that the crystallinity of the ZnO thin film on the CNF substrate was closer to an amorphous structure by Ar plasma. The suppression of cracks on the CNF substrate is attributed to the increased flexibility of the ZnO film as it approaches an amorphous structure. These reductions in ZnO crystallinity are thought to be due to changes in the crystallinity of the CNF substrate itself and changes in its surface chemistry, which prevent crystal growth and detailed investigation will be conducted in the future.

Conclusion

Ar plasma treatment suppressed the cracks in the ZnO thin film observed on the untreated CNF substrate.This is due to the change in surface chemistry state and the surface etching caused by the Ar plasma treatment in which improved adhesion. Ar plasma treatment not only modified the surface of the CNF substrate, but also affected the crystal structure of the ZnO thin film on the CNF substrate. These results demonstrate the effectiveness of ar plasma treatment in surface modification of CNF substrates and bring us closer to future applications in flexible devices.

Acknowledgments

The CNF samples used in this work were provided by Oji Holdings Co., Ltd.

References:

[1] Y.Kimura et al. J.Mater.Sci., 61, pp760-765 (2012).
[2] S.Iwamor. *Fundamentals and Applications of Polymer Surfaces*, Kagakudojin publication, 1986: pp.76-77.
[3] Y.Ikada. *Polymer surface processing* , Dihodo publication, 2005: pp.89-91.
[4] S.M.Pelagade et al. Nuclear Instruments and Methodsin physics Research., B 289, pp34-38 (2012).

Comparison of α-particle Detection Property of α-Ga_2O_3 and α-GIO Alloys Grown by Mist CVD

Kai Yamada[1], Kotono Yamada[1], Rie Yamada[1], Takumi Yamamoto[1], Tatsuhiro Sakurai[2], Ryohei Kudo[2], Takeyoshi Onuma[1, 3], Tomohiro Yamaguchi[1, 3], Toru Aoki[4], Takayuki Nakano[2, 4], and Tohru Honda[1, 3]

1. Department of Electrical Engineering and Electronics, Graduate School of Engineering, Kogakuin University, Tokyo, Japan
2. Department of Electronics and Materials Science, Shizuoka University, Shizuoka, Japan
3. Department of Applied Physics, School of Advanced Engineering, Kogakuin University, Tokyo, Japan
4. Research Institute of Electronics, Shizuoka University, Shizuoka, Japan

E-mail: cm22045@ns.kogakuin.ac.jp

Abstract

α-Ga_2O_3 and α-GIO thin films were grown by Mist CVD on α-Al_2O_3 substrates. Comb-shaped MSM double Schottky detectors were fabricated using the α-Ga_2O_3 and α-GIO thin films, and α-particle detection properties were evaluated. Detection signal increased by increasing applied bias voltage. Detection signal in α-GIO was larger than that in α-Ga_2O_3.

Introduction

Gallium Indium Oxide [$(Ga_{1-x}In_x)_2O_3$:GIO] is an alloy of Ga_2O_3 and In_2O_3. The combination of wide bandgap in Ga_2O_3 and superior electrical conductivity in In_2O_3 is a big advantage to apply for GIO TFTs in displays[1]. Ga_2O_3 and In_2O_3 have several different polymorphs, among which the corundum-structured α phase has the widest band gaps of 5.3 eV and 3.7 eV, respectively[2, 3]. Therefore, the corundum-structured α-GIO is also expected to be a transparent conducting film for ultrawide band gap optoelectronic devices. The corundum structure is thermally stable phase in α-Al_2O_3 (Sapphire), but is a metastable in Ga_2O_3 and In_2O_3. Growths of high quality α-Ga_2O_3 and α-In_2O_3 have been reported by employing the Mist chemical vapor deposition (Mist CVD)[2, 4]. α-GIO is expected to be applied for radiation detectors because of its large band gap and the fact that its electrical properties are expected to be improved over Ga_2O_3 by the addition of Indium. In this study, α-Ga_2O_3 and α-GIO alloy thin films were grown by Mist CVD. The grown films were irradiated with α particles to compare their detection properties.

Experiment

Ga_2O_3 and GIO alloy were grown on (0001)α-Al_2O_3 substrates by Mist CVD. Experimental conditions are shown in Table 1. The grown thin films were characterized by X-ray diffraction (XRD) and scanning electron microscopy (SEM).

Table 1 Growth Conditions.

Substance	Ga_2O_3	GIO
Solutions	$Ga(C_5H_7O_2)_3$	$Ga(C_5H_7O_2)_3$, $In(C_5H_7O_2)_3$
Temperature	460°C	550°C
Growth Time	60 min	Ga:15min, Ga+In:45min
HCl Conc.	0.10 mol/L	1.2 mol/L

The α particle detectors were fabricated by forming a comb-shaped MSM double Schottky electrode (Au 20 nm/Ni 30 nm) on the α-Ga_2O_3 and α-GIO alloy thin films. The detectors were characterized by irradiating ^{241}Am α particles.

Results and Discussion

Figure 1 shows the XRD patterns of the Ga_2O_3 and GIO alloy films. For the Ga_2O_3 film, 0006 α-Ga_2O_3 diffraction peak was dominantly observed accompanied by the one for 0004 ε-Ga_2O_3. For the GIO film, 0006 diffraction peaks for the α-Ga_2O_3 and α-GIO layers were observed. The In composition of α-GIO was estimated to be 17% from Vegard's law. The MSM detectors of α-Ga_2O_3 and α-GIO were irradiated with ^{241}Am α particles and a bias voltage was applied to obtain a detected pulse signal on an oscilloscope. The dependence on the applied bias voltage was evaluated. Figure 2 shows the measured 2D energy spectra for irradiating α-particles in the α-Ga_2O_3 and α-GIO detectors, where the bias voltages of 50 and 150 V were applied. With increasing applied bias voltage, the α particle detection signal increased in both detectors. The detection signal for the GIO detector was larger than that for the Ga_2O_3 detector.

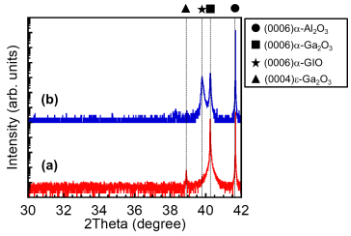

Fig. 1 XRD patterns of (a)Ga_2O_3 (b)GIO alloy films.

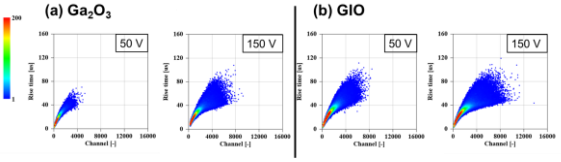

Fig. 2 2D energy spectrum for irradiating α particles in (a)α-Ga_2O_3 and (b)α-GIO detectors at applied bias voltages of 50 and 150 V.

References:

[1] Y. Terai, Sony Co., The Journal of the Institute of Image Information and Television Engineer, **66**, j339 (2012).
[2] D. Shinohara and S. Fujita, Jpn. J. Appl. Phys. **47**, 7311 (2008).
[3] S. Fujita and K. Kaneko, J. Cryst. Growth **401**, 588 (2014).
[4] N. Suzuki, K. Kaneko, and S. Fujita, J. Cryst. Growth **364**, 30 (2013).

ASSESSING SPATIAL ELEMENTS FOR ENHANCED CREATIVITY: A COMPARATIVE STUDY WITHIN KOGAKUIN UNIVERSITY'S CAMPUS

Keigo Hayakawa[1,a] and Daigo Misaki[1,b,*]

[1]Department of Mechanical Engineering, Kogakuin University, Tokyo, Japan
E-mail: [a]am22050@ns.kogakuin.ac.jp, [b]misaki@cc.kogakuin.ac.jp

Abstract

The COVID-19 pandemic has prompted a shift towards remote education in universities and telecommuting in businesses, necessitating a reassessment of conventional campus and office designs. This shift has heightened interest in spaces that enhance creativity, spanning creative environments, workplaces, and educational settings that nurture the design process. In this setting, ten spatial elements believed to boost creativity were proposed. However, their efficacy remains speculative. We examined six pieces in a comparative study within Kogakuin University's campus.

Introduction

While much research has delved into the effect of physical space on productivity in work and educational settings, the impact of spatial design on creativity remains less explored. As we enter an age where artificial intelligence could replace many roles, creativity remains an essential skill to address the challenges of the 21st century. Understanding how specific spatial designs foster creativity can lead to more effective environments that support and accelerate the human creative process.

Earlier studies, such as those by Katja et al. [1], have explored the potential effects of creative spaces on the design process, especially in design thinking, pedagogy, and practical application. They identified five types of spatial configurations essential for creative work. In this context, "spatial attributes" refer to the ability of a space to serve its intended function. Building on this, they proposed ten hypotheses about how spatial designs might impact creativity, though these are yet to be empirically tested [2]. Our study aims to test these hypotheses using Kogakuin University's campus as a case study.

Located in Shinjuku and Hachioji City, Tokyo, Kogakuin University is a private institution with a rich history. Its predecessor, the Koshu Gakko (School of Engineering), established in 1887, was among Japan's earliest private engineering universities. It was founded to prepare engineers to lead industrial advancements, crucial for Japan's modernization. Today, this mission continues as the university seeks to produce science and engineering professionals ready to drive commerce and innovation, reinforcing Japan's position as a global tech leader. Furthermore, the university significantly emphasizes nurturing creativity, leading to continuous updates in its curriculum and campus infrastructure to support this key competence.

Method

Thirteen engineering scholars, all with a background in mechanical engineering, participated in a study at Kogakuin University. Based on their experiences in five specific spaces (illustrated in Figures 1-6) used for various educational activities like lectures, practical exercises, lab sessions, and academic assignments, these scholars assessed six specific spatial attributes related to fostering creativity, as highlighted in previous research. [2] These attributes were analyzed using a 7-point Likert scale questionnaire, depicted graphically in Figure 7. The survey was administered via Google Forms.

It's worth noting that four of the proposed initially ten spatial attributes were omitted from this investigation due to discrepancies that arose during translation from English to Japanese. Thus, our focus was on attributes 1 through 6. To clarify, Space A (Figure 1) is a standard classroom mainly used for lectures on design education for mechanical engineering students. Space B (Figure 2) is a room where students complete lecture assignments individually or in groups. Space C (Figure 3) is designed with whiteboards, seating, and communal workstations, offering an open environment enhanced by background music. Space D (Figure 4) is a dedicated space for lab research discussions between students, instructors, and peers. Space E (Figure 5) is a newly built classroom with a large display and spacious seating. Finally, Space F (Figure 6) is a workshop primarily for mechanical engineering students, mainly for material cutting and fabrication tasks.

Figure 1. Space A

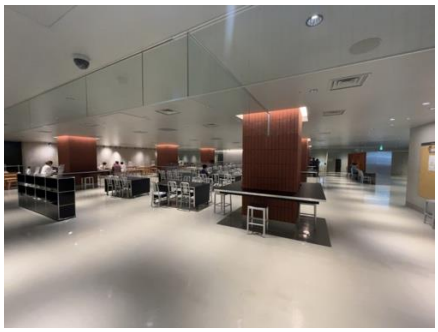

Figure 2. Space B

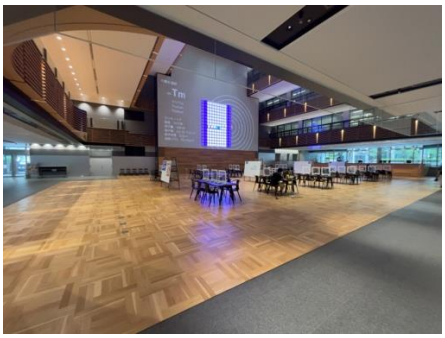

Figure 3. Space C

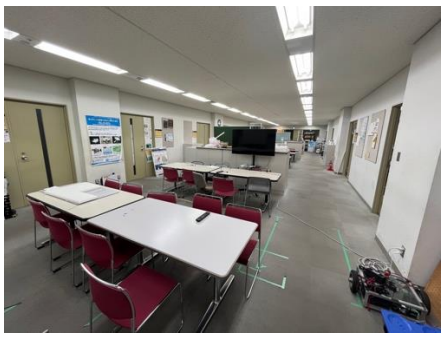

Figure 4. Space D

Figure 5. Space E

Figure 6. Space F

Proposition 1. Space that provides visible sources is conducive to creativity
Proposition 2. Space that provides a void is conducive to creativity
Proposition 3. Space that facilitates encounters and social interaction is conducive to creativity
Proposition 4. Space that provides seclusion and reduced social interaction is conducive to creativity
Proposition 5. Space that provides a balanced ambiance is conducive to creativity
Proposition 6. Space that provides views is conducive to creativity
Proposition 7. Space that provides visual cues is conducive to creativity
Proposition 8. Space that activates bodily movement and participation is conducive to creativity
Proposition 9. Space that provides a platform for ideas is conducive to creativity
Proposition 10. Space that provides variation and change is conducive to creativity

Figure 7. Ten Propositions Proposed

Results and Discussion

Based on the seven-point Likert scale, the findings from our box-and-whisker plot analysis are detailed below. A particular focus is placed on two of the six datasets. The charted data reinforces the assertion: Figure 8 shows that response to "Proposition 1: Space that provides visible source is conductive cues to creativity." In Space B, there's a pronounced level of visual stimulation, positioning it as a prime locale for fostering creativity. On the other hand, while Spaces A and C also present visual stimuli, they do so to a lesser degree than Space B. The data from Spaces D to F show more diversity. It's worth noting that the presence and nature of visual cues in an environment might be influenced by its primary function and the personal inclinations of those using the space. This points to the need for further nuanced exploration.

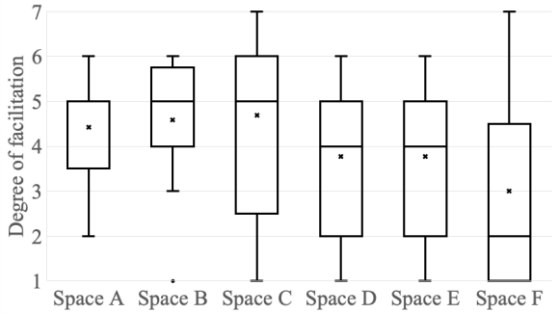

Figure 8. Responses to "Proposition 1: Space that provides visible source is conductive cues to creativity."

Figure 9 depicts the feedback regarding the influence of scenic vistas on creativity. In Space A, there's a narrow range of responses, displaying a notably high average. The classroom's placement on the 16th floor of a high-rise building, offering panoramic views, largely explains this result. Similarly, Space C shows a compact range of feedback, with a high average, further reinforcing the idea that environments with picturesque views may enhance creativity.

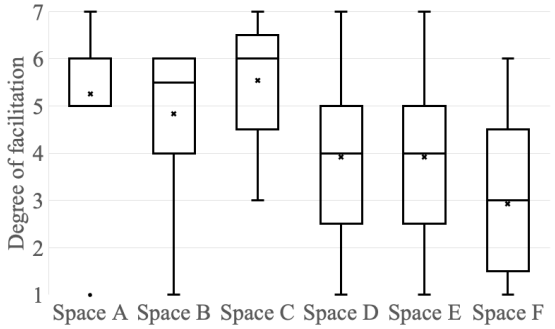

Figure 9. Responses to "Proposition 6: Space that provides views is conductive to creativity."

Conclusion

Our research introduced and applied an analytical method for evaluating Creative Space in higher education, using Kogakuin University as our case study. The results confirmed the method's efficacy, demonstrating its utility for designing Creative Spaces. Moving forward, a potential challenge will be to expand our survey to include a more diverse demographic. Presently, the study targets only mechanical engineering students. We suggest broadening the survey's scope to incorporate students from architecture and information science disciplines, ensuring a more holistic understanding.

References:

[1] Thoring, Katja, Pieter Desmet, and Petra Badke-Schaub. "Creative environments for design education and practice: A typology of creative spaces." Design Studies 56 (2018): 54-83.

[2] Thoring, K., Gonçalves, M., Mueller, R., Desmet, P., & Badke-Schaub, P. 2021 Aug 31. The Architecture of Creativity: Toward a Causal Theory of Creative Workspace Design. International Journal of Design

Analysis of Echocardiographic Probe Attitude for Improve Technical Proficiency

Daiki Sekine[1], Junji Yamato[2], Dan Mikami[3], Yasuyoshi Takei. MD. PhD[4]

Informatics Program, Graduate School of Engineering, Kogakuin University[1]
Department of Information Science, Kogakuin University[2]
Department of Computer Science, Kogakuin University[3]
Department of Cardiology, Tokyo Medical University[4]
E-mail: em23024@g.kogakuin.jp

Abstract

The purpose of this study is to effectively support the improvement of health care provider's proficiency. To achieve this, we investigated the movements that affect the accuracy of measuring cardiac function indicators by sensing the echocardiographic probe and differences in movement across years of experience. We attached a 9-axis sensor [4] to the probe to perform sensing, and we used Euler angles x-y-z for analysis, with the left ventricular ejection fraction (EF) value serving as the indicator for cardiac function. Additionally, differences around the y-axis were observed across years of experience, suggesting a relationship between the length of experience and measurement accuracy.

1. Introduction

1.1. Background

An echocardiography is a common test that measures and evaluates cardiac function, including blood flow and heart movement, from cross-sectional images of the heart (echocardiogram). Echocardiograms are obtained by directly placing a device called an echocardiographic probe, which emits ultrasound, on the patient's skin. Ultrasound refers to sound waves with a frequency exceeding 20KHz. There are various types of echo probes, and the frequency of sound waves they emit and the shape of the probe vary depending on the location to be examined. In this echocardiography, the probe emits ultrasound waves with frequencies ranging from 1 to 5MHz, which are then reflected back to the probe. The reflected sound waves are captured by the probe and converted into image by a computer. Therefore, to obtain clear echocardiograms, it is necessary to accurately position the probe each time, and it is estimated that approximately 10,000 examinations are required to become proficient. In other words, the technician's skill is a critical factor in cardiac echocardiography. After obtaining the echocardiograms, cardiac function indicators are measured and evaluated.

Previous research on echocardiography has mainly focused on the automatic measurement of cardiac function indicators [1][2][3]. Many of these studies assume the presence of clear echocardiograms. However, there is limited quantitative research on obtaining clear echocardiograms and research on improving technical proficiency.

1.2. Objective

Our objective is to support the improvement of health care provider's proficiency. Therefore, in this study, we investigate the impact of movements related to the probe's attitude on the accuracy of cardiac function indicators and explore differences in the probe's attitude across years of experience.

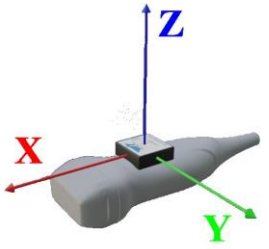

Fig. 1 Relationship between the Probe and Axes

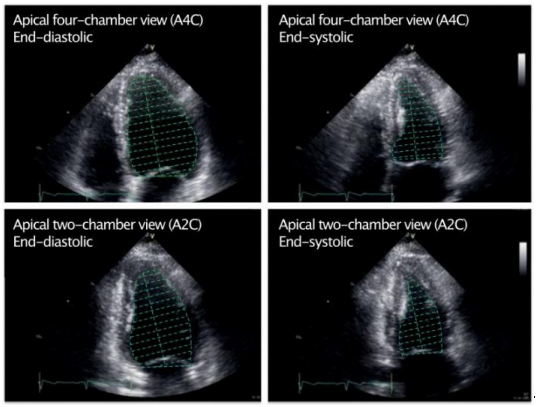

Fig. 2 Illustration of Two echocardiograms during Diastole and Systole. [5]

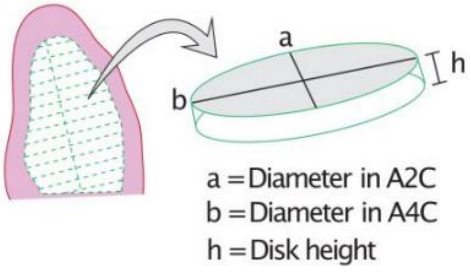

Fig. 3 Calculation of Volume. [5]

2. Methods

We attached a 9-axis sensor [4] to the probe to perform sensing. The measurements from this 9-axis sensor were angles corrected for gyro drift using a Kalman filter, representing Euler angles in the z-y-x sequence. The angle accuracy is ±0.05 degrees. Additionally, the orientation representation within the experiments used Euler angles x-y-z, which were transformed using rotation matrices. The relationship between the sensor's axes and the probe is as shown in Figure 1, with rotations around each axis being recorded. The EF value of the left ventricle, obtained using the Simpson method, was used as the cardiac function indicator. According to reference [5], "Simpson's biplane method requires tracing (i.e drawing a line along) the endocardium in apical four-chamber view (A4C) and apical two-chamber view (A2C) in diastole and systole. The entire endocardium, from mitral annulus to mitral annulus must be traced (Figure 2). The ultrasound system then divides the area into a number of equal disks and reconstructs these so that volumes can be calculated." The volume calculation formula is as follows:

$$V = \frac{\pi}{4}\sum_{i=1}^{n} a_i b_i \frac{L}{n}$$

It is understood that A4C and A2C are orthogonal for the volume calculation formula. Additionally, the EF value is determined using the formula below, which utilizes the left ventricular end-diastolic volume (LVEDV) and left ventricular end-systolic volume (LVESV) obtained during the diastolic and systolic phases, respectively. The calculation formula is as follows:

$$EF = \frac{(LVEDV - LVESV)}{LVEDV} \times 100$$

2.1 Experiment1

In Experiment 1, we measured the changes in the probe attitude from A4C to A2C and investigated the actual state of echocardiography. In particular, the experiment focuses on the rotation around the x-axis. This is to verify whether the probe has rotated 90 degrees around the x-axis as part of measuring the EF value using the Simpson method. The data was obtained from a total of 51 measurements, including three veterans with over 10 years of experience and two novices with less than 5 years of experience. There were two patients, both of whom were healthy individuals without any heart conditions. We also conducted a correlation analysis to examine the relationship between rotations along each axis and EF values. It aims to elucidate the movements of axes that can affect measurement accuracy within the range of movements that frequently occur during actual measurements through correlation analysis.

2.2 Experiment2

In Experiment 2, we performed a more detailed analysis of the effects of rotations around the x-axis and y-axis on EF.

We use the X-Plane feature, which is a part of the xMATRIX technology developed by Philips, to analyze movements around the axes. Specifically, it is known as iRotate and allows the rotation of the ultrasound beam inside the probe while keeping the probe's attitude fixed. This enables visualization even in obstructed views between the ribs. In Experiment 2, we employ this functionality to acquire data when rotating only around the x-axis.

For movements around the y-axis, we perform geometric numerical simulations using Python. The simulation involves conducting a virtual echocardiography in a virtual space (Figure 4). We define an equation for an ellipsoid that resembles the shape of the left ventricle and, similar to the ultrasound beam, determine the intersection between the plane and the ellipsoid. The intersection takes on a shape akin to cutting the ellipsoid in half, from which we apply the Simpson's rule on the plane's coordinates to calculate the EF value. The equation for the ellipsoid is as follows, with parameters set based on actual echocardiogram.

$$\begin{cases} \begin{cases} \left(\frac{2.1}{x}\right)^2 + \left(\frac{2.1}{y}\right)^2 + \left(\frac{2.0}{z}\right)^4 & (LVEDV) \\ \left(\frac{1.6}{x}\right)^2 + \left(\frac{1.6}{y}\right)^2 + \left(\frac{1.6}{z}\right)^4 & (LVESV) \end{cases} & (z \geq 0) \\ \begin{cases} \left(\frac{2.1}{x}\right)^2 + \left(\frac{2.1}{y}\right)^2 + \left(\frac{6.0}{z}\right)^4 & (LVEDV) \\ \left(\frac{1.6}{x}\right)^2 + \left(\frac{1.6}{y}\right)^2 + \left(\frac{4.8}{z}\right)^4 & (LVESV) \end{cases} & (z < 0) \end{cases}$$

These analyses allow for a more detailed and quantitative examination of movements related to the axes that affect measurement accuracy.

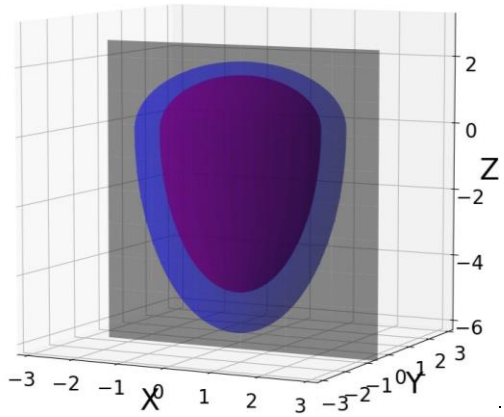

Fig. 4 Virtual Echocardiography Simulation Using Geometric Numerical Simulation.
LVEDV is represented in blue, LVESV in red, and the gray plane represents the ultrasound beam.

2.3 Experiment3

In Experiment 3, we analyzed differences in probe attitude between veterans and novices. We constructed a prediction model for distinguishing veterans from novices based on the changes in attitude between two views using the K-nearest neighbors (KNN) method. The data used in Experiment 2 were the same as in Experiment 1, but this time they were labeled as "veteran" and "novice". The training and test data were split into a 7:3 ratio for random, and the accuracy was computed as the average of 1000 repetitions. we used the permutation feature importance (PFI) value to measure the axis with the most significant impact on predictions in the model. The PFI value was also averaged over 1000 repetitions.

3. Results

3.1 Changes in Probe Attitude from A4C to A2C

The result presents the changes in probe attitude from A4C to A2C, as shown in Figure 5. The results indicated rotations of approximately -25 to -50 degrees around the x-axis, 0 to 5 degrees around the y-axis, and 0 to 10 degrees around the z-axis. It was evident that the two view were not orthogonal. When we conducted a correlation analysis between each axis and EF values, the x-axis showed -0.17, the y-axis -0.17, and the z-axis -0.36, suggesting weak negative correlations for all axes.

3.2 Impact of x-axis and y-axis on EF Values

We analyzed the relationship between x-axis rotations and EF values using xPlane, as shown in Figure 6. The results revealed that rotations around the x-axis had little influence on EF values. Furthermore, a geometric numerical simulation was used to analyze the relationship between y-axis rotations and EF values (see Figure 7). This analysis demonstrated that rotations around the y-axis and EF values had an exponential relationship. It indicated that EF values sharply increased when there was more than a 5-degree rotation around the y-axis between A4C and A2C. However, we also demonstrated that in cases where there is a translational movement in the z-axis direction from the A4C position, adjusting the y-axis can maintain the accuracy of EF value measurements.

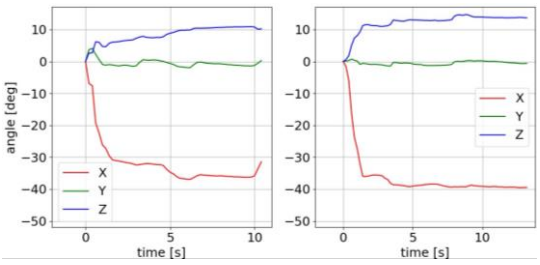

Fig. 5 Changes in Probe Orientation from A4C to A2C.
X-axis is predicted as -90 degrees, but the results are -30 degrees and -40 degrees.

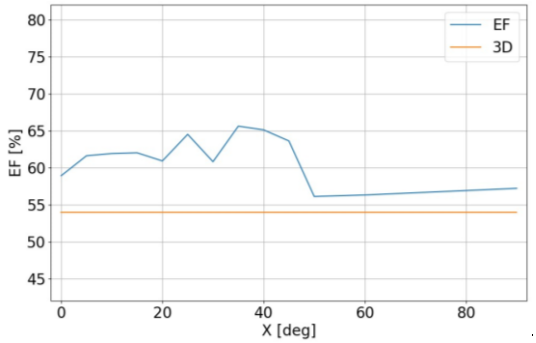

Fig. 6 Influence of x-Axis on EF Values.
Rotating around the x-axis does not significantly affect EF values (measurement error is 5%)

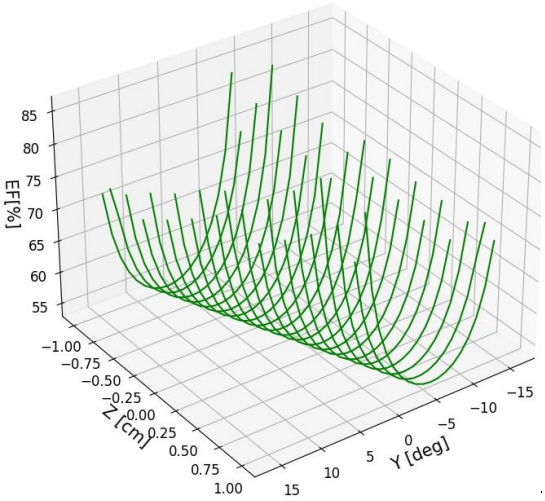

Fig. 7 Influence of y-Axis on EF Values.
Rotation around the y-axis leads to an exponential increase in EF values.

3.3 Analysis of Probe Attitudes for Veterans and Novices

We built a prediction model using KNN to classify the probe attitude changes between veterans and novices in Experiment 3. The results showed that a model with an accuracy of 0.77 could be created. Additionally, the average PFI values for the model were 0.03 for the x-axis, 0.29 for the y-axis, and 0.04 for the z-axis. Thus, it was demonstrated that the y-axis had a significant impact on the prediction errors between veterans and novices. Furthermore, a difference was observed, where veterans tended to incline the y-axis negatively, while novices inclined it positively (see Figure 8).

4. Discussion

4.1. X-axis Did Not Rotate 90 Degrees

The reason for the x-axis movement range being between -25 to -50 degrees is believed to be due to the limited movement around the x-axis, as the vertical dimension of the fifth intercostal space, which captures the apex of the heart, is shorter than the width of the probe. Additionally, movements around the y-axis and z-axis are considered necessary to obtain clear echocardiograms.

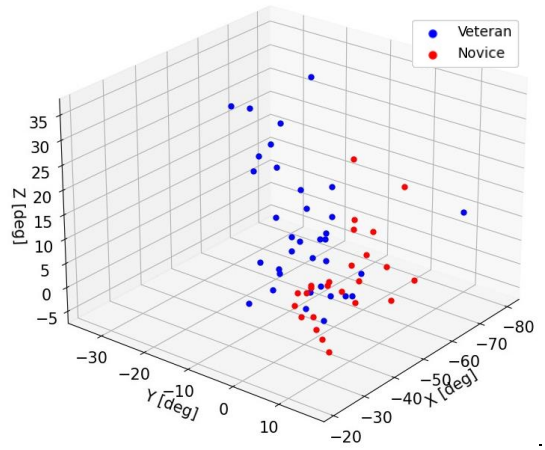

Fig. 8 Scatterplot of Changes from A4C to A2C. Veterans rotate in the negative direction around the y-axis, while novices rotate in the positive direction.

4.2. Y-axis Had a Strong Impact on EF Values

Regarding the relationship between the x-axis and EF values, we found no significant impact. This is likely because the echocardiogram of the left ventricle when sliced in the long axis direction is close to a perfect circle. Moreover, errors related to angular displacement in x-axis rotations are canceled out in the EF value calculation formula, resulting in a weak influence of x-axis movements on EF value fluctuations. On the other hand, y-axis rotations had a strong impact on EF values. This is because differences in the direction of cardiac muscle motion occur between the disks of the left ventricle within the echocardiogram. In other words, all the cardiac muscle segments within the view, needs to move in the same direction. However, tilting along the y-axis results in differences in cardiac muscle motion between the apex and the mitral valve regions, leading to significant variations in the end diastole and end systole volumes. We believe that this difference becomes more pronounced with increasing displacement along the y-axis, suggesting an exponential relationship between these variables. Nevertheless, it was found that intentionally adjusting the y-axis when there is translational movement in the z-axis direction from the A4C position can maintain the accuracy of EF value measurements. Hence, we consider that adjustments along the y-axis may be necessary depending on the situation. Furthermore, movements around the z-axis are considered irrelevant to EF value measurement accuracy.

4.3. There Was a Strong Relationship Between Years of Experience and y-axis Fluctuation

The angle that significantly influences KNN prediction errors is the y-axis. Regarding the y-axis, we believe that the strong impact of y-axis rotations on EF value measurement accuracy is why veterans tend to take measurements in the probe attitude where errors are less likely to occur. Additionally, the reason veterans often move the y-axis in the negative direction is to compensate for discrepancies caused by translational movements in the z-axis direction.

5. Conclusion

The results of this study imply a close relationship between the probe attitude and the accuracy of cardiac function indicators. Furthermore, it implied technicians with longer years of experience can measure cardiac function indicators with higher accuracy. In the future, we will conduct further analysis to enhance the health care provider's proficiency. Specifically, we will perform more detailed analyses by incorporating probe's fluctuation movements resulting from the motion around the y-axis. Additionally, we will utilize eye-tracking cameras to analyze differences in gaze between different years of experience.

6. References

[1] Kai WANG, Jiwei ZHANG, Takeshi HOZUMI, Haiyuan WU, Autonomaed Segmentation of Left Ventirular Wall and Extraction of Left Ventricular Cavity in Echocardiographic Images by Deep Learning, 59−64 (2021)

[2] Kiyoko YOSHIZUMI, Hiroyuki TODE, Yuki OKANIWA, Mihoka IWASAKI, Yasuyuki KOBAYASHI, Eiji YAMASHITA, Availability of Semi-automatic Measurements of Left Vetricular Volume and Ejection Fraction by 2D and 3D Echocardiography, 181−190 (2012)

[3] Naruhiro Yoshimura, Akira Shiozaki, Yutaka Hirano, Hisakazu Uehara, Tohru Masuyama, Endocardial Contour Extraction of Echocardiogram, 337−338 (2005)

[4] WT901BLECL MPU9250, WiTmotion, 23/07/2023, https://www.wit-motion.com/

[5] a"Simpson's biplane method for calculation of eje-ction fraction(EF)", ECG & ECHO LEARNING, 10/09/2023, https://ecgwaves.com/

[6] Xmatrix Transducer Technology is changing the exam experience, PHILIPS, 11/09/2023, https://www.philips.co.jp/

Early Detection of Cognitive Decline Using Anteroposterior Asymmetry of Brain Activity During Visual Attention Task

Hiroyuki ABE [1]*, Hisaya TANAKA [1], Akito TSUGAWA [2], Naoto TAKENOSHITA [2], Tomohiko SATO [2], and Soichiro SHIMIZU [2]

[1] Graduate School of Engineering, Kogakuin University, Tokyo, Japan
[2] Department of Geriatric Medicine, Tokyo Medical University, Tokyo, Japan
*E-mail: em23002@ns.kogakuin.ac.jp

Abstract
This study aimed to clarify the relationship between cognitive decline and changes in electroencephalogram characteristics, which revealed a significant difference in the anteroposterior asymmetry of the alpha wave band between cognitively healthy individuals and those with mild cognitive impairment.

1. Introduction
The increasing number of individuals with dementia worldwide has become a social issue. In contrast, advances in medical science have facilitated early dementia detection while improving the control of symptom progression and the implementation of appropriate treatments to gain normal health [1]. Therefore, early detection of mild cognitive impairment, which precedes dementia, is essential.

Our research group is developing a dementia screening tool using the P300 speller, a character-input brain-computer interface (BCI). Kurihara et al. demonstrated the relationship between spelling-error distance value and cognitive decline [2]. Fukushima et al. developed a machine learning classification model using electroencephalogram (EEG) indicators obtained with the P300 speller and achieved high accuracy for the classification of individuals with and without dementia [3]. In contrast, this machine learning model has not yet achieved sufficient accuracy in the classification of mild cognitive impairment and healthy individuals and lacks an effective EEG indicator as a feature.

Elderly individuals initially exhibit impaired frontal lobe function, and temporal and occipital lobe function declines with dementia progression [4]. Given that Nishizawa et al. observed that functional connectivity determined with EEG during tasks increased with cognitive decline [5], we hypothesized that the anteroposterior asymmetry in brain activity decreased with mild cognitive impairment.

The present study aimed to identify biologic indicators for the early detection of mild cognitive decline. We examined changes in the anteroposterior asymmetry of brain activity during visual attention tasks in association with cognitive decline. The identification of biologic indicators associated with early cognitive decline will enable the early diagnosis of mild cognitive impairment.

2. Experiment
2.1. Subject details
The study included 73 patients with ages ranging from 64 to 91 years, with a mean age of 79.19 ± 5.49 years, who visited the Department of Geriatric Medicine in Tokyo Medical University from 2016 to 2022 and were classified as those without dementia based on a Mini-Mental State Examination score of 24–30. Based on the frontal assessment battery scores, the subjects were classified into the cognitively healthy (F0) group (≥12 points) and mild cognitive impairment (F1) group (<12 points). The study was approved by the Ethics Research Committees of Kogakuin University (approval no. 2021–B–30) and Tokyo Medical University (approval no. 2016–083) and performed in accordance with the tenets of the Declaration of Helsinki.

2.2. BCI Task
In this experiment, the P300 speller was used as the stimulus presentation device for the visual attention task [2]. Figure 1 demonstrates the dial of the BCI screen from the subject's perspective. Figure 2 shows the experiment landscape. The display illuminated rows and columns in a random sequence. Each row and column blinked 5 times, and each letter blinked 10 times. The stimulus interval was 210 ms, including 120 ms for the letters to light up and 90 ms for the lights to go off. Subjects were instructed to vocalize the target letter each time it blinked on the Japanese letter dial. This was repeated for the specified number of characters in each trial. The trial was conducted four times in total.

2.3. BCI System
The BCI system used in this experiment is shown in Figure 3. EEG measured by active wet electrodes (LADYbird electrode; g.tec Medical Engineering,

Fig. 1. Dial of the BCI screen

Fig. 2. Experiment landscape

Schiedlberg, Austria) and active seal electrodes (g,GAMMAclip electrode; g.tec Medical Engineering) were placed in an electrode box (g.GAMMAbox; g.tec Medical Engineering). The signals were then amplified by a bio-amplifier (g.USBamp; g.tec Medical Engineering) and observed on a laptop computer. The low-pass, high-pass, and notch filters were set at 30, 0.5, and 50 Hz, respectively. Stimulus presentation of the dial was controlled from a laptop computer and output was visualized on a display (G227HQL; Acer, New Taipei City, Taiwan) via a video graphics array connector. EEG measurements and stimulus presentation were performed using a numerical analysis software (MATLAB 2012a; MathWorks, Massachusetts, USA). The numerical analysis software (MATLAB R2023a; MathWorks) was used for analysis and statistical processing. Active wet electrodes were placed on eight locations (F_Z, C_Z, P_3, P_Z, P_4, PO_7, O_Z, and PO_8) according to the extended 10–20 system [6]. Similarly, active seal electrodes were placed at the center of the forehead (FP_Z) as the ground electrode and at the earlobe (A2) as the reference electrode.

2.4. Analysis

Measured EEG data from 100 ms before the first letter illumination to 700 ms after the last letter illumination were extracted. Cumulative spectral intensity was calculated for each frequency band specified for the extracted EEG data, and the difference in the proportion of the cumulative spectral intensities for the frontal (F_Z) and occipital (O_Z) areas based on the extended 10–20 system was calculated in each band. The sampling frequency was 256 Hz. In the present study, the frequency bands of delta (0.5–4 Hz), theta (4–8 Hz), alpha (8–13 Hz), and delta (13–30 Hz) waves were analyzed. The calculated value was defined as the anteroposterior asymmetry of EEG components. Statistical analysis included Welch's *t* test of the anteroposterior asymmetry between the cognitively healthy participants and those with mild cognitive impairment.

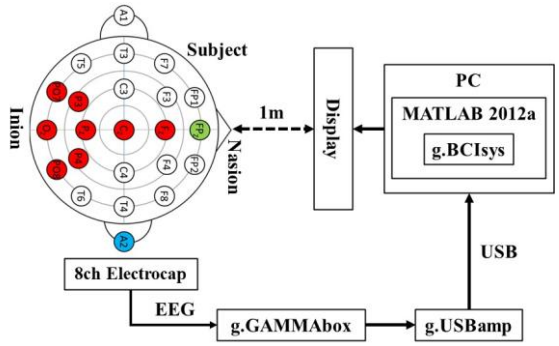

Fig. 3. System configuration for BCI

3. Results and Discussion

Figure 4 shows the anteroposterior asymmetry of EEG components in each cognitive function. The anteroposterior asymmetry of EEG components in all four frequency bands was lower in the mild cognitive impairment group than in the cognitively healthy group. The anteroposterior asymmetry in the alpha wave band was significantly different between the cognitively healthy and the mild cognitive impairment groups by Welch's *t* test ($p < 0.05$).

The observed decrease in the anteroposterior asymmetry associated with early cognitive decline appeared to be due to reduced frontal lobe function. These results are consistent with previous studies showing increased connectivity and brain activity with cognitive decline. In the present study, the difference in the anteroposterior asymmetry in the low-frequency band was due to the slowing of the EEG. Patients with dementia have slow brain waves [7], which leads to increased low-frequency bands components that increases the anteroposterior

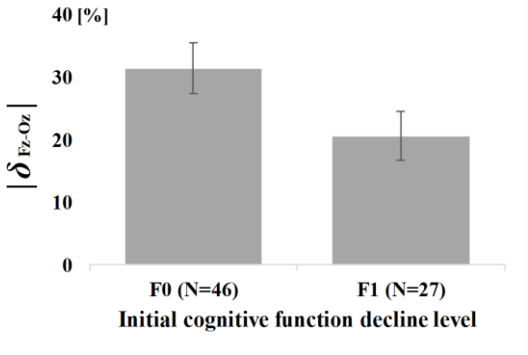

Fig. 4.1. Comparison of the anteroposterior asymmetry of delta wave band between the two groups

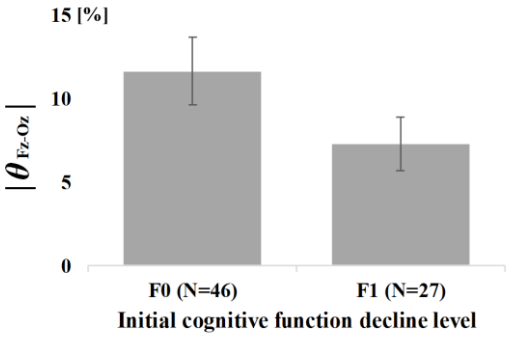

Fig. 4.2. Comparison of the anteroposterior asymmetry of theta wave band between the two groups

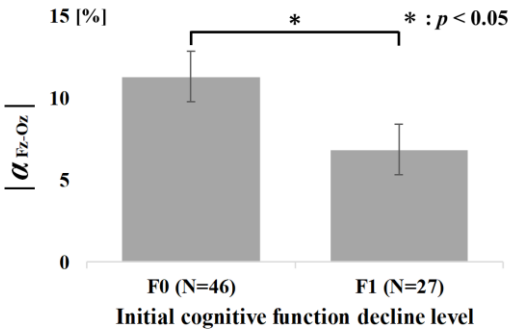

Fig. 4.3. Comparison of the anteroposterior asymmetry of alpha wave band between the two groups

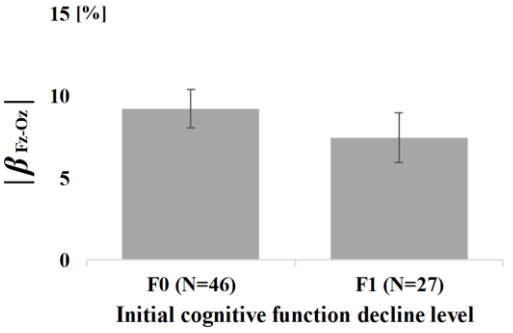

Fig. 4.4. Comparison of the anteroposterior asymmetry of beta wave band between the two groups

asymmetry. On the other hand, the difference in anteroposterior asymmetry between the cognitively healthy participants and those with mild cognitive impairment was smaller in the delta and theta wave bands than that observed in the alpha wave band. The differences were influenced by the frequency of the visual stimuli. The frequency of the visual stimuli in this study was 4.8 Hz. The F_Z electrode was close to the eyes; thus, event-related potentials due to visual stimulation were included in the EEG component. The consequently increased delta and theta wave components in the frontal area of both the cognitively healthy participants and those with mild cognitive impairment led to reduced differences in the anteroposterior asymmetry between the two groups. Overall, these results indicated that the anteroposterior asymmetry was effective in the early detection of cognitive decline.

4. Conclusion

The present study aimed to identify biologic indicators for the development of a screening tool for the early detection of cognitive decline. We examined changes in the anteroposterior asymmetry of brain activity during a visual attention task in participants with cognitive decline.

Our analyses revealed a decreasing trend of anteroposterior asymmetry of the EEG component with cognitive decline. In addition, the anteroposterior asymmetry in the alpha wave bands was significantly different between cognitively healthy participants and those with mild cognitive impairment. These results indicated that the decrease in anteroposterior asymmetry of brain activity follows a decline in frontal lobe function in the early stages of dementia and increased connectivity and brain function in early cognitive decline.

Overall, these results indicate that the anteroposterior asymmetry during the visual attention task is an effective indicator of early cognitive decline. In future studies, we will develop a cognitive function classification model based on EEG indicators.

Acknowledgements

We are extremely grateful for the cooperation of all participants who were involved in the study. We also want to thank Tokyo Medical University Hospital Elderly General Medicine Field who helped secure and implement the experiment space. A research grant from Tokyo Medical University and Kogakuin University for joint research on medical-engineering collaboration helped fund part of this study. Furthermore, this study was funded by the JSPS Grant-in-Aid for Scientific Research (JP22K12913).

References

[1] J. Wu and S. Tsumoto, “Neuromedical Engneering -Integration of Neuroscience, Engineering, and Information Science-”, Ohmsha, (2009).

[2] R. Kurihara, R. Morooka, S. Hamanaka, H. Tanaka, T. Umahara, A. Tsugawa, and H. Hanyu, “A New Method for the Cognitive Function in Dementia Using the Spelling-BCI”, *The Transactions of Human Interface Society*, **21**(1), 21–30 (2019).

[3] A. Fukushima, R. Morooka, H. Tanaka, H. Kentaro, A. Tugawa, and H. Hanyu, “Classification of Dementia Type Using the Brain-Computer Interface”, *Artificial Life and Robotics*, **26**(2), 216–221 (2021).

[4] M. Kaneko, “Dementia and Frontal Lobe Function”, *Higher Brain Function Research*, **10**(2), 127–131 (1990).

[5] Y. Nishizawa, H. Tanaka, A. Tsugawa, S. Shimizu, T. Sato, and R. Fukasawa, “Prediction of Mild Cognitive Impairment Using P300-Speller BCI – Studies of the EEG with Tsallis Entropy and Coherence –”, *The Transactions of Human Interface Society*, **25**(1), 1–10 (2023).

[6] F. Sharbrough, G.E. Chatrian, R.P. Lesser, H. Luders, M. Nuwer, T. Picton, “American Electroencephalographic Society Guidelines for Standard Electrode Position Nomenclature”. *Journal of Clinical Nurophysiology*, **8**(2), 200-202 (1991).

[7] Japan Society for Dementia Research, “Dementia Textbook”, Chugaiigakusha, (2008).

2023 International Symposium on Advanced Technology (ISAT-22)
Tainan City, Taiwan, October 19-20, 2023

Dependence of N^+ or N_2^+ ion implantation on photocatalytic properties of anodic niobium oxides

Masayuki Ikeya*, Hidetaka Asoh and Ichiro Takano*****

*Electrical engineering and electronics, Graduate school of engineering, Kogakuin university, Tokyo, Japan
E-mail: cm23004@g.kogakuin.jp
**Department of applied chemistry, School of advanced engineering, Kogakuin university, Tokyo, Japan
E-mail: asoh@cc.kogakuin.ac.jp
***Department of electrical and electronic engineering, School of engineering, Kogakuin university, Tokyo, Japan
E-mail: ct97912@ns.kogakuin.ac.jp

Abstract

Previous studies have reported that implantation of nitrogen ions into niobium oxide layers prepared by anodic oxidation improves the photocatalytic effect. In this study, dependence of photocatalytic effects on implantation doses or depth was investigated by using N^+ or N_2^+ ions for implantation.

Photocatalytic materials have been studied mainly on oxides of transition metals such as Ti and Ta. On the other hand, Nb which is in the same family as Ta, is also attracting attention as one of new photocatalytic materials. However, the photocatalytic effect of niobium oxides is not sufficient under visible light, and expansion of the absorption wavelength range is a problem. There are methods to expand the absorption wavelength of photocatalysts by adding impurities such as nitrogen.[1] By doping nitrogen, a portion of oxygen is replaced by nitrogen atoms to form a new order at the band gap edge of the conductor, thereby expanding the absorption wavelength and enabling a response to visible light. Among various methods of nitrogen doping, the ion implantation method, which allows any combination of implanted ion species and substrate, is used for nitrogen doping.

The sample substrate was a 0.3 mm thick niobium foil (99.9%) cut into 20 × 20 mm. After ultrasonic cleaning with acetone for 3 minutes, the substrate was charged with a phosphoric acid solution with a concentration of 0.01 mol/dm^2 as the electrolyte solution for 10 minutes at a voltage of 60 V and an electric field temperature of 20 °C to produce a barrier film of Nb_2O_5.

For ion implantation into Nb_2O_5 thin films, an ion beam line of the multi-process coating system was used. An N_2 gas was ionized in a Freeman-type ion source, and after the ions were extracted from acceleration electrodes, only N^+ or N_2^+ ions were selected by a mass spectrometer. In this experiment, the energy and irradiation time of an ion beam with φ20 mm were varied.

Photocatalytic effects were measured by a methylene-blue solution immersion test. A quartz cell was filled with the methylene-blue solution at a concentration of 10 ppm and the immersed samples were irradiated an artificial sunlight lamp. Using a spectrophotometer, the chromaticity changes (667 nm) of the solution were measured on a regular basis for 6 hours and evaluated as the photocatalytic effect.

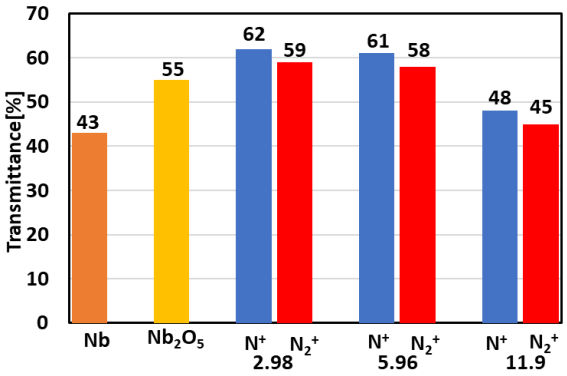

Fig.1 Photocatalytic properties by the methlenen blueimmersion test

The transmittance of the methylene blue immersion test at 6 hours is shown in Fig. 1. In all samples, an increase in transmittance over the spontaneous degradation of the methylene blue solution due to light irradiation was observed. In the case of the N^+ ion implantation, the sample irradiated with 2.98×10^{16} ions/cm^2 increased 9 points and 5.96×10^{16} ions/cm^2 increased 5points against the unirradiated sample. In the case of the N_2^+ ion implantation, the sample irradiated with 2.98×10^{16} ions/cm^2 increased 6 points and 5.96×10^{16} ions/cm^2 increased 8 points against the unirradiated sample. In general, the implanted depth of N_2^+ ions is half that of N^+ ions and the amount of N atoms implanted is twice as much. In Figure 1, N^+ ions with deeper implantation depths showed higher transmittance.

In this study, the relationship between nitrogen implantation depth and irradiation dose into Nb_2O_5 was investigated and the effect of nitrogen implantation was obtained on the photocatalytic effect.

References:

[1] R.Asahi, T.Morikawa, T.Ohwaki and Y.Taga; “Visible-light photocatalysis in nitrogen-doped titanium oxides”; Science 293, 269-271(2001)

2023 International Symposium on Advanced Technology (ISAT-22)
Tainan City, Taiwan, October 19-20, 2023

Improved Simulation for Statistical Integrated Analysis Method of MicroRNA and Gene Expression

Keita Kodama and Yutaka Fukuoka

Department of Electrical and Electronic Engineering, Kogakuin University, Tokyo, Japan
E-mail: cm23026@ns.kogakuin.ac.jp, fukuoka@cc.kogakuin.ac.jp

Abstract

MicroRNA (miRNA) is known to suppress the expression of target genes and there is an increasing number of studies analyzing various miRNAs in cancer. It is often difficult to obtain a significant result by an integrated analysis of miRNA and gene expressions with a small amount of data. The authors proposed a method that allows integrated analysis even with a small amount of miRNA and gene expression data, and examined its validity. However, the condition used in the simulation was too ideal, and the condition was highly unlikely in reality. In this study, we employed a more realistic condition, a many-to-many relationship between miRNAs and genes, in the simulation. We then investigated the effectiveness of the proposed method. The simulation results indicated that the proposed method allows us to extract gene functions of differentially expressed target genes regulated by a specific miRNA with a small amount of data.

1. Introduction

MicroRNA (miRNA), a type of non-coding RNA, is known to suppress the expression of target genes and there is an increasing number of studies analyzing various miRNAs in cancer [1]. In an integrated analysis of miRNA and gene expressions, it is often difficult to obtain a significant result with a small amount of data.

The authors proposed a method that allows integrated analysis even with a small amount of miRNA and gene expression data, and examined its validity [2]. The method is based on a group comparison between target genes having specific functions controlled by a specific miRNA and a background group of randomly selected genes. We conducted a simulation to verify the validity of the proposed method. However, the condition used in the simulation was too ideal, i.e., the expressions of all target genes of a specific miRNA were changed according to the expression level of the miRNA. This is highly unlikely in reality.

In this study, we employed a more realistic condition in the simulation. In the simulation, we assumed that only a part of the target genes of a specific miRNA are changed according to the expression level of the miRNA. The simulation results indicated that the proposed method was still able to detect significant differences in expression of target genes controlled by a miRNA showing significant expression change. We then applied the proposed method to real data derived from multiple myeloma cells.

2. Simulation

The purpose of the simulation was to verify whether the distribution of t-statistics of target genes regulated by a miRNA varies in response to a change in expression level of the miRNA. We used expression data obtained from four cell lines derived from multiple myeloma measured twice under two conditions (normal and hypoxia). The measurements were performed using Affymetrix genechips. For miRNAs, their expression levels were measured once in each cell line under each condition with the Taqman PCR method. In total, there were 16 expression values for each gene and 8 values for each miRNA. The data set was provided by the Division of Molecular Oncology, Institute of Medical Science, Tokyo Medical University.

First, the mean value and standard deviation of the expression levels of all genes were calculated. The mean value and the standard deviation were used to generate simulation data following a normal distribution with the mean value and the standard deviation. We set three different expression levels of miRNA-regulated genes to investigate the effect of expression change on the result: the mean value, 50% of the mean value, and 30% of the mean value. There was no change in expression when the mean value itself was used for the simulation while significant change in expression (i.e., differential expression) may occur when the 50% and 30% of the mean value were used.

As mentioned earlier, the relationship between miRNAs and genes is assumed to be many-to-many, i.e., only a part of the target genes was regulated by a miRNA. We used three different percentages: i) 20% of the target genes were changed with the expression of the miRNA in question (miRNA-93 in this study), ii) 10% and iii) 5% of the target genes were changed with the miRNA expression. In i), the other 80% of the target genes are assumed to be regulated by other miRNAs and factors.

Using these simulation data, the expression levels of the genes with specific functions regulated by miRNA-93 were compared with the background expression levels (1000 randomly selected genes), and the p-values were calculated using the Wilcoxon rank sum test. This is performed 100 times for each

data set to examine how the p-values vary with the expression levels of the genes and the percentage of the target genes regulated by the specific miRNA.

3. Results and Discussion

Figure 1 shows the p-values from the Wilcoxon rank some test comparing the target genes having a specific gene function (total number of genes: 192) and the background genes when the 20% of the target genes regulated by miRNA-93 were changed. In the figure. results from 100 trials under three different expression changes. As shown in Fig. 1, the distribution of t-statistics for the randomly selected gene group (background) and the miRNA-regulated gene group showed marked differences when 50% and 30% of the mean value were used to generate the simulation data, demonstrating that the resultant p-value changed in response to the expression change in the expression levels of the miRNA-regulated gene group.

It was suggested that a smaller p-value in the real data on multiple myeloma indicates a significant change in the expression levels of genes regulated by a specific miRNA. It is, therefore, considered that the p-value can be used as an indicator of the degree of differential expression among the genes having a specific function.

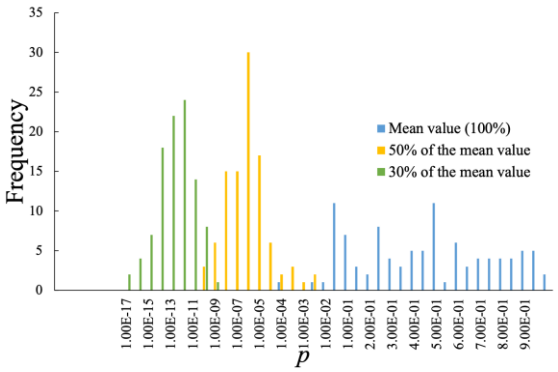

Fig. 1 Distribution of p-values for 20% of the genes regulated by miRNA-93

4.Summary

In this study, simulations were conducted assuming a many-to-many relationship between miRNAs and genes. The simulation results indicated a significance probability (p-value) can be used as an indicator of the degree of differential expression of target genes having a specific function, suggesting the effectiveness of the proposed method even under a realistic condition.

References:

[1] S. Nam, M. Li, K. Choi, C. Balch, S. Kim, K.P. Nephew, *Nucleic Acids Res*., **37**, Web Server issue, W356–W 362 (2009).

[2] T. Oki, Y. Fukuoka, T. Umezu, J. Ohyashiki, *IEICE Tech Rep*., MBE2016-101 (2017) (in Japanese).

Formation of ITO electrodes on InGaN-based p-n junction ordered nanocolumn arrays with different column periods

R. Shindo[1]*, H. Akagawa[1], T. Yamaguchi[1], R. Togashi[2,3], I. Nomura[2,3], T. Onuma[1], T. Honda[1], and K. Kishino[2]

1. Department of Electrical Engineering and Electronics, Graduate School of Engineering, Kogakuin University, Japan
2. Sophia Nanotechnology Research Center, Sophia University, Japan
3. Department of Engineering and Applied Sciences, Sophia University, Japan

E-mail: cm23040@gmail.com

We are dedicated to improving the device performance of InGaN-based nanocolumns. Under the conventional device process, unsmooth electrodes caused inhomogeneous current injection into the ordered nanocolumn array. In this study, to get the homogeneous current injection, we developed a new process and succeeded in obtaining a smooth electrode and improving luminous area.

InGaN-based materials are attracting attention because it can emit light in the full visible light range and nanocolumns possess the effects of threading dislocation filtering [1], strain relaxation [2], and increased critical film thickness [3], that can contribute to the improvement luminescence efficiency. Moreover, different emission wavelengths can be obtained by changing the column diameter in nanocolumn arrays [4]. The diameter depends on column periods, but it is difficult to form smooth electrodes for the different column shapes. Nanocolumn LEDs with circular ITO transparent electrodes with the diameter of 40 μm were fabricated using ordered InGaN-based nanocolumn arrays grown through Ti mask selective area growth (SAG) by RF-MBE [5]. In the conventional process, the space between nanocolumns was just filled with an ALD-Al_2O_3 (ALD: atomic layer deposition) of 70 nm thickness and the nanocolumn tops were exposed by etching, followed by the deposition of Ni/ITO (300 nm) electrodes. However, the periodic asperity corresponding to the nanocolumn apex was remained on top surface. The sputter deposition of ITO electrode provides that ITO film was stacked on convex column tops, resulting in an insufficient bridging between adjacent nanocolumns by ITO as shown in Fig. 1 (a). The spot-like inhomogeneous luminescence image was observed (Fig. 1 (b)).

To get the homogeneous current injection into the ordered nanocolumn array, the ITO formation process was developed. In the new process, the thickness of the ALD-Al_2O_3 was simply increased to 250 nm. A smooth top-surface of Al_2O_3 was obtained and then the concavity and convexity of surface was sufficiently suppressed when the nanocolumn tops were exposed by etching. The spacing between nanocolumns was smoothly filled by Al_2O_3 and then the Ni/ITO electrode was deposited on that. Figure 2 shows the top-view SEM images of InGaN-based p-n junction nanocolumn arrays with periods (L) of 600, 500, 400 nm. After the deposition of Ni/ITO electrode on these columns with various periods via newly developed process, the rather smooth top surfaces were obtained, attaining a satisfied electrode-bridging between nanocolumns (Fig. 3). Figure 4 shows an EL spectrum and near field emission image of the LEDs with L=600 nm. The smooth electrode urged to improvement in luminous area with wavelength of 605 nm.

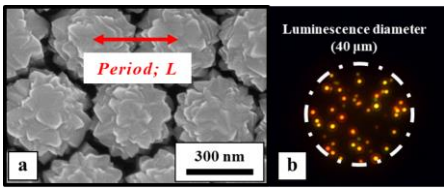

Fig. 1 (a) top-view SEM image of nanocolumn arrays after deposition of Ni/ITO electrode and (b) near-field electroluminescence (EL) emission image.

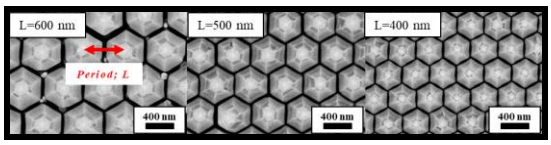

Fig. 2. Top-view SEM images of InGaN-based p-n junction nanocolumn arrays with different L.

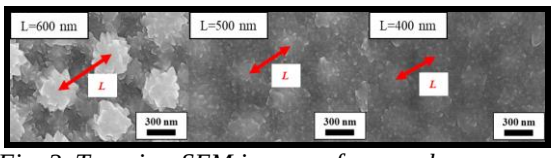

Fig. 3. Top-view SEM images of nanocolumn arrays after formation of Ni/ITO electrode.

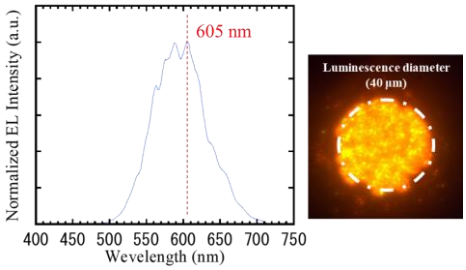

Fig. 4. EL spectrum and near-field emission image of InGaN-based nanocolumn LEDs with L=600 nm.

References:

[1] K. Kishino *et al*, Nanotechnology **26**, 225602. (2015)., [2] Y. Kawakami *et al*, J. Appl. Phys. **107**, 023522 (2010)., [3] T. Oto *et al*, AIP Adv. **6**, 115214 (2016)., [4] H. Sekiguchi *et al*, Appl. Phys. Lett. **96**, 231104 (2010)., [5] K. Kishino *et al*, J. Cryst. Growth **311**, 2063 (2009).

Inter-Disaster Communities and Memorial and Media in Disaster and Non-disaster Areas:Inter-disaster communities and memorials to share Knowledge from the Great East Japan Earthquake and the Great Kanto Earthquake.

Haruka Sakuma

Architecture Program, Kogakuin University Graduate School, Tokyo

Email: dm23045@g.kogakuin.jp

Abstract

There is a need to rethink how to disseminate and communicate the knowledge learned from the Great East Japan Earthquake and other disasters in areas that have not recently experienced catastrophes. Therefore, I propose a design for a disaster prevention community base in an area that has not experienced any disaster recently; the aim is to heighten awareness about disaster prevention and preparedness in a community that may have become complacent. The target site is Sumida Park, and its surrounding area, in Sumida Ward, Tokyo, which was damaged in the 1923 Great Kanto Earthquake. This park was built on a former residential site that contained many single-family dwellings that were destroyed by the 1923 Great Kanto Earthquake. The project proposes a memorial that houses multimedia exhibits focusing on disasters that have occurred in the various regions of Japan throughout its history. It will be a place for exchanging information about and between multiple disaster areas from multiple time frames, and it will exhibit the trajectory of pre-disaster status, destruction, and post-disaster reconstruction and attempt to pass on the knowledge the architectural field has gained through these experiences.

2023 International Symposium on Advanced Technology (ISAT-22)
Tainan City, Taiwan, October 19-20, 2023

Functionally Graded Porous Metals with Multiple Materials

Hidekazu Miyazaki* and Masanori Shiomi

Graduate School of Engineering, Kogakuin University, Tokyo, Japan
E-mail: am22062@ns.kogakuin.ac.jp

Abstract

To fabricate functionally graded porous metals, foamable solid aluminums made of two types of aluminum powders and a foaming agent were arranged and foamed in a mold. The experimental results showed that the two aluminums had different expansion forces. The porous metals with smooth pore distribution were obtained by the vertical arrangement with the aluminum of larger expansion force at the bottom and the horizontal arrangement.

Introduction

Porous metals are materials that have many pores inside [1]. Their features are excellent shock absorption, thermal and electrical conductivities, sound insulation and permeability. Expecting applications are parts of automobiles, railways, spacecrafts and ships as a lightweight shock absorber. In order to enhance the porous metals, functionally graded porous metals by combining multiple materials are one of the possibilities. Therefore, in this paper, the powder metallurgy process of fabricating functionally graded porous metals is conducted.

Experiments

The materials used in the experiments are two kinds of aluminum alloys: A6061 (Al-Mg-Si alloy) and ADC12 (Al-11Si-3Cu alloy) in JIS, in which the strength of ADC12 is higher than that of A6061. Each powder was mixed with a foaming agent (TiH_2) of 1 mass% and compacted with hot powder extrusion to make two kinds of foamable solid bars of A6061 and ADC12. The size of the foamable solid bar was 10 mm in diameter. Foamable solids of A6061 and ADC12 were cut, arranged within the mold and heated in a furnace to become a functionally graded porous metal. The vertical and horizontal arrangements were examined. The temperature of foaming was 650 °C.

Fig. 1 shows the cross section of porous aluminum made of A6061 and ADC12. Two foamable solids of the same size were arranged vertically, with ADC12 at the top and A6061 at the bottom. The size of pores in the both area of A6061 and ADC12 is similar, and the distribution of pores is smooth, so that the properties of the porous alulminum could be graded. On the other hand, the foamable solid of ADC12 could not expand enough in the case of bottom position. It is considered that the expanding force of A6061 is larger than that of ADC12.

Fig. 2 shows the cross section of porous aluminum with the horizontal arrangement. Although the size of the foamable solid A6061 is smaller than that of ADC12, the porous aluminum is well formed. Functionally graded porous metals could be obtained.

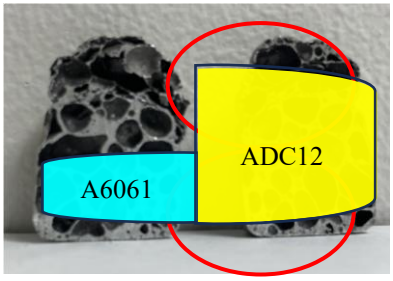

(a) Arrangement of A6061 and ADC12

Fig. 1. Porous metal made of two kinds of aluminum arranged vertically.

(b) Fabricated porous metal

Fig. 2. Porous metal made of A6061 and ADC12 arranged side by side.

Conclusion

Porous aluminum was obtained by foaming process of two kinds of foamable solids. The mechanical properties of porous metals will be examined in the future work.

References:

[1] J. Banhart, Metal Foams: Production and Stability, *Advanced Engineering Materials*, **8**, 781−794 (2006).

Fabrication of top-down and bottom-up MOSFET using α-In_2O_3 films grown by Mist CVD

Y. Hayashi, A. Taguchi, S. Yamadera, T. Yamamoto, S. Aikawa, T. Onuma, H. Honda, T. Yamaguchi

Department of Electrical Engineering and Electronics, Graduate School of Engineering,
Kogakuin University, Tokyo Japan
E-mail: cm23056@ns.kogakuin.ac.jp

Abstract

In this study, MOSFET devices were fabricated with top-down and bottom-up approaches using α-In_2O_3 films grown by Mist CVD. The device fabricated with top-down approach operated at a negative turn-on voltage of -21 V. The ON/OFF ratio was 10^5. Thus, the MOSFET operation was clearly confirmed. However, the maximum field-effect mobility was estimated to be 1.0 cm^2 V^{-1} s^{-1}. The electrical characteristics for the MOSFET devices with top-down and bottom-up approaches are comprehensively discussed.

Introduction:

Crystalline rhombohedral corundum-structured indium oxide (α-In_2O_3) is expected to be applied as an active element for a power switching electronic device by taking advantages of a large bandgap energy of 3.7 eV[1] and a high electron mobility of over 140 cm^2 V^{-1} s^{-1} [2]. We have succeeded in obtaining the high-quality 4.2-μm-thick α-In_2O_3 film with superior electrical properties, with a carrier concentration of 3×10^{17} cm^{-3} and a Hall mobility of 240 cm^2 V^{-1} s^{-1} at room temperature[3], grown by mist chemical vapor deposition (Mist CVD) method epitaxially on α-Al_2O_3 substrates[4]. We are now ready to develop device applications, such as metal-oxide field-effect transistor (MOSFET), using the α-In_2O_3 films grown by Mist CVD. For controlling the electron flow using depletion region in MOSFET, the film thickness of α-In_2O_3 needs to be controlled to about 100 nm for the film with carrier concentrations of 10^{17}-10^{18} cm^{-3}. For controlling film thickness, the top-down approach using etching process from high-quality thick film and the bottom-up approach using a thin film crystal growth process are possible.

In this study, we fabricated MOSFET with bottom-up and top-down and bottom-up approaches using α-In_2O_3 films grown by Mist CVD.

Experiments:

(0001)α-In_2O_3 films were grown at 550°C by Mist CVD on (0001)α-Al_2O_3 substrates. For top-down approach, the sample was prepared by growing α-In_2O_3 film with a thickness of 300 nm and subsequently etching down to 100 nm with inductively coupled plasma reactive ion etching (ICP-RIE). For bottom-up approach, the sample was prepared by growing α-In_2O_3 film with a thickness of 120 nm. The MOSFET device structure, shown in Fig. 1, was fabricated using 100-120 nm-thick α-In_2O_3 films prepared by the top-down and bottom-up approaches. The MOSFET device is consist of 100-120 nm of channel thickness, 350 μm of channel distance, 900 nm of insulating film on top of channel layer, and Au/Ti electrodes as source/drain contacts. The gate voltage was varied from -40 to 40 V.

Results and discussion:

Figure 2 shows the transfer characteristics and field-effect mobility of the MOSFET fabricated using the top-down process. The device operated at a negative turn-on voltage of -21 V. The ON/OFF ratio was 10^5. Thus, the MOSFET operation was clearly confirmed. However, the maximum field-effect mobility was estimated to be 1.0 cm^2 V^{-1} s^{-1}. Such a small mobility is attributed to be due to the plasma damage of the channel surface.

In the presentation, the electrical characteristics for the MOSFET devices with top-down and bottom-up approaches are comprehensively discussed.

References:

[1] N. Suzuki et al., J. Cryst. Growth **401**, 670 (2014).
[2] K. Kaneko et al., MRS Advances **2**, 301 (2017).
[3] A. Taguchi et al., Jpn. J. Appl. Phys. **62** SF1023 (2023).
[4] T. Yamaguchi et al., Appl. Phys. Express **13**, 075504 (2020).

Figures:

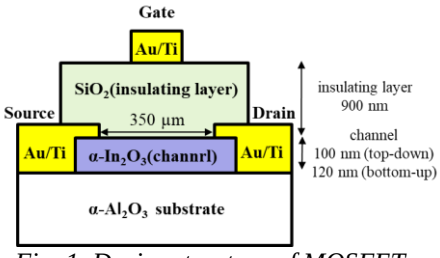

Fig. 1. Device structure of MOSFETs.

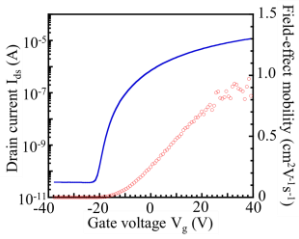

Fig. 2. Transfer characteristics and field-effect mobility of top-down MOSFETs.

Integrating Generative AI into Electronic Engineering Curricula: A Case Study on Digital System Design

Jung-Lin Yang* and Yi-Wen Chan

Department of Electronic Engineering, Southern Taiwan University of Science and Technology, Tainan, Taiwan
E-mail: jyang@stust.edu.tw

Abstract

This brief study was conducted at Southern Taiwan University of Science and Technology (STUST) and has yielded positive results for our students. We are eager to share our experience with fellow educators who face similar teaching challenges. The diminishing birth rate has resulted in a substantial decrease in the potential count of university freshman students. Despite this challenge, STUST has managed to sustain a satisfactory student enrollment level. Consequently, a notable portion of our student body lacks the foundational background knowledge required by conventional teaching methods. In response to this challenge, we put forward a holistic strategy that integrates the programmable system-on-chip (PSoC) platform with generative AI to elevate the instruction of the "Digital System Design" course. By incorporating the flipped teaching approach into the curriculum, we have witnessed its effectiveness in engaging students, addressing diverse learning needs, and bolstering their understanding of digital systems. While the t-test analysis indicates that the improvements have not yet reached a statistically significant level, the potential for further exploration and development remains promising.

The flipped teaching approach has proven to be effective in higher education, as demonstrated by a meta-analysis comparing it to traditional lecture-based courses[1]. Students in flipped classrooms exhibited improved performance in foundational knowledge, critical thinking, and professional skills. Additionally, they reported higher levels of satisfaction. Educators should seriously contemplate the adoption of the flipped learning methodology due to its evident benefits. In our study, we employed an innovative flipped teaching approach, incorporating minimal assistance from generative AI, to enhance the effectiveness of constructing fundamental knowledge in digital systems.

Throughout our substantial three-year engagement in the Ministry of Education (MOE) "Teaching Practice Research Program," we have consistently introduced and refined the implementation of flipped teaching methodologies. In the context of this study, we seamlessly integrated and gradually refined the utilization of the PSoC platform along with generative AI tools, namely ChatGPT and New Being. These advancements were strategically directed at enriching students' hardware description language (HDL) development proficiencies and fostering their English language aptitude within the framework of the “Digital System Design” course.

Our pivotal role encompasses skillfully guiding students in the effective and purposeful utilization of these tools for educational objectives, thereby ensuring meticulous design verification. Our research unequivocally demonstrates that this approach nurtures a positive learning attitude and significantly enhances students' grasp of the fundamental principles underpinning digital system design. The synergistic collaboration between flipped teaching, the PSoC platform, and generative AI collectively bolsters students' academic advancement and proficiency elevation.

Following the launch of ChatGPT, discussions have arisen regarding the impact of AI in the classroom. Pertinent articles harmoniously align with our aim to incorporate AI tools into education. These articles delve profoundly into the implications of generative AI for both educators and students, offering valuable insights for a considerate implementation. While AI facilitates tasks like feedback and personalization, the articles underscore the importance of fostering autonomous thinking in assignments, rather than exclusively relying on AI. The enthusiastic embrace of generative AI by educators for amplified pedagogy is indeed profoundly inspiring[2][3].

PSoC-Centric Testing Platform

The integration of generative AI and the PSoC platform has brought about a significant transformation in the realm of learning. This integration has opened new avenues for students to engage with the subject matter. As depicted in Fig. 1, students are now actively involved, demonstrating critical thinking and collaboration. This, in turn, has led to the refinement of their problem-solving abilities and sparked their creativity.

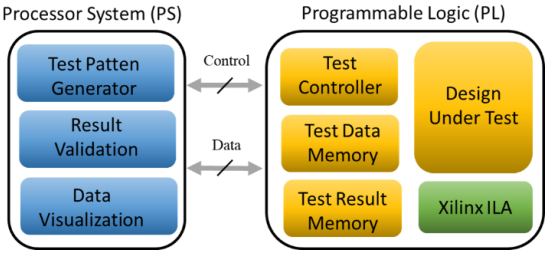

Fig. 1. PSoC-Centric Testing Platform

To enhance the platform's testing capabilities, we've incorporated an Integrated Logic Analyzer (ILA) from Xilinx. This sophisticated addition facilitates precise measurement and comprehensive analysis of circuit signals. As a result, students are equipped with a comprehensive toolkit that empowers them to explore, experiment, and refine their understanding of digital circuits and system behavior.

Experimental Case Studies

Classroom practices and the final mini-project for this new teaching method are outlined. Before the midterm exam, we implemented an improved flipped teaching approach and incorporated generative AI tools to aid in solving digital system design problems. Starting with a complex logic problem, students were guided toward AI-assisted solutions. A student's rapid success, solving it in 10 minutes, piqued others' interest, fostering engagement and a dynamic atmosphere. The course concludes with the creation of an SPI-based basic ALU that executes commands (SET, ADD, SUB, MUL, AND, OR, NOT, XOR) on received data. The ALU is synthesized onto the PSoC board and connected to Raspberry Pi Pico (Fig. 2) for comprehensive testing.

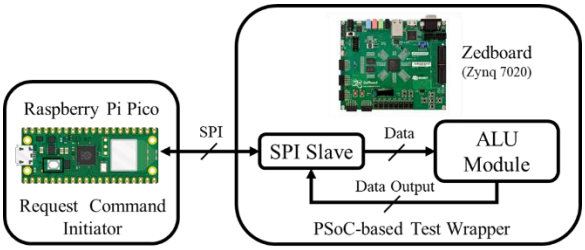

Fig. 2. Mini-project SPI-based ALU

Moreover, we subdivided the mini-project into three discrete components: a clock frequency divider, an SPI master clock generator, and an SPI slave module with parallel accessibility. This division was essential due to the varying levels of student proficiency, acknowledging that not all students could seamlessly navigate the mini-project with AI support. While introducing the new teaching methodology earlier might yield advantages, the task of evaluating these potential benefits is intricate without a direct comparison to the conventional approach.

Findings and Analysis

Prior to implementing the new approach in the classroom, less than a quarter of the students encountered difficulties in completing the classroom exercises before the class session ended. However, with the integration of generative AI and the prototyping platform, over fifty percent of the students managed to successfully submit their solutions within the allocated timeframe. What's even more noteworthy is that nearly all the students proactively engaged in tackling the classroom exercises with the assistance of generative AI.

The insights drawn from the t-test findings, as presented in Table 1, illuminate the consequences of integrating generative AI and a PSoC test platform into a digital system design course utilizing the flipped teaching approach. The central aim of this study was to appraise the potential amplifications in efficacy that result from the application of this pedagogical methodology. Upon analyzing intrinsic motivation, a modest elevation from a pre-test mean of 5.67 to a post-test mean of 6.02 was discerned. Nonetheless, this variance did not attain statistical significance ($t = -1.13$, $p = 0.13$). This trend persisted in the examination of both identified and extrinsic motivations, where incremental shifts in means were observed, yet without reaching statistical significance.

Table 1. T-test analysis of contextual motivation

	Pre-test		Post-test			
	Mean	Var.	Mean	Var.	t	P
Intrinsic	5.67	1.20	6.02	1.48	-1.13	0.13
Identified	5.77	0.99	6.04	1.19	-0.95	0.17
Extrinsic	5.67	1.14	5.98	1.37	-1.05	0.15
Amotivation	4.23	1.49	4.01	2.22	0.61	0.27

Regarding amotivation, there was a small decrease in mean scores from 4.23 to 4.01, suggesting a potentially positive trend. However, this change was not statistically significant ($t = 0.61$, $p = 0.27$).

Conclusion

In summary, the initial analysis does not reveal statistically significant changes in contextual motivation measures following the integration of generative AI and the PSoC test platform through the flipped teaching approach. However, notable evidence suggests an improvement in students' active participation in class exercises and discussions. This underscores the potential for further advancing the teaching approach introduced. To establish more definitive conclusions regarding the efficacy enhancements brought about by this instructional strategy, further investigation is warranted.

References:

[1] Li, R., Lund, A., & Nordsteien, A.: 'The link between flipped and active learning: a scoping review', Teaching in Higher Education, 2021. https://doi.org/10.1080/13562517.2021.1943655

[2] Seo, K., Tang, J., Roll, I. et al. The impact of artificial intelligence on learner–instructor interaction in online learning. Int J Educ Technol High Educ 18, 54 (2021). https://doi.org/10.1186/s41239-021-00292-9

[3] Chaudhry, M.A., Kazim, E. Artificial Intelligence in Education (AIEd): a high-level academic and industry note 2021. AI Ethics 2, 157–165 (2022). https://doi.org/10.1007/s43681-021-00074-z

Controllable Hortensia-like MnO_2 as an Efficient Electrocatalyst for Supercapacitor

Yu-Ming Chang[1], Chao-Ming Huang[2], and Yu-Chu M. Li[1,*]
[1]Department of Mechanical Engineering, Southern Taiwan University of Science and Technology
Tainan, Taiwan
[2]Department of Advanced Applied Materials Engineering, Kun Shan University, Tainan, Taiwan
[*]Corresponding author's e-mail: maxli@stust.edu.tw

Abstract

Four MnO_2/Ni foam composite electrodes with hortensia-like structures were prepared using a facile electroless plating (EP) method. The microstructure characterization of as-prepared MnO_2 film is conducted by SEM, TEM, XRD, and BET measurements, and the plating time markedly influenced the surface morphological, textural, and supercapacitive properties of the MnO_2/Ni electrodes. The obtained MnO_2 film electrode without binder additive shows excellent pseudocapacitance behavior, delivering the maximum capacitance of 932 F g^{-1} in 3 M $LiNO_3$ aqueous solution with a current density of 5 A g^{-1}. This study provides a facile method for preparing three-dimensional self-stand MnO_2 film with efficient supercapacitive properties.

1. Introduction

It has been reported that MnO_2 thin film electrodes without organic binder generally possess better electrochemical properties, reaching a capacitance as high as 350-750 F g^{-1} [1-3]. Moreover, three-dimensional (3D) materials can provide more active sites for shortening transport path length for both electrons and ions within the electrolyte, enhancing the electrochemical performance. Usually, the 3D MnO_2 films were prepared by hydrothermal synthesis and sol-gel method [4-6]. However, these processes are limited for large-scale industrial production because of energy consumption and harsh reaction conditions. The electroless plating (EP) method is regarded as a low-cost and simple procedure for large-scale preparation of 3D materials [7-9].

In this study, 3D MnO_2 thin film was directly prepared by EP upon nickel foam. The electrochemical properties of this 3D MnO_2 material was elucidated in $LiNO_3$ aqueous electrolyte and galvanostatic charge/discharge measurements. An outstanding enhanced performance was achieved by this 3D structure as composite electrode for supercapacitor.

2. Experimental

3D MnO_2 film was prepared by the EP method. Clean Ni foam was vertically immersed in the aqueous solution containing 0.12 M $KMnO_4$ and 0.05 M $MnSO_4 \cdot H_2O$ in the bath at 90 ℃ for 20, 30, 45, and 60 m. The samples were washed with deionized water, dried, and then calcined at 250 ℃ for 2 h in the air; the composites were labeled EP20, EP30, EP45, and EP60, according to their respective plating times.

3. Results and discussion

The SEM images of the samples are shown in Fig. 1. As shown in Fig. 1a, MnO_2 (EP20), with a deposition time of 20 m, has a porous structure over the skeleton of the Ni foam substrate. Fig. 1b shows the SEM image of MnO_2 film (EP30), indicating a large number of nanoplatelets cross-linked with each other of a hortensia-like sphere with a diameter in the range of 100 nm and thickness of less than 10 nm of each nanoplatelet. As the plating time was increased, the thickness of the MnO_2 film increased obviously, as shown in Fig. 1c. It can be seen from Fig. 1d that the hortensia-like nanosphere aggregated together (EP60).

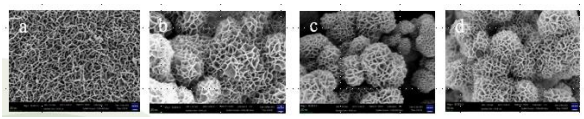

Fig. 1. SEM images of MnO_2/NF electrodes plated at (a) 20 m, (b) 30 m, (c) 45 m, and (d) 60 m.

Meanwhile, the representative TEM image (Figure 2) shows that the EP30 had a hortensia-like morphology. The hortensia-like MnO_2 is well anchored on the surface of NF, forming an interconnected network to shorten the ion diffusion pathway and provide a direct electron transfer pathway.

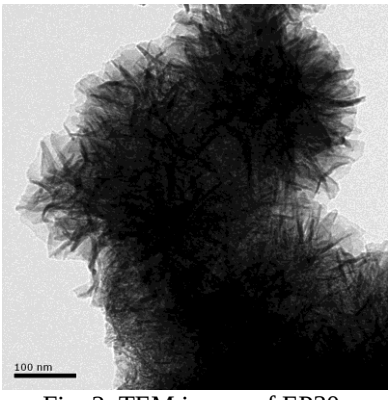

Fig. 2. TEM image of EP30.

Figure 3 shows the XRD patterns of as-prepared samples. As shown, the peaks at 2θ of 36.68 and 41.82, correspond to (211) and (301), respectively, indicating the high purity of the synthesized α-MnO_2 nanoparticles (JCPDS Card No. 44-0141).

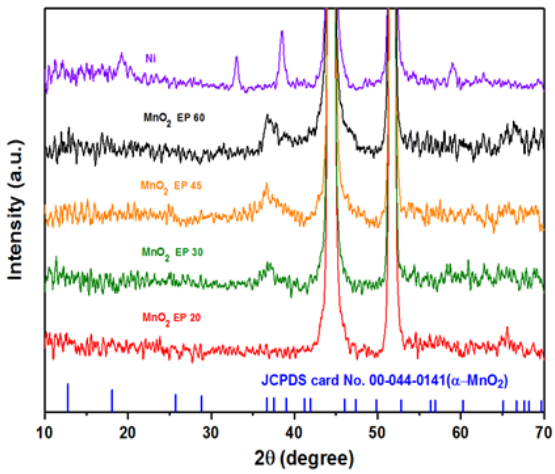

Fig. 3 XRD patterns of EP20, EP30, EP45, and EP60.

Nitrogen adsorption-desorption isotherms and the corresponding pore-size distributions of the as-prepared samples are shown in Figure 4. Type IV isotherms with hysteresis loops can be seen, demonstrating that all electrodeposited MnO2/NF samples had a typical mesoporous structure. The triangular shape and a steep desorption branch of the isotherms forms a H_2-type hysteresis loop, suggesting the presence of highly interconnected pores with narrow mouths and wider bodies (ink-bottle-like pores).

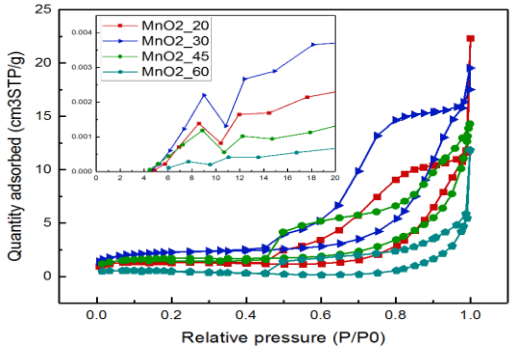

Fig. 4. (a) N_2 adsorption/desorption isotherms; and (b) corresponding pore size distributions of EP20, EP30, EP45, and EP60.

Fig. 5 displays the GCD plots of MnO_2/NF electrodes deposited at various plating times tested in 3 M $LiNO_3$ at the current density of 5 A g^{-1}. An obvious deviation from the ideal triangular charge-discharge curve was observed in the porous structure composed of hortensia-like nanosheet MnO_2 nanostructures. This deviation was attributed to Faradic oxidation-reduction (pseudocapacitive). The specific capacitances for the four electrodes for various times were 670, 932, 580, and 238 Fg^{-1}, respectively, for plating time at 20, 30, 45, and 60 m. This porous structure creates the fast electrochemical accessibility of the Li^+ ions to the bulk of the MnO_2 phase.

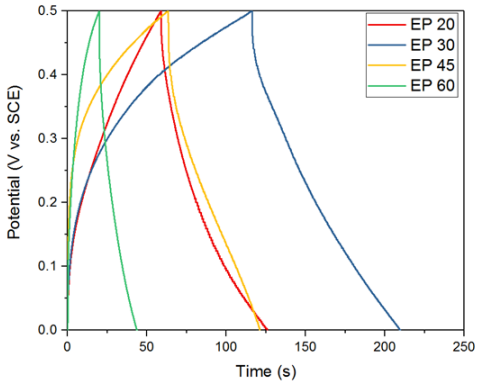

Fig. 5 GCD curves at 5 A g^{-1} for various MnO_2/Ni electrodes.

4. Conclusion

A porous 3D hortensia-like sphere of MnO_2 is successfully grown on Ni metal form followed by calcining at 250 °C. The morphology of MnO_2 film can be regulated by adjusting the plating time. A high specific capacitance of 932 F/g at a scan rate of 5 A/G is achieved at 30 m plating time.

References:

[1] T. Xuo, C.L. Xu, D.D. Zha, X.H. Li, H.L. Li, *J. Power Sources* **164**, 953-958 (2007).
[2] J.N. Broughton, M.J. Brett, *Electrochim. Acta* **50**, 4814-4819 (2005).
[3] J. Wei, N. Nagarajan, I. Zhitomirsky, *J. Mater. Process. Technol.* **186**, 356-361 (2007).
[4] A. Sarkar, A.K. Satpati, V. Kumar, S. Kumar, *Electrochim. Acta* **167**, 126-131 (2015).
[5] Y. Hu, J. Wang, *J. Power Sources* **286**, 394-399 (2015).
[6] D. Yan, Z. Guo, G. Zhu, Z. Yu, H. Xu, A. Yu, *J. Power Sources* **199**, 409-412 (2012).
[7] H. Vnuma, T. Kanehama, K. Yamamoto, Watanabe, T. Ogta, M. Suggawara, *J. Mater. Sci.* **38,** 255-259 (2003).
[8] D. Yan, Z. Guo, G. Zhu, H. Yang, R. Wei, H. Xu, A. Yu, *Mater. Lett.* **82,** 156-158 (2012).
[9] Y. Hu, J. Wang, X. Jiang, Y. Zheng, Z. Chen, *Appl. Surf. Sci.* **271,** 193-201 (2013).

Fabrication of Birefringent PEN Transducer for Flow Speed Variation Measurements

Chang-Hui Chen, Wen-Chi Hsu, and Ruey-Ching Twu*

Department of Semiconductor and Electro-Optical Engineering, Southern Taiwan University of Science and Technology, Tainan, Taiwan
*E-mail: rctwu@stust.edu.tw

Abstract

The measurement of fluid flow speed variation is very important for industrial applications [1]. Especially in semiconductor process or chemical process, the flow speed monitoring of many special gases or chemical fluids plays an important role in the stability of the process. The fiber transducers have been widely used as a design of flow meter [2, 3]. Similar to a typical mass flow meter, the liquid flow can reduce media temperature, therefore the refractive index variations can change the resonance condition of the probe light in a surface plasmon resonance sensing scheme [4]. PEN (Polyethylene Naphthalate) is a transparent polymer substrate that is often used in the production of displays, wearable sensors, and solar cells [5]. In this study, flexible and birefringent PEN transducer has been tried firstly for the flow speed variation measurements.

Figure 1 illustrates a schematic of flow speed variation measurement system based on a heterodyne interferometer. The probe light is irradiated from a stabilized He-Ne laser. The intensity and polarizations can be adjusted by a polarizer (GPL), half waveplate (HWP), and attenuator (AT). To improve phase measurement resolution, the phase-delay modulations between two orthogonal polarizations are generated by using an electro-optic modulator (EOM). The probe light is divided into two paths after passing through a beam splitter (BS). The transmitted light passing through a flow cell (FC) is a sensing signal, and the reflected one is a reference signal. After the corresponding two analyzers AL1 and AL2, both interferometric signals are sinusoidal waves. They were received by the photo detectors PD1 and PD2. The phase values can be obtained through a lock-in-amplifier (LIA) by comparing the two sinusodial like signals from PD1 and PD2. Figure 2 shows the flow cell (FC) structure. A birefringent PEN sheet of 125μm thickness which was attached on a supporting glass plate, then the glass plate was fixed on the bottom of FC. The probe light transmits through the PEN fin, and the flow pressure onto the surface of PEN sheet applies the bending force to change the incident angle of probe light (θ_i). The higher flow speed makes the incident angle becoming smaller. The phase delay between the two orthogonal polarizations is dependent on the incident angle variation ($\Delta\theta$). The calculated phase change versus the incident angle variation is shown in Fig. 3. If the initial incident angle of 45°, the incident angle is decreased due to the flow speed increased. The realtion between the phase change and the incident angle is linear under the angle variation of 0.5°.

There are two different shapes of PEN fin, which are adopted to optimize the measurement range of flow speeds. Figure 4(a) gives the geometrical size of rectangular fin, and the measured phase variation dependence of flow speed is shown in Fig. 4(b). The linearity after fitting curve shows that the R-square value is close to 0.92. Figure 5 expresses the geometrical size of recessed PEN fin and the photo taken by the FC. According to previous study, the higher incident angle can achieve larger sensitivity in the PEN sensors. There are three different initial incident angles ($45^\circ, 50^\circ, 60^\circ$) to comparing the measurement performance as shown in Fig. 6. However, the phase signal becomes worse in the flow cell at incident angle of 60°.

In summary, the recessed PEN fin is more sensitivity than the rectangular type, but the R-square value is decreased gradually. Fine optimizations are necessary for improving the good linearity.

References:

[1] Wu, Zhao, Gan, & Ma. (2019). Measuring Surface Velocity of Water Flow by Dense Optical Flow Method. Water, 11(11), 2320.
[2] Lien, V., & Vollmer, F. (2007). Microfluidic flow rate detection based on integrated optical fiber cantilever. Lab on a Chip, 7(10), 1352-1356.
[3] Hu, R. P., & Huang, X. G. (2009). A simple fiber-optic flowmeter based on bending loss. IEEE Sensors journal, 9(12), 1952-1955.
[4] Deng, S., Wang, P., Liu, S., Zhao, T., Xu, S., Guo, M., & Yu, X. (2016). A novel microfluidic flow rate detection method based on surface plasmon resonance temperature imaging. Sensors, 16(7), 964.
[5] Rezem, M., Günther, A., Roth, B., Reithmeier, E., & Rahlves, M. (2016). Low-cost fabrication of all-polymer components for integrated photonics. Journal of Lightwave Technology, 35(2), 299-308.

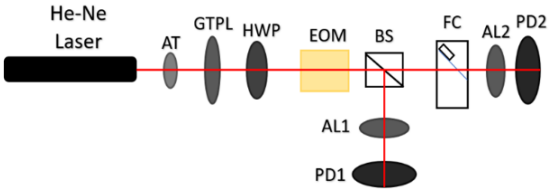

Fig. 1 Experimental setup for a flow speed variation measurement system in a heterodyne interferometer: AT, attenuator; GTPL, Glan-Taylor polarizer; HWP, half-wave plate; EOM, electro-optic modulator; BS, beam splitter; FC, flow cell; AL, analyzer; PD, photodetector.

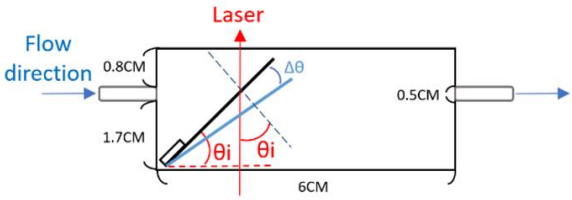

Fig. 2 Schematic diagram of the probe light path in the FC and PEN fin arrangement.

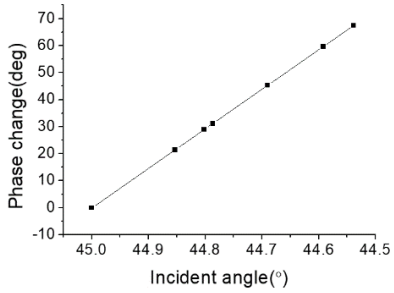

Fig. 3 The calculated phase change versus incident angle.

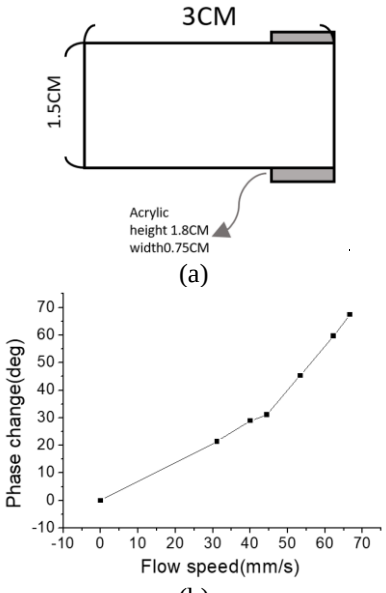

Fig. 4 (a) Rectangular shape PEN fin. (b) Phase versus flow speed.

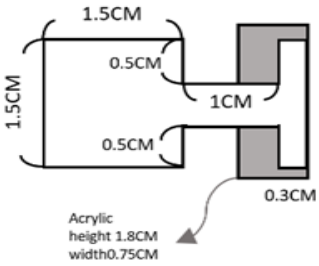

(a)

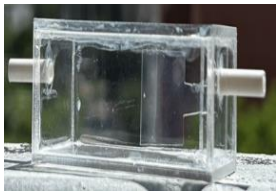

(b)

Fig. 5 (a) Recessed PEN fin structure. (b) Photo of the FC including the recessed fin.

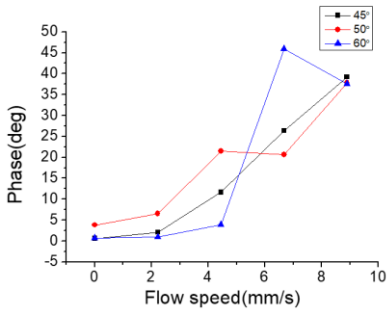

Fig.6 Phase versus flow speed with the recessed fin.

Effect of Film Thickness on the Ethanol Sensing Sensitivity of Titanium Dioxide Gas Sensor

Hsyi-En Cheng [1]*, Bo-Jia Lin [2†], and Zu-Po Yang [2]

[1]Department of Semiconductor and Electro-Optical Engineering, Southern Taiwan University of Science and Technology, Tainan, Taiwan
[2]Instititute of Photonic System, National Yang Ming Chiao Tung University, Tainan, Taiwan
[†]Presenter: **Bo-Jia Lin**
[*]Corresponding author's e-mail:*sean@stust.edu.tw*

Abstract

Titanium dioxide film sensors with film thicknesses between 15 and 40 nm were prepared on glass substrates for detecting ethanol gas at room temperature. The effect of film thickness on the sensing sensitivity was investigated. The results demonstrate that the thinner the TiO_2 film, the higher the sensitivity to ethanol gas. Compared with the Debye length at the film surface, it was found that the thin film sensor will have higher sensing sensitivity when the film thickness is thinner than the Debye length.

Titanium dioxide (TiO_2) films with thicknesses of 15, 27 and 40 nm were grown on glass substrates at 300ºC using atomic layer deposition. Nickel film with thickness of 300 nm was used as the electrodes for the titanium dioxide gas sensor. Figure 1 shows the electrode structure. The spacing between two nickel electrodes for sensing the ethanol gas is 0.1 mm. For sensing experiments, the sensor was placed in a gas flow tube at room temperature and illuminated with 2.2 mW of 310 nm UV light. The typical electrical resistance curve of the sensor affected by UV light and ethanol gas is shown in Figure 2. When the UV lamp was turned on, the resistance of the TiO_2 film dropped sharply, as shown in b in Figure 2, and then the resistance slowly increased and reached the saturation value. At this time, ethanol gas can be injected into the tube for detection. When ethanol gas was injected, the resistance of the TiO_2 film dropped again. After injection for 300 s, the ethanol gas was turned off, and the ethanol response value S was calculated from equation 1.

$$S = \frac{R_a - R_g}{R_a} = \frac{\Delta R}{R_a} \qquad (1)$$

Where Ra is the resistance in air before injection of ethanol gas, and Rg is the resistance in the presence of ethanol gas.

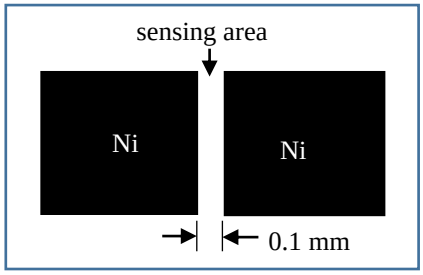

Fig. 1. The electrode structure for ethanol sensors.

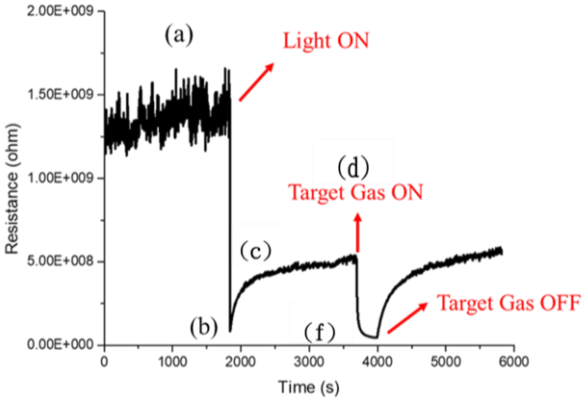

Fig. 2. Typical resistance curve of the sensor when the UV lamp is turned on and ethanol gas is injected.

The effects of ethanol concentration and TiO_2 film thickness on the response value of sensor was shown in Figure 3. When the ethanol concentration exceeds 50 ppm, the response value increases almost linearly with the ethanol concentration. However, at ethanol concentrations below 50 ppm, the response deviates from linearity and decreases rapidly. The ethanol sensing sensitivity of the 27 and 40 nm thin film sensors is too low to discern ethanol concentrations below 20 ppm. In comparison, the 15 nm thin film sensor is sensitive enough to identify ethanol concentrations below 20 ppm.

Although the thinner the TiO_2 film, the higher its sensitivity to ethanol gas, it does not change linearly with the thickness. The ethanol gas response of the 15 nm film is much higher than that of the other two films. By calculating the Debye length of the film in dry air [1], it was found that for the 15 nm film, the Debye length was thicker than the film thickness, but for the 27 and 40 nm films, the Debye length was thinner than the film thickness, as shown in Table 1. This means that the electron carriers in the 15 nm film

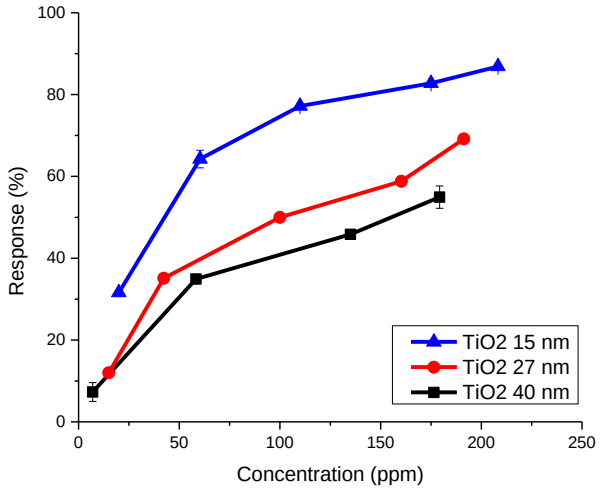

Fig. 3. Response as a function of ethanol gas concentration for TiO_2 gas sensor with various film thicknesses.

were completely depleted, while those in the 27 and 40 nm films were only partially depleted. This indicates that thin film sensors with depletion regions across the entire film thickness have higher sensing sensitivity.

Table 1. Debye length of TiO_2 thin films with various film thicknesses under 2.2 mW 310 nm UV light irradiation.

TiO_2 film thickness (nm)	Debye length (nm)
15	57
27	14
40	16

References:

[1] Wilson, R.; Simion, C.; Blackman, C.; Carmalt, C.; Stanoiu, A.; Di Maggio, F.; Covington, J. The Effect of Film Thickness on the Gas Sensing Properties of Ultra-Thin TiO_2 Films Deposited by Atomic Layer Deposition. *Sensors*, **18**(3), 735. doi:10.3390/s18030735 (2018).

Using FreeCAD as BIM Modeling tool

Po-Ming Lee

Department of Electronic Engineering, Southern Taiwan University of Science and Technology, Tainan, Taiwan
E-mail: pmlee@stust.edu.tw

Abstract

Building Information Modeling (BIM) is the most valued development direction in the Architecture Engineering Construction (AEC) industry in recent years. Its primary goal is to connect the entire AEC industry from upstream to downstream through open specification file exchange formats. In recent years, Taiwan has also begun to adopt BIM workflows, hoping to promote the digitization of the construction industry to enhance operational efficiency and reduce costs. However, the progress has been hindered by the high prices of traditional commercial software and the complexities of licensing agreements.

The construction industry is known for its conservative nature, as buildings have lifespans spanning several decades and are intricately linked to people's daily lives. Consequently, the design and construction methods are highly meticulous to ensure the safety and longevity of the structures. Introducing new design approaches or construction techniques in the construction industry requires extensive evaluation and confirmation of their feasibility before being adopted industry-wide. In recent years, with the advancement of information technology, the design process of buildings has evolved from traditional hand drawings and 2D CAD drafting to modern 3D modeling and beyond.

Currently, the most widely used commercial CAD software for architectural design are ArchiCAD and Revit, while FreeCAD serves as a viable alternative as an open-source software solution.

In recent years, almost all commercial software has undergone a significant shift in their licensing models, transitioning from perpetual licensing – where consumers purchase the software and own it indefinitely – to subscription-based licensing, where users have to pay a recurring fee annually to continue using the software. In essence, this licensing approach has transformed software usage from a one-time purchase to a leasing arrangement, requiring customers to make annual payments to the software companies. Some even jokingly refer to this licensing method as "software tax." Importantly, the subscription fees have been increasing by 5% to 20% annually, which poses significant disadvantages for consumers.

Currently, Autodesk is the dominant player in the AEC industry, with a market share as high as 66% [1]. In recent years, particularly within architectural firms, there has been considerable dissatisfaction with Autodesk's development of Revit. As a result, in 2020 and again in 2022, these firms jointly issued open letters [2]、[3] urging Autodesk to make improvements. The signatories of these open letters wield significant influence, making their actions highly indicative for the entire industry.

In this report we proposes the use of FreeCAD[4], an open-source software, for the localization of Building Information Modeling (BIM) in the field of architecture. FreeCAD is a parametric 3D modeling software that began development in January 2001. The developer, Jürgen Riegel is a German engineer currently employed at DaimlerChrysler. He initiated the development of the Open Cascade project in January 2001, which served as the foundation for FreeCAD, developed in 2003. As of now, the stable version of FreeCAD is 0.21.1, with the current development version being 1.0. More detailed version history can be found on its historical webpage (https://wiki.freecadweb.org/History).

FreeCAD adopts a modular design with various workbenches, each capable of performing different tasks. This sets FreeCAD apart from traditional CAD software, which is often primarily focused on mechanical drafting and limited to mechanical modeling. FreeCAD does not face this limitation. Although originally developed for mechanical modeling, its modular design allows it to be effectively used in the field of architecture as well. A key contributor to its development in the architectural domain is Yorik van Havre, who joined the FreeCAD team in 2008 and started developing the Draft and Arch (now BIM) workbenches. Through Yorik's efforts and the contributions of other volunteers on the internet, FreeCAD quickly became the top choice as an open-source software for BIM in architectural workflows. Due to FreeCAD's inherent capabilities in mechanical modeling, it can create complex architectural models with advanced modeling capabilities compared to other commercial software primarily focused on "building" tasks.

One of the most praised features of FreeCAD is its powerful modeling capability. Since the software was originally developed for mechanical modeling, it can handle all types of mechanical-related complex geometries. This includes commonly used

components like screws, gears, various surface shapes, and even curved surfaces, which can all be easily created using FreeCAD. As for geometrically simpler architectural models, FreeCAD excels in effortlessly completing the modeling tasks.

Fig. 1. Skew Wall created by FreeCAD

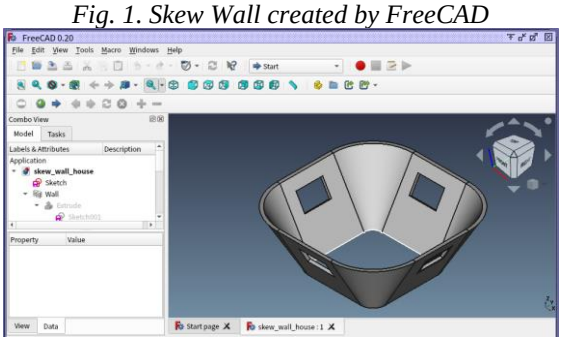

Another example can be observed from the Alturis winery in Italy [5], where the exterior wall features a wine glass-shaped structure, as shown in Figure 2. Using FreeCAD, we can easily create a model of this intricate design, as depicted in Figure 3.

Fig. 2. Alturis outside wall

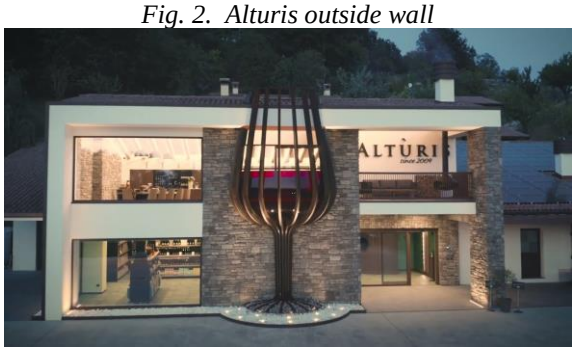

Fig. 3. Model created by FreeCAD

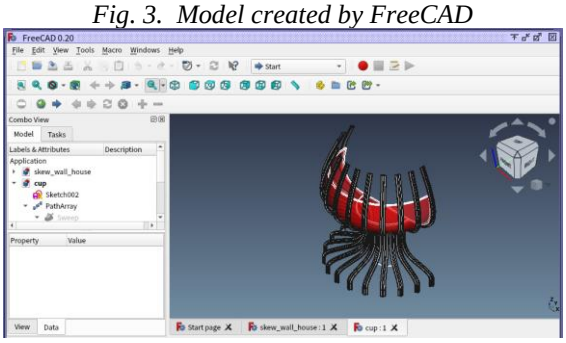

Conclusion

In this abstract, we have discussed practical issues in current BIM applications, the software landscape in the market, and the challenges faced by both domestic and international vendors. We have also attempted to promote the development and utilization of FOSS BIM through the use of FreeCAD. In addition to localizing the FreeCAD interface to Chinese, the primary contribution of this paper has been the introduction of a 2D plan expansion feature for door and window objects, validated through numerous examples. In the future, we hope that FreeCAD will be adopted and used by relevant industries in our country, allowing more people to appreciate the benefits of open-source software, fully enjoy software freedom, break free from the constraints of commercial software, and reclaim their intellectual property rights.

References:

[1] Jan Paul Schop, ” Market overview of BIM and CAD software usage of European.” www.linkedin.com. https://www.linkedin.com/pulse/market-overview-bim-cad-software-usage-european-architects-schop (accessed Sep. 24, 2023).

[2] "An open letter that reflects customer perspectives on Autodesk in 2020." aecmag.com. http://aecmag.s3.amazonaws.com/AEC_Autodesk_customer_letter.pdf (accessed Sep. 24, 2023).

[3] Martyn Day, ” Autodesk AEC customers demand better value. ” aecmag.com. https://aecmag.com/bim/lettertoautodeskaec-customersdemandbettervalue/ (accessed Sep. 24, 2023).

[4] FreeCAD, https://www.freecadweb.org/ (accessed Sep. 24, 2023)

[5] Alturis, https://alturis.it/ (accessed Sep. 24, 2023)

2023 International Symposium on Advanced Technology (ISAT-22)
Tainan City, Taiwan, October 19-20, 2023

The Effect of Moisture on the Texture Properties of Dry Fruit (Banana)

Quoc Thien Pham[1], Md Niyaz Ahmad[2], Sheng-En Lu[2], Ya-Chi Kuo[2], Cheng-Wei Shih[2], De-Xian Lai[2], and Nai-Shang Liou[2]*

[1]HUTECH University, Ho Chi Minh, Vietnam

[2]Department of Mechanical Engineering, Southern Taiwan University of Science and Technology, Taiwan

E-mail: nliou@stust.edu.tw

Abstract

This study analyzed the texture and mechanical properties of vacuum-freezing dried banana samples with different weight ratios of moisture content using a double-bite compression test. The fresh banana and dried samples exposed to moisture for 0, 2, and 24 hours were tested. Texture properties such as hardness, fracturability, cohesiveness, springiness, gumminess, chewiness, and resilience were determined. The results show an essential correlation between moisture and texture properties. As moisture content increased, there was a decrease in hardness and an increase in the chewiness of dried banana. Furthermore, the resilience suggests that moisture plays a vital role in determining the elasticity of dried bananas. This study used fresh and dried banana specimens of vacuum freezing drying.

Keywords: Moisture, texture properties, double-bite compression, texture profile analysis.

Introduction

Dried bananas, a nutritious snack, have become popular for their easy access, natural sweetness, and extended shelf life. The quality of dried bananas, including their texture properties, is paramount for consumer acceptance and overall product success. Texture properties play a vital role in storing and packaging dried bananas.

The TPA method provides a double-bite compression test on food specimens at a certain compression speed and distance to gain some mechanical properties of food that can be interpreted as hardness, fracturability, cohesiveness, springiness, chewiness, gumminess, and resilience[1]. Among the various factors that influence the texture of dried bananas, moisture content plays a pivotal role. This study aims to examine the effect of moisture content on the texture attributes of dried bananas[2]. This study reveals a correlation between moisture content and texture properties of dried bananas.

Understanding how moisture content interacts with the texture of dried bananas and how different drying methods can influence these properties is crucial for both the food industry and consumers. Optimal moisture levels and overall quality of dried banana products while extending their shelf life. This study aims to contribute valuable insights into the science and technology behind the dried banana product, ultimately benefiting producers and consumers alike.

Results and Discussion

Fig.1 shows all texture attributes of bananas before and after drying and exposed to moisture. An increase in hardness of 1930%,2378% and 136% can be found in new, 2 hours and 1 day vacuum drying process. All of the texture attributes except springiness show a similar increase after drying, and only springiness shows a decrease of 44%, 28%, and 5%, in new specimens and specimens exposed to moisture for 2 hours and one day respectively. Loss of water after drying makes bananas less springy, and hence, there is a decrease in springiness.

Conclusion

In this study, it can be found that there is a correlation between hardness and moisture. With the increase in moisture, there is a decrease in hardness. Hence, moisture in fresh bananas is maximum with low hardness, and moisture in 2 hours drying process in a vacuum is minimum with the highest hardness.

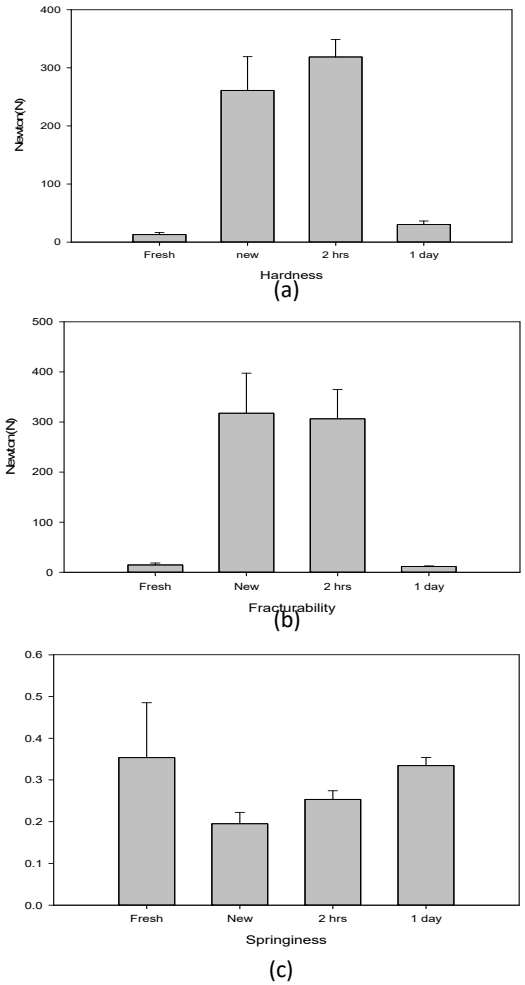

Fig. 1 Texture attributes of banana before and after drying.Graph (a) hardness (b)fracturability (c)springiness.New is immediately dried banana .

References

[1]Pham, Q.T. and N.-S. Liou, *Investigating texture and mechanical properties of Asian pear flesh by compression tests.* Journal of Mechanical Science and Technology, 2017.

*[2]*Ansari, S., et al., *Effect of moisture content on textural attributes of dried figs.* International Agrophysics, 2014.

BASED ON PHOTOGRAPHY 3D RECONSTRUCTION ALGORITHM COMBINED WITH AUTONOMOUS DRONE

Jia-Shing Shih, Cheng-Dian Zhan, FAN WEI-CHIEH ,Ming-Sian Chen , and Chong-Xiang Jian
Department of Electrical Engineering, Southern Taiwan University of Science and Technology, Tainan, Taiwan
E-mail: jasonshih@stust.edu.tw

Abstract

We control the flight controller using software to implement functionality design. We achieve this by utilizing a single-board computer to design functions and feedback systems, gathering data through sensors and devices. Through this process, we create the specific functionalities we require, combining them to achieve 3D modeling of spaces or objects, as well as enabling autonomous assistance and safety control of the drone.

Basic Theory

Instant-NGP

Instant-NGP[1] is an algorithm developed by Nvidia, and it is based on the Neural Radiance Field (NeRF)[2]. NeRF is a neural network that generates three-dimensional models from two-dimensional pixel data extracted from photos, requiring extensive computational power. Utilizing Nvidia GPUs equipped with CUDA technology can significantly enhance the computational speed for this task.

By capturing multiple images of a scene or object and using this information to create a training database, the NeRF algorithm can estimate the Radiance Function for each scene. This enables the reconstruction of scenes or objects with high accuracy and detail. After training is completed, it becomes possible to obtain color values and opacity at any position, leading to more precise and realistic rendering.

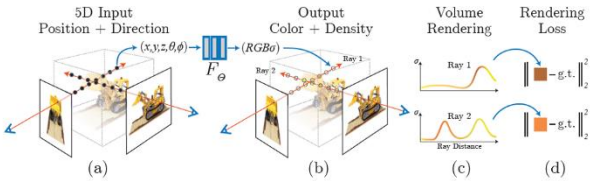

Fig. 1. Figure The NeRF volume rendering and training process. Images sourced from [3]. (a) illustrates the selection of sampling points for individual pixels in a to-be-synthesized image. (b) illustrates the generation of densities and colors at the sampling points using NeRF MLP(s). (c) and (d) illustrate the generation of individual pixel color(s) using in-scene color(s) and densities along the associated camera ray(s) via volume rendering, and the comparison to ground truth pixel color(s), respectively.

Optical Obstacle Avoidance

The principle of optical obstacle avoidance is that the optical radar rotates and emits infrared rays in all directions to detect the distance between the radar and surrounding objects. We use the VFH algorithm [4] in conjunction with optical radar and flight control to achieve automatic obstacle avoidance and ensure flight safety. When the radar detects that the drone is too close to an object, it causes the aircraft to move in the opposite direction. If there are obstacles on both sides, the aircraft will search for a third-party direction to enter. If there are obstacles on more than three sides, the aircraft will hover in place.

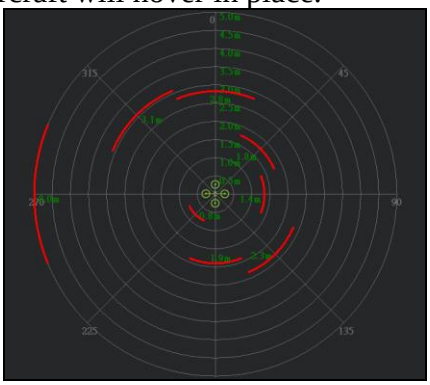

Fig. 2. Figure Optical LIDAR return signal image

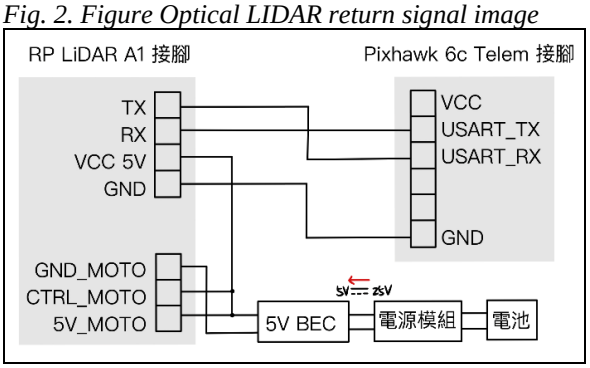

Fig. 3. Figure Optical LIDAR and Flight Controller Circuit Diagram

Table 1. Optical LIDAR Parameter Table

參數	Meaning
SERIAL5_PROTOCOL = 11	LiDAR360
SERIAL5_BAUD = 115	Baud Rate
PRX1_TYPE = 5	What type of

	proximity sensor is connected
PRX1_ORIENT = 0	Proximity sensor orientation

Flight control software

We developed a graphical user interface (GUI) using C# WinForm and integrated mavlink.net[4] to facilitate automated flight capture. Through Mavlink Parameter Protocol [5], we can modify the PID settings of the flight control, adjust parameters such as waypoint altitude, track number, waypoint wandering, gradient or spiral flight, and even configure landing or return mode.

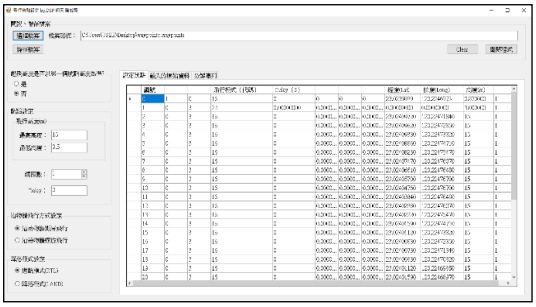

Fig. 3. Figure Waypoint Planning Graphical User Interface

Operational Workflow:

1. Obtain GPS information.
2. Plan the flight path through a Graphical User Interface (GUI).
3. Write the path into the flight controller.
4. Power on the onboard computer and check for connectivity with the flight controller.
5. Execute the planned route.
6. During the flight, utilize Optical Obstacle Avoidance to enable the aircraft to automatically navigate around objects or obstacles when approaching them closely, ensuring a certain level of safety.
7. Capture images during the flight.
8. Upload the captured images to the cloud using Python scripts and libraries such as GoogleAuth and GoogleDrive.
9. Retrieve image data from the cloud
10. Use instant-ngp for modeling purposes.

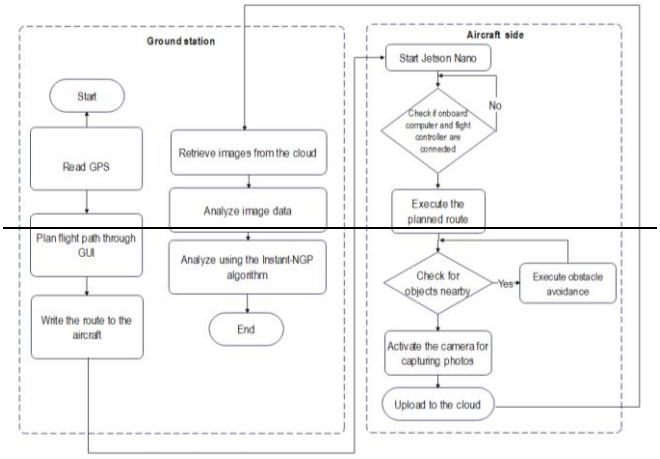

Fig. 4. Operation Workflow Chart

conclusion

Using GPS for location, planning waypoints in flight control software, capturing photos at each waypoint, uploading them to the cloud, and then automatically downloading them to a computer for analysis. Utilizing the Instant-NGP algorithm to reconstruct 3D models from the photos, all while incorporating obstacle avoidance for added safety.

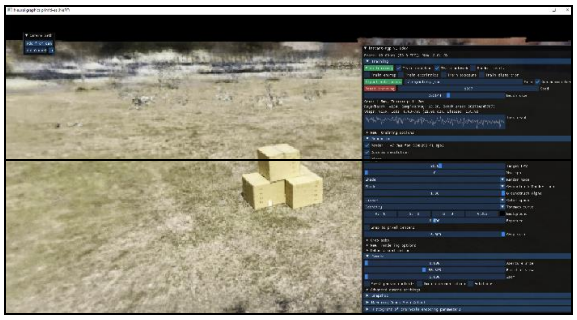

Fig. 1. Modeling results.

References:

[1] Stephens, J. (2022, January 14). Getting Started with NVIDIA Instant NeRFs. Nvidia Developer. https://developer.nvidia.com/blog/getting-started-with-nvidia-instant-nerfs/

[2] Ben Mildenhall, Pratul P. Srinivasan, Matthew Tancik, Jonathan T. Barron, Ravi Ramamoorthi, Ren Ng. (2020). NeRF: Representing Scenes as Neural Radiance Fields for View Synthesis. https://arxiv.org/abs/2003.08934

[3] B. Mildenhall, P. P. Srinivasan, M. Tancik, J. T. Barron, R. Ramamoorthi, and R. Ng, "NeRF: Representing scenes as neural radiance fields for view synthesis," in European conference on computer vision. Springer, 2020, pp. 405–421

[4] VFH algorithm, https://blog.csdn.net/minenine/article/details/107683316

[5] Mavlink Parameter Protocol, https://mavlink.io/en/services/parameter.html

A Deep Learning Framework for Steady-State Visual Evoked Potential Rapid Recognition - TransRANet

Yeou-Jiunn Chen* and Pin-Wei You

Department of Electrical Engineering, Southern Taiwan University of Science and Technology, Tainan, Taiwan
E-mail: chenyj@stust.edu.tw

Abstract

Steady-state visually evoked potentials (SSVEP) are specific neural responses generated within the parietal and occipital areas of the brain when exposed to flickering visual stimuli. In modern brain-computer interface (BCI) systems, SSVEP responses have been increasingly recognized as primary control signals. Their inherent high signal-to-noise ratio, swift transmission rate, and straightforward recording procedure make SSVEP advantageous over other signals. Such benefits, particularly the elimination of complex user training, have piqued the interest of numerous researchers in the field. As of late, SSVEP-BCIs have provided patients suffering from neuromuscular injuries with the ability to command various devices, enhancing their overall quality of life significantly. However, for BCIs to function optimally, the precise and consistent recognition of SSVEP is crucial. Addressing this need, our research presents a novel SSVEP identification system, inspired by transformer architectures, and integrates both ResNet and Attention mechanisms, named TransRANet. We rigorously tested our approach on a public benchmark dataset involving 35 subjects and 40 targets, later juxtaposing our findings with traditional techniques. The empirical outcomes underscored the superior efficacy of our proposed model in SSVEP detection, signaling its promising role in the evolution of SSVEP BCI systems.

1. Introduction

Brain-computer interfaces (BCI) facilitate communication between the human brain and external devices without the need for neural and muscular activity. As such, BCIs are ideally suited for development as assistive communication systems, aiding individuals with neuromuscular injuries in interacting with others. In contemporary BCI research, the majority of studies lean towards non-invasive BCIs that utilize electroencephalogram (EEG) signals as their mode of control. Given EEG's high temporal resolution, portability, and cost-effectiveness, EEG-based BCIs have been broadly integrated into a variety of applications [1].

The steady-state visually evoked potential (SSVEP) is an oscillatory response triggered by repetitive stimuli at certain consistent frequencies, aimed at provoking brain reactions in the primary visual cortex. These are captured in electroencephalograms, with the response frequency aligning with that of the flickering stimuli. When compared to other BCIs, SSVEP-based BCIs have emerged as one of the most successful interfaces due to their ease of recording and high signal-to-noise ratio [2]. As a result, SSVEP-based BCIs have found applications in various fields, such as visual spelling and decoding user intentions for operating assistive devices. Nonetheless, accuracy plays a pivotal role in determining the acceptance of SSVEP-based BCIs. Therefore, enhancing the accuracy of SSVEP-based BCIs is crucial for bolstering user acceptance.

2. Methods

In this study, we employ an architecture similar to the Transformer to develop an SSVEP-based BCI [3]. The TransRANet architecture is divided into five sections: input, time-frequency feature processing, channel combination, feature learning, and classification decision. We use the Fcomp (complex spectrum) from prior research as the neural network input. SSVEP data is typically acquired from multiple channels and includes various artifacts that can interfere with classification. Therefore, we use channel combination to compute a weighted combination of all channels, aiming to suppress noise and enhance the SSVEP components beneficial for classification. Subsequently, a residual attention mechanism is utilized for feature learning, allowing the model to better discriminate target features and amplify critical characteristics in the SSVEP signal. Finally, data decision classification is carried out through two fully connected layers.

3. Results

To validate the proposed method, a benchmark dataset consisting of 35 subjects was employed. Furthermore, a leave-one-subject-out approach was used to determine the performance of our model in a calibration-free and user-independent scenario. Experimental results showed that the TransRANet model proposed in this study achieved an accuracy rate of 80%.

4. Conclusion

In this study, we successfully developed an across-subjects classification system for SSVEP-based BCI, named TransRANet. Within the TransRANet architecture, we utilized channel combination to compute a weighted amalgamation of all channels, aiming to suppress noise and amplify the SSVEP components beneficial for classification. Furthermore, a residual attention mechanism was employed for feature learning to enhance key characteristics within the SSVEP signal. Experimental results indicated that

the proposed model outperformed other methods currently introduced, based on evaluations with public benchmark datasets. This demonstrates the considerable potential of the introduced TransRANet architecture for practical application and development in future SSVEP-based BCI systems.

References:

[1] J. R. Wolpaw, N. Birbaumer, D. J. McFarland, G. Pfurtscheller, and T. M. Vaughan, Brain–computer interfaces for communication and control. *Clinical neurophysiology*, **113**(6), 767−791 (2002).

[2] L. F. Nicolas-Alonso and J. Gomez-Gil, J. Brain Computer Interfaces, a Review. *Sensors*, **12**(2), 1211–1279 (2012).

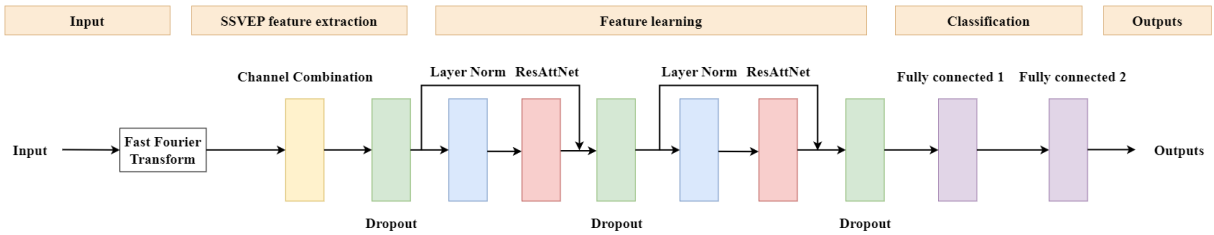

Fig. 1. Figure captions should be centered and placed below the figure.

Optical-Sensing Devices with Resonant-Cavity-Enhanced Structures of Porous-Silicon for Applications in Si-based Optoelectronic Integrated Circuits (OEIC's)

Kuen-Hsien Wu* and Hung-Yi Li

Department of Electrical Engineering, Southern Taiwan University of Science and Technology, Tainan, Taiwan
E-mail: khwu@stust.edu.tw

Abstract

Optical-sensing devices with highly ultra-violet photo-responses had been successfully implemented on Si substrates with resonant-cavity-enhanced (RCE) structures of porous-silicon and zinc-oxide Bragg reflectors. Because the fabrication of the developed devices was compatible to the standard silicon manufacturing process, the proposed RCE-devices are promising for applications in Si-based optoelectronic integrated circuits.

Porous silicon (PS) is a multi-functional material that has many unique features including modulated energy bandgap, high resistivity, extremely large surface-area-to-volume ratio and the same single-crystalline structure as the bulk-Si [1-2]. These advantages make this material especially suitable for optical-sensing applications. One of the importantly promising applications of PS is to develop Si-based optoelectronic integrated circuits (Si-OEIC's), in which PS electroluminescence devices combined with photodetectors, light wave-guides and other optical components are made monolithically on a single Si chip.

To realize Si-OEIC's, producing high-quality Si-based various photonic devices on Si substrate, including high-efficiency LEDs as well as high-performance photodetectors, is an important key point. The published studies revealed that PS photodetectors (PD) got high quantum efficiency and photoresponse, while they still suffered from some drawbacks, like large dark current, unstable device characteristics, luck of wavelength-selectivity and slow response speed [3-4].

The above problems can be solved by incorporation of resonant-cavity-enhanced (REC) structures. In a REC-PD, the absorption region is placed inside a Fabry-Pérot microcavity. For a specific wavelength of an incident light at the resonant condition, a constructive inference occurs within the cavity to enhance largely the internal optical field. The increased optical field allows PDs to be made thinner and therefore leads to wider bandwidth (BW) and higher quantum efficiency (QE) [5-6]. It is a significant approach to overcome the trade-off dilemma between QE and BW. Unfortunately, most of the RCE-PDs were made from compound semiconductors that are not compatible to Si-based fabrication process.

Zinc-oxide (ZnO) is a suitable material for use of constructing distributed-Bragg-reflectors (DBRs) and REC structures in the applications of optoelectronic devices [7-8]. This paper reported the fabrication of Si-based UV PDs with RCE structures on Si substrates, in which oxidized-nano-porous-Si (ONPS) active layers are sandwiched between ZnO upper reflectors and PS bottom DBRs. By incorporating the RCE structures, the developed photodetectors achieved much higher UV photoresponsivity as compared to the non-RCE devices.

In this work, the PS lower reflector of the REC structures were prepared on heavily doped n^+-type (100) Si substrates by periodically switching the etching current density in an anodic etching process. As followed, ONPS thin layers that serve as the central layers were formed by electrochemical-etching process with low etching current density and a subsequent rapid-thermal-oxidization (RTO) process. Thereafter, ZnO films were deposited on ONPS by a sol-gel spin coating process [9-10] to serve as the upper reflector. Finally, inter-digitated nickel (Ni) electrodes were evaporated on the front sides of the devices to complete the structure of the optical-sensing devices. The schematic device structure of the developed REC-PD is illustrated in Fig.1.

Figure 2 shows the SEM image of a cross-sectional structure of the fabricated REC-PD on a Si substrate. It can be observed that a 250-nm active layer of ONPS is located between the ZnO upper reflector and the bottom PS-DBR. The optical bandgap of the ONPS layer was estimated about 4.0 eV from the Tauc's plot. The PS-DBR is composed of 3-period L/H PS double layers, in which the low porosity layer (L) is about 0.4μm and high porosity layer (H) is about 0.5μm.

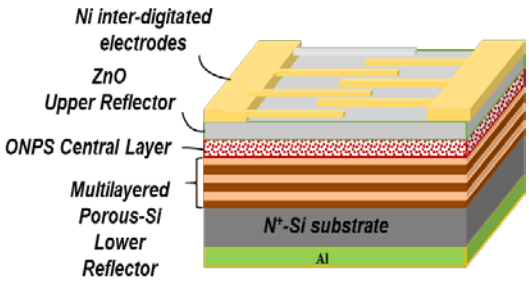

Fig. 1. The schematic device structure of the developed REC-PD.

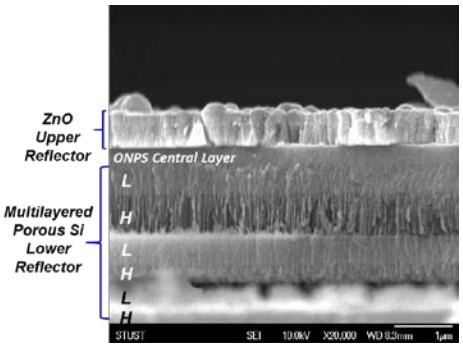

Fig. 2. The SEM image of the cross-sectional structure of the fabricated REC-PD on a Si substrate.

From the SEM image, it can be observed that the prepared ZnO films by the spin coating sol-gel method has good crystallinity and well film-quality [12], indicating the stress coming from the material mismatch between ZnO and ONPS was greatly relieved. The high quality of the ZnO upper reflectors is crucial for implementing REC structures.

With the PS-DBR, the REC-PD got high photoresponsivity of 88 mA/W that is twice larger than that of a non-REC device without a PS-DBR at an incident light of 265nm, as shown in Fig.3. It is thought that the enhanced UV photoresponses is mainly owing to the RCE effect appearing in the devices after introducing the bottom PS-DBR, which effectively enhanced the light-absorption of ONPS active layers and hence the photocurrent of devices. As shown in Fig.4, the developed REC-PD obtained a high photo-to-dark current ratio (PDCR) of 87 at 5V for an incident light of 265nm, indicating that the proposed REC-PD have high UV-sensing sensitivity and selectivity.

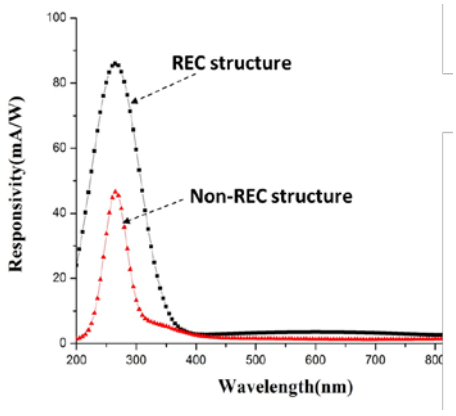

Fig. 3. Spectral photoresponses of Si-based photodetectors with a REC and a non-REC structure.

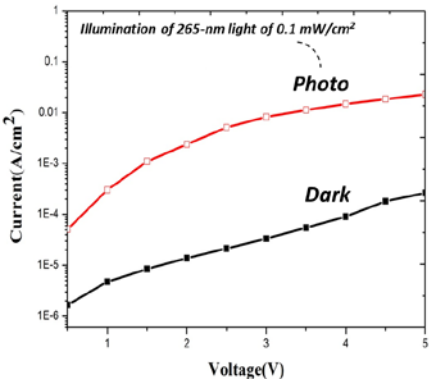

Fig. 4. Photo- and dark current-voltage characteristics of the developed REC-PD

Si-based REC-PDs with high UV photoresponses and large PDCR were successfully developed on Si substrates by use of conventional Si-compatible fabrication processes. The experimental results demonstrated that the developed technology is very promising for fabrication of high-performance Si-based photodetectors in Si-OEIC's applications.

References:

[1] R. L. Smith and S. D. Collins, *J. Appl. Phys.*, **71**, R1-R22 (1992).

[2] V. Parkhutik, *Solid-State Electronics*, **43**, 1121-1141 (1999).

[3] R. J. Martin-Palma, R. Guerrero-Lemus, J. D. Moreno, J. M. Martmez-Duart, A. Gras, D. Levy, *Materials Science and Engineering*, **B69-70**, pp. 87-91 (2000).

[4] L. A. Balagurov, S. C. Bayliss, S. Ya. Andnishm, A. F. Orlov, B. Unal, D. G. Yarkin, E. A. Petrova, *Solid-Slate Electronics*, **45**, 1607-1611 (2001).

[5] M. K. Emsley, O. Dosummu and M. S. Ünlü, *IEEE Photon. Technol. Lett.*, **14**, 519-521 (2002).

[6] K. Kishino, M. S. Ünlü, J. Chyi, J. Reed, and H. Markoç, *IEEE J. Quantum Electron.*, **27**, 2025-2034 (1991).

[7] Aqing Chen, Zhian Chen, Kaigui Zhu, and Zhenguo Ji, **19**, 6 pages (2017).

[8] Y. S. Huang, C. C. Chang, J. W. Lee, Y. C. Lee, C. C. Huang, Z. K. Wun and K. K. Tiong, *Phys. Scr.*, **T157**, 014034, 4 pages (2013).

[9] C. Shaoqiang, Z. Jian, F. Xiaoa, W. Xiaohua, L. laiqiang, S. Yanling, X. Qingsong, W. Chang Z. Jianzhong and Z. Ziqiang, *Applied Surface Science*, **241**, 348-391 (2005).

[10] T. Ivanova, A. Harizanova, T. Koutzarova and B. Vertruyen, *Materials Letters*, **64**, 1147-1149 (2010).